

# UC San Diego

## UC San Diego Electronic Theses and Dissertations

### Title

Biomimetic Nanoparticles for Targeted Delivery and Removal

### Permalink

<https://escholarship.org/uc/item/4983z3nf>

### Author

Dehaini, Diana

### Publication Date

2019

Peer reviewed|Thesis/dissertation

UNIVERSITY OF CALIFORNIA SAN DIEGO

**Biomimetic Nanoparticles for Targeted Delivery and Removal**

A dissertation submitted in partial satisfaction of the requirements for the degree Doctor of  
Philosophy

in

Nanoengineering

by

Diana Dehaini

Committee in charge:

Professor Liangfang Zhang, Chair  
Professor Shaochen Chen  
Professor Yi Chen  
Professor Andrew C. Kummel  
Professor Dong-Er Zhang

2019

©

Diana Dehaini, 2019

All rights reserved

The Dissertation of Diana Dehaini is approved, and it is acceptable in quality and form for publication on microfilm and electronically:

---

---

---

---

---

Chair

University of California San Diego

2019



## **DEDICATION**

This dissertation is dedicated my family, who encouraged me to learn and explore from a young age, to my husband, who provided loving support and stability during my PhD, and to my mentors and coworkers, who helped me grow to be the person I am today. I will be forever grateful to each and every one of the people who have inspired me to design and develop new ideas, and those who taught me to turn creativity into scientific productivity.

## EPIGRAPH

*"I am among those who think that science has great beauty. A scientist in his laboratory is not a mere technician: he is also a child confronting natural phenomena that impress him as though they were fairy tales."*

*Marie Curie*

## TABLE OF CONTENTS

Signature Page .....	iii
Dedication .....	iv
Epigraph .....	v
Table of Contents .....	vi
List of Figures .....	xi
Acknowledgements .....	xii
Vita .....	xvi
Abstract of the Dissertation .....	xviii
Chapter 1 Introduction .....	1
1.1 Biomimetic Strategies for Targeted Nanoparticle Delivery .....	2
1.1.1 Introduction .....	2
1.1.2 Small Molecules .....	5
1.1.3 Carbohydrates .....	7
1.1.4 Peptides .....	11
1.1.5 Proteins .....	16
1.1.6 Pathogen-derived particles .....	20
1.1.7 Mammalian cell membranes .....	22
1.1.8 Conclusions .....	27
Chapter 2 Ultra-Small Lipid Polymer Hybrid NP for Drug Delivery .....	45
2.1 Nanoparticles for Tumor Penetrating Drug Delivery .....	46
2.1.1 Introduction .....	46
2.1.2 Materials and Methods .....	49
2.1.3 Results and Discussion .....	54
2.1.4 Conclusions .....	66
Chapter 3 Red Blood Cell Membrane Coated Nanoparticles as a Drug Delivery Platform .....	71
3.1 Erythrocyte Membrane-Cloaked Polymeric Nanoparticles for Controlled Drug Loading and Release .....	72
3.1.1 Introduction .....	72
3.1.2 Experimental Methods .....	73
3.1.3 Results and Discussion .....	78
3.1.4 Conclusions .....	89

3.2 Interfacial Interactions Between Natural RBC Membranes and Synthetic Polymeric Nanoparticles .....	95
3.2.1 Introduction.....	95
3.2.2 Experimental Methods .....	97
3.2.3 Results and Discussion .....	100
3.2.4 Conclusions.....	108
3.3 Safe and Immunocompatible Canocarriers Cloaked in RBC Membranes for Drug Delivery to Treat Solid Tumors .....	112
3.3.1 Introduction.....	112
3.3.2 Experimental Methods .....	113
3.3.3 Results and Discussion .....	116
3.3.4 Conclusions.....	124
3.4 Remote Loading of Small Molecule Therapeutics into Cholesterol-Enriched Cell Membrane-Derived Vesicles .....	130
3.4.1 Introduction.....	130
3.4.2 Results and Discussion .....	133
3.4.3 Experimental .....	139
3.4.4 Conclusions.....	145
3.5 Nanoparticle-Based Anti-Virulence Vaccine for the Management of Methicillin-Resistant Staphylococcus aureus Skin Infection.....	149
3.3.1 Introduction.....	149
3.3.2 Results and Discussion .....	151
3.3.3 Materials and Methods.....	159
3.3.4 Conclusions.....	163
Chapter 4 Platelet and Neutrophil Membrane Coated Nanoparticles for Inflammation Targeting .....	168
4.1 Nanoparticle Functionalization with Platelet Membrane Enables Multi-Factored Biological Targeting and Detection of Atherosclerosis.....	169
4.1.1 Introduction.....	169
4.1.2 Materials and Methods.....	171
4.1.3 Results and Discussion .....	176
4.1.4 Conclusions.....	186
4.2 Neutrophil Membrane-Coated Nanoparticles Suppress Synovial Inflammation and Ameliorate Joint Destruction in Inflammatory Arthritis .....	192
4.2.1 Introduction.....	192

4.2.2 Results and Discussion .....	195
4.2.3 Materials and Methods.....	210
4.2.4 Conclusions.....	222
Chapter 5 Cell Membrane Fusion Platforms for Multifunctional Nanoparticles .....	229
5.1 Erythrocyte-Platelet Hybrid Membrane Coating for Enhanced Nanoparticle Functionalization.....	230
5.1.1 Introduction.....	230
5.1.2 Results and Discussion .....	231
5.1.3 Materials and Methods.....	239
5.1.4 Conclusions.....	245
5.2 Hybrid Biomembrane-Functionalized Nanorobots for Concurrent Removal of Pathogenic Bacteria and Toxins.....	249
5.2.1 Introduction.....	249
5.2.2 Results and Discussion .....	254
5.2.3 Experimental .....	265
5.2.4 Conclusions.....	270
Chapter 6 Conclusions .....	277

## LIST OF FIGURES

<b>Figure 1.1.1</b>	Schematic of biomimetic targeting strategies.....	3
<b>Figure 1.1.2</b>	Examples of targeting strategies using small molecules .....	6
<b>Figure 1.1.3</b>	Examples of targeting strategies using carbohydrates.....	9
<b>Figure 1.1.4</b>	Examples of targeting strategies using peptides.....	13
<b>Figure 1.1.5</b>	Examples of targeting strategies using proteins .....	18
<b>Figure 1.1.6</b>	Examples of targeting strategies using pathogen-derived particles.....	21
<b>Figure 1.1.7</b>	Examples of targeting strategies using mammalian cell membranes .....	23
<b>Figure 2.1.1</b>	Schematic of synthesis and physicochemical characterization .....	48
<b>Figure 2.1.2</b>	Optimization of ultra-small hybrid nanoparticle fabrication .....	56
<b>Figure 2.1.3</b>	Ultra-small hybrid nanoparticle stability studies.....	57
<b>Figure 2.1.4</b>	Introduction of targeting functionality .....	58
<b>Figure 2.1.5</b>	Drug loading and characterization of ultra-small hybrid nanoparticles ..	62
<b>Figure 2.1.6</b>	In vivo characterization of ultra-small hybrid nanoparticles.....	64
<b>Figure 2.1.7</b>	In vivo antitumor efficacy . .....	65
<b>Figure 3.1.1</b>	Preparation process RBC NPs .....	78
<b>Figure 3.1.2</b>	Doxorubicin loading yields in the RBC NPs.....	80
<b>Figure 3.1.3</b>	<i>In vivo</i> stability test and morphology of doxorubicin-loaded particles ...	82
<b>Figure 3.1.4</b>	Drug release profiles and kinetics. ....	85
<b>Figure 3.1.5</b>	Cytotoxicity study in leukemia cell line .....	89
<b>Figure 3.2.1</b>	Controlled CD47 functionalization enabled by RBC membrane .....	96
<b>Figure 3.2.2</b>	Characterization and quantification of CD47 on the RBC-NPs .....	101

<b>Figure 3.2.3</b> CD47 orientation on the RBC-NPs .....	106
<b>Figure 3.2.4</b> Inhibition of macrophage uptake.....	107
<b>Figure 3.3.1</b> Physicochemical characterization and drug loading of RBC-NPs. ....	118
<b>Figure 3.3.2</b> In vitro antitumor efficacy and uptake .....	119
<b>Figure 3.3.3</b> In vivo treatment of solid tumors .....	120
<b>Figure 3.3.4</b> In vivo treatment of solid tumors. ....	122
<b>Figure 3.3.5</b> In vivo immunogenicity of RBC-NP.....	124
<b>Figure 3.4.1.</b> Schematic of remote loading into RBC vesicles .....	131
<b>Figure 3.4.2.</b> Remotely loaded RBC vesicles fabrication .....	132
<b>Figure 3.4.3</b> Characterization of cholesterol-enriched RBC vesicles .....	133
<b>Figure 3.4.4.</b> Dox loading into RBC vesicles .....	135
<b>Figure 3.4.5.</b> Antitumor activity of Dox-RBC .....	136
<b>Figure 3.4.6.</b> Vanc loading into RBC vesicles .....	138
<b>Figure 3.5.1.</b> Schematic of nanotoxoid protection against MRSA infection. ....	152
<b>Figure 3.5.2.</b> Nanotoxoid(Hla) characterization .....	153
<b>Figure 3.5.3.</b> Germinal center formation and antibody production .....	155
<b>Figure 3.5.4.</b> Effect of nanotoxoid vaccination on MRSA skin colonization.....	156
<b>Figure 3.5.5.</b> Effect of nanotoxoid vaccination on MRSA invasiveness .....	158
<b>Figure 4.1.1.</b> Platelet membrane-coated nanoparticle characterization .....	178
<b>Figure 4.1.2.</b> In vitro targeting of PNPs to atherosclerosis .....	180
<b>Figure 4.1.3.</b> Ex vivo binding to atherosclerotic plaque .....	181
<b>Figure 4.1.4</b> In vivo targeting of atherosclerotic plaque.....	183
<b>Figure 4.1.5.</b> Live imaging of atherosclerotic plaque .....	184

<b>Figure 4.2.1.</b> Preparation and characterization of neutrophil-NPs.....	194
<b>Figure 4.2.2.</b> Neutrophil-NPs inhibit pro-arthritis factors in vitro.....	197
<b>Figure 4.2.3.</b> Neutrophil-NPs enhance cartilage penetration .....	202
<b>Figure 4.2.4.</b> Neutrophil-NPs ameliorate joint destruction in a mouse.....	206
<b>Figure 4.2.5.</b> Neutrophil-NPs ameliorate joint destruction.....	209
<b>Figure 5.1.1.</b> Fabrication of RBC-platelet hybrid membrane-coated .....	232
<b>Figure 5.1.2.</b> Physicochemical characterization of hybrid particles .....	233
<b>Figure 5.1.3.</b> Nanoparticle stability.....	235
<b>Figure 5.1.4.</b> Protein characterization .....	236
<b>Figure 5.1.5.</b> Membrane biological function assays .....	237
<b>Figure 5.1.6.</b> In vivo characterization .....	239
<b>Figure 5.2.1.</b> Preparation and characterization of RBC-PL-robots.....	253
<b>Figure 5.2.2.</b> Propulsion performance and anti-biofouling.....	255
<b>Figure 5.2.3.</b> Binding and isolation of PL-adhering pathogens .....	257
<b>Figure 5.2.4.</b> Binding and neutralization of $\alpha$ -toxins .....	258
<b>Figure 5.2.5.</b> In situ concurrent removal of MRSA bacteria.....	263



## ACKNOWLEDGEMENTS

First and foremost, I would like to thank my advisor, Professor Liangfang Zhang. I am deeply grateful he allowed me the opportunity to learn and grow in his lab beginning in 2011. I am dually grateful he believed in my ability to do meaningful research on my own, and helped me continue from undergraduate to graduate research in his lab. I have learned so much, and have grown into a different person than I would have become without his mentorship and the opportunity he provided me.

The help and support of my labmates made my PhD possible. Together we built a collaborative environment, which made my years of grad school actually enjoyable. We weren't just working independently on research in parallel, but actively collaborating to create a larger story, where each of us led our own chapter. I would have been only a fraction as productive and well-published without my labmates, and I enjoyed every moment of growth with these amazing scientists. A special thank you to Ronnie Fang, for helping me grow as a researcher and writer, and a person. Ronnie truly embodies the spirit of self improvement and excellence, and can excel (and teach others to excel) at anything he chooses. I would like to thank Ashley Kroll, Yao Jiang and Xiaoli Wei for being both my labmates and my officemates, and supporting me emotionally and intellectually over the years. They are some of the strongest and smartest women I know, and I don't know where I'd be without them. I respect and value all the members of Dr. Zhang's lab who have similarly helped me grow and learn over the years: Dr. Che-Ming Hu, Dr. Weiwei Gao, Dr. Brian Luk, Dr. Pavimol Angsantikul, Yue Zhang, Qiangzhe Zhang, Sarah Masson, and too many others to list.

Thank you to the National Institutes of Health for supporting me and providing my stipend and school fees over the past few years, and for believing in the scientific merit behind

my proposal on disease targeted platelet nanoparticles. This funding was crucial to my financial ability to pursue my PhD and I am extremely grateful.

I would like to thank the Nanoengineering Department at UC San Diego, with all its faculty and administrative staff, for their help and support over the years. I took a chance and chose a young field with brand new bachelors program, and they took a chance by accepting 18-year-old me. A special thanks to Dana Jiminez, I deeply appreciate all her cheery and knowledgeable help over the years.

I am extremely grateful UC San Diego is the hub of scientific advancement that it is, and that I was allowed a place here. UC San Diego has been my work and home for almost nine years, and I have become a different person from the ideas, growth, and inspiration I've experienced here. I was born at UCSD hospital, I met my husband in the Revelle College dorms at UCSD, and I even got married at a UCSD venue, Scripps Seaside Forum. Thank you, UCSD, for playing such a central role in my life. I cannot wait to see the new ideas and advancements that happen here in the future.

Chapter 1, in full, is a reprint of the material as it appears in Bioengineering and Translational Medicine, 2016, Diana Dehaini, Ronnie H. Fang, and Liangfang Zhang. The dissertation author was the primary author.

Chapter 2, in full, is a reprint of the material as it appears in Nanoscale, 2016, Diana Dehaini, Ronnie H. Fang, Brian T. Luk, Zhiqing Pang, Che-Ming J. Hu, Ashley V. Kroll, Chun Lai Yu, Weiwei Gao, and Liangfang Zhang. The dissertation author was the primary author.

Chapter 3.1, in full, is a reprint of the material as it appears in Nanomedicine, 2013, Aryal, S.; Hu, C-M.; Fang, R.; Dehaini, D.; Carpenter, C.; Zhang, D-E.; Zhang, L. The dissertation author was a major contributor and co-author of this paper.

Chapter 3.2, in full, is a reprint of the material as it appears in *Nanoscale*, 2014, Brian Luk, Che-Ming Hu, Ronnie Fang, Diana Dehaini, Cody Carpenter, Weiwei Gao, and Liangfang Zhang. The dissertation author was a major contributor and co-author of this paper.

Chapter 3.3, in full, is a reprint of the material as it appears in *Theranostics*, 2016, Luk, B.; Fang, R.; Hu, C-M.; Copp, J.; Thamphiwatana, S.; Dehaini, D.; Gao, W.; Zhang, K.; Li, S.; Zhang, L. The dissertation author was a major contributor and co-author of this paper.

Chapter 3.4 is, in full, is a reprint of the material as it appears in *Angewandte Chemie International Edition*, 2018, Zhang, X.; Angsantikul, P.; Ying, M.; Zhuang, J.; Zhang, Q.; Wei, X.; Jiang, Y.; Zhang, Y.; Dehaini, D.; Chen, M.; Chen, Y.; Gao, W.; Fang, R.; Zhang, L. The dissertation author was a major contributor and co-author of this paper.

Chapter 3.5, in full, is a reprint of the material as it appears in *Advanced Functional Materials*, 2016, Fei Wang, Ronnie H. Fang, Brian T. Luk, Che-Ming J. Hu, Soracha Thamphiwatana, Diana Dehaini, Pavimol Angsantikul, Ashley V. Kroll, Zhiqing Pang, Weiwei Gao, Weiyue Lu, and Liangfang Zhang. The dissertation author was a major contributor and co-author of this paper.

Chapter 4.1, in full, is a reprint of the material as it appears in *ACS Nano*, 2019, Wei, X.; Ying, M.; Dehaini, D.; Su, Y.; Kroll, A.; Zhou, J.; Gao, W.; Fang, R.; Chien, S. and Zhang, L. The dissertation author was a major contributor and co-author of this paper.

Chapter 4.2 is, in full, is a reprint of the material as it appears in *Nature Nanotechnology*, 2018, Qiangzhe Zhang, Diana Dehaini, Yue Zhang, Julia Zhou, Xiangyu Chen, Lifan Zhang, Ronnie H. Fang, Weiwei Gao, Liangfang Zhang. The dissertation author was a major contributor and co-author of this paper.

Chapter 5.1 is, in full, is a reprint of the material as it appears in *Advanced Materials*, 2017, Dehaini, D.; Wei, X.; Fang, R.; Masson, S.; Angsantikul, P.; Luk, B.; Zhang, Y.; Ying, M.; Jiang, Y.; Kroll, A.; Gao, W.; Zhang, L. The dissertation author was the primary author.

Chapter 5.2, in full, is a reprint of the material as it appears in *Science Robotics*, 2018, Berta Esteban-Fernández de Ávila, Pavimol Angsantikul, Doris E. Ramírez-Herrera, Fernando Soto, Hazhir Teymourian, Diana Dehaini, Yijie Chen, Liangfang Zhang and Joseph Wang. The dissertation author was a contributor and co-author of this paper.

## VITA

- 2014 B.S. in Nanoengineering, University of California San Diego
- 2016 M.S. in Nanoengineering, University of California San Diego
- 2019 Ph.D. in Nanoengineering, University of California San Diego

## PUBLICATIONS

1. Aryal, S.; Hu, C-M.; Fang, R.; Dehaini, D.; Carpenter, C.; Zhang, D-E.; Zhang, L. Erythrocyte membrane-cloaked polymeric nanoparticles for controlled drug loading and release, *Nanomedicine* 2013, 8, 1271-1280
2. Luk, B.T., Hu, C.M.J., Fang, R.H., Dehaini, D., Carpenter, C., Gao, W. and Zhang, L., 2014. Interfacial interactions between natural RBC membranes and synthetic polymeric nanoparticles. *Nanoscale*, 6(5), pp.2730-2737
3. Hu, C.M.J., Fang, R.H., Wang, K.C., Luk, B.T., Thamphiwatana, S., Dehaini, D., Nguyen, P., Angsantikul, P., Wen, C.H., Kroll, A.V. and Carpenter, C....Zhang, L., 2015. Nanoparticle biointerfacing by platelet membrane cloaking. *Nature*, 526(7571), pp.118-121.
4. Wang, F., Fang, R.H., Luk, B.T., Hu, C.M.J., Thamphiwatana, S., Dehaini, D., Angsantikul, P., Kroll, A.V., Pang, Z., Gao, W. and Lu, W., Zhang, L. 2016. Nanoparticle - Based Antivirulence Vaccine for the Management of Methicillin - Resistant *Staphylococcus aureus* Skin Infection. *Advanced Functional Materials*.
5. Luk, B.T., Fang, R.H., Hu, C.M.J., Copp, J.A., Thamphiwatana, S., Dehaini, D., Gao, W., Zhang, K., Li, S. and Zhang, L., 2016. Safe and immunocompatible nanocarriers cloaked in RBC membranes for drug delivery to treat solid tumors. *Theranostics*, 6(7) p.1004.
6. Dehaini, D., Fang, R.H., Luk, B.T., Pang, Z., Hu, C.M.J., Kroll, A.V., Yu, C.L., Gao, W. and Zhang, L., 2016. Ultra-small lipid-polymer hybrid nanoparticles for tumor-penetrating drug delivery. *Nanoscale*, 8(30), pp.14411-14419.
7. Dehaini, D., Fang, R.H. and Zhang, L., 2016. Biomimetic strategies for targeted nanoparticle delivery. *Bioengineering & Translational Medicine*.
8. Wei, X., Gao, J., Fang, R.H., Luk, B.T., Kroll, A.V., Dehaini, D., Zhou, J., Kim, H.W., Gao, W., Lu, W. and Zhang, L., 2016. Nanoparticles camouflaged in platelet membrane coating as an antibody decoy for the treatment of immune thrombocytopenia. *Biomaterials*, 111, pp.116-123.
9. Dehaini, D., Xiaoli Wei, Ronnie H. Fang, Sarah Masson, Pavimol Angsantikul, Brian T. Luk, Yue Zhang, Man Ying, Yao Jiang, Ashley V. Kroll, Weiwei Gao, Liangfang Zhang.

- Erythrocyte–Platelet Hybrid Membrane Coating for Enhanced Nanoparticle Functionalization. *Advanced Materials*, 29(16) 2017.
10. Zhang, X.; Angsantikul, P.; Ying, M.; Zhuang, J.; Zhang, Q.; Wei, X.; Jiang, Y.; Zhang, Y.; Dehaini, D.; Chen, M.; Chen, Y.; Gao, W.; Fang, R.; Zhang, L.\* "Remote loading of small molecule therapeutics into cholesterol-enriched cell membrane-derived vesicles", *Angewandte Chemie International Edition* 2017, 56, 14075-14079.
  11. Kroll, A.; Fang, R.; Jiang, Y.; Zhou, J.; Wei, X.; Yu, C-L.; Gao, J.; Luk, B.; Dehaini, D.; Gao, W.; Zhang, L. Nanoparticulate delivery of cancer cell membrane elicits multi-antigenic antitumor immunity, *Advanced Materials* 2017, 29, 1703969.
  12. Wei, X.; Ying, M.; Dehaini, D.; Su, Y.; Kroll, A.; Zhou, J.; Gao, W.; Fang, R.; Chien, S.; Zhang, L. Nanoparticle functionalization with platelet membrane enables multi-factored biological targeting and detection of atherosclerosis, *ACS Nano* 2018, 12, 109-116.
  13. Ying, M.; Zhuang, J.; Wei, X.; Zhang, X.; Zhang, Y.; Jiang, Y.; Dehaini, D.; Chen, M.; Gu, S.; Gao, W.; Lu, W.; Fang, R.; Zhang, L. Remote-loaded platelet vesicles for disease-targeted delivery of therapeutics, *Advanced Functional Materials* 2018, 28, 1801032.
  14. Esteban-Fernandez de Avila, B.; Angsantikul, P.; Ramirez-Herrera, D.; Soto, F.; Teymourian, H.; Dehaini, D.; Chen, Y.; Zhang, L., Wang, J. Hybrid-biomembrane functionalized nanorobots for concurrent removal of pathogenic bacteria and toxins, *Science Robotics* 2018, 3, eaat0485.
  15. Zhang, Q.; Dehaini, D.; Zhang, Y.; Zhou, J.; Chen, X.; Zhang, L.; Fang, R.; Gao, W.; Zhang, L. Neutrophil membrane-coated nanoparticles inhibit synovial inflammation and alleviate joint damage in inflammatory arthritis, *Nature Nanotechnology* 2018, 13, 1182-1190.

## **ABSTRACT OF THE DISSERTATION**

### **Biomimetic Nanoparticles for Targeted Delivery and Removal**

by

Diana Dehaini

Doctor of Philosophy in Nanoengineering

University of California San Diego, 2019

Professor Liangfang Zhang, Chair

Nanoparticle drug delivery has revolutionized the way we think of disease treatment over the last decade. The encapsulation of drugs into nanoparticles has led to better bioavailability, longer circulation times and an extended therapeutic window, and fewer off target effects than free drug administration. Nanoparticles are able to be tailored to specific applications through their size, shape, and surface design. Nanoparticles are just beginning to see clinical translation and FDA approval. Recently, significant efforts have been put into creating biomimetic targeting, particularly utilizing cell membrane coatings. Cell membrane can be used as a biomaterial to “cloak” nanoparticles, endowing them with the surface properties of the parent

cell. Each different cell type in the body has a distinct surface structure with lipids, proteins, and receptors perfectly tailored to its purpose and location. Some of these proteins, such as CD47 or the selectins, have well known purposes like immune evasion or specific receptor targeting respectively. Additionally, there are yet undescribed and uncharacterized surface moieties on cells whose properties can be retained by using the entire cell membrane as a biomaterial. By cloaking nanoparticles in cell membrane, they retain many of the properties of the original cell type. We show that this allows for new biointerfacing abilities and a highly specific drug delivery vehicle. This new technology also promises future clinical translation, as the materials are inherently biocompatible.

Herein, we will discuss engineered nanoparticle platforms that utilize this biomimetic cell membrane coating technology to improve the delivery of drugs, and additionally the detoxification and removal of pathogens. The biomimetic techniques developed during this PhD range from novel formulations of classical small molecule targeting for cancer therapy, to new methods of utilizing a fusion of natural cell membranes to create custom tailored targeting. These improvements to the field of targeted drug delivery will hopefully lead to better use of drugs and treatment of disease, and a higher level of tailoring ability available to engineers designing future platforms.



# Chapter 1

---

Introduction

# **Biomimetic Strategies for Targeted Nanoparticle Delivery**

## **1.1 Introduction**

The advent of nanoparticle technology has enabled the development of a wide range of novel therapeutic and diagnostic platforms. Employing nanoparticulate delivery vehicles offers many distinct advantages, including the solubilization of hydrophobic payloads, extended blood residence times, and the ability to better target a region of interest.[1-3] One area in which nanoparticles have particularly excelled is cancer treatment, where there are numerous clinically approved nanoformulations of chemotherapeutics indicated for a variety of cancer types.[4] At their size scale, nanoparticles can take advantage of the enhanced permeation and retention (EPR) effect, enabling them to preferentially localize to tumor vasculature.[5, 6] First generation nanoparticle therapeutics generally relied on this passive targeting mechanism to improve efficacy over traditional free-drug formulations, which often have severe systemic side effects. As nanoparticle technology has further matured, researchers have found ways to easily introduce ligands onto their surfaces. This has enabled the development of actively targeted formulations, which take advantage of very specific binding interactions with their targets to further enhance delivery. Such a targeting strategy enables the fabrication of nanoparticle platforms for the treatment and detection of diseases beyond cancer, where the EPR effect does not exist. As the result of significant research on the subject, there are many targeted nanoformulations that are currently under clinical investigation.[7]

Traditional targeting ligands can broadly be characterized into a few different categories, including small molecules, peptides, aptamers, and antibodies. These ligands are generally

incorporated onto nanoparticle surfaces by means of facile conjugation chemistries, either pre- or post-synthesis.[8, 9] Other strategies involve pre-conjugation onto an anchoring molecule followed by post-insertion via physical interactions.[10] While most of these traditional ligands exist in certain forms within living systems,[11] their use as agents for targeted delivery generally depends on workflows to create novel specificities not found naturally. This is done via approaches that require extensive screening. For example, new aptamers or peptides with high binding affinities to desired targets can be discovered via systematic evolution of ligands by exponential enrichment (SELEX) or phage display, respectively.[12, 13] Monoclonal antibodies are generated by screening hybridomas derived from the B cells of antigen-exposed organisms. Because, in the absence of autoimmunity, B cells that produce antibodies against most endogenous targets are usually subject to negative selection, most antibodies for clinical use further go through a humanization process.[14, 15] Ultimately, these methods of targeting ligand generation enable the creation of wide-ranging specificities against almost any target.

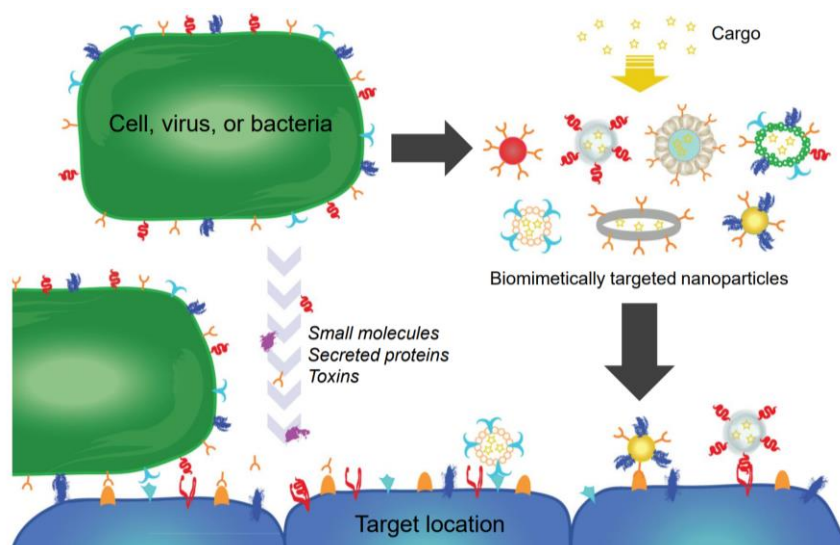


**Figure 1.1.1** Schematic of biomimetic targeting strategies. Targeting affinities exist among cells, small molecules, proteins, and toxins. These can be directly leveraged to create targeted nanoparticle formulations for therapeutics and imaging.

Despite the flexibility offered by traditional routes of targeting ligand discovery, there has more recently been a significant focus on deliberately leveraging targeting specificities found directly in nature for the creation of targeted nanodelivery systems (**Figure 1**). The movement towards biomimetic systems has been ushered in by an increased understanding of the different biological interactions that exist within the body.[16, 17] One major advantage of such an approach is the reliance on biological mechanisms that have already been optimized by evolution over the course of millions of years. In the field of nanomedicine, one recent example has involved the enhancement of nanoparticle circulation time and the immune evasion properties.[18] This is an area where synthetic polyethylene glycol (PEG) coatings, which present a steric barrier for decreased biological interactions, have long been the gold standard.[19, 20] Biomimetic methods, rather than attempt to stealth themselves from the immune system, directly interact act with it in order to convince the body that it belongs. Examples include use of red blood cell (RBC)-derived immunomodulatory signals or even the direct use of RBC membrane as a surface coating material.[21-23] Regarding targeting applications, there are countless receptor-ligand, binding, and adhesion interactions that can be taken advantage of. Natural targeting mechanisms exist both within and across different species; they can be sourced from many different organisms, ranging from pathogens to mammalian cells, and vary greatly in form and function, ranging from small molecules for targeting nutrient receptors to whole cell membranes for the faithful replication of multiple cell functions. Taking advantage of the way cells naturally interact with each other and their environment opens new avenues for the development targeted therapeutics.

In this review, we specifically focus on biomimetic nanoparticle platforms that employ targeting specificities that can be found naturally in living systems. We begin our discussion with the use of individual targeting ligands such as small molecules, carbohydrate-based structures, and

peptides. Also in this category is the use of whole proteins, both secreted and membrane-bound. Subsequently, pathogen-derived nanostructures, both from viruses and bacteria, are covered. The final topic we will discuss involves the direct use of cellular membranes as a means to introduce both nanoparticle targeting functionality and efficient interfacing capabilities with the body's biological systems. In each section, we first introduce the targeting functionality in its natural context before describing current works that employ it. The review concludes with our thoughts on the future of biomimetic targeting.

## 1.2 Small Molecules

### Folate

Folate, or vitamin B<sub>9</sub>, is an example of a naturally occurring ligand that has been widely used by researchers to introduce targeting functionalization onto nanoparticles. The molecule is essential to cellular function, as it plays a major role in DNA and RNA production.[24] On cancer cells, the overexpression of folate receptors is commonly seen, which helps to drive their aggressive phenotypes.[25, 26] It has been demonstrated that, by adding folate molecules to the surface of nanoparticles, it is possible to preferentially target folate receptor-overexpressing cancer cells.[27, 28] For drug delivery, this has enabled more effective localization of nanoparticle-loaded chemotherapeutic to tumor sites.[27-29] Red blood cell membrane-coated nanoparticles have been functionalized with lipid-PEG-anchored folate, which can be inserted post-synthesis to preserve the biological function of the natural coating (**Figure 2a-c**).[10] The resulting targeted nanoparticle showed significantly enhanced uptake in a folate receptor-overexpressing KB cell line. In a different work, doxorubicin-loaded heparin-folate-paclitaxel nanoparticles were able to both

extend release of the drug *in vitro* and localize within tumors *in vivo*, significantly slowing their growth (Figure 2d).[30] Microbubbles have been of interest lately in ultrasound-mediated cancer therapy, and folate-targeted microbubbles have been fabricated, improving the ability of the particles to localize to tumor and subsequently ablate them.[31] Beyond drug delivery, this targeting strategy has also been used extensively in imaging applications. For example, folate-functionalized iron oxide nanoparticles have been used to detect cancer using MRI.[32] Functionalization with folate allowed the particles to be taken up preferentially by cancer cells while retaining their superparamagnetic properties. Other folate-targeted MRI contrast particles include gadolinium-loaded dendrimers[33] and rare-earth metal yttrium-oxide particles that avoid the use of heavy metals for imaging.[34]

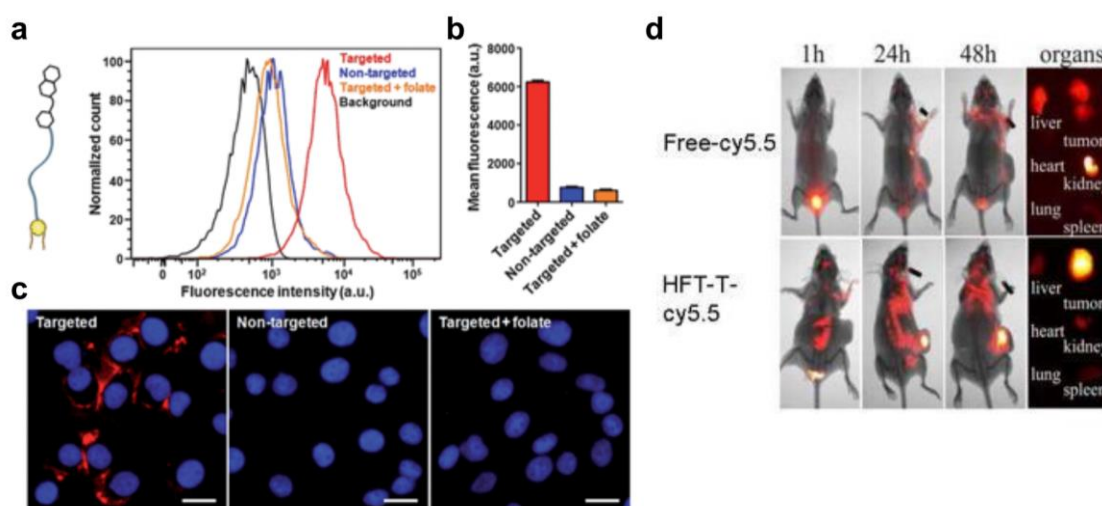


**Figure 1.1.2.** Examples of targeting strategies using small molecules. a-c) Targeting of red blood cell membrane-coated nanoparticles (RBC-NPs) with folate using a membrane-anchoring approach. a) Schematic of a folate molecule conjugated to a lipid-PEG tether along with a flow cytometry histogram demonstrating that targeted RBC-NPs display increased affinity to folate receptor-overexpressing cells. The targeting is abrogated in the presence of free folate. b) Quantification of mean fluorescence intensities from the experiment in a). c) Fluorescent imaging demonstrating targeting capability of targeted RBC-NPs. Red: dye labeled nanoparticles; blue: DAPI-stained nuclei. Scale bar = 25  $\mu\text{m}$ . d) Heparin-folate-paclitaxel nanoparticles (HFT-Ts) target folate receptors in a KB xenograft tumor model *in vivo*. Particles were labeled with Cy5.5 dye for *in vivo* fluorescence imaging. a-c) adapted with permission from ref [10]. Copyright 2013, The Royal Society of Chemistry. d) adapted with permission from ref [30]. Copyright 2011, American Chemical Society.

## **Riboflavin**

Riboflavin, better known as vitamin B<sub>2</sub>, is a small molecule with potential implications for targeted delivery. The cofactors of riboflavin, flavin adenine dinucleotide (FAD) and flavin mononucleotide (FMN), are required for the metabolism of folate, and depletion of these cofactors has been found to slow metabolism within cells.[35] The exact nature of riboflavin's role in cancer pathogenesis is unclear,[36, 37] although it is known that riboflavin carrier protein is overexpressed on many types of cancer.[38] This fact, along with the molecule's close relationship to folate metabolism, suggests that it can play a role in the design of cancer therapeutics and diagnostics. An FAD-conjugated ultra-small superparamagnetic iron oxide nanoparticle has been reported as a targeted imaging strategy for tumor vascular metabolism.[39] The nanoparticles were able to effectively target riboflavin carrier protein and highlight sites of angiogenesis *in vivo*. A similar platform based on FMN as the targeting ligand has also been reported.[40] For the delivery of cancer therapeutics, dendrimers have been used in conjunction with riboflavin as the targeting agent. Methotrexate-riboflavin dendrimer conjugates were able to target and specifically inhibit the growth of KB cells *in vitro*. [41] Despite the fact that the exact pathways and relationship between riboflavin and cancer have not been fully elucidated, the works here serve as a foundation for further study of the molecule as a targeting agent.

## **1.3 Carbohydrates**

### **Simple Sugars**

The targeting of simple carbohydrate receptors using naturally occurring sugars is a commonly used method of modulating nanoparticle localization. One such example is mannose, which is expressed on many types of cells, notably immune cells.[42] Targeting of dendritic cells,

which highly express mannose receptors, has been used to enhance the activity of nanoparticle vaccine formulations. In one example, lipid-calcium-phosphate (LCP) nanoparticles loaded with both an adjuvant, CpG oligodeoxynucleotide, and a melanoma-associated antigen, Trp2, were functionalized with mannose to create a therapeutic anticancer vaccine.[43] The nanoformulation was able to reduce tumor growth in both subcutaneous and metastatic models of murine B16-F10 melanoma. In a follow-up work, the LCPs were combined with liposome-protamine-hyaluronic acid nanoparticles delivering siRNA against TGF- $\beta$  as a combinatorial treatment, further boosting vaccine efficacy.[44] Mannose can also be used as a ligand to target cancer through tumor-associated macrophages, which aid the growth of tumors by releasing protein factors that stimulate tumor growth.[45] A PEG-sheddable mannose-modified platform has been reported that takes advantage of this targeting mechanism.[46] The pH-sensitive outer layer of the nanoparticles is labile in the low pH tumor microenvironment, resulting in the exposure of a mannose-functionalized layer that enables efficient binding to tumor-associated macrophages and subsequent payload delivery.

Galactose is a simple sugar that is also frequently used for targeted delivery, and it has a high affinity for asialoglycoprotein receptors found on hepatocytes.[47] As an example, PEG-stabilized gold nanoparticles with galactose as a targeting ligand exhibited increased uptake in a HepG2 liver cell line.[48] The targeting effect was shown to be specific, as the presence of free asialoglycoprotein receptor ligands markedly decreased gold nanoparticle uptake. Further, it has been demonstrated that galactose-functionalized micelles can target the liver with high efficiency *in vivo* (**Figure 3a,b**).[49] Galactose-modified liposomes can be highly effective at hepatic siRNA delivery; compared with the bare nucleic acid, liposome-encapsulated siRNA was delivered much more efficiently to the liver *in vivo*. [50] Galactose-mediated liver targeting has also been used for



antiviral therapy, enabling delivery of antiviral p41 peptide nanocomplexes against hepatitis C.[51]

For imaging purposes, iron oxide nanoparticles functionalized with a galactose-containing polymer displayed increased accumulation in the liver, demonstrating their utility as contrast agent for liver magnetic resonance imaging.[52]

Figure 3

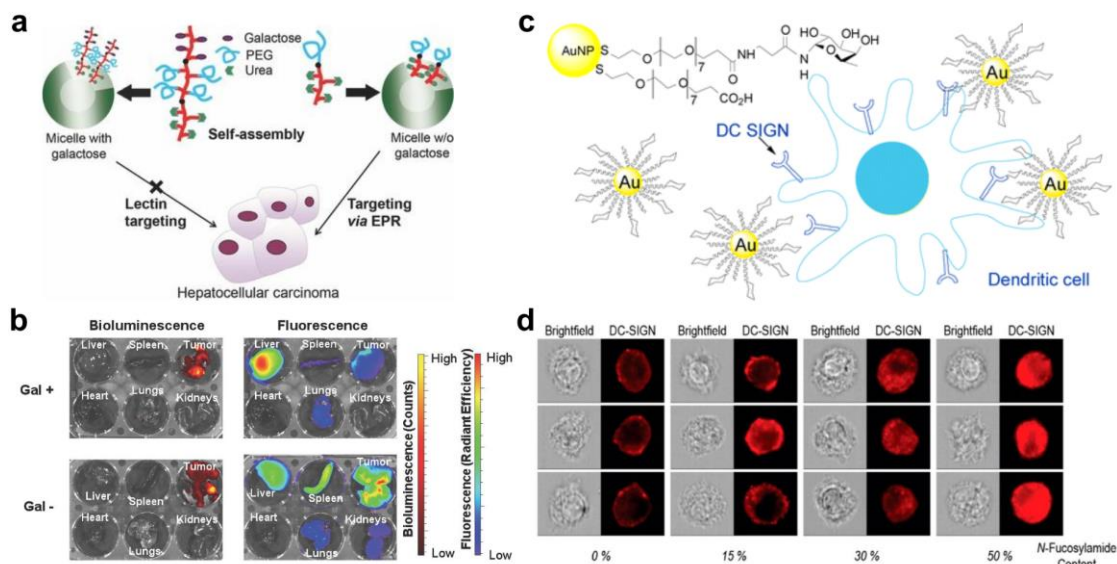


**Figure 1.1.3.** Examples of targeting strategies using carbohydrates. a-b) Galactose-functionalized micelles for liver targeting. a) Schematic of micelles functionalized with and without galactose-PEG ligands. Galactose-targeted particles are localized in the liver, and non-targeted particles are localized in the tumor. b) In vivo biodistribution of galactose-targeted and non-targeted particles 48 hours after intravenous administration. Bioluminescence originates from luciferase-expressing tumor cells. c-d) Glycan-functionalized gold nanoparticles (AuNPs) for dendritic cell targeting. c) Glycomimetic  $\alpha$ -fucosylamide functionalization scheme of gold nanoparticles, these nanoparticles can be taken up preferentially by dendritic cells via DC-SIGN lectins. d) Internalization of  $\alpha$ -fucosylamide functionalized gold nanoparticles (with either 0, 15, 30, or 50%  $\alpha$ -fucosylamide linked ligands on the surface) by dendritic cells. Increasing the amount of  $\alpha$ -fucosylamide on the surface increases percent of nanoparticles internalized by the dendritic cells. a-b) adapted with permission from ref [49]. Copyright 2014, John Wiley & Sons, Inc. c-d) adapted with permission from ref [59]. Copyright 2014, American Chemical Society.

## Glycans and Glycan-Binding Lectins

Glycans represent more complex carbohydrates that are often anchored onto either membrane lipids or proteins, and these biomacromolecules have important implications in many natural binding interactions.[53, 54] Dendritic cell-specific intercellular adhesion molecule-3-grabbing non-integrin (DC-SIGN) is a popular C-type lectin on the surface of dendritic cells that

can be targeted by highly mannosylated or Lewis-type glycan structures.[55] Both Lewis X and Lewis B glycans have been used to modify liposomes, and it was demonstrated that PEGylation inhibits their binding activity.[56] The same modifications were later made on antigen-carrying liposomes, and the targeted formulations led to markedly enhanced presentation of the antigens to CD4<sup>+</sup> and CD8<sup>+</sup> effector T cells driven by dendritic cells pulsed with the nanoformulation.[57] In another example, Lewis X-functionalized iron oxide nanoparticles were used as a means for both dendritic cell detection and isolation.[58] Gold nanoparticles have also been used to show preferential targeting and internalization by targeting DC-SIGN on dendritic cells (Figure 3c,d).[59] Gangliosides such as GM1 are lipid-anchored glycan structures that have been functionalized on nanoparticle surfaces for the binding and detection of toxins, including cholera toxin secreted by *Vibrio cholera*. [60] The fact that such gangliosides can also mediate direct binding interactions with pathogens such as *Streptococcus pneumoniae* suggest that such ganglioside-functionalized nanoparticles have utility for bacteria targeting applications.[61, 62]

Conversely, lectins, which are a class of proteins that regulate bioadhesion and cell recognition,[63, 64] have been used as a means to target glycan structures. This has important implications for gastrointestinal tract targeting, as their bioadhesive properties can enable them to navigate through mucosal layers, cross epithelial barriers, and enter cells.[63, 65] *Ulex europaeus* 1 lectin (UEA-1) was shown to be taken up quickly and preferentially by M cells *in vivo*. [66] Due to the role of M cells in immunity, a PLGA nanoparticle vaccine against hepatitis B was targeted to M cells using UEA-1, and it was observed that the immune response was improved compared to a non-targeted control.[67] A similar platform was reported using chitosan nanoparticles coated with a UEA-1-conjugated alginate gel capable of protecting the antigen from the acidic stomach environment,[68] and a nasally administered vaccine against *Staphylococcus aureus* has also been

developed using similar principles.[69] Wheat germ agglutinin (WGA) from *Triticum vulgaris* is another lectin that has been used for targeted nanoparticle delivery. It has been shown that functionalization of PLGA nanoparticles with WGA can facilitate increased endocytic uptake.[70] In a rat model, WGA nanoparticles improved the bioavailability of the steroid medication budesonide in the lungs when administered intratracheally compared with an unconjugated control.[71] Regarding cancer therapy, WGA-conjugated PLGA nanoparticles have been used to deliver the chemotherapeutic paclitaxel to different cell types and show promise as a mode of treatment.[72, 73]

## **1.4 Peptides**

### **Targeting Peptides**

Peptides are a popular class of targeting ligand, and can be used to help modulate bodily localization.[74, 75] While many peptides that are identified via the phage display screening approach result in novel sequences, there are many examples of ligands that are either naturally occurring or derived from naturally occurring proteins. A prime example is RGD, a sequence motif identified in fibronectin that binds cell surface receptors known as integrins.[76]  $\alpha_v\beta_3$  is an important RGD-binding integrin implicated in tumor angiogenesis and has served as the target for many RGD-functionalized nanotherapeutics.[77] Given its utility as a cancer-targeting agent, RGD has been widely employed to create targeted therapeutic and imaging platforms.[78, 79] Folate functionalized mesoporous silica-encapsulated gold nanoparticles loaded with DOX were used as a combination photothermal therapy and chemotherapy to promote significant control of tumor growth while lowering systemic toxicity.[80] In an example of gene silencing, RGD-decorated chitosan nanoparticles loaded with siRNA were examined for their ability to selectively

deliver their cargo to tumor endothelial cells, and the strategy promoted antitumor effects in a model of ovarian carcinoma.[81] RGD is also a highly utilized peptide for targeted imaging and detection techniques, and, in one example, quantum dots coated with paramagnetic lipids and RGD-conjugated lipids were tested as bimodal imaging probes.[82] By further modifying nanoparticles with additional binding peptides, researchers were able to target both integrin  $\alpha_{IIb}\beta_3$  and P-selectin on activated platelets using RGD and EWVDV peptides, respectively, resulting in better retention under flow conditions.[83] A recently reported novel application of natural peptide functionalized nanoparticles involves their use as hemostatic agents.[84] Flexible nanoparticles were conjugated with both an RGD-containing peptide sequence as well as a von Willebrand factor-binding peptide derived from factor VIII, helping to promote platelet aggregation and reduce bleeding time in a mouse model.

Toxins are crafted by nature to target cellular surfaces, and their activity on host cells can cause major disruption of cellular processes.[85] Many have binding sequences that are designed to target membrane receptors with high specificity. Chlorotoxin, an amino acid from scorpion venom that was originally found to block chloride ion channels, is a highly used targeting peptide.[86] Although the exact mechanism of chlorotoxin's binding is still under some controversy,[87] it has been shown to preferentially bind several types of cancers.[88, 89] Gliomas in particular are highly sensitive to the peptide, which binds to the cells via both high and low affinity sites,[90] making it a good ligand to use for imaging of brain tumors.[91-93] Multiple platforms have used chlorotoxin to target particles to cancer cells for both imaging and therapeutics.[90-92] Targeting of nanoparticles to the brain was greatly enhanced by the addition of chlorotoxin to the surface of iron oxide particles (**Figure 4a,b**).[91] Chlorotoxin has been used to “paint” tumors using fluorescent dyes as well,[93] and other imaging modalities, including

quantum dots, have been used in conjunction with this targeting method.[94] In other cancer types such as metastatic breast cancer, chlorotoxin was able to enhance the cellular uptake and cytotoxicity of liposomes in a murine model of the disease.[95] Other than its specificity to cancer, chlorotoxin has shown efficacy in targeting Parkinson's disease as well, as it has a specificity for proliferating endothelial cells.[96] This allowed researchers to target brain microvascular endothelial cells and deliver levodopa within the brain to treat the disease.[97]

Figure 4

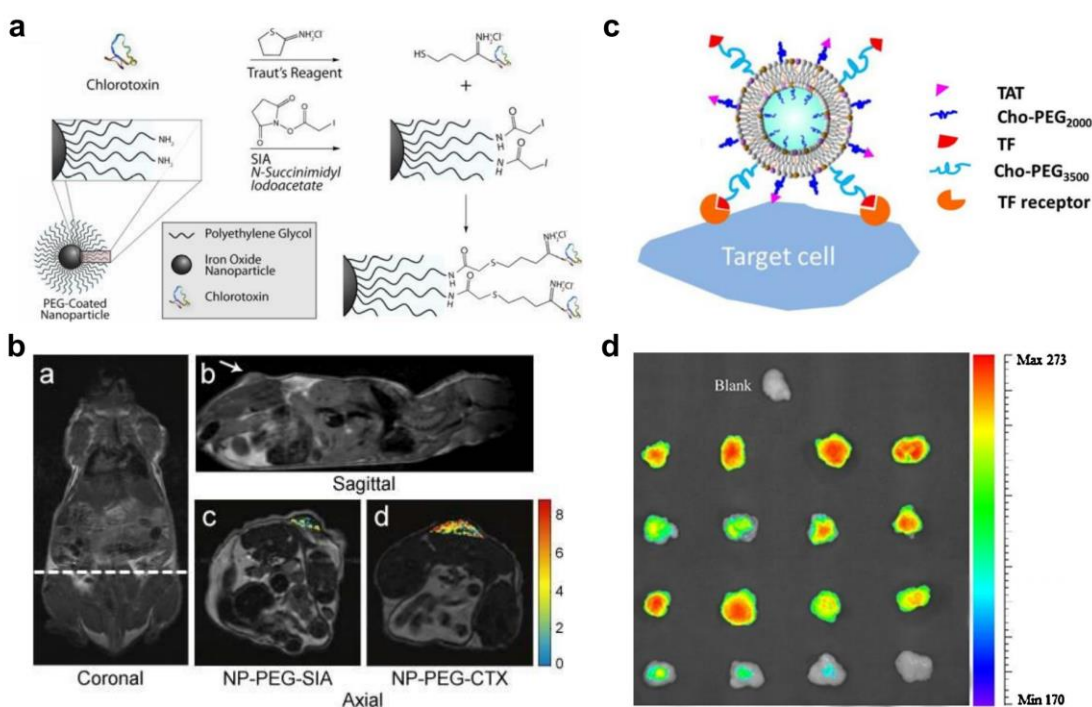


Fig 1.4.

**Figure 1.1.4.** Examples of targeting strategies using peptides. a-b) Chlorotoxin (CTX)-functionalized iron oxide nanoparticles for glioma targeting. a) Schematic showing conjugation scheme for CTX functionalization of PEGylated iron oxide nanoparticles. b) MRI images of CTX nanoprobe localization in tumor xenograft. CTX-targeted particles showed higher accumulation in tumors than a control particle, NP-PEG-SIA. c-d) TAT-functionalized liposomes for enhanced tumor entry. c) Schematic of nanoformulation functionalized with both TAT peptide and transferrin (TF) using cholesterol-PEG (Cho-PEG) conjugates. TF enables cell targeting while the TAT enhances cellular entry. d) Fluorescently-labeled liposome uptake by tumors in an in vivo xenograft model. Formulations, from top to bottom, were liposomes with TAT and TF, liposomes with TAT only, liposomes with TF only, and bare liposomes. a-b) adapted with permission from ref [91]. Copyright 2008, John Wiley & Sons, Inc. c-d) adapted with permission from ref [106]. Copyright 2013, Elsevier.

Candoxin is a component of snake venom from *Bungarus candidus* that produces a neuromuscular blockade in the central nervous system that was recently shown to have brain targeting properties.[98] The toxin binds to nicotinic acetylcholine receptors, which facilitates their uptake into brain cells.[99] Researchers have taken advantage of the toxin's binding specificity to derive a peptide sequence (CDX) for use in brain-targeted nanoparticle delivery.[100] PEG-poly(lactic acid) (PEG-PLA) micelles coated with CDX were able to achieve a significant increase in brain distribution, highlighting their potential use as a targeting mechanism for human glioblastoma multiforme therapies. The same group later used a more stable D-peptide version of the CDX ligand to target liposomal doxorubicin in a mouse model of glioma, demonstrating enhanced brain uptake and increased survival with the targeted formulation.[101] To further increase efficacy, liposomes were later functionalized with both CDX and an RGD-containing peptide, and the resulting nanoformulation showed better tumor control compared with liposomes functionalized with either ligand individually.[102]

### **Cell Penetrating Peptides**

Rather than enabling targeting to a specific bodily location, cell penetrating peptides are natural moieties often employed by pathogens that aid in the disruption of cell membrane bilayers and allow entry into a cell.[103, 104] Researchers have employed such peptides to improve intracellular delivery of nanoparticle payloads. HIV trans-activator of transcription (TAT) is a protein with cell-penetrating properties that the virus uses to efficiently enter cells via endocytic pathways.[105] A TAT-derived peptide has been used frequently as a surface ligand for cancer drug delivery applications in order to increase uptake of chemotherapeutic payloads. Liposomes functionalized with both TAT and transferrin showed highly cancer-specific delivery of cargo directly into tumor cells (Figure 4c,d).[106] Tumors subject to particles functionalized with both

TAT and transferrin had the highest intensity of fluorescent localization. A TAT-functionalized PEG-PLA platform coated in poly(methacryloyl sulfadimethoxine) (PSD)-b-PEG has been used as a responsive targeted drug delivery system.[107] The particles exhibited increased uptake at lower pH values due to exposure of the TAT ligands after shedding of the PSD-b-PEG layer. In addition to potential drug delivery applications, TAT has been tested for gene therapy uses. TAT-functionalized liposomes were reported to induce transfection in lung carcinoma cells,[108] and TAT-conjugated PEG-polyethylenimine nanoparticles were successfully used for *in vivo* gene delivery to the lungs.[109] For imaging purposes, a TAT-functionalized dual fluorochrome magnetic particle has been reported for looking at the metabolism and movement of cells *in vivo* using both MRI and fluorescent imaging techniques.[110] The TAT peptide may also be helpful for brain delivery, where PEG micelles functionalized with the peptide and loaded with the antibiotic ciprofloxacin have the potential to treat brain infection.[111] These TAT peptide-functionalized micelles showed significant brain uptake in rats 4 hours after intravenous injection. PEGylated chitosan nanoparticles with TAT have also been shown to enter the brain after intranasal administration, and these particles have potential in the treatment of neurodegenerative disorders.[112]

Penetratin is a cell-penetrating peptide derived the *Drosophila* Antennapedia homeodomain that also aids in delivery across the cell membrane.[113] Gold nanoparticles with penetratin on their surface fabricated using laser ablation in a solution containing the peptide were able to enter cells more effectively than their non-functionalized counterparts.[114] Curcumin, used against neurodegenerative disorders, was delivered to the brain using penetratin-functionalized micelles.[115] Fluorescent-magnetic nanoparticles have also been coated with the peptide, and the resulting targeted formulation exhibited enhanced endocytosis in the presence of

a magnetic field.[116] Penetratin, like TAT, has shown benefit as a brain delivery platform, where functionalized PEG-PLA nanoparticles were able to more efficiently cross the blood-brain barrier *in vivo* when compared with non-penetratin decorated particles.[117]

## **1.5. Proteins**

### **Transferrin Family Proteins**

Transferrins are glycoproteins which bind iron ions in the serum and transport them to cells via transferrin receptors.[118, 119] These receptors can be highly overexpressed on certain cancers, and transferrin receptor-targeting strategies represent one of the more widely studied methods for targeted delivery of therapeutic and imaging agents.[119] Transferrin functionalization has been reported for many different nanoparticle platforms, including liposomes,[120-122] polymeric nanoparticles,[123, 124] gold nanoparticles,[125, 126] and iron oxide nanoparticles.[126] Interestingly, it was found in one study that functionalizing gold nanoparticles with transferrin did not significantly influence their overall biodistribution, but it did strongly influence localization to certain cells types within different organs and within tumors.[125] Environmentally responsive microgels decorated with transferrin have been design for cancer treatment and displayed triggered release of a doxorubicin payload in the low pH of lysosomes.[127] This targeting strategy has also been used for photothermal therapy, where gold nanorods targeted to the transferrin receptor showed significant excitation upon exposure to a low energy laser due to enhanced cellular uptake.[128] Cadmium sulfide quantum dots with transferrin on the surface have been designed for imaging purposes, and the particles were readily taken up in cancer cells, resulting in bright illumination.[129]

Lactoferrin is another glycoprotein in the transferrin family that is naturally produced in milk, saliva and tears. It plays a role in transfer of immunity to infants, immune response, and



protection against microbial infection.[130, 131] Lactoferrin has been used as a natural brain-targeting ligand due to its receptor-mediated ability to cross the blood-brain barrier, one of the greatest challenges in the treatment of brain cancers.[132] Along these lines, PEG-coated bovine serum albumin nanoparticles functionalized with lactoferrin have been used to deliver doxorubicin for glioma treatment *in vivo*. [133] The targeted particles were able to increase the efficacy of DOX against gliomas and increase the nanoparticle concentration in tumors compared to non-targeted particles. Lactoferrin has also been used to improve brain imaging techniques; coated superparamagnetic iron oxide nanoparticles were used to enhance imaging resolution for brain tumor detection (**Figure 5a,b**). [134, 135] Nanoparticles coated with lactoferrin and labeled with a far-red fluorescent dye have also been evaluated for brain tumor imaging and showed promising results for this application.[136] In addition to cancers, brain targeting via lactoferrin can also be useful for treating neural disorders such as Alzheimer's. Lactoferrin coated nanoparticles delivering deferasirox, an iron chelator, were able to protect the brain from amyloid accumulation and subsequent neurodegeneration in a rat model of the disease.[137] For regulating the chemical balance within the brain, lactoferrin-functionalized liposomes were used to deliver senktide, an NK<sub>3</sub> receptor agonist that normally does not cross the blood-brain barrier but is important in the evaluation of novel antipsychotics.[138]

### **Lipoproteins**

High density lipoproteins (HDL) are involved in the transportation of lipid material and have implications in many common diseases, include heart disease and cancer.[139, 140] Due its ability to target specific cell types, HDL particles have been used extensively in drug delivery. Reconstituted HDL nanoparticles containing fluorescent calcium carbonate were able to serve as a probe for lung cancer *in vivo*. [141] Their targeting mechanism relied on targeting scavenger

receptor class B member I (SR-BI), which is highly expressed on some cancerous cells and has an affinity to HDL.[141] In another example, lymphoma cells that express SR-BI were also targeted effectively *in vivo* with synthetic, gold-templated HDL nanoparticles.[142] Given that the main role of HDL is lipid transport, it also plays a pivotal role in atherosclerosis.[143, 144] HDL-mimetic particles have been used to target atherosclerotic plaques for imaging,[145] and HDL has also been used to deliver therapeutic statins to reduce inflammation and atherosclerotic plaque buildup (Figure 5c,d).[146]

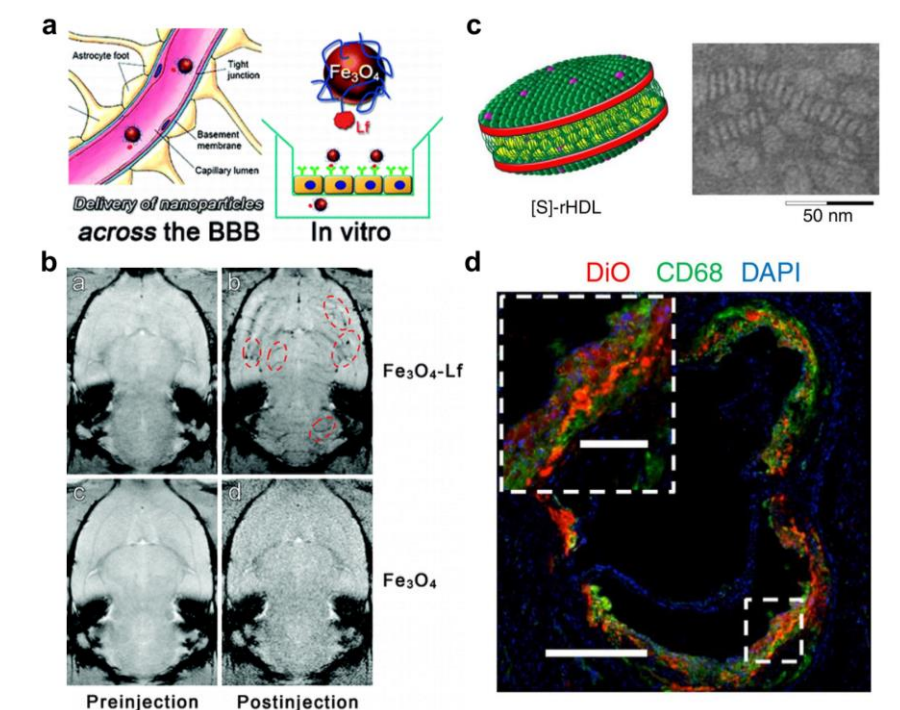


**Figure 1.1.5.** Examples of targeting strategies using proteins. a-b) Lactoferrin (Lf)-functionalized iron oxide nanoparticles for delivery across the blood-brain barrier (BBB). a) Schematic of Lf-coated iron-oxide nanoparticles demonstrating the interactions between the nanoparticles and brain endothelial cells. b) In vivo MRI image showing brain uptake of Lf-coated iron-oxide nanoparticles. Red dotted lines encircle areas of contrast where nanoparticles are present. c-d) HDL nanoparticles for delivery to atherosclerotic plaque. c) Schematic (left) and transmission electron microscopy image (right) of statin-loaded recombinant HDL nanoparticles ([S]-rHDL). TEM image shows [S]-rHDL were 26 nm in diameter. d) Fluorescent imaging shows co-localization between the [S]-rHDL particles labeled with dye and macrophages (CD68) at sites of plaque in an aorta. Scale bars = 400 μm for main panel and 100 μm for inset. a-b) adapted with permission from ref [134]. Copyright 2012, American Chemical Society. c-d) adapted with permission from ref [146]. Copyright 2014, Macmillan Publishers Ltd.

## Adhesion Proteins

Cell adhesion molecules are proteins that cells use to bind other cells or extracellular matrix, and these comprise of immunoglobulins, cadherins, selectins, and integrins as the main subtypes.[147-149] They are employed by a variety of cells, most notably on blood components, such as platelets and leukocytes, or those comprising endothelial surfaces. Despite their favorable binding characteristics and often site-specific upregulation, the use of adhesion proteins in their entirety has not been commonly reported, most like due to the difficulty associated with functionalizing nanoparticles using membrane-bound proteins. In one example, P-selectin glycoprotein ligand-1 (PSGL-1) conjugated onto microbeads was used to study neutrophil rolling interactions as well as elucidate binding interactions of the ligand with E-selectin.[150, 151] In order to overcome difficulties with their use, researchers often rely on the use of binding domains derived from these adhesion proteins, which enables more facile conjugation to nanoparticle surfaces. Leukocyte-mimetic iron oxide nanoparticles were created by coating with lymphocyte function-associated antigen 1 (LFA-1) I domain, which targets intercellular adhesion molecule 1 (ICAM-1).[152] These particles were able to target inflamed tumor vasculature due to leukocyte-endothelial cell interactions under inflammatory conditions, and could serve as a cancer imaging agent. Flexible particles coated in the GPIIb $\alpha$  amino terminal domain, a derivative of a critical binding protein on platelets, were able to partly mimic the binding properties of the cells by showing affinity for von Willebrand factor.[153]

## 1.6 Pathogen-Derived Particles

### Viruses

Virus-like particles (VLPs), which have been extensively studied for their ability to deliver different payloads, mimic naturally occurring viral capsids.[154, 155] These represent a promising form of targeted delivery given that many viruses gain cellular entry via specific interactions with cell surface receptors.[156, 157] One example is the human rhinovirus, which targets the ICAM-1 protein that is present on the surface of many immune cells.[158] Hepatitis B envelope L proteins can form hollow nanoparticles with liver-targeting properties, and this was leveraged to deliver human clotting factor IX genes for potential treatment of hemophilia B.[159] A VLP based on the penton capsid proteins of adenovirus serotype 5 was likewise able to recapitulate the cellular targeting and entry characteristics of the original virus.[160] Derivatives of this platform have been used to deliver doxorubicin to HER2-expressing cells for use in cancer therapy.[161] Canine parvovirus capsid-based VLPs were shown to target transferrin receptor-overexpressing cells, and the effect was demonstrated using fluorescent dye-conjugated particles as a proof-of-concept (**Figure 6a,b**).[162] Interestingly, VLPs have also been used to encapsulate other nanoparticles for enhanced imaging techniques. Hepatitis B VLPs were loaded with iron oxide nanoparticles, and the resulting formulation could be efficiently taken up intracellularly for improved MRI contrast.[163]

### Bacteria

Like viruses, bacteria have also evolved high affinities to specific mammalian cells and systems. Many bacteria display ligands that specifically target cellular receptors, an example being SraP on *Staphylococcus aureus*, which specifically binds platelets.[164] Many bacteria actually have natural cancer-targeting properties due to adhesion molecules on their surfaces. Bacterial

ghosts derived from *Mannheimia haemolytica* bacteria were loaded with doxorubicin and demonstrated the ability to target colorectal adenocarcinoma cells more specifically than control ghosts derived from *Escherichia coli* (Figure 6c,d).[165] Due to their affinity to certain immune cells, which are adept at recognizing and binding bacteria, ghosts have also been used to improve vaccine design.[166, 167] Likewise, bacterial outer membrane vesicles (OMVs), which have been recognized as promising delivery vehicles, have been used to deliver antigenic material while also boosting immunogenicity.[168] For example, *E. coli* OMVs have been used to generate strong immune responses against green fluorescent protein, and the resulting titers were much higher than

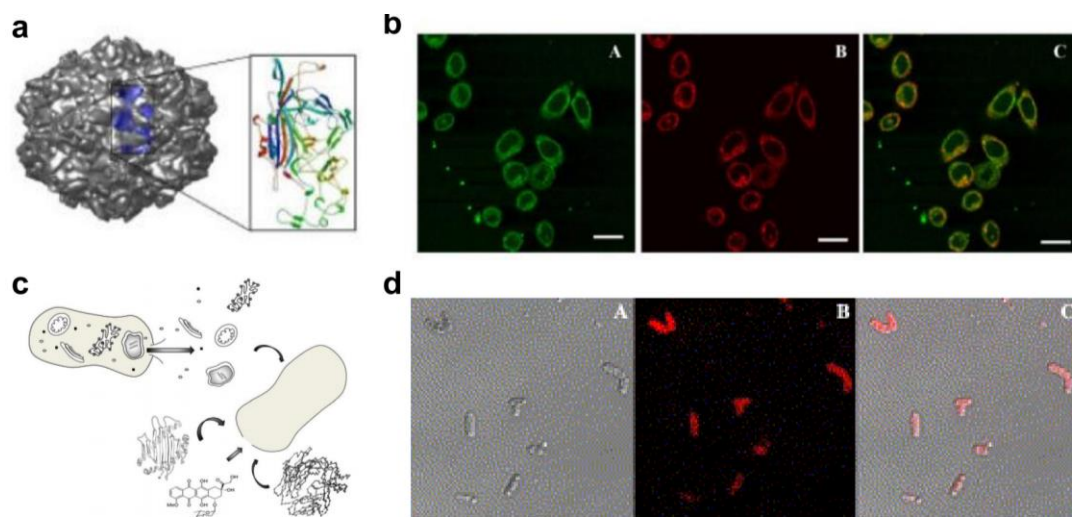


**Figure 1.1.6** Examples of targeting strategies using pathogen-derived particles. a-b) Canine parvovirus-like particles (CVP-VLPs) for delivery to tumors. a) Model of the protein capsid with a single subunit depicted on the inset. b) CVP-VLPs were internalized by HeLa cells, as shown by co-localization of antibody-labeled CVP-VLPs (green) and dye-conjugated transferrin (red). Scale bar = 25  $\mu\text{m}$ . c-d) Bacteria ghosts for delivery to tumors. c) Schematic showing formation of bacterial ghosts through evacuation of the intra-bacterial contents and loading with therapeutic or imaging agents. d) Doxorubicin-loaded bacterial ghosts as targeted drug delivery vehicles. Microscopy images show bacterial ghosts (brightfield) and doxorubicin (red) overlaid. a-b) adapted with permission from ref [162]. Copyright 2006, BioMed Central Ltd. c) adapted with permission from ref [167]. Copyright 2014, Medknow. d) adapted with permission from ref [165]. Copyright 2009, Elsevier.

what could be achieved by administration of the free protein alone.[169] There are many future applications that can be pursued given the wide range of specificities that bacteria demonstrate, including to endothelial cells and epithelial cells.[167, 170] Additionally, it has been demonstrated

that bacterial membrane can be coated onto nanoparticle surfaces, further introducing new functionalities to these naturally derived platforms.[171]

## **1.7 Mammalian Cell Membranes**

### **Exosomes**

The direct use of naturally derived cell membranes in nanomedicine is a growing field that has the potential to lead to many novel and improved delivery platforms.[17, 172, 173] One major advantage of the approach is that it enables direct use of multivalent cell membrane markers concurrently. This can include both targeting molecules as well as immunomodulatory surface markers, which better enable platforms developed using this approach to excel within complex, biological systems. One type of natural membrane structure that has been employed is exosomes, which are vesicular fragments filled with intracellular content that break off of cells and play roles in signaling and transport.[174] They have a natural affinity to many locations within the body due to their role in signaling and have wide-ranging implications for drug delivery and imaging applications. Recently, the natural affinity of tumor-derived exosomes to specific organs was studied.[175] It was shown that, depending on the source tumor, the exosomes had varied biodistributions; this correlated with sites of future metastasis and was integrin-dependent. In a different study, macrophage-derived exosomes were used for delivery of doxorubicin due to their natural targeting ability to tumors.[176] It was shown that the tumor-targeting mechanism of the exosomes could be attributed to several CAM-like and other adhesion molecules on their surfaces. Exosomes from dendritic cells can be used to modulate the immune system by interacting with the T cells responsible for downstream immune activity.[177] When using exosomes from immature dendritic cells pre-treated with interleukin-10, it has been possible to generate immune tolerance

for alleviating arthritic conditions.[178] Additionally, exosomes derived from macrophages can deliver cargo to the brain through receptor-based interactions with potential implications for Parkinson's disease therapy (**Figure 7a,b**).[179]

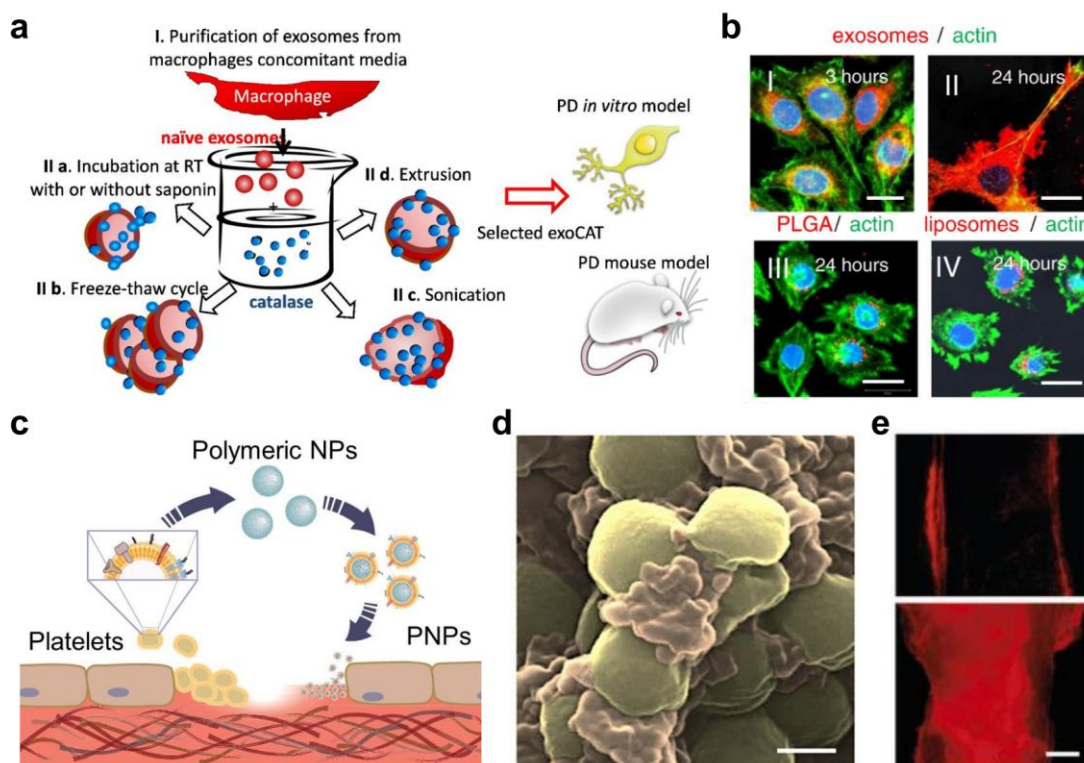


**Figure 1.1.7.** Examples of targeting strategies using mammalian cell membranes. a-b) Macrophage exosomes for delivery to the brain. a) Schematic of macrophage exosome derivation and application. Catalase-loaded macrophage exosomes were designed as a brain-targeted Parkinson's disease (PD) therapy. b) Exosome formulations were tested for uptake in PC12 neuronal cells compared with control particles. Macrophage-derived exosomes (I and II) showed greatly enhanced uptake compared to non-targeted polymeric PLGA particles (III) and liposomes (IV) at 24 hours. Scale bar = 20  $\mu\text{m}$ . c-e) Platelet membrane-coated nanoparticles (PNPs) for delivery to bacteria and damaged vasculature. c) Schematic of fabrication and targeting abilities of PNPs. d) False-colored scanning electron microscopy image of PNPs (orange) naturally targeting MRSA252 bacteria (gold). Scale bar = 400 nm. e) Targeting of fluorescently-labeled PNPs (red) to intact carotid artery (top) and damaged artery (bottom). PNPs show preferential binding to damaged areas. Scale bar = 500  $\mu\text{m}$ . a-b) adapted with permission from ref [179]. Copyright 2015, Elsevier. d-e) adapted with permission from ref [188]. Copyright 2015, Macmillan Publishers Ltd.

## Platelets

Platelets are critical in maintaining hemostasis and are the front line in wound healing, where they mediate the clotting cascade.[180, 181] Due to their complex nature, including the fact that their membrane displays numerous cell and extracellular matrix adhesion proteins, platelets

are implicated in many pathologies, including cancer,[182] cardiovascular disease,[183] and infections.[184] Cell membrane-coated nanoparticles have recently been reported that mimic the natural function of the source cells.[21] The faithful translocation of membrane onto the nanoparticle surface preserves the original functionality, including the ability to actively reduce immune uptake[185] or to bind cell-specific toxins.[186, 187] Along these lines, a platelet membrane-coated polymeric nanoparticle (PNP) has recently been reported that takes advantage of the varied binding properties of platelets (Figure 7c-e).[188] The nanoparticles, which consist of PLGA as the core material and a naturally derived membrane bilayer as the shell, recapitulate many of the original binding properties of platelets. It was shown that the PNPs could be used for multiple purposes, including for the targeting and treatment of antibiotic-resistant bacteria as well as for delivering cytotoxic payloads to regions of damaged vasculature for preventing restenosis.

Such membrane-coated nanoparticles have also been used for cancer treatment, where platelets and growing tumors have a very multifaceted and complex relationship.[182] There are many methods by which cancer cells can bind to and activate platelets, and platelet-mimicking imaging and therapeutic platforms can use this to their advantage. Platelet membrane-coated particles have recently been investigated for use as drug delivery vehicles to both tumors and circulating tumor cells.[189] The nanoformulation was both loaded with doxorubicin and conjugated with tumor necrosis factor-related apoptosis inducing ligand (TRAIL); they efficiently localized to tumor cells *in vivo*, resulting in impressive control of both tumor growth and the amount of metastatic nodules in the lung. In a similar example, silica particles functionalized with platelet membrane and conjugated with TRAIL were also able to reduce metastasis in a mouse breast cancer model.[190]



## **Leukocytes**

White blood cells, or leukocytes, are immune cells that play a major role in the detection and elimination of foreign or malignant entities. Of note, leukocytes can target endothelium, and silica particles coated with membrane derived from these cells were shown to bind to endothelial cells in an ICAM-1-dependent manner.[191] These membrane-coated particles were able to successfully traverse the endothelium and retained their properties when administered *in vivo*. In a different example, silica particles coated with macrophage cell membrane were loaded with doxorubicin and used for tumor treatment.[192] The particles exhibited extended blood circulation times and enhanced tumor accumulation, leading to significant control of tumor growth in a mouse xenograft model. Leukocyte membrane-coated polymeric capsules were also shown to enhance cancer cell-targeting capability compared with unmodified particles.[193] In a recent study using Janus particles in which one side was coated with gold and the other with leukocyte membrane, it was demonstrated that the particles with membrane coatings could preferentially bind to cancer cells over healthy endothelial cells.[194] Interestingly, the authors noted that the particles entered via the membrane-coated hemisphere, demonstrating the utility of the biological coating for cancer targeting.

## **Stem Cells**

Mesenchymal stem cells (MSCs) have unique tumor-targeting abilities given that they are recruited by tumors to enhance their proliferation.[195, 196] These are mediated in part by direct cell-cell interactions, suggesting utility of stem cell-derived membrane for targeted delivery.[197] “Nanoghosts” derived directly from MSC membranes were recently reported as a potential platform for targeted therapy of prostate cancer.[198] The vesicles were loaded with soluble

TRAIL (sTRAIL) by a physical extrusion method and were shown to retain their tumor-binding properties both *in vitro* and *in vivo*. Compared with free sTRAIL, the nanoghost formulation showed significantly enhanced control of tumor growth. Further, the particles were shown to be non-immunogenic, highlighting their potential for translation. Iron oxide nanoparticles coated with stem cell membrane have also been recently reported that have potential for both therapeutic and diagnostic applications.[199] The coating process involved a sonication method that forced cell membrane to re-assemble onto the surface of the nanoparticles, and the final particles were shown to exhibit reduced macrophage uptake compared with bare particles.

### **Cancer Cells**

Cancer cells often upregulate a variety of integrins and receptors on their surfaces that allow them to spread, bind, and aggregate together to metastasize and form tumors.[200-202] While many of the binding mechanisms are heterotypic, many homotypic binding mechanisms, where cancer cells bind to each other, have also been enumerated.[203, 204] Recently, a cancer cell membrane-coated nanoparticle (CCNP) has been fabricated to demonstrate the utility of a homotypic approach for cancer targeting.[205] It was demonstrated that the particles retained membrane-bound antigens that were present on the original cells. Compared with red blood cell membrane-coated nanoparticles, the CCNPs bound preferentially to the original cancer cell. Further it was shown that the CCNPs did not bind to normal, healthy cells, demonstrating the specificity of the targeting. While such a strategy needs to be further explored and validated, it represents a unique method for the fabrication of naturally cancer-targeting nanoparticles.

## Conclusions

Biomimetically targeted nanoparticle platforms leverage nature's own binding specificities to preferentially localize to regions of interest within the body. Unlike traditional approaches, which often depend on approaches involving lengthy discovery and validation, the use of naturally occurring binding mechanisms has the potential to speed up workflows for new targeting ligand identification. Binding interactions among cells, small molecules, biomolecules, and surfaces are a fundamental part of biological systems, and the character of these interactions can vary greatly depending on the biological function. As illustrated in this review, natural biomimetic targeting strategies can be employed using anything from small molecule vitamins to entire cell membranes.

Looking towards the future, it can be envisioned that multi-ligand strategies for targeted nanoparticle delivery will be increasingly explored. This stems from the fact that biological interactions are incredibly complex and seldom singular. By employing multiple targeting ligands, it may ultimately be possible to design delivery platforms with exquisite specificity and sensitivity. In order to accomplish this, it may be necessary to develop novel synthetic strategies for the controlled incorporation of multiple moieties onto the surface of nanoparticles. An alternative approach already described is the use of cell membrane coatings, a top-down strategy that circumvents the need for complicated chemistries. Employing cell membranes not only enables the facile incorporation of multiple ligands and functionalities, but it also does so at stoichiometries found inherently in nature. Regardless of the method, as targeting strategies continue to develop and become more sophisticated over time, the ability of nanoparticle platforms to address pressing health issues will continue to improve.

## **Acknowledgements**

Chapter 1, in full, is a reprint of the material as it appears in Bioengineering and Translational Medicine, 2016, Diana Dehaini, Ronnie H. Fang, and Liangfang Zhang. The dissertation author was the primary author.

## References

- [1] A.Z. Wang, R. Langer, O.C. Farokhzad, Nanoparticle delivery of cancer drugs, *Annu Rev Med*, 63 (2012) 185-198.
- [2] M.W. Tibbitt, J.E. Dahlman, R. Langer, Emerging Frontiers in Drug Delivery, *J Am Chem Soc*, 138 (2016) 704-717.
- [3] G. Bao, S. Mitragotri, S. Tong, Multifunctional nanoparticles for drug delivery and molecular imaging, *Annu Rev Biomed Eng*, 15 (2013) 253-282.
- [4] O.C. Farokhzad, R. Langer, Impact of nanotechnology on drug delivery, *ACS Nano*, 3 (2009) 16-20.
- [5] H. Maeda, Toward a full understanding of the EPR effect in primary and metastatic tumors as well as issues related to its heterogeneity, *Adv Drug Deliv Rev*, 91 (2015) 3-6.
- [6] Y.H. Bae, K. Park, Targeted drug delivery to tumors: myths, reality and possibility, *J Control Release*, 153 (2011) 198-205.
- [7] V. Sanna, N. Pala, M. Sechi, Targeted therapy using nanotechnology: Focus on cancer, *Int J Nanomedicine*, 9 (2014) 467-483.
- [8] N. Kamaly, Z. Xiao, P.M. Valencia, A.F. Radovic-Moreno, O.C. Farokhzad, Targeted polymeric therapeutic nanoparticles: design, development and clinical translation, *Chem Soc Rev*, 41 (2012) 2971-3010.
- [9] B. Mishra, B.B. Patel, S. Tiwari, Colloidal nanocarriers: a review on formulation technology, types and applications toward targeted drug delivery, *Nanomedicine*, 6 (2010) 9-24.
- [10] R.H. Fang, C.M. Hu, K.N. Chen, B.T. Luk, C.W. Carpenter, W. Gao, S. Li, D.E. Zhang, W. Lu, L. Zhang, Lipid-insertion enables targeting functionalization of erythrocyte membrane-cloaked nanoparticles, *Nanoscale*, 5 (2013) 8884-8888.
- [11] S.J. Brouns, M.M. Jore, M. Lundgren, E.R. Westra, R.J. Slijkhuis, A.P. Snijders, M.J. Dickman, K.S. Makarova, E.V. Koonin, J. van der Oost, Small CRISPR RNAs guide antiviral defense in prokaryotes, *Science*, 321 (2008) 960-964.
- [12] D.A. Daniels, H. Chen, B.J. Hicke, K.M. Swiderek, L. Gold, A tenascin-C aptamer identified by tumor cell SELEX: Systematic evolution of ligands by exponential enrichment, *Proc Natl Acad Sci U S A*, 100 (2003) 15416-15421.
- [13] F. Nilsson, L. Tarli, F. Viti, D. Neri, The use of phage display for the development of tumour targeting agents, *Adv Drug Deliv Rev*, 43 (2000) 165-196.

- [14] H.R. Hoogenboom, Selecting and screening recombinant antibody libraries, *Nature Biotechnol*, 23 (2005) 1105-1116.
- [15] M.A. Roguska, J.T. Pedersen, C.A. Keddy, A.H. Henry, S.J. Searle, J.M. Lambert, V.S. Goldmacher, W.A. Blattler, A.R. Rees, B.C. Guild, Humanization of murine monoclonal-antibodies through variable domain resurfacing, *Proc Natl Acad Sci U S A*, 91 (1994) 969-973.
- [16] N.A. Peppas, Intelligent therapeutics: biomimetic systems and nanotechnology in drug delivery, *Adv Drug Deliv Rev*, 56 (2004) 1529-1531.
- [17] J.W. Yoo, D.J. Irvine, D.E. Discher, S. Mitragotri, Bio-inspired, bioengineered and biomimetic drug delivery carriers, *Nat Rev Drug Discov*, 10 (2011) 521-535.
- [18] P.L. Rodriguez, T. Harada, D.A. Christian, D.A. Pantano, R.K. Tsai, D.E. Discher, Minimal "self" peptides that inhibit phagocytic clearance and enhance delivery of nanoparticles, *Science*, 339 (2013) 971-975.
- [19] H. Otsuka, Y. Nagasaki, K. Kataoka, PEGylated nanoparticles for biological and pharmaceutical applications, *Adv Drug Deliv Rev*, 55 (2003) 403-419.
- [20] R. Gref, A. Domb, P. Quellec, T. Blunk, R.H. Muller, J.M. Verbavatz, R. Langer, The controlled intravenous delivery of drugs using PEG-coated sterically stabilized nanospheres, *Adv Drug Deliv Rev*, 64 (2012) 316-326.
- [21] C.M.J. Hu, L. Zhang, S. Aryal, C. Cheung, R.H. Fang, L.F. Zhang, Erythrocyte membrane-camouflaged polymeric nanoparticles as a biomimetic delivery platform, *Proc Natl Acad Sci U S A*, 108 (2011) 10980-10985.
- [22] C.M. Hu, R.H. Fang, B.T. Luk, L. Zhang, Polymeric nanotherapeutics: Clinical development and advances in stealth functionalization strategies, *Nanoscale*, 6 (2014) 65-75.
- [23] R.H. Fang, C.M.J. Hu, L.F. Zhang, Nanoparticles disguised as red blood cells to evade the immune system, *Expert Opin Biol Ther*, 12 (2012) 385-389.
- [24] B. Kamen, Folate and antifolate pharmacology, *Semin Oncol*, 24 (1997) S18-30-S18-39.
- [25] T.W.B. Liu, J. Chen, G. Zheng, Peptide-based molecular beacons for cancer imaging and therapy, *Amino Acids*, 41 (2011) 1123-1134.
- [26] L.F. Petersen, N.T. Brockton, A. Bakkar, S.H. Liu, J. Wen, A.M. Weljie, T.A. Bismar, Elevated physiological levels of folic acid can increase in vitro growth and invasiveness of prostate cancer cells, *BJU Int*, 109 (2012) 788-795.
- [27] A. Garcia-Bennett, M. Nees, B. Fadeel, In search of the Holy Grail: Folate-targeted nanoparticles for cancer therapy, *Biochem Pharmacol*, 81 (2011) 976-984.
- [28] X. Zhao, H. Li, R.J. Lee, Targeted drug delivery via folate receptors, *Expert Opin Drug Deliv*, 5 (2008) 309-319.

- [29] J.N. Weinstein, L.D. Leserman, Liposomes as drug carriers in cancer-chemotherapy, *Pharmacol Ther*, 24 (1984) 207-233.
- [30] X. Wang, J. Li, Y. Wang, L. Koenig, A. Gjyzezi, P. Giannakakou, E.H. Shin, M. Tighiouart, Z.G. Chen, S. Nie, D.M. Shin, A folate receptor-targeting nanoparticle minimizes drug resistance in a human cancer model, *ACS Nano*, 5 (2011) 6184-6194.
- [31] Y. Zhou, Z. Wang, Y. Chen, H. Shen, Z. Luo, A. Li, Q. Wang, H. Ran, P. Li, W. Song, Z. Yang, H. Chen, Z. Wang, G. Lu, Y. Zheng, Microbubbles from gas-generating perfluorohexane nanoemulsions for targeted temperature-sensitive ultrasonography and synergistic HIFU ablation of tumors, *Adv Mater*, 25 (2013) 4123-4130.
- [32] C. Sun, R. Sze, M. Zhang, Folic acid-PEG conjugated superparamagnetic nanoparticles for targeted cellular uptake and detection by MRI, *J Biomed Mater Res A*, 78 (2006) 550-557.
- [33] S.D. Swanson, J.F. Kukowska-Latallo, A.K. Patri, C.Y. Chen, S. Ge, Z.Y. Cao, A. Kotlyar, A.T. East, J.R. Baker, Targeted gadolinium-loaded dendrimer nanoparticles for tumor-specific magnetic resonance contrast enhancement, *Int J Nanomedicine*, 3 (2008) 201-210.
- [34] S. Setua, D. Menon, A. Asok, S. Nair, M. Koyakutty, Folate receptor targeted, rare-earth oxide nanocrystals for bi-modal fluorescence and magnetic imaging of cancer cells, *Biomaterials*, 31 (2010) 714-729.
- [35] R.S. Rivlin, Riboflavin and cancer: A review, *Cancer Res*, 33 (1973) 1977-1986.
- [36] R.S. Rivlin, R. Hornibrook, M. Osnos, Effects of riboflavin deficiency upon concentrations of riboflavin, flavin mononucleotide, and flavin adenine dinucleotide in Novikoff hepatoma in rats, *Cancer Res*, 33 (1973) 3019-3023.
- [37] C.J. Kensler, K. Sugiura, N.F. Young, C.R. Halter, C.P. Rhoads, Partial protection of rats by riboflavin with casein against liver cancer caused by dimethyl-aminoazobenzene, *Science*, 93 (1941) 308-310.
- [38] L.A. Bareford, P.W. Swaan, Endocytic mechanisms for targeted drug delivery, *Adv Drug Deliv Rev*, 59 (2007) 748-758.
- [39] J. Jayapaul, S. Arns, W. Lederle, T. Lammers, P. Comba, J. Gatjens, F. Kiessling, Riboflavin carrier protein-targeted fluorescent USPIO for the assessment of vascular metabolism in tumors, *Biomaterials*, 33 (2012) 8822-8829.
- [40] J. Jayapaul, M. Hodenius, S. Arns, W. Lederle, T. Lammers, P. Comba, F. Kiessling, J. Gaetjens, FMN-coated fluorescent iron oxide nanoparticles for RCP-mediated targeting and labeling of metabolically active cancer and endothelial cells, *Biomaterials*, 32 (2011) 5863-5871.
- [41] T.P. Thomas, S.K. Choi, M.H. Li, A. Kotlyar, J.R. Baker, Jr., Design of riboflavin-presenting PAMAM dendrimers as a new nanoplatform for cancer-targeted delivery, *Bioorg Med Chem Lett*, 20 (2010) 5191-5194.

- [42] J.M. Irache, H.H. Salman, C. Gamazo, S. Espuelas, Mannose-targeted systems for the delivery of therapeutics, *Expert Opin Drug Deliv*, 5 (2008) 703-724.
- [43] Z.H. Xu, S. Ramishetti, Y.C. Tseng, S.T. Guo, Y.H. Wang, L. Huang, Multifunctional nanoparticles co-delivering Trp2 peptide and CpG adjuvant induce potent cytotoxic T-lymphocyte response against melanoma and its lung metastasis, *J Control Release*, 172 (2013) 259-265.
- [44] Z. Xu, Y. Wang, L. Zhang, L. Huang, Nanoparticle-delivered transforming growth factor- $\beta$  siRNA enhances vaccination against advanced melanoma by modifying tumor microenvironment, *ACS Nano*, 8 (2014) 3636-3645.
- [45] A. Mantovani, B. Bottazzi, F. Colotta, S. Sozzani, L. Ruco, The origin and function of tumor-associated macrophages, *Immunol Today*, 13 (1992) 265-270.
- [46] S.J. Zhu, M.M. Niu, H. O'Mary, Z.R. Cui, Targeting of tumor-associated macrophages made possible by PEG-sheddable, mannose-modified nanoparticles, *Mol Pharm*, 10 (2013) 3525-3530.
- [47] M. Hashida, M. Nishikawa, F. Yamashita, Y. Takakura, Cell-specific delivery of genes with glycosylated carriers, *Adv Drug Deliv Rev*, 52 (2001) 187-196.
- [48] Y. Ding, J.J. Liang, D.D. Geng, D. Wu, L. Dong, W.B. Shen, X.H. Xia, C. Zhang, Development of a liver-targeting gold-PEG-galactose nanoparticle platform and a structure-function study, *Part Part Syst Char*, 31 (2014) 347-356.
- [49] A.B.E. Attia, P. Oh, C. Yang, J.P.K. Tan, N. Rao, J.L. Hedrick, Y.Y. Yang, R.W. Ge, Insights into EPR effect versus lectin-mediated targeted delivery: Biodegradable polycarbonate micellar nanoparticles with and without galactose surface decoration, *Small*, 10 (2014) 4281-4286.
- [50] A. Sato, M. Takagi, A. Shimamoto, S. Kawakami, M. Hashida, Small interfering RNA delivery to the liver by intravenous administration of galactosylated cationic liposomes in mice, *Biomaterials*, 28 (2007) 1434-1442.
- [51] J.J. Zhang, J.C. Garrison, L.Y. Poluektova, T.K. Bronich, N.A. Osna, Liver-targeted antiviral peptide nanocomplexes as potential anti-HCV therapeutics, *Biomaterials*, 70 (2015) 37-47.
- [52] M.K. Yoo, I.Y. Kim, E.M. Kim, H.J. Jeong, C.M. Lee, Y.Y. Jeong, T. Akaike, C.S. Cho, Superparamagnetic iron oxide nanoparticles coated with galactose-carrying polymer for hepatocyte targeting, *J Biomed Biotechnol*, 2007 (2007) 94740.
- [53] B. Adamczyk, T. Tharmalingam, P.M. Rudd, Glycans as cancer biomarkers, *Biochimica Et Biophysica Acta*, 1820 (2012) 1347-1353.
- [54] A. Varki, Glycan-based interactions involving vertebrate sialic-acid-recognizing proteins, *Nature*, 446 (2007) 1023-1029.
- [55] B. Lepenies, J. Lee, S. Sonkaria, Targeting C-type lectin receptors with multivalent carbohydrate ligands, *Adv Drug Deliv Rev*, 65 (2013) 1271-1281.



- [56] M.D. Joshi, W.W.J. Unger, A.J. van Beelen, S.C. Bruijns, M. Litjens, L. van Bloois, H. Kalay, Y. van Kooyk, G. Storm, DC-SIGN mediated antigen-targeting using glycan-modified liposomes: Formulation considerations, *Int J Pharm*, 416 (2011) 426-432.
- [57] W.W. Unger, A.J. van Beelen, S.C. Bruijns, M. Joshi, C.M. Fehres, L. van Bloois, M.I. Verstege, M. Ambrosini, H. Kalay, K. Nazmi, J.G. Bolscher, E. Hooijberg, T.D. de Gruijl, G. Storm, Y. van Kooyk, Glycan-modified liposomes boost CD4<sup>+</sup> and CD8<sup>+</sup> T-cell responses by targeting DC-SIGN on dendritic cells, *J Control Release*, 160 (2012) 88-95.
- [58] S.H. Rouhanifard, R. Xie, G.X. Zhang, X.M. Sun, X. Chen, P. Wu, Detection and isolation of dendritic cells using Lewis X-functionalized magnetic nanoparticles, *Biomacromolecules*, 13 (2012) 3039-3045.
- [59] D. Arosio, F. Chiodo, J.J. Reina, M. Marelli, S. Penades, Y. van Kooyk, J.J. Garcia-Vallejo, A. Bernardi, Effective targeting of DC-SIGN by  $\alpha$ -fucosylamide functionalized gold nanoparticles, *Bioconj Chem*, 25 (2014) 2244-2251.
- [60] A.K. Singh, S.H. Harrison, J.S. Schoeniger, Gangliosides as receptors for biological toxins: Development of sensitive fluoroimmunoassays using ganglioside-bearing liposomes, *Anal Chem*, 72 (2000) 6019-6024.
- [61] M. Sundberg-Kovamees, T. Holme, A. Sjogren, Interaction of the C-polysaccharide of *Streptococcus pneumoniae* with the receptor asialo-GM1, *Microb Pathog*, 21 (1996) 223-234.
- [62] H.H. Tong, M.A. McIver, L.M. Fisher, T.F. DeMaria, Effect of lacto-N-neotetraose, asialoganglioside-GM1 and neuraminidase on adherence of otitis media-associated serotypes of *Streptococcus pneumoniae* to chinchilla tracheal epithelium, *Microb Pathog*, 26 (1999) 111-119.
- [63] T. Minko, Drug targeting to the colon with lectins and neoglycoconjugates, *Adv Drug Deliv Rev*, 56 (2004) 491-509.
- [64] N. Sharon, H. Lis, Lectins: cell-agglutinating and sugar-specific proteins, *Science*, 177 (1972) 949-959.
- [65] C. Bies, C.M. Lehr, J.F. Woodley, Lectin-mediated drug targeting: History and applications, *Adv Drug Deliv Rev*, 56 (2004) 425-435.
- [66] M.A. Clark, M.A. Jepson, N.L. Simmons, B.H. Hirst, Selective binding and transcytosis of *Ulex-Europaeus* 1 lectin by mouse Peyer's patch M-cells in vivo, *Cell Tissue Res*, 282 (1995) 455-461.
- [67] P.N. Gupta, K. Khatri, A.K. Goyal, N. Mishra, S.P. Vyas, M-cell targeted biodegradable PLGA nanoparticles for oral immunization against hepatitis B, *J Drug Target*, 15 (2007) 701-713.
- [68] B. Malik, A.K. Goyal, T.S. Markandeywar, G. Rath, F. Zakir, S.P. Vyas, Microfold-cell targeted surface engineered polymeric nanoparticles for oral immunization, *J Drug Target*, 20 (2012) 76-84.

- [69] K. Misstear, E.A. McNeela, A.G. Murphy, J.A. Geoghegan, K.M. O'Keeffe, J. Fox, K. Chan, S. Heuking, N. Collin, T.J. Foster, R.M. McLoughlin, E.C. Lavelle, Targeted nasal vaccination provides antibody-independent protection against *Staphylococcus aureus*, *J Infect Dis*, 209 (2014) 1479-1484.
- [70] Y. Mo, L.Y. Lim, Mechanistic study of the uptake of wheat germ agglutinin-conjugated PLGA nanoparticles by A549 cells, *J Pharm Sci*, 93 (2004) 20-28.
- [71] N. Surti, A. Misra, Wheat germ agglutinin-conjugated nanoparticles for sustained cellular and lung delivery of budesonide, *Drug Deliv*, 15 (2008) 81-86.
- [72] Y. Mo, L.Y. Lim, Preparation and in vitro anticancer activity of wheat germ agglutinin (WGA)-conjugated PLGA nanoparticles loaded with paclitaxel and isopropyl myristate, *J Control Release*, 107 (2005) 30-42.
- [73] C. Wang, P.C. Ho, L.Y. Lim, Wheat germ agglutinin-conjugated PLGA nanoparticles for enhanced intracellular delivery of paclitaxel to colon cancer cells, *Int J Pharm*, 400 (2010) 201-210.
- [74] T.M. Allen, Ligand-targeted therapeutics in anticancer therapy, *Nat Rev Cancer*, 2 (2002) 750-763.
- [75] P. Sapra, T.M. Allen, Ligand-targeted liposomal anticancer drugs, *Prog Lipid Res*, 42 (2003) 439-462.
- [76] E. Ruoslahti, RGD and other recognition sequences for integrins, *Annu Rev Cell Dev Biol*, 12 (1996) 697-715.
- [77] J.M. Healy, O. Murayama, T. Maeda, K. Yoshino, K. Sekiguchi, M. Kikuchi, Peptide ligands for integrin  $\alpha_v\beta_5$  selected from random phage display libraries, *Biochemistry*, 34 (1995) 3948-3955.
- [78] W.J.M. Mulder, D.P. Cormode, S. Hak, M.E. Lobatto, S. Silvera, Z.A. Fayad, Multimodality nanotracers for cardiovascular applications, *Nat Clin Pract Cardiovasc Med*, 5 (2008) S103-S111.
- [79] F. Danhier, A. Le Breton, V. Preat, RGD-based strategies to target  $\alpha_v\beta_3$  integrin in cancer therapy and diagnosis, *Mol Pharm*, 9 (2012) 2961-2973.
- [80] S. Shen, H. Tang, X. Zhang, J. Ren, Z. Pang, D. Wang, H. Gao, Y. Qian, X. Jiang, W. Yang, Targeting mesoporous silica-encapsulated gold nanorods for chemo-photothermal therapy with near-infrared radiation, *Biomaterials*, 34 (2013) 3150-3158.
- [81] H.D. Han, L.S. Mangala, J.W. Lee, M.M.K. Shahzad, H.S. Kim, D.Y. Shen, E.J. Nam, E.M. Mora, R.L. Stone, C.H. Lu, S.J. Lee, J.W. Roh, A.M. Nick, G. Lopez-Berestein, A.K. Sood, Targeted gene silencing using RGD-labeled chitosan nanoparticles, *Clin Cancer Res*, 16 (2010) 3910-3922.

- [82] W.J. Mulder, R. Koole, R.J. Brandwijk, G. Storm, P.T. Chin, G.J. Strijkers, C. de Mello Donega, K. Nicolay, A.W. Griffioen, Quantum dots with a paramagnetic coating as a bimodal molecular imaging probe, *Nano Lett*, 6 (2006) 1-6.
- [83] C.L. Modery, M. Ravikumar, T.L. Wong, M.J. Dzuricky, N. Durongkaveroj, A. Sen Gupta, Heteromultivalent liposomal nanoconstructs for enhanced targeting and shear-stable binding to active platelets for site-selective vascular drug delivery, *Biomaterials*, 32 (2011) 9504-9514.
- [84] A.C. Anselmo, C.L. Modery-Pawłowski, S. Menegatti, S. Kumar, D.R. Vogus, L.L. Tian, M. Chen, T.M. Squires, A. Sen Gupta, S. Mitragotri, Platelet-like nanoparticles: Mimicking shape, flexibility, and surface biology of platelets to target vascular injuries, *ACS Nano*, 8 (2014) 11243-11253.
- [85] C. Lesieur, B. Vecsey-Semjen, L. Abrami, M. Fivaz, F. Gisou van der Goot, Membrane insertion: The strategies of toxins (review), *Mol Membr Biol*, 14 (1997) 45-64.
- [86] J.A. DeBin, G.R. Strichartz, Chloride channel inhibition by the venom of the scorpion *Leiurus quinquestriatus*, *Toxicon*, 29 (1991) 1403-1408.
- [87] L. Dardevet, D. Rani, T.A. Aziz, I. Bazin, J.M. Sabatier, M. Fadl, E. Brambilla, M. De Waard, Chlorotoxin: A helpful natural scorpion peptide to diagnose glioma and fight tumor invasion, *Toxins (Basel)*, 7 (2015) 1079-1101.
- [88] A.K. Al-Asmari, M. Islam, A.M. Al-Zahrani, Analysis of the anticancer properties of scorpion venom in colorectal and breast cancer cell lines, *Oncol Lett*, 11 (2016) 1256-1262.
- [89] S.A. Lyons, J. O'Neal, H. Sontheimer, Chlorotoxin, a scorpion-derived peptide, specifically binds to gliomas and tumors of neuroectodermal origin, *Glia*, 39 (2002) 162-173.
- [90] L. Soroceanu, Y. Gillespie, M.B. Khazaeli, H. Sontheimer, Use of chlorotoxin for targeting of primary brain tumors, *Cancer Res*, 58 (1998) 4871-4879.
- [91] C. Sun, O. Veiseh, J. Gunn, C. Fang, S. Hansen, D. Lee, R. Sze, R.G. Ellenbogen, J. Olson, M. Zhang, In vivo MRI detection of gliomas by chlorotoxin-conjugated superparamagnetic nanoprobe, *Small*, 4 (2008) 372-379.
- [92] O. Veiseh, C. Sun, J. Gunn, N. Kohler, P. Gabikian, D. Lee, N. Bhattarai, R. Ellenbogen, R. Sze, A. Hallahan, J. Olson, M.Q. Zhang, Optical and MRI multifunctional nanoprobe for targeting gliomas, *Nano Lett*, 5 (2005) 1003-1008.
- [93] M. Veiseh, P. Gabikian, S.B. Bahrami, O. Veiseh, M. Zhang, R.C. Hackman, A.C. Ravanpay, M.R. Stroud, Y. Kusuma, S.J. Hansen, D. Kwok, N.M. Munoz, R.W. Sze, W.M. Grady, N.M. Greenberg, R.G. Ellenbogen, J.M. Olson, Tumor paint: A Chlorotoxin : Cy5.5 bioconjugate for intraoperative visualization of cancer foci, *Cancer Res*, 67 (2007) 6882-6888.
- [94] L. Zhao, X. Shi, J. Zhao, Chlorotoxin-conjugated nanoparticles for targeted imaging and therapy of glioma, *Curr Top Med Chem*, 15 (2015) 1196-1208.

- [95] C. Qin, B. He, W. Dai, H. Zhang, X. Wang, J. Wang, X. Zhang, G. Wang, L. Yin, Q. Zhang, Inhibition of metastatic tumor growth and metastasis via targeting metastatic breast cancer by chlorotoxin-modified liposomes, *Mol Pharm*, 11 (2014) 3233-3241.
- [96] Y. Xiang, L. Liang, X. Wang, J. Wang, X. Zhang, Q. Zhang, Chloride channel-mediated brain glioma targeting of chlorotoxin-modified doxorubicine-loaded liposomes, *J Control Release*, 152 (2011) 402-410.
- [97] Y. Xiang, Q. Wu, L. Liang, X. Wang, J. Wang, X. Zhang, X. Pu, Q. Zhang, Chlorotoxin-modified stealth liposomes encapsulating levodopa for the targeting delivery against Parkinson's disease in the MPTP-induced mice model, *J Drug Target*, 20 (2012) 67-75.
- [98] S. Nirathanan, E. Charpantier, P. Gopalakrishnakone, M.C. Gwee, H.E. Khoo, L.S. Cheah, R.M. Kini, D. Bertrand, Neuromuscular effects of candoxin, a novel toxin from the venom of the Malayan krait (*Bungarus candidus*), *Br J Pharmacol*, 139 (2003) 832-844.
- [99] S. Nirathanan, E. Charpantier, P. Gopalakrishnakone, M.C.E. Gwee, H.E. Khoo, L.S. Cheah, D. Bertrand, R.M. Kini, Candoxin, a novel toxin from *Bungarus candidus*, is a reversible antagonist of muscle ( $\alpha\beta\gamma\delta$ ) but a poorly reversible antagonist of neuronal  $\alpha 7$  nicotinic acetylcholine receptors, *J Biol Chem*, 277 (2002) 17811-17820.
- [100] C.Y. Zhan, B. Li, L.J. Hu, X.L. Wei, L.Y. Feng, W. Fu, W.Y. Lu, Micelle-based brain-targeted drug delivery enabled by a nicotine acetylcholine receptor ligand, *Angew Chem Int Ed Engl*, 50 (2011) 5482-5485.
- [101] X. Wei, C. Zhan, Q. Shen, W. Fu, C. Xie, J. Gao, C. Peng, P. Zheng, W. Lu, A D-peptide ligand of nicotine acetylcholine receptors for brain-targeted drug delivery, *Angew Chem Int Ed Engl*, 54 (2015) 3023-3027.
- [102] X.L. Wei, J. Gao, C.Y. Zhan, C. Xie, Z.L. Chai, D. Ran, M. Ying, P. Zheng, W.Y. Lu, Liposome-based glioma targeted drug delivery enabled by stable peptide ligands, *J Control Release*, 218 (2015) 13-21.
- [103] M. Zorko, U. Langel, Cell-penetrating peptides: Mechanism and kinetics of cargo delivery, *Adv Drug Deliv Rev*, 57 (2005) 529-545.
- [104] F. Heitz, M.C. Morris, G. Divita, Twenty years of cell-penetrating peptides: From molecular mechanisms to therapeutics, *Br J Pharmacol*, 157 (2009) 195-206.
- [105] J.P. Richard, K. Melikov, H. Brooks, P. Prevot, B. Lebleu, L.V. Chernomordik, Cellular uptake of unconjugated TAT peptide involves clathrin-dependent endocytosis and heparan sulfate receptors, *J Biol Chem*, 280 (2005) 15300-15306.
- [106] J. Tang, L. Zhang, Y.Y. Liu, Q.Y. Zhang, Y. Qin, Y.J. Yin, W.M. Yuan, Y.T. Yang, Y.F. Xie, Z.R. Zhang, Q. He, Synergistic targeted delivery of payload into tumor cells by dual-ligand liposomes co-modified with cholesterol anchored transferrin and TAT, *Int J Pharm*, 454 (2013) 31-40.

- [107] V.A. Sethuraman, Y.H. Bae, TAT peptide-based micelle system for potential active targeting of anti-cancer agents to acidic solid tumors, *J Control Release*, 118 (2007) 216-224.
- [108] L. Hyndman, J.L. Lemoine, L. Huang, D.J. Porteous, A.C. Boyd, X. Nan, HIV-1 Tat protein transduction domain peptide facilitates gene transfer in combination with cationic liposomes, *J Control Release*, 99 (2004) 435-444.
- [109] E. Kleemann, M. Neu, N. Jekel, L. Fink, T. Schmehl, T. Gessler, W. Seeger, T. Kissel, Nano-carriers for DNA delivery to the lung based upon a TAT-derived peptide covalently coupled to PEG-PEI, *J Control Release*, 109 (2005) 299-316.
- [110] A.M. Koch, F. Reynolds, M.F. Kircher, H.P. Merkle, R. Weissleder, L. Josephson, Uptake and metabolism of a dual fluorochrome Tat-nanoparticle in HeLa cells, *Bioconj Chem*, 14 (2003) 1115-1121.
- [111] L. Liu, K. Guo, J. Lu, S.S. Venkatraman, D. Luo, K.C. Ng, E.A. Ling, S. Mochhala, Y.Y. Yang, Biologically active core/shell nanoparticles self-assembled from cholesterol-terminated PEG-TAT for drug delivery across the blood-brain barrier, *Biomaterials*, 29 (2008) 1509-1517.
- [112] M. Malhotra, C. Tomaro-Duchesneau, S. Saha, S. Prakash, Intranasal, siRNA delivery to the brain by TAT/MGF tagged PEGylated chitosan nanoparticles, *J Pharm (Cairo)*, 2013 (2013) 812387.
- [113] F. Madani, S. Lindberg, U. Langel, S. Futaki, A. Graslund, Mechanisms of cellular uptake of cell-penetrating peptides, *J Biophys*, 2011 (2011) 414729.
- [114] S. Petersen, A. Barchanski, U. Taylor, S. Klein, D. Rath, S. Barcikowski, Penetratin-conjugated gold nanoparticles - design of cell-penetrating nanomarkers by femtosecond laser ablation, *J Phys Chem C*, 115 (2011) 5152-5159.
- [115] D. Goswami, H.A. Vitorino, M.T. Machini, B.P. Esposito, Self-assembled penetratin-deferasirox micelles as potential carriers for hydrophobic drug delivery, *Biopolymers*, 104 (2015) 712-719.
- [116] T. Dejardin, J. de la Fuente, P. del Pino, E.P. Furlani, M. Mullin, C.A. Smith, C.C. Berry, Influence of both a static magnetic field and penetratin on magnetic nanoparticle delivery into fibroblasts, *Nanomedicine*, 6 (2011) 1719-1731.
- [117] H.M. Xia, X.L. Gao, G.Z. Gu, Z.Y. Liu, Q.Y. Hu, Y.F. Tu, Q.X. Song, L. Yao, Z.Q. Pang, X.G. Jiang, J. Chen, H.Z. Chen, Penetratin-functionalized PEG-PLA nanoparticles for brain drug delivery, *Int J Pharm*, 436 (2012) 840-850.
- [118] K. Thorstensen, I. Romslo, The role of transferrin in the mechanism of cellular iron uptake, *Biochem J*, 271 (1990) 1-9.
- [119] T.R. Daniels, E. Bernabeu, J.A. Rodriguez, S. Patel, M. Kozman, D.A. Chiappetta, E. Holler, J.Y. Ljubimova, G. Helguera, M.L. Penichet, The transferrin receptor and the targeted delivery of therapeutic agents against cancer, *Biochim Biophys Acta*, 1820 (2012) 291-317.

- [120] L.S. Mendonca, F. Firmino, J.N. Moreira, M.C.P. de Lima, S. Simoes, Transferrin receptor-targeted liposomes encapsulating anti-*BCR-ABL* siRNA or asODN for chronic myeloid leukemia treatment, *Bioconjug Chem*, 21 (2010) 157-168.
- [121] H. Iinuma, K. Maruyama, K. Okinaga, K. Sasaki, T. Sekine, S. Ishida, N. Ogiwara, K. Johkura, Y. Yonemura, Intracellular targeting therapy of cisplatin-encapsulated transferrin-polyethylene glycol liposome on peritoneal dissemination of gastric cancer, *Int J Cancer*, 99 (2002) 130-137.
- [122] J.D. Glickson, S. Lund-Katz, R. Zhou, H. Choi, I.W. Chen, H. Li, I. Corbin, A.V. Popov, W. Cao, L. Song, C. Qi, D. Marotta, D.S. Nelson, J. Chen, B. Chance, G. Zheng, Lipoprotein nanoplatform for targeted delivery of diagnostic and therapeutic agents, *Adv Exp Med Biol*, 645 (2009) 227-239.
- [123] M. Hong, S. Zhu, Y. Jiang, G. Tang, C. Sun, C. Fang, B. Shi, Y. Pei, Novel anti-tumor strategy: PEG-hydroxycamptothecin conjugate loaded transferrin-PEG-nanoparticles, *J Control Release*, 141 (2010) 22-29.
- [124] Y. Zheng, B. Yu, W. Weecharangsan, L. Piao, M. Darby, Y. Mao, R. Koynova, X. Yang, H. Li, S. Xu, L.J. Lee, Y. Sugimoto, R.W. Brueggemeier, R.J. Lee, Transferrin-conjugated lipid-coated PLGA nanoparticles for targeted delivery of aromatase inhibitor 7 $\alpha$ -APTADD to breast cancer cells, *Int J Pharm*, 390 (2010) 234-241.
- [125] C.H. Choi, C.A. Alabi, P. Webster, M.E. Davis, Mechanism of active targeting in solid tumors with transferrin-containing gold nanoparticles, *Proc Natl Acad Sci U S A*, 107 (2010) 1235-1240.
- [126] D. Hogemann-Savellano, E. Bos, C. Blondet, F. Sato, T. Abe, L. Josephson, R. Weissleder, J. Gaudet, D. Sgroi, P.J. Peters, J.P. Basilion, The transferrin receptor: A potential molecular imaging marker for human cancer, *Neoplasia*, 5 (2003) 495-506.
- [127] M. Das, S. Mardyani, W.C.W. Chan, E. Kumacheva, Biofunctionalized pH-responsive microgels for cancer cell targeting: Rational design, *Adv Mater*, 18 (2006) 80-83.
- [128] J.L. Li, D. Day, M. Gu, Ultra-low energy threshold for cancer photothermal therapy using transferrin-conjugated gold nanorods, *Adv Mater*, 20 (2008) 3866-3871.
- [129] P. Pedram, M. Mahani, M. Torkzadeh-Mahani, Z. Hasani, H.X. Ju, Cadmium sulfide quantum dots modified with the human transferrin protein siderophiline for targeted imaging of breast cancer cells, *Microchim Acta*, 183 (2016) 67-71.
- [130] P.P. Ward, O.M. Conneely, Lactoferrin: Role in iron homeostasis and host defense against microbial infection, *Biometals*, 17 (2004) 203-208.
- [131] J.C. Fleet, A new role for lactoferrin: DNA binding and transcription activation, *Nutr Rev*, 53 (1995) 226-227.

- [132] C. Fillebeen, L. Descamps, M.P. Dehouck, L. Fenart, M. Benaissa, G. Spik, R. Cecchelli, A. Pierce, Receptor-mediated transcytosis of lactoferrin through the blood-brain barrier, *J Biol Chem*, 274 (1999) 7011-7017.
- [133] Z.G. Su, L. Xing, Y.N. Chen, Y.R. Xu, F.F. Yang, C. Zhang, Q.N. Ping, Y.Y. Xiao, Lactoferrin-modified poly(ethylene glycol)-grafted BSA nanoparticles as a dual-targeting carrier for treating brain gliomas, *Mol Pharm*, 11 (2014) 1823-1834.
- [134] R. Qiao, Q. Jia, S. Huwel, R. Xia, T. Liu, F. Gao, H.J. Galla, M. Gao, Receptor-mediated delivery of magnetic nanoparticles across the blood-brain barrier, *ACS Nano*, 6 (2012) 3304-3310.
- [135] H. Xie, Y.H. Zhu, W.L. Jiang, Q. Zhou, H. Yang, N. Gu, Y. Zhang, H.B. Xu, H.B. Xu, X.L. Yang, Lactoferrin-conjugated superparamagnetic iron oxide nanoparticles as a specific MRI contrast agent for detection of brain glioma in vivo, *Biomaterials*, 32 (2011) 495-502.
- [136] L. Jiang, Q. Zhou, K. Mu, H. Xie, Y. Zhu, W. Zhu, Y. Zhao, H. Xu, X. Yang, pH/temperature sensitive magnetic nanogels conjugated with Cy5.5-labeled lactoferrin for MR and fluorescence imaging of glioma in rats, *Biomaterials*, 34 (2013) 7418-7428.
- [137] G. Kamalinia, F. Khodagholi, F. Atyabi, M. Amini, F. Shaerzadeh, M. Sharifzadeh, R. Dinarvand, Enhanced brain delivery of deferasirox-lactoferrin conjugates for iron chelation therapy in neurodegenerative disorders: in vitro and in vivo studies, *Mol Pharm*, 10 (2013) 4418-4431.
- [138] M.A. De Luca, F. Lai, F. Corrias, P. Caboni, Z. Bimpisidis, E. Maccioni, A.M. Fadda, G. Di Chiara, Lactoferrin- and antitransferrin-modified liposomes for brain targeting of the NK3 receptor agonist senktide: Preparation and in vivo evaluation, *Int J Pharm*, 479 (2015) 129-137.
- [139] A.M. Kucharska-Newton, W.D. Rosamond, P.J. Mink, A.J. Alberg, E. Shahar, A.R. Folsom, HDL-cholesterol and incidence of breast cancer in the ARIC cohort study, *Ann Epidemiol*, 18 (2008) 671-677.
- [140] D.J. Rader, G.K. Hovingh, HDL and cardiovascular disease, *Lancet*, 384 (2014) 618-625.
- [141] H.X. Lu, H.G. Zhang, D. Zhang, H.W. Lu, D.D. Ma, A biocompatible reconstituted high-density lipoprotein nano-system as a probe for lung cancer detection, *Med Sci Monit*, 21 (2015) 2726-2733.
- [142] S. Yang, M.G. Damiano, H. Zhang, S. Tripathy, A.J. Luthi, J.S. Rink, A.V. Ugoikov, A.T. Singh, S.S. Dave, L.I. Gordon, C.S. Thaxton, Biomimetic, synthetic HDL nanostructures for lymphoma, *Proc Natl Acad Sci U S A*, 110 (2013) 2511-2516.
- [143] P. Conca, G. Franceschini, Synthetic HDL as a new treatment for atherosclerosis regression: has the time come?, *Nutr Metab Cardiovasc Dis*, 18 (2008) 329-335.
- [144] R. Ohashi, H. Mu, X. Wang, Q. Yao, C. Chen, Reverse cholesterol transport and cholesterol efflux in atherosclerosis, *QJM*, 98 (2005) 845-856.

- [145] J.C. Frias, K.J. Williams, E.A. Fisher, Z.A. Fayad, Recombinant HDL-like nanoparticles: a specific contrast agent for MRI of atherosclerotic plaques, *J Am Chem Soc*, 126 (2004) 16316-16317.
- [146] R. Duivenvoorden, J. Tang, D.P. Cormode, A.J. Mieszawska, D. Izquierdo-Garcia, C. Ozcan, M.J. Otten, N. Zaidi, M.E. Lobatto, S.M. van Rijs, B. Priem, E.L. Kuan, C. Martel, B. Hewing, H. Sager, M. Nahrendorf, G.J. Randolph, E.S. Stroes, V. Fuster, E.A. Fisher, Z.A. Fayad, W.J. Mulder, A statin-loaded reconstituted high-density lipoprotein nanoparticle inhibits atherosclerotic plaque inflammation, *Nat Commun*, 5 (2014) 3065.
- [147] K. Chen, X. Chen, Integrin targeted delivery of chemotherapeutics, *Theranostics*, 1 (2011) 189-200.
- [148] R.O. Hynes, A reevaluation of integrins as regulators of angiogenesis, *Nat Med*, 8 (2002) 918-921.
- [149] S. Armeanu-Ebinger, A. Hoh, J. Wenz, J. Fuchs, Targeting EpCAM (CD326) for immunotherapy in hepatoblastoma, *Oncoimmunology*, 2 (2013) e22620.
- [150] E.Y.H. Park, M.J. Smith, E.S. Stropp, K.R. Snapp, J.A. DiVietro, W.F. Walker, D.W. Schmidtke, S.L. Diamond, M.B. Lawrence, Comparison of PSGL-1 microbead and neutrophil rolling: Microvillus elongation stabilizes P-selectin bond clusters, *Biophys J*, 82 (2002) 1835-1847.
- [151] X.Y. Zou, V.R.S. Patil, N.M. Dagia, L.A. Smith, M.J. Wargo, K.A. Interliggi, C.M. Lloyd, D.F.J. Tees, B. Walcheck, M.B. Lawrence, D.J. Goetz, PSGL-1 derived from human neutrophils is a high-efficiency ligand for endothelium-expressed E-selectin under flow, *Am J Physiol Cell Physiol*, 289 (2005) C415-C424.
- [152] X. Chen, R. Wong, I. Khalidov, A.Y. Wang, J. Leelawattanachai, Y. Wang, M.M. Jin, Inflamed leukocyte-mimetic nanoparticles for molecular imaging of inflammation, *Biomaterials*, 32 (2011) 7651-7661.
- [153] N. Doshi, J.N. Orje, B. Molins, J.W. Smith, S. Mitragotri, Z.M. Ruggeri, Platelet mimetic particles for targeting thrombi in flowing blood, *Adv Mater*, 24 (2012) 3864-3869.
- [154] C. Georgens, J. Weyermann, A. Zimmer, Recombinant virus like particles as drug delivery system, *Curr Pharm Biotechnol*, 6 (2005) 49-55.
- [155] R.L. Garcea, L. Gissmann, Virus-like particles as vaccines and vessels for the delivery of small molecules, *Curr Opin Biotechnol*, 15 (2004) 513-517.
- [156] M. Marsh, A. Helenius, Virus entry: Open sesame, *Cell*, 124 (2006) 729-740.
- [157] A.E. Smith, A. Helenius, How viruses enter animal cells, *Science*, 304 (2004) 237-242.
- [158] J.M. Greve, G. Davis, A.M. Meyer, C.P. Forte, S.C. Yost, C.W. Marior, M.E. Kamarck, A. McClelland, The Major Human Rhinovirus Receptor Is ICAM-1, *Cell*, 56 (1989) 839-847.



- [159] T. Yamada, Y. Iwasaki, H. Tada, H. Iwabuki, M.K. Chuah, T. VandenDriessche, H. Fukuda, A. Kondo, M. Ueda, M. Seno, K. Tanizawa, S. Kuroda, Nanoparticles for the delivery of genes and drugs to human hepatocytes, *Nat Biotechnol*, 21 (2003) 885-890.
- [160] L.K. Medina-Kauwe, M. Maguire, N. Kasahara, L. Kedes, Nonviral gene delivery to human breast cancer cells by targeted Ad5 penton proteins, *Gene Ther*, 8 (2001) 1753-1761.
- [161] H. Agadjanian, D. Chu, J.Y. Hwang, S. Wachsmann-Hogiu, A. Rentsendorj, L. Song, V. Valluripalli, J. Lubow, J. Ma, B. Sharifi, D.L. Farkas, L.K. Medina-Kauwe, Chemotherapy targeting by DNA capture in viral protein particles, *Nanomedicine (Lond)*, 7 (2012) 335-352.
- [162] P. Singh, G. Destito, A. Schneemann, M. Manchester, Canine parvovirus-like particles, a novel nanomaterial for tumor targeting, *J Nanobiotechnology*, 4 (2006) 2.
- [163] L.H. Shen, J. Zhou, Y.X. Wang, N. Kang, X.B. Ke, S.L. Bi, L. Ren, Efficient encapsulation of Fe<sub>3</sub>O<sub>4</sub> nanoparticles into genetically engineered Hepatitis B core virus-like particles through a specific interaction for potential bioapplications, *Small*, 11 (2015) 1190-1196.
- [164] I.R. Siboo, H.F. Chambers, P.M. Sullam, Role of SraP, a serine-rich surface protein of *Staphylococcus aureus*, in binding to human platelets, *Infect Immun*, 73 (2005) 2273-2280.
- [165] S. Paukner, G. Kohl, W. Lubitz, Bacterial ghosts as novel advanced drug delivery systems: Antiproliferative activity of loaded doxorubicin in human Caco-2 cells, *J Control Release*, 94 (2004) 63-74.
- [166] F. Kudela, S. Paukner, U.B. Mayr, D. Cholujova, A. Schwarczova, J. Sedlak, J. Bizik, W. Lubitz, Bacterial ghosts as novel efficient targeting vehicles for DNA delivery to the human monocyte-derived dendritic cells, *Journal of Immunother*, 28 (2005) 136-143.
- [167] A. Ganeshpurkar, A. Ganeshpurkar, V. Pandey, A. Agnihotri, D. Bansal, N. Dubey, Harnessing the potential of bacterial ghost for the effective delivery of drugs and biotherapeutics, *Int J Pharm Investig*, 4 (2014) 1-4.
- [168] R. Acevedo, S. Fernandez, C. Zayas, A. Acosta, M.E. Sarmiento, V.A. Ferro, E. Rosenqvist, C. Campa, D. Cardoso, L. Garcia, J.L. Perez, Bacterial outer membrane vesicles and vaccine applications, *Front Immunol*, 5 (2014) 121.
- [169] D.J. Chen, N. Osterrieder, S.M. Metzger, E. Buckles, A.M. Doody, M.P. DeLisa, D. Putnam, Delivery of foreign antigens by engineered outer membrane vesicle vaccines, *Proc Natl Acad Sci U S A*, 107 (2010) 3099-3104.
- [170] M. Groger, W. Holnthoner, D. Maurer, S. Lechleitner, K. Wolff, B.B. Mayr, W. Lubitz, P. Petzelbauer, Dermal microvascular endothelial cells express the 180-kDa macrophage mannose receptor in situ and in vitro, *J Immunol*, 165 (2000) 5428-5434.
- [171] W. Gao, R.H. Fang, S. Thamphiwatana, B.T. Luk, J. Li, P. Angsantikul, Q. Zhang, C.M. Hu, L. Zhang, Modulating antibacterial immunity via bacterial membrane-coated nanoparticles, *Nano Lett*, 15 (2015) 1403-1409.

- [172] S.M. van Dommelen, P. Vader, S. Lakhali, S.A. Kooijmans, W.W. van Solinge, M.J. Wood, R.M. Schiffelers, Microvesicles and exosomes: Opportunities for cell-derived membrane vesicles in drug delivery, *J Control Release*, 161 (2012) 635-644.
- [173] B.T. Luk, L. Zhang, Cell membrane-camouflaged nanoparticles for drug delivery, *J Control Release*, 220 (2015) 600-607.
- [174] R. van der Meel, M.H.A.M. Fens, P. Vader, W.W. van Solinge, O. Eniola-Adefeso, R.M. Schiffelers, Extracellular vesicles as drug delivery systems: Lessons from the liposome field, *J Control Release*, 195 (2014) 72-85.
- [175] A. Hoshino, B. Costa-Silva, T.L. Shen, G. Rodrigues, A. Hashimoto, M. Tesic Mark, H. Molina, S. Kohsaka, A. Di Giannatale, S. Ceder, S. Singh, C. Williams, N. Soplop, K. Uryu, L. Pharmed, T. King, L. Bojmar, A.E. Davies, Y. Ararso, T. Zhang, H. Zhang, J. Hernandez, J.M. Weiss, V.D. Dumont-Cole, K. Kramer, L.H. Wexler, A. Narendran, G.K. Schwartz, J.H. Healey, P. Sandstrom, K.J. Labori, E.H. Kure, P.M. Grandgenett, M.A. Hollingsworth, M. de Sousa, S. Kaur, M. Jain, K. Mallya, S.K. Batra, W.R. Jarnagin, M.S. Brady, O. Fodstad, V. Muller, K. Pantel, A.J. Minn, M.J. Bissell, B.A. Garcia, Y. Kang, V.K. Rajasekhar, C.M. Ghajar, I. Matei, H. Peinado, J. Bromberg, D. Lyden, Tumour exosome integrins determine organotropic metastasis, *Nature*, 527 (2015) 329-335.
- [176] S.C. Jang, O.Y. Kim, C.M. Yoon, D.S. Choi, T.Y. Roh, J. Park, J. Nilsson, J. Lotvall, Y.K. Kim, Y.S. Gho, Bioinspired exosome-mimetic nanovesicles for targeted delivery of chemotherapeutics to malignant tumors, *ACS Nano*, 7 (2013) 7698-7710.
- [177] N.R. Bianco, S.H. Kim, A.E. Morelli, P.D. Robbins, Modulation of the immune response using dendritic cell-derived exosomes, *Methods Mol Biol*, 380 (2007) 443-455.
- [178] S.H. Kim, E.R. Lechman, N. Bianco, R. Menon, A. Keravala, J. Nash, Z.B. Mi, S.C. Watkins, A. Gambotto, P.D. Robbins, Exosomes derived from IL-10-treated dendritic cells can suppress inflammation and collagen-induced arthritis, *J Immunol*, 174 (2005) 6440-6448.
- [179] M.J. Haney, N.L. Klyachko, Y.L. Zhao, R. Gupta, E.G. Plotnikova, Z.J. He, T. Patel, A. Piroyan, M. Sokolsky, A.V. Kabanov, E.V. Batrakova, Exosomes as drug delivery vehicles for Parkinson's disease therapy, *J Control Release*, 207 (2015) 18-30.
- [180] S.V. Mallett, D.J. Cox, Thrombelastography, *Br J Anaesth*, 69 (1992) 307-313.
- [181] E.W. Davie, K. Fujikawa, W. Kisiel, The coagulation cascade: Initiation, maintenance, and regulation, *Biochemistry*, 30 (1991) 10363-10370.
- [182] L.J. Gay, B. Felding-Habermann, Contribution of platelets to tumour metastasis, *Nat Rev Cancer*, 11 (2011) 123-134.
- [183] L. Badimon, T. Padro, G. Vilahur, Atherosclerosis, platelets and thrombosis in acute ischaemic heart disease, *Eur Heart J Acute Cardiovasc Care*, 1 (2012) 60-74.

- [184] J.R. Fitzgerald, T.J. Foster, D. Cox, The interaction of bacterial pathogens with platelets, *Nat Rev Microbiol*, 4 (2006) 445-457.
- [185] C.M.J. Hu, R.H. Fang, B.T. Luk, K.N.H. Chen, C. Carpenter, W.W. Gao, K. Zhang, L.F. Zhang, 'Marker-of-self' functionalization of nanoscale particles through a top-down cellular membrane coating approach, *Nanoscale*, 5 (2013) 2664-2668.
- [186] C.M. Hu, R.H. Fang, J. Copp, B.T. Luk, L. Zhang, A biomimetic nanosponge that absorbs pore-forming toxins, *Nat Nanotechnol*, 8 (2013) 336-340.
- [187] C.M. Hu, R.H. Fang, B.T. Luk, L. Zhang, Nanoparticle-detained toxins for safe and effective vaccination, *Nat Nanotechnol*, 8 (2013) 933-938.
- [188] C.M. Hu, R.H. Fang, K.C. Wang, B.T. Luk, S. Thamphiwatana, D. Dehaini, P. Nguyen, P. Angsantikul, C.H. Wen, A.V. Kroll, C. Carpenter, M. Ramesh, V. Qu, S.H. Patel, J. Zhu, W. Shi, F.M. Hofman, T.C. Chen, W. Gao, K. Zhang, S. Chien, L. Zhang, Nanoparticle biointerfacing by platelet membrane cloaking, *Nature*, 526 (2015) 118-121.
- [189] Q. Hu, W. Sun, C. Qian, C. Wang, H.N. Bomba, Z. Gu, Anticancer platelet-mimicking nanovehicles, *Adv Mater*, 27 (2015) 7043-7050.
- [190] J. Li, Y. Ai, L. Wang, P. Bu, C.C. Sharkey, Q. Wu, B. Wun, S. Roy, X. Shen, M.R. King, Targeted drug delivery to circulating tumor cells via platelet membrane-functionalized particles, *Biomaterials*, 76 (2016) 52-65.
- [191] A. Parodi, N. Quattrocchi, A.L. van de Ven, C. Chiappini, M. Evangelopoulos, J.O. Martinez, B.S. Brown, S.Z. Khaled, I.K. Yazdi, M.V. Enzo, L. Isenhardt, M. Ferrari, E. Tasciotti, Synthetic nanoparticles functionalized with biomimetic leukocyte membranes possess cell-like functions, *Nat Nanotechnol*, 8 (2013) 61-68.
- [192] M. Xuan, J. Shao, L. Dai, Q. He, J. Li, Macrophage cell membrane camouflaged mesoporous silica nanocapsules for in vivo cancer therapy, *Adv Healthc Mater*, 4 (2015) 1645-1652.
- [193] C. Gao, Z. Wu, Z. Lin, X. Lin, Q. He, Polymeric capsule-cushioned leukocyte cell membrane vesicles as a biomimetic delivery platform, *Nanoscale*, 8 (2016) 3548-3554.
- [194] W. He, J. Frueh, Z. Wu, Q. He, How leucocyte cell membrane modified janus microcapsules are phagocytosed by cancer cells, *ACS Appl Mater Interfaces*, 8 (2016) 4407-4415.
- [195] M. Studeny, F.C. Marini, J.L. Dembinski, C. Zompetta, M. Cabreira-Hansen, B.N. Bekele, R.E. Champlin, M. Andreeff, Mesenchymal stem cells: Potential precursors for tumor stroma and targeted-delivery vehicles for anticancer agents, *J Natl Cancer Inst*, 96 (2004) 1593-1603.
- [196] J. Stagg, Mesenchymal stem cells in cancer, *Stem Cell Rev*, 4 (2008) 119-124.
- [197] B.D. Roorda, A. Elst, T.G. Boer, W.A. Kamps, E.S. de Bont, Mesenchymal stem cells contribute to tumor cell proliferation by direct cell-cell contact interactions, *Cancer Invest*, 28 (2010) 526-534.

- [198] N.E. Toledano Furman, Y. Lupu-Haber, T. Bronshtein, L. Kaneti, N. Letko, E. Weinstein, L. Baruch, M. Machluf, Reconstructed stem cell nanoghosts: A natural tumor targeting platform, *Nano Lett*, 13 (2013) 3248-3255.
- [199] P.Y. Lai, R.Y. Huang, S.Y. Lin, Y.H. Lin, C.W. Chang, Biomimetic stem cell membrane-camouflaged iron oxide nanoparticles for theranostic applications, *RSC Adv*, 5 (2015) 98222-98230.
- [200] D. Hanahan, R.A. Weinberg, Hallmarks of cancer: The next generation, *Cell*, 144 (2011) 646-674.
- [201] D. Hanahan, R.A. Weinberg, The hallmarks of cancer, *Cell*, 100 (2000) 57-70.
- [202] J.A. Joyce, J.W. Pollard, Microenvironmental regulation of metastasis, *Nat Rev Cancer*, 9 (2009) 239-252.
- [203] V.V. Glinsky, G.V. Glinsky, O.V. Glinskii, V.H. Huxley, J.R. Turk, V.V. Mossine, S.L. Deutscher, K.J. Pienta, T.P. Quinn, Intravascular metastatic cancer cell homotypic aggregation at the sites of primary attachment to the endothelium, *Cancer Res*, 63 (2003) 3805-3811.
- [204] S.K. Khaldoyanidi, V.V. Glinsky, L. Sikora, A.B. Glinskii, V.V. Mossine, T.P. Quinn, G.V. Glinsky, P. Sriramaraio, MDA-MB-435 human breast carcinoma cell homo- and heterotypic adhesion under flow conditions is mediated in part by Thomsen-Friedenreich antigen-galectin-3 interactions, *J Biol Chem*, 278 (2003) 4127-4134.
205. R.H. Fang, C.M. Hu, B.T. Luk, W. Gao, J.A. Copp, Y. Tai, D.E. O'Connor, L. Zhang, Cancer cell membrane-coated nanoparticles for anticancer vaccination and drug delivery, *Nano Lett*, 14 (2014) 2181-2188.

# Chapter 2

---

## Ultra-Small Lipid Polymer Hybrid NP for Drug Delivery

## **2.1 Ultra-Small Lipid-Polymer Hybrid Nanoparticles for Tumor Penetrating Drug Delivery**

### **2.1.1 Introduction**

Nanoparticle technology has facilitated a great deal of improvement in the field of drug delivery over the past several decades.(2) Newer generation nanocarriers have built upon the success of traditional platforms with further optimizations in material, size, and structural properties in order to ultimately improve their therapeutic potential.(3, 4) Lipid-polymer hybrid nanoparticles are one such example, as they combine the merits of liposomes and polymeric nanoparticles,(5) both of which have been extensively evaluated in the clinic.(6, 7) The hybrid nanoparticles comprise of a biodegradable polymeric core surrounded by a lipid layer with a polyethylene glycol (PEG) coating. The hydrophobic nature of the core enables simple encapsulation and delivery of hydrophobic drugs,(5, 8) which typically have poor bioavailability when administered *in vivo* and cannot be used in their free form. Dual loading of two different payloads, including both hydrophobic and hydrophilic drugs within the same particle, has also been demonstrated.(9) Further, the degradability of the particles can be modulated by adjusting polymer properties or employing stimuli-responsive materials, enabling fine-tuned drug release profiles.(10-12) The outer layer provides a biocompatible, stealth coating that enhances residence time in the bloodstream while also acting as a diffusional barrier against drug release.(5, 13) It has been demonstrated that lipid-polymer hybrid nanoparticles are facile to synthesize,(14) and they are also highly scalable, with clinically relevant quantities easily fabricated using fluidic mixing devices.(15, 16) Many different therapeutic and imaging agents have shown improved delivery and efficacy upon formulation inside the hybrid nanoparticles,

including chemotherapeutics,(8, 9, 17) nucleic acids,(18, 19) and smaller metallic nanoparticles(20) among many others.

Altering the size of nanoparticles can drastically alter their performance *in vivo* by impacting important parameters such as circulation time and biodistribution.(21) Larger nanoparticles are readily cleared by the liver and spleen, while nanoparticles smaller than approximately 5 nm in size will be filtered by the kidney.(22, 23) There is much debate on the ideal size of nanoparticles for drug delivery, which suggests that optimal sizing may be dependent on both the specific platform in question as well as the intended application.(21, 24, 25) As an example, delivery of nanoparticles to the brain via systemic injection is particularly difficult due to the blood-brain barrier, but it has been shown that ultra-small particles can experience improved localization to the organ.(26, 27) The influence of nanoparticle size on tumor treatment has been also investigated; particles smaller than 50 nm can more easily penetrate deeper into the center of tumors, where the cancer stem-like cells responsible for controlling tumor proliferation and recurrence are thought to reside.(24, 25, 28, 29) Given the potential benefits, the ability to push the lower limits of size for nanoparticle platforms that have traditionally existed in larger forms is highly desirable.

Here, we demonstrate a facile synthesis scheme for “ultra-small” lipid-polymer hybrid nanoparticles with a final size less than 25 nm (Fig. 1a). Previously reported sizes of hybrid nanoparticles have ranged from around 50 nm to greater than 200 nm, and synthesis at the lower range has generally required the fine-tuning of solvent composition, polymer concentration, and lipid-to-polymer ratios.(8) In order to fabricate ultra-small hybrids, an adapted nanoprecipitation approach employing charge-based polymer stabilization was used.(30) After optimizing nanoparticle synthesis parameters, the stability of the final formulation under different

physiologically relevant conditions was tested. Further, we examined the ability to introduce cancer targeting functionality as well as encapsulate a chemotherapeutic payload. *In vivo*, both the circulation time and the final biodistribution of the nanoparticles were characterized. Finally, the potential of a folate-functionalized ultra-small hybrid formulation loaded with docetaxel was evaluated for cancer treatment in a mouse xenograft tumor model. The results were compared to those obtained from a clinically used formulation of the same drug. Overall, the ability to engineer an ultra-small version of the lipid-polymer hybrid nanoparticle has the potential to further boost the utility of this already promising platform for a variety of different applications.

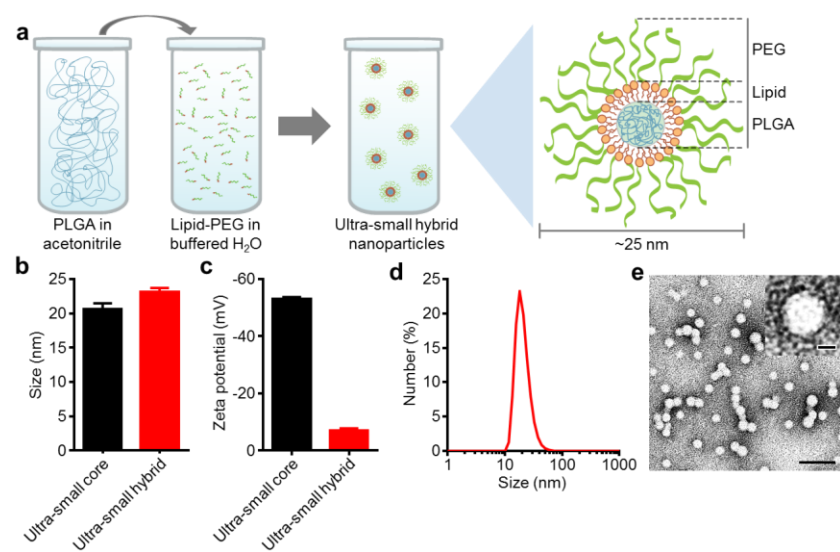


**Figure 2.1.1.** Schematic of synthesis and physicochemical characterization of ultra-small lipid-polymer hybrid nanoparticles. (a) Schematic displaying the process for fabricating ultra-small hybrid nanoparticles. Poly(lactic-co-glycolic acid) (PLGA) dissolved in acetonitrile is added to a buffered aqueous solution containing lipid-PEG, resulting in the formation of sub-25 nm nanoparticles with a core-shell structure. (b) Number-weighted size measurements of ultra-small PLGA cores and ultra-small hybrid nanoparticles ( $n = 3$ ; mean  $\pm$  SD). (c) Zeta potential of ultra-small PLGA cores and ultra-small hybrid nanoparticles ( $n = 3$ ; mean  $\pm$  SD). (d) Number-based size distribution of a representative ultra-small hybrid nanoparticle sample. (e) Transmission electron micrograph of ultra-small hybrid nanoparticles (scale bar = 100 nm). Inset shows a single particle (scale bar = 10 nm).



## 2.1.2 Materials and Methods

Ultra-small lipid-polymer hybrid nanoparticles were prepared using a modified nanoprecipitation process. 1,2-distearoyl-sn-glycero-3-phosphoethanolamine-N-[methoxy(polyethylene glycol)-2000] (DSPE-PEG2000; Avanti Polar Lipids) dissolved in chloroform was deposited in a glass vial, and the solvent was allowed to evaporate. The resulting thin film was then hydrated in water containing Tris-HCl at pH 8 (Affymetrix). Carboxylic acid-terminated poly(lactic-co-glycolic acid) (PLGA-COOH; 0.67 dL/g, 50:50 ratio; Lactel Absorbable Polymers) dissolved at 1 mg/mL in acetonitrile was added rapidly to the DSPE-PEG2000-containing aqueous phase. Particles were purified by washing with water 3 times using 100 kDa MWCO Amicon centrifugal filters (EMD Millipore). Size and zeta potential were measured by dynamic light scattering (DLS) using a Malvern ZEN 3600 Zetasizer. Transmission electron microscopy (TEM) was conducted by depositing nanoparticle samples on a glow-discharged, carbon-coated 400-mesh copper grid (Electron Microscopy Sciences). The grid was then washed using distilled water and stained with 1 wt% uranyl acetate (Electron Microscopy Sciences). Imaging was carried out on a Zeiss Libra 120 PLUS EF-TEM transmission electron microscope. Bare PLGA cores were prepared similarly to the hybrid nanoparticles, but without DSPE-PEG2000 in the aqueous phase. Stability of the ultra-small hybrid nanoparticles was analyzed in 10 mM Tris-HCl at pH 8, phosphate buffered saline (PBS), and fetal bovine serum (FBS). For stability in 10 mM Tris-HCl, hybrid nanoparticles, as well as PLGA cores, were synthesized as described above at a final polymer concentration of 1 mg/mL. To test the stability in 1X PBS, nanoparticles samples at 2 mg/mL were added to an equal volume of 2X PBS. The size of the samples in both 10 mM Tris-HCl and 1X PBS were measured by DLS daily for 8 days, at which point they were measured every two days until day 14. For the serum stability

study, an absorbance-based approach was employed.<sup>31</sup> 100% FBS was concentrated to 2X protein concentration using 10 kDa MWCO Amicon centrifugal filters (EMD Millipore). An equal volume of either 10 mM Tris-HCl or the FBS concentrate was then added to nanoparticle suspensions at 2 mg/mL in 10 mM Tris-HCl aliquoted into the wells of a clear 96-well plate (Corning). Absorbance of the samples were measured in a Tecan Infinite M200 plate reader at a wavelength of 560 nm. Signals were adjusted by subtracting the reading of equivalent blank solutions without nanoparticles at the same wavelength. Hybrid nanoparticles targeting the folate receptor were synthesized by replacing 10 wt% of the DSPE-PEG2000 in the optimized formulation with folate-conjugated DSPE-PEG2000 (Nanocs). To evaluate the targeted formulation in vitro, KB cells (CCL17; American Type Culture Collection) were cultured in RPMI-1640 media (Mediatech). At 24 hours prior to the start of the experiment, the media was changed to folate-free RPMI-1640 (Life Technologies). Fluorescently labeled hybrid nanoparticles, either non-targeted or targeted, were fabricated by the addition of 0.1 wt% 1,1'-dioctadecyl-3,3,3',3'-tetramethylindodicarbocyanine, 4-chlorobenzenesulfonate salt (DiD; Biotium) to the organic phase during synthesis. The particles were added to the KB cells at a final concentration of 0.25 mg/mL and allowed to incubate at 37 °C for 30 minutes. The cells were then washed 3 times with 1X PBS and finally suspended in VECTASHIELD Antifade mounting media with DAPI (Vector Laboratories). Fluorescent imaging was performed on a KEYENCE BZ-X710 fluorescence microscope with a 20X objective using both the DAPI and Cy5 filters with consistent exposure times. The two channels were overlaid and all images were subject to the same brightness and contrast adjustments. For flow cytometric analysis, cells were incubated with nanoparticles the same as above, and then detached using trypsin-EDTA (Life Technologies). The collected cells were washed 3 times with 1X PBS and measured on a Becton

Dickinson FACSCanto II flow cytometer using the red laser and Alexa Fluor 647 filter. Data analysis to find the mean fluorescence intensity of each sample was performed using Treestar Flowjo software.

To examine the *in vivo* tumor penetration, 6-week-old female nu/nu (nude) mice (obtained from a breeding colony at the University of California, San Diego) were subcutaneously implanted with  $1 \times 10^6$  KB cells using 50% Matrigel (BD Biosciences) in the hind flank region. All animal experiments were performed in accordance with NIH guidelines and approved by the Institutional Animal Care and Use Committee (IACUC) of the University of California, San Diego. After 3 weeks, mice were injected intravenously via the tail vein with 200  $\mu$ L of 15 mg/mL DiD-labeled hybrid nanoparticles, either non-targeted or targeted. The mice were euthanized after 24 hours and the tumors were extracted. Tumors were flash frozen in Tissue-Tek O.C.T. compound (Sakura Finetek) and sectioned for histological analysis. FITC-conjugated anti-mouse CD31 (Clone: MEC13.3; Biolegend) was used to label tumor vasculature. Images were taken on a KEYENCE BZ-X710 fluorescence microscope with a 10X objective using both the GFP and Cy5 filters with consistent exposure times. The two channels were overlaid and all images were subject to the same brightness and contrast adjustments.

The chemotherapeutic docetaxel (Biotang) was loaded into the ultra-small hybrid nanoparticles by physical encapsulation. Drug was dissolved with PLGA in the organic phase, and the synthesis proceeded as described above. Particles were washed 3 times with 100 kDa MWCO Amicon centrifugal filters to remove unencapsulated docetaxel. In order to quantify the amount of drug loaded, the purified nanoparticles were lyophilized and dissolved in acetonitrile to release the drug. Samples were analyzed on a PerkinElmer Series 200 high performance liquid chromatography (HPLC) system using a C18 analytical column (Brownlee) with a mobile phase

of 50:50 water to acetonitrile and a detection wavelength of 230 nm. Different weight ratios of drug to polymer, ranging from 0% to 20% were tested in order to optimize drug loading. Known concentrations of docetaxel were used to generate a standard curve. Drug release over time was characterized by dialyzing samples against 1X PBS in 10 kDa MWCO Slide-A-Lyzer MINI dialysis cups (Thermo Scientific). The amount of drug retained in the nanoparticle samples was assessed at 0, 1, 2, 4, 6, 12, 24, 48, and 72 hours. Samples were collected, lyophilized, and then analyzed by HPLC as described above.

Cytotoxicity of the nanoparticles was evaluated by seeding KB cells at 15,000 per well in a 96-well plate. Serially diluted solutions of docetaxel-loaded ultra-small hybrids or Taxotere (Sanofi), giving final drug concentrations starting at 100 ng/mL, were incubated with the cells for a period of 72 hours. After drug incubation, the wells were washed with 1X PBS and a 3-(4,5-dimethylthiazol-2-yl)-2,5-diphenyltetrazolium bromide (MTT) assay was used to quantify cell viability. The MTT reagent (Invitrogen) was incubated with the cells for 4 hours, after which the solution was carefully aspirated and the precipitated crystals dissolved using dimethyl sulfoxide. Absorbance was read at 560 nm on a Tecan Infinite M200 plate reader. Cells lysed with 0.5% Triton-X 100 (Sigma Aldrich) in PBS and untreated cells were used to establish 0% and 100% viability, respectively. IC<sub>50</sub> values were determined by fitting the data using a dose-response inhibition curve in Graphpad Prism. To study the circulation time of ultra-small hybrids in vivo, DiD-labeled nanoparticles, 200  $\mu$ L at 10 mg/mL, were injected via the tail vein of 6-week-old male CD1 mice (Harlan Laboratories). Approximately 100  $\mu$ L of blood was collected by cheek puncture via the submandibular vein at the following timepoints: right after injection and 0.33, 1, 3, 8, 24, 48, and 72 hours. Samples were diluted by 10 times in water and the fluorescence quantified on a Tecan Infinite M200 plate reader at excitation and emission

wavelengths of 630 nm and 670 nm, respectively. Blank signal from diluted blood was subtracted from all measurements, and the data was normalized to the signal from the timepoint right after injection. The data was first fitted using a decay regression model in Graphpad Prism, and the program was used to interpolate the time corresponding to 50% clearance. To calculate the elimination half-life, the normalized signal was transformed using natural log, and the resulting data was fitted using a linear regression curve. Elimination half-life was calculated as  $t_{1/2} = \ln[2]/\beta$ , where  $\beta$  is the negative slope obtained from the fit.

To study the biodistribution of ultra-small hybrid nanoparticles, a DiD-labeled formulation was administered via the tail vein at 10 mg/mL in a volume of 200  $\mu$ L. At 24 hours after injection, the mice were euthanized and subject to whole body perfusion with 1X PBS. Afterwards, the heart, lungs, spleen, kidneys, and liver were harvested and homogenized using a Biospec Mini-Beadbeater-16. Organ fluorescence values were obtained by measuring the homogenate on a Tecan Infinite M200 plate reader at excitation and emission wavelengths of 630 nm and 670 nm, respectively. Background signal was subtracted using organ samples collected from mice not injected with nanoparticles. 6-week-old female nude mice were subcutaneously implanted with  $1 \times 10^6$  KB cells using 50% Matrigel in the hind flank region. At the beginning of week 3, corresponding to 14 days after implantation, tumors were palpable and treatment was initiated with the following: blank solution, non-targeted ultra-small hybrid nanoparticles, targeted ultra-small hybrid nanoparticles, and Taxotere. All drug-containing formulations were administered at 4 mg/kg of docetaxel. Treatments were administered twice per week on weeks 3 and 5 for a total of 4 treatments. Tumor dimensions were measured every other day and the total volume was calculated by the equation  $V = (\text{width}^2 \times \text{length})/2$ , where width and length represent the smallest and largest dimensions, respectively, in the same plane as

the skin surface. Body weight was also monitored every other day. Mice were euthanized when their tumor volume exceeded a predetermined threshold of 2,000 mm<sup>3</sup>.

### **2.1.3 Results and Discussion**

#### **Fabrication and optimization of formulation parameters**

Ultra-small lipid-polymer hybrid nanoparticles were fabricated using a modified nanoprecipitation reaction. Carboxylic acid-terminated poly(lactic-co-glycolic acid) (PLGA-COOH) was dissolved in acetonitrile and added into an aqueous phase buffered with Tris-HCl at pH 8 containing polyethylene glycol (PEG)-conjugated lipids (lipid-PEG). After ultrafiltration, the resulting nanoparticles were characterized by dynamic light scattering (DLS) (Fig. 1b-d). According to the measurements, hybrid nanoparticles were several nanometers larger than the bare PLGA cores, and the zeta potential increased significantly from less than -50 mV to greater than -10 mV when the uncharged lipid-PEG layer was introduced. The data suggests successful surface functionalization of the bare PLGA cores with a layer of lipid-PEG. Further, the number-based size distribution curve obtained from DLS showed a tight grouping around the average nanoparticle size. Visual observation using transmission electron microscopy (TEM) of the hybrid nanoparticles negatively stained with uranyl acetate confirmed that there was a monodisperse population less than 25 nm in size (Fig. 1e).

To optimize the buffer conditions for size minimization, PLGA cores were prepared with varying amounts of buffer in the aqueous phase, ranging from 0 mM to 20 mM Tris-HCl at pH 8 (Fig. 2a). The smallest nanoparticle cores at just over 20 nm in size were observed when using 10 mM Tris-HCl, and this buffering condition was selected for further studies. Minimization at an intermediate concentration suggests that sufficient buffering capacity and charge screening

represent two opposing factors affecting the final size. Next, the amount of lipid-PEG necessary for stabilization of the PLGA cores under physiological conditions was assessed (Fig. 2b). Nanoparticles were synthesized in 10 mM Tris-HCl at pH 8 with lipid-PEG to PLGA weight ratios ranging 0% to 40%, and the solutions were subsequently adjusted to 1X phosphate buffered saline (PBS). Bare cores with no lipid-PEG coating immediately aggregated upon introduction of PBS due to charge screening, an expected outcome given that the particles rely solely on charge stabilization. With increasing amounts of lipid-PEG, the particles exhibited a trend of diminishing size increase after adjusting to 1X PBS. Size minimization occurred approximately at a 30% ratio, and a conservative ratio of 40% lipid-PEG to PLGA was used for further studies. The amount of lipid-PEG necessary to stabilize a given amount of ultra-small PLGA cores was higher than that previously reported for larger hybrid nanoparticle formulations,<sup>5</sup> a difference that reflects the increased surface area of the ultra-small particles at constant mass.

### **Nanoparticle stability**

The stability over time of the final ultra-small hybrid formulation was evaluated over time in both 10 mM Tris-HCl and PBS (Fig. 3a). Bare PLGA cores immediately aggregated in PBS to over 1  $\mu$ m but stayed stable in water over a period of two weeks. In contrast, the hybrid nanoparticle formulation exhibited no increase in size for the duration of the study under both conditions, demonstrating their ability to be stored long-term in solution. Stability of the nanoparticles in 100% fetal bovine serum (FBS) was analyzed using an absorbance-based method (Fig. 3b).<sup>31</sup> Upon addition of FBS to the bare PLGA cores, a marked increase in absorbance was observed, reflecting increased scattering by newly formed particle aggregates. An increase in absorbance was not observed for ultra-small hybrid nanoparticles subjected to the

same treatment, indicating particle stability in the presence of serum proteins. Taken together, the stability characteristics of the final hybrid formulation indicated their suitability for further in vitro and in vivo evaluation.

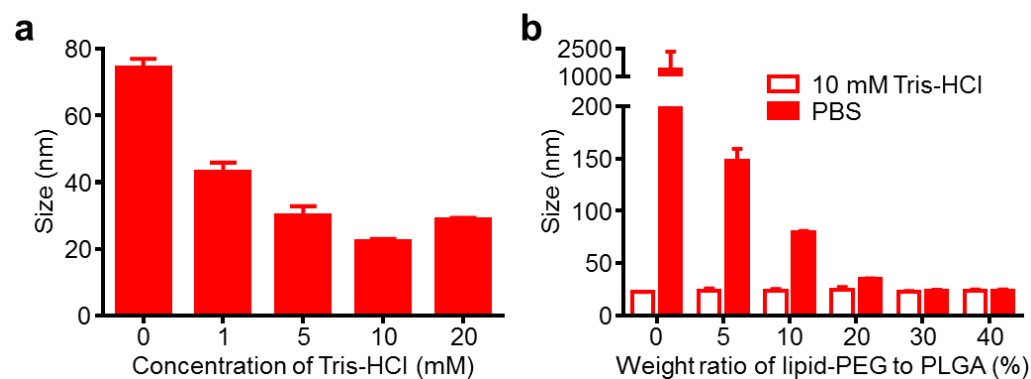


**Figure. 2.1.2.** Optimization of ultra-small hybrid nanoparticle fabrication. (a) Size measurements of PLGA cores precipitated into different concentrations of Tris-HCl buffer at pH 8 ( $n = 3$ ; mean  $\pm$  SD). (b) Size measurements of hybrid nanoparticles synthesized at varying lipid-PEG to PLGA weight ratios ( $n = 3$ ; mean  $\pm$  SD). Measurements were taken after synthesis in 10 mM Tris-HCl at pH 8 and after adjusting to 1X PBS (pH 7.4).



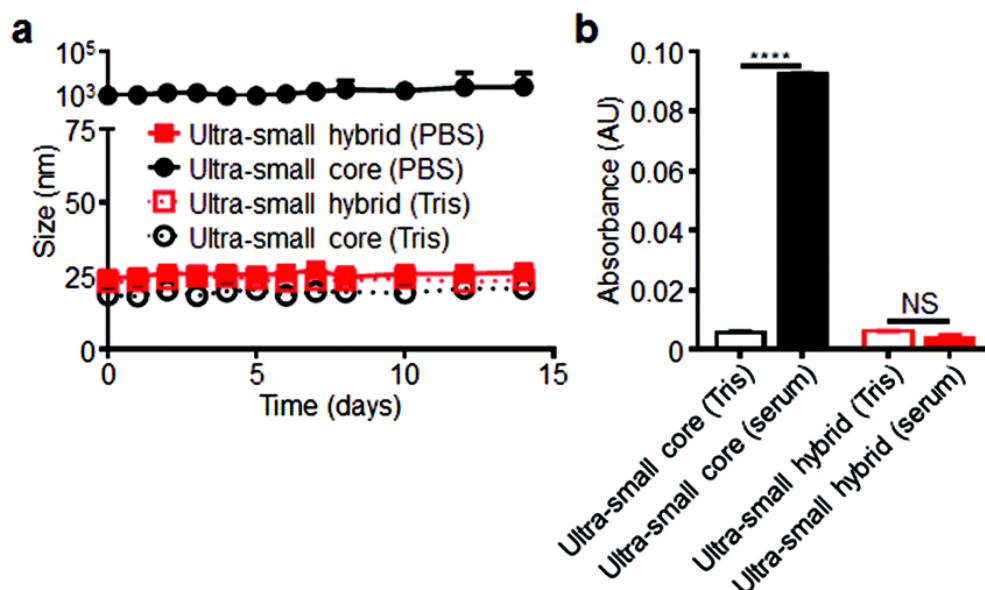


**Figure. 2.1.3.** Ultra-small hybrid nanoparticle stability studies. (a) Size measurements of ultra-small hybrid nanoparticles and ultra-small PLGA cores over the course of 2 weeks in both 10 mM Tris-HCl at pH 8 and 1× PBS (n = 3; mean ± SD). (b) Absorbance at 560 nm of ultra-small hybrid nanoparticles and ultra-small PLGA cores both in 10 mM Tris-HCl at pH 8 and after adjusting to 100% fetal bovine serum (n = 3; mean ± SD). Background signal was subtracted using corresponding blank solutions with no nanoparticles. \*\*\*\*P < 0.0001, NS = not significant, Student's t-test.

## Introduction of targeting functionality

The ability to introduce targeting functionality onto the surface of nanoparticles can help to facilitate more efficient localization to a site of interest.(31-33) In order to demonstrate this for ultra-small hybrid nanoparticles, we used folate, a classical targeting ligand that takes advantage of the fact that many cancers overexpress the folate receptor.(34, 35) Folate-functionalized nanoparticles were fabricated by substituting 10% of the lipid-PEG in the optimized hybrid nanoparticle formulation with lipid-PEG pre-conjugated with folate. The targeting property of this formulation was tested on KB cells, which are known to overexpress the folate receptor (Fig. 4a,b).(36) Fluorescent dye-labeled ultra-small hybrids with or without folate functionality, respectively referred to as targeted or non-targeted formulations, were incubated with the cells, and fluorescence microscopy revealed significantly higher uptake for the targeted formulation.

This was further confirmed by flow cytometry, as the mean fluorescence intensity indicated that the targeted formulation had approximately 3 times the uptake compared to the non-targeted formulation. For cells initially blocked with free folate, the level of uptake for the targeted formulation was reduced to that of the non-targeted, indicating that the increased uptake was receptor specific.

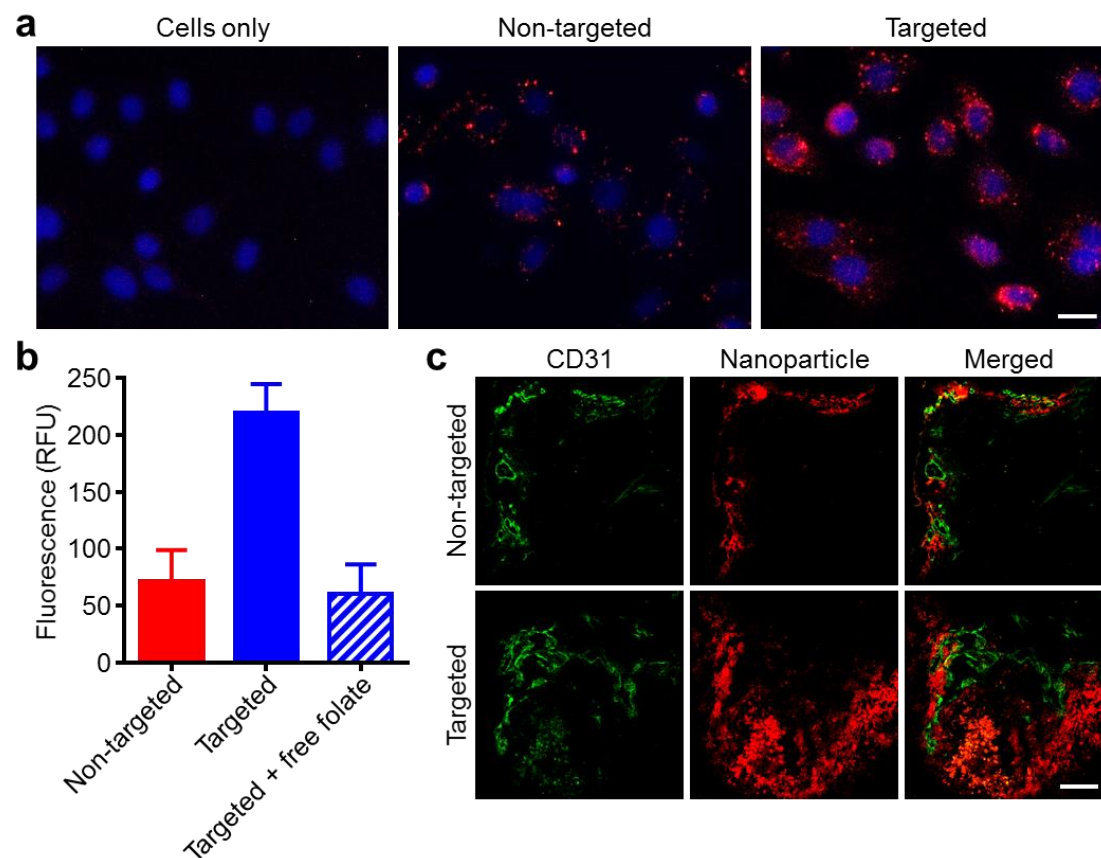


**Figure. 2.1.4.** Introduction of targeting functionality onto ultra-small hybrid nanoparticles. (a) Fluorescent microscopy visualization of KB cells incubated with fluorescent dye-labeled non-targeted or folate receptor-targeted ultra-small hybrid nanoparticles (red: nanoparticles, blue: cell nuclei; scale bare = 20  $\mu$ m). (b) Mean fluorescent intensities as quantified by flow cytometry of KB cells incubated with either non-targeted ultra-small hybrid nanoparticles, targeted hybrid nanoparticles, or targeted hybrid nanoparticles with KB cells blocked with free folate ( $n = 3$ ; mean  $\pm$  SD). (c) Fluorescent microscopy visualization of histological sections from xenograft KB tumors of mice administered with either fluorescent dye-labeled non-targeted or targeted ultra-small hybrid nanoparticles (red: nanoparticles, green: tumor vasculature; scale bare = 100  $\mu$ m).

Next, we examined the ability of the ultra-small hybrid nanoparticles to penetrate into tumors after systemic administration in a folate receptor-overexpressing murine xenograft tumor model. The same KB cell line used for the *in vitro* targeting evaluation was grown subcutaneously in nude mice, and fluorescently labeled targeted or non-targeted hybrid nanoparticles were administered via the tail vein (Fig. 4c). After 24 hours, the mice were euthanized for histological analysis of the tumors. The non-targeted formulation was shown to localize near areas staining positive for the endothelial marker CD31, which was used to delineate tumor vasculature.<sup>(37)</sup> In contrast, the targeted hybrid nanoparticles were found much deeper within the tumor and further away from the vasculature. The difference demonstrates that the additional folate functionality of the targeted nanoparticles can be used to improve tumor penetration by enhancing retention via receptor-specific interactions. Regarding the low presence of non-targeted nanoparticles away from the vasculature, it has been discussed previously that small nanoparticles can penetrate deeper into tumors due to their size, but without a targeting ligand they are also subject to rapid clearance by the same mechanism.<sup>(29)</sup> The ability to target payloads to all areas of a tumor has important implications for treatment and can potentially be used to more effectively destroy cancer stem cells.<sup>(38)</sup>

The ability to introduce targeting functionality onto the surface of nanoparticles can help to facilitate more efficient localization to a site of interest.<sup>32-34</sup> In order to demonstrate this for ultra-small hybrid nanoparticles, we used folate, a classical targeting ligand that takes advantage of the fact that many cancers overexpress the folate receptor.<sup>35, 36</sup> Folate-functionalized nanoparticles were fabricated by substituting 10% of the lipid-PEG in the optimized hybrid nanoparticle formulation with lipid-PEG pre-conjugated with folate. The targeting property of this formulation was tested on KB cells, which are known to overexpress the folate receptor (Fig.

4a,b).<sup>37</sup> Fluorescent dye-labeled ultra-small hybrids with or without folate functionality, respectively referred to as targeted or non-targeted formulations, were incubated with the cells, and fluorescence microscopy revealed significantly higher uptake for the targeted formulation. This was further confirmed by flow cytometry, as the mean fluorescence intensity indicated that the targeted formulation had approximately 3 times the uptake compared to the non-targeted formulation. For cells initially blocked with free folate, the level of uptake for the targeted formulation was reduced to that of the non-targeted, indicating that the increased uptake was receptor specific.

Next, we examined the ability of the ultra-small hybrid nanoparticles to penetrate into tumors after systemic administration in a folate receptor-overexpressing murine xenograft tumor model. The same KB cell line used for the in vitro targeting evaluation was grown subcutaneously in nude mice, and fluorescently labeled targeted or non-targeted hybrid nanoparticles were administered via the tail vein (Fig. 4c). After 24 hours, the mice were euthanized for histological analysis of the tumors. The non-targeted formulation was shown to localize near areas staining positive for the endothelial marker CD31, which was used to delineate tumor vasculature.<sup>38</sup> In contrast, the targeted hybrid nanoparticles were found much deeper within the tumor and further away from the vasculature. The difference demonstrates that the additional folate functionality of the targeted nanoparticles can be used to improve tumor penetration by enhancing retention via receptor-specific interactions. Regarding the low presence of non-targeted nanoparticles away from the vasculature, it has been discussed previously that small nanoparticles can penetrate deeper into tumors due to their size, but without a targeting ligand they are also subject to rapid clearance by the same mechanism.<sup>29</sup> The ability to target

payloads to all areas of a tumor has important implications for treatment and can potentially be used to more effectively destroy cancer stem cells.

### **Drug loading and cytotoxicity**

The drug loading capacity of the ultra-small hybrid nanoparticles was evaluated using docetaxel, a hydrophobic chemotherapeutic commonly used to treat a variety of cancer types in the clinic.<sup>(39)</sup> In order to optimize the loading of docetaxel into the nanoparticles, drug input to PLGA weight ratios ranging from 0% to 20% were tested (Fig. 5a). After removal of free drug by ultrafiltration, the drug loading was quantified by high performance liquid chromatography (HPLC). There was a trend of increasing amounts of loaded docetaxel with increasing initial inputs that remained fairly linear up to 15% drug input. Maximal loading was observed at 20%, and it should be noted that, at higher concentrations, drug-loaded particles were not stable and precipitated out of solution. Thus, a drug-loaded formulation employing the 20% input with a final drug loading of approximately 2% was used for further studies. Next, a drug release study was conducted by dialyzing the docetaxel-loaded ultra-small particles against 1X PBS (Fig. 5b). An initial burst was observed during the first 12 hours, with approximately 50% of the docetaxel released during this period. By the conclusion of the study at 72 hours, a large majority of the drug had been released. Finally, the activity of the drug-loaded formulation was tested by assessing the cytotoxicity of the particles *in vitro* (Fig. 5c). KB cells were incubated for 72 hours with either Taxotere, a clinically used formulation of docetaxel, or drug-loaded ultra-small hybrid nanoparticles at equivalent drug concentrations. The cytotoxicity profile of the two formulations were nearly identical, and IC<sub>50</sub> values were calculated to be 731 pg/mL and 624 pg/mL for the ultra-small hybrid and Taxotere formulations, respectively. This finding suggests

that the activity of the drug remained largely unaltered after being loaded into the hybrid nanoparticles.

### ***In vivo* circulation and biodistribution**

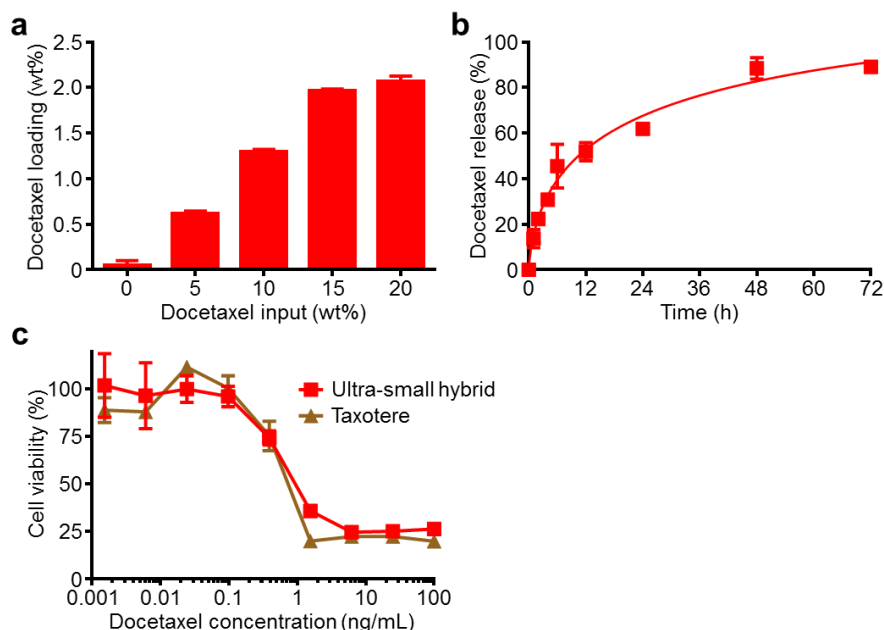


**Figure. 2.1.5.** Drug loading and characterization of ultra-small hybrid nanoparticles. (a) Drug loading quantification of hybrid nanoparticles fabricated at increasing docetaxel input to PLGA weight ratios ( $n = 3$ ; mean  $\pm$  SD). (b) Cumulative release profile of docetaxel-loaded ultra-small hybrid nanoparticles with 2 wt% docetaxel loading over the course of 72 hours in 1X PBS ( $n = 3$ ; mean  $\pm$  SD). (c) Cell viability of KB cells treated with either docetaxel-loaded ultra-small hybrid nanoparticles or Taxotere for 72 hours ( $n = 3$ ; mean  $\pm$  SD). Samples were normalized according to lysed cell and untreated controls.

The fate of ultra-small hybrid nanoparticles after intravenous injection was evaluated. First, the blood circulation in mice was studied after administration of fluorescently labeled nanoparticles via the tail vein (Fig. 6a). Blood was drawn immediately after injection and at timepoints of 0.33, 1, 3, 8, 24, 48, and 72 hours. According to the data, 50% of the particles were cleared by 3.4 hours, and approximately 10% of particles were remaining at 24 hours. Further analysis using a two-compartment model yielded an elimination half-life of approximately 11.5 hours. The ability of the ultra-small hybrid formulation to circulate for an extended period of time can be attributed to the stabilizing properties of the lipid-PEG outer layer, which prevents

non-specific protein interactions that facilitate nanoparticle clearance *in vivo*. This is in stark contrast to bare PLGA cores, which are known to exhibit extremely short blood circulation times.(40)

Next, a biodistribution study was conducted to study organ-level localization of the nanoparticles after intravenous injection (Fig. 6b). Mice were administered with fluorescently labeled ultra-small hybrid nanoparticles. After 24 hours, the mice were euthanized, and the heart, lungs, spleen, kidneys, and liver were collected. After mechanical homogenization, the signal from each organ was quantified. It was shown that the highest absolute amount of fluorescence was present in the liver, an expected outcome given that the organ has been widely shown to play an important role in nanoparticle clearance.(22) There were relatively low amounts of signal in the other organs tested. Notably, the signal in the lungs was very low, a desirable finding given the potential toxicity associated with over-accumulation.(41, 42) The results observed are in line with previously reported data for similarly structured nanoparticles.(13, 40, 43)

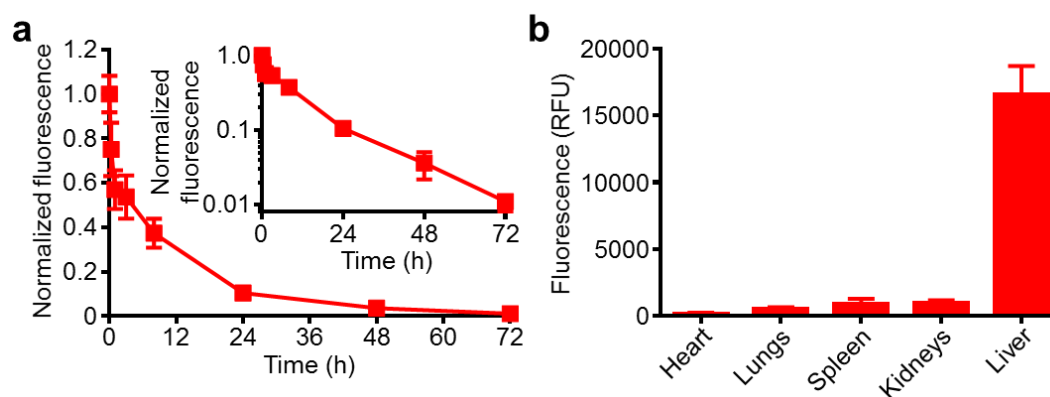


**Figure. 2.1.6.** *In vivo* characterization of ultra-small hybrid nanoparticles. (a) Circulation time of fluorescent dye-labeled ultra-small hybrid nanoparticles after intravenous administration ( $n = 6$ ; mean  $\pm$  SD). Blood samples were collected at designated timepoints and measured for fluorescence intensities. Signals were normalized according to the first collected sample right after injection. Inset shows the data on a semi-log plot. (b) Biodistribution of fluorescent dye-loaded ultra-small hybrid nanoparticles 24 hours after intravenous administration ( $n = 3$ ; mean  $\pm$  SD). Fluorescent signal was measured from homogenized organs after whole body perfusion.

### ***In vivo* tumor treatment efficacy**

Given the stability of the ultra-small hybrid nanoparticles both *in vitro* and *in vivo*, their capacity for drug loading, and their ability to be functionalized with an active targeting ligand, we tested their potential for cancer treatment in a murine xenograft tumor model. KB cells were implanted in nude mice and allowed to develop into palpable tumors over the course of two weeks. Afterwards, docetaxel-loaded ultra-small hybrids, both targeted and non-targeted, were administered a total of 4 times (twice per week on weeks 3 and 5) at a dosage of 4 mg/kg (Fig. 7a-c). Taxotere, at the same drug dosage, as well as blank solution were used as controls. As expected, the tumors in mice treated with blank solution continued to progress, with a median survival of 38 days after tumor implantation. Both the non-targeted ultra-small formulation and



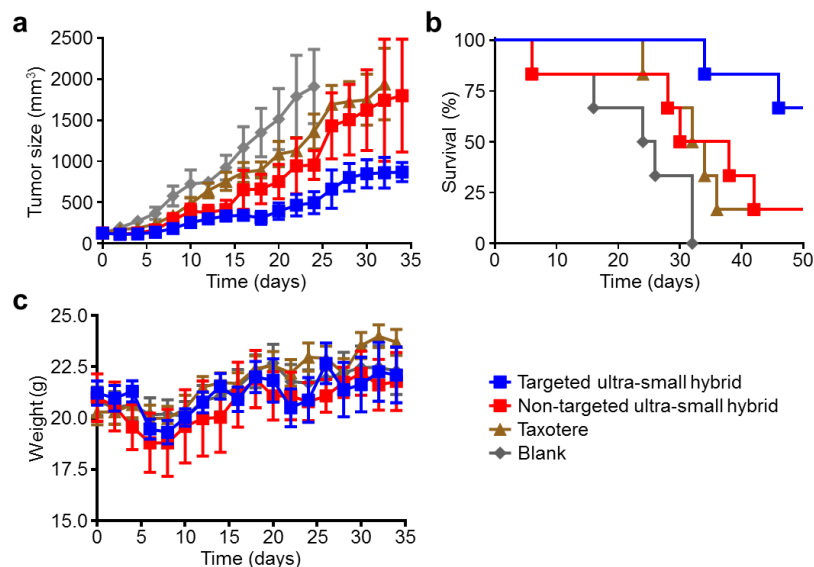


**Figure. 2.1.7** *In vivo* tumor treatment using drug-loaded ultra-small hybrid nanoparticles. (a) Growth kinetics of KB tumors implanted into nude mice and treated with either blank solution, Taxotere, docetaxel-loaded non-targeted hybrid nanoparticles, or docetaxel-loaded folate receptor-targeted hybrid nanoparticles with 4 total doses (twice a week on weeks 3 and 5) at 4 mg/kg of docetaxel each (n = 6; mean  $\pm$  SEM). (b) Survival curve of mice in (a). Mice were euthanized when tumor volume exceeded 2,000 mm<sup>3</sup>. (c) Body weight measurements of mice in (a) (mean  $\pm$  SEM). All times on x-axes start with the initiation of treatment, corresponding to 14 days after tumor implantation.

Taxotere showed similar growth kinetics, showing moderate control of tumor growth and extending median survival to 44 and 46 days, respectively. The targeted ultra-small formulation performed the best, significantly suppressing tumor growth, and more than half of the mice were still alive at 64 days after tumor challenge. As an indicator of global health, body weights were monitored over the course of the study. The measurements from the treatment groups were not significantly different from those treated with blank solution, suggesting that it may be possible to raise the dosing in future studies. It should be noted that the docetaxel dosage used in the present study is lower than previously determined values for the maximum tolerated dose of the Taxotere formulation.(44, 45) The ability to generate a targeted ultra-small hybrid nanoparticle formulation that significantly outperforms a clinically used formulation highlights the benefit of the platform for tumor treatment applications and suggests that further study may be warranted along these lines.

## 2.1.4 Conclusion

In conclusion, we have demonstrated the fabrication and application of ultra-small lipid-polymer hybrid nanoparticles under 25 nm in size. A simple, charge-based stabilization strategy was employed for the synthesis of a monodisperse population of these particles, which were significantly smaller than previously reported lipid-polymer hybrids. It was shown that the particles retained the advantageous properties of the hybrid nanoparticle platform, including excellent stability *in vitro* and *in vivo*, drug loading capability, and facile incorporation of targeting functionality. Targeted ultra-small hybrids demonstrated effective localization to regions deep within tumors, and, when loaded with the chemotherapeutic docetaxel, were able to outperform a clinically used formulation of the drug. Given that these ultra-small hybrid nanoparticles are fabricated from FDA-approved materials and employ a facile synthesis scheme, they appear primed for translation, although further studies on the scale-up of this specific formulation are warranted. Ultimately, the addition of an ultra-small version to the size repertoire of hybrid nanoparticles helps to further boost the utility of the platform and may provide a means of improving the therapeutic profile of drug payloads across a wide range of different applications.

## Acknowledgements

This work is supported by the National Science Foundation Grant DMR-1505699 and the National Institute of Diabetes and Digestive and Kidney Diseases of the National Institutes of Health under Award Number R01DK095168.

Chapter 2.1, in full, is a reprint of the material as it appears in Nanoscale, 2016, Diana Dehaini, Ronnie H. Fang, Brian T. Luk, Zhiqing Pang, Che-Ming J. Hu, Ashley V. Kroll, Chun

Lai Yu, Weiwei Gao, and Liangfang Zhang. The dissertation author is the primary author of this work.

## References

1. L. Brannon-Peppas, J.O. Blanchette, Nanoparticle and Targeted Systems for Cancer Therapy, *Adv. Drug Deliv. Rev.*, 56 (2004) 1649-1659.
2. V. Wagner, A. Dullaart, A.K. Bock, A. Zweck, The Emerging Nanomedicine Landscape, *Nat. Biotechnol.*, 24 (2006) 1211-1217.
3. A.Z. Wang, R. Langer, O.C. Farokhzad, Nanoparticle Delivery of Cancer Drugs, *Annu. Rev. Med.*, 63 (2012) 185-198.
4. O.C. Farokhzad, R. Langer, Impact of Nanotechnology on Drug Delivery, *ACS Nano*, 3 (2009) 16-20.
5. L. Zhang, J.M. Chan, F.X. Gu, J.W. Rhee, A.Z. Wang, A.F. Radovic-Moreno, F. Alexis, R. Langer, O.C. Farokhzad, Self-Assembled Lipid-Polymer Hybrid Nanoparticles: A Robust Drug Delivery Platform, *ACS Nano*, 2 (2008) 1696-1702.
6. N. Kamaly, Z. Xiao, P.M. Valencia, A.F. Radovic-Moreno, O.C. Farokhzad, Targeted Polymeric Therapeutic Nanoparticles: Design, Development and Clinical Translation, *Chem. Soc. Rev.*, 41 (2012) 2971-3010.
7. B.S. Pattni, V.V. Chupin, V.P. Torchilin, New Developments in Liposomal Drug Delivery, *Chem. Rev.*, 115 (2015) 10938-10966.
8. J.M. Chan, L. Zhang, K.P. Yuet, G. Liao, J.W. Rhee, R. Langer, O.C. Farokhzad, PLGA-Lecithin-PEG Core-Shell Nanoparticles for Controlled Drug Delivery, *Biomaterials*, 30 (2009) 1627-1634.
9. S. Aryal, C.M.J. Hu, V. Fu, L. Zhang, Nanoparticle Drug Delivery Enhances the Cytotoxicity of Hydrophobic-Hydrophilic Drug Conjugates, *J. Mater. Chem.*, 22 (2012) 994-999.
10. R. Cheng, F. Meng, C. Deng, H.A. Klok, Z. Zhong, Dual and Multi-Stimuli Responsive Polymeric Nanoparticles for Programmed Site-Specific Drug Delivery, *Biomaterials*, 34 (2013) 3647-3657.
11. H.K. Makadia, S.J. Siegel, Poly Lactic-co-Glycolic Acid (PLGA) as Biodegradable Controlled Drug Delivery Carrier, *Polymers (Basel)*, 3 (2011) 1377-1397.

12. C. Clawson, L. Ton, S. Aryal, V. Fu, S. Esener, L. Zhang, Synthesis and Characterization of Lipid-Polymer Hybrid Nanoparticles with pH-Triggered Poly(ethylene glycol) Shedding, *Langmuir*, 27 (2011) 10556-10561.
13. R. Gref, A. Domb, P. Quellec, T. Blunk, R.H. Muller, J.M. Verbavatz, R. Langer, The Controlled Intravenous Delivery of Drugs Using PEG-Coated Sterically Stabilized Nanospheres, *Adv. Drug Deliv. Rev.*, 16 (1995) 215-233.
14. R.H. Fang, S. Aryal, C.M. Hu, L. Zhang, Quick Synthesis of Lipid-Polymer Hybrid Nanoparticles with Low Polydispersity Using a Single-Step Sonication Method, *Langmuir*, 26 (2010) 16958-16962.
15. P.M. Valencia, O.C. Farokhzad, R. Karnik, R. Langer, Microfluidic Technologies for Accelerating the Clinical Translation of Nanoparticles, *Nat. Nanotechnol.*, 7 (2012) 623-629.
16. R. Karnik, F. Gu, P. Basto, C. Cannizzaro, L. Dean, W. Kyei-Manu, R. Langer, O.C. Farokhzad, Microfluidic Platform for Controlled Synthesis of Polymeric Nanoparticles, *Nano Lett.*, 8 (2008) 2906-2912.
17. S. Aryal, C.M.J. Hu, L. Zhang, Polymeric Nanoparticles with Precise Ratiometric Control over Drug Loading for Combination Therapy, *Molecular pharmaceuticals*, 8 (2011) 1401-1407.
18. W. Hasan, K. Chu, A. Gullapalli, S.S. Dunn, E.M. Enlow, J.C. Luft, S.M. Tian, M.E. Napier, P.D. Pohlhaus, J.P. Rolland, J.M. DeSimone, Delivery of Multiple siRNAs Using Lipid-Coated PLGA Nanoparticles for Treatment of Prostate Cancer, *Nano Lett.*, 12 (2012) 287-292.
19. X.F. Su, J. Fricke, D.G. Kavanagh, D.J. Irvine, In Vitro and in Vivo mRNA Delivery Using Lipid-Enveloped pH-Responsive Polymer Nanoparticles, *Molecular pharmaceuticals*, 8 (2011) 774-787.
20. S.D. Kong, M. Sartor, C.M. Hu, W. Zhang, L. Zhang, S. Jin, Magnetic Field Activated Lipid-Polymer Hybrid Nanoparticles for Stimuli-Responsive Drug Release, *Acta Biomater.*, 9 (2013) 5447-5452.
21. J.W. Yoo, E. Chambers, S. Mitragotri, Factors that Control the Circulation Time of Nanoparticles in Blood: Challenges, Solutions and Future Prospects, *Curr. Pharm. Des.*, 16 (2010) 2298-2307.
22. F. Alexis, E. Pridgen, L.K. Molnar, O.C. Farokhzad, Factors Affecting the Clearance and Biodistribution of Polymeric Nanoparticles, *Molecular pharmaceuticals*, 5 (2008) 505-515.
23. E. Blanco, H. Shen, M. Ferrari, Principles of Nanoparticle Design for Overcoming Biological Barriers to Drug Delivery, *Nat. Biotechnol.*, 33 (2015) 941-951.
24. L. Tang, N.P. Gabrielson, F.M. Uckun, T.M. Fan, J. Cheng, Size-Dependent Tumor Penetration and in Vivo Efficacy of Monodisperse Drug-Silica Nanoconjugates, *Molecular pharmaceuticals*, 10 (2013) 883-892.

25. C.M. Hu, R.H. Fang, K.C. Wang, B.T. Luk, S. Thamphiwatana, D. Dehaini, P. Nguyen, P. Angsantikul, C.H. Wen, A.V. Kroll, C. Carpenter, M. Ramesh, V. Qu, S.H. Patel, J. Zhu, W. Shi, F.M. Hofman, T.C. Chen, W. Gao, K. Zhang, S. Chien, L. Zhang, Nanoparticle biointerfacing by platelet membrane cloaking, *Nature*, 526 (2015) 118-121.
26. M. Bramini, D. Ye, A. Hallerbach, M.N. Raghnaill, A. Salvati, C. Aberg, K.A. Dawson, Imaging Approach to Mechanistic Study of Nanoparticle Interactions with the Blood-Brain Barrier, *ACS Nano*, 8 (2014) 4304-4312.
27. D.H. Jo, J.H. Kim, T.G. Lee, J.H. Kim, Size, Surface Charge, and Shape Determine Therapeutic Effects of Nanoparticles on Brain and Retinal Diseases, *Nanomedicine*, 11 (2015) 1603-1611.
28. W. Rao, H. Wang, J. Han, S. Zhao, J. Dumbleton, P. Agarwal, W. Zhang, G. Zhao, J. Yu, D.L. Zynger, X. Lu, X. He, Chitosan-Decorated Doxorubicin-Encapsulated Nanoparticle Targets and Eliminates Tumor Reinitiating Cancer Stem-Like Cells, *ACS Nano*, 9 (2015) 5725-5740.
29. L. Tang, X. Yang, Q. Yin, K. Cai, H. Wang, I. Chaudhury, C. Yao, Q. Zhou, M. Kwon, J.A. Hartman, I.T. Dobrucki, L.W. Dobrucki, L.B. Borst, S. Lezmi, W.G. Helferich, A.L. Ferguson, T.M. Fan, J. Cheng, Investigating the Optimal Size of Anticancer Nanomedicine, *Proc. Natl. Acad. Sci. USA*, 111 (2014) 15344-15349.
30. A. Reisch, A. Runser, Y. Arntz, Y. Mely, A.S. Klymchenko, Charge-Controlled Nanoprecipitation as a Modular Approach to Ultrasmall Polymer Nanocarriers: Making Bright and Stable Nanoparticles, *ACS Nano*, 9 (2015) 5104-5116.
31. C.M. Hu, L. Zhang, S. Aryal, C. Cheung, R.H. Fang, L. Zhang, Erythrocyte Membrane-Camouflaged Polymeric Nanoparticles as a Biomimetic Delivery Platform, *Proc. Natl. Acad. Sci. USA*, 108 (2011) 10980-10985.
32. D. Dehaini, R.H. Fang, L. Zhang, Biomimetic Strategies for Targeted Nanoparticle Delivery, *Bioeng. Transl. Med.*, [Online early access]. DOI: 10.1002/btm1002.10004. Published Online: Apr 10009, 12016.
33. R. Bazak, M. Hourri, S. El Achy, S. Kamel, T. Refaat, Cancer Active Targeting by Nanoparticles: A Comprehensive Review of Literature, *J. Cancer Res. Clin. Oncol.*, 141 (2015) 769-784.
34. C.M. Hu, S. Kaushal, H.S. Tran Cao, S. Aryal, M. Sartor, S. Esener, M. Bouvet, L. Zhang, Half-Antibody Functionalized Lipid-Polymer Hybrid Nanoparticles for Targeted Drug Delivery to Carcinoembryonic Antigen Presenting Pancreatic Cancer Cells, *Molecular pharmaceuticals*, 7 (2010) 914-920.
35. J. Sudimack, R.J. Lee, Targeted Drug Delivery via the Folate Receptor, *Adv. Drug Deliv. Rev.*, 41 (2000) 147-162.
36. M.O. Oyewumi, R.A. Yokel, M. Jay, T. Coakley, R.J. Mumper, Comparison of Cell Uptake, Biodistribution and Tumor Retention of Folate-Coated and PEG-Coated Gadolinium

Nanoparticles in Tumor-Bearing Mice, *J. Control. Release*, 95 (2004) 613-626.

37. J.A. Reddy, L.S. Haneline, E.F. Srouf, A.C. Antony, D.W. Clapp, P.S. Low, Expression and Functional Characterization of the  $\beta$ -Isoform of the Folate Receptor on CD34+ Cells, *Blood*, 93 (1999) 3940-3948.

38. D. Wang, C.R. Stockard, L. Harkins, P. Lott, C. Salih, K. Yuan, D. Buchsbaum, A. Hashim, M. Zayzafoon, R.W. Hardy, O. Hameed, W. Grizzle, G.P. Siegal, Immunohistochemistry in the Evaluation of Neovascularization in Tumor Xenografts, *Biotech. Histochem.*, 83 (2008) 179-189.

39. S. Vinogradov, X. Wei, Cancer Stem Cells and Drug Resistance: The Potential of Nanomedicine, *Nanomedicine*, 7 (2012) 597-615.

40. R.H. Earhart, Docetaxel (Taxotere): Preclinical and General Clinical Information, *Semin. Oncol.*, 26 (1999) 8-13.

41. Card JW, Zeldin DC, Bonner JC, & Nestmann ER (2008) Pulmonary applications and toxicity of engineered nanoparticles. *American journal of physiology. Lung cellular and molecular physiology* 295(3):L400-411.

42. Xie G, Sun J, Zhong G, Shi L, & Zhang D (2010) Biodistribution and toxicity of intravenously administered silica nanoparticles in mice. *Archives of toxicology* 84(3):183-190.

43. Jokerst JV, Lobovkina T, Zare RN, & Gambhir SS (2011) Nanoparticle PEGylation for imaging and therapy. *Nanomedicine (Lond.)* 6(4):715-728.

44. Vanhoefer U, Cao S, Harstrick A, Seeber S, & Rustum YM (1997) Comparative antitumor efficacy of docetaxel and paclitaxel in nude mice bearing human tumor xenografts that overexpress the multidrug resistance protein (MRP). *Ann Oncol* 8(12):1221-1228.

45. Desai N, Trieu V, Soon-Shiong P, & Hawkins M (2005) Abraxane (ABI-007) vs Taxotere: a preclinical comparison of toxicity and efficacy. *Cancer Res.* 65(9 Supplement):336-3

# Chapter 3

---

Red blood cell membrane coated nanoparticles  
as a drug delivery platform

## **3.1 Erythrocyte membrane-cloaked polymeric nanoparticles for controlled drug loading and release**

### **3.1.1 Introduction**

In recent decades, advances in engineering materials at the nanometer scale have resulted in a myriad of nanoparticle (NP)-based drug-delivery systems for clinical applications [1, 2]. The unique advantages of these nanomedicines, particularly their improvement on existing therapeutic agents through altered pharmacokinetics and biodistribution profiles, hinge on their ability to circulate in the bloodstream for a prolonged period of time [3, 4]. As a result, considerable research interest has focused on the search for novel materials, both natural and synthetically made, that allow NPs to bypass macrophage uptake and systemic clearance [5, 6]. Meanwhile, strategies aimed at extending particle residence time *in vivo* through modifying the physicochemical properties of NPs (including size, shape, deformity and surface characteristics) have also been extensively explored [7, 8].

In this regard, the authors recently developed a red blood cell membrane (RBCm)-cloaked NP drug-delivery system with the combined advantages of a long circulation lifetime (from RBCs), and controlled drug retention and release (from polymeric particles) [9]. The authors top-down approach, based on the extrusion of polymeric particles mixed with preformed RBCm-derived vesicles, translocated the entire RBCm with preserved membrane proteins to the surface of sub 100-nm polymeric cores, resulting in NPs cloaked by the erythrocyte exterior for longer systemic circulation. This cell-mimicking strategy provides a cellular membrane medium surrounding polymeric cores for transmembrane protein anchorage, hence avoiding chemical modifications in conventional NP surface fictionalizations that could compromise the integrity



and functionalities of the proteins.

As part of continuing efforts to further develop this cell-mimicking NP platform for advanced drug-delivery applications, the authors report formulation strategies for loading small-molecule chemotherapy drugs such as doxorubicin (DOX), a model anticancer drug, into NPs and study drug-release kinetics with an emphasis on the role played by RBCm cloaks in drug retention. Specifically, to load DOX molecules into the NP core, two distinct strategies were explored: physically encapsulating drug molecules into the polymer matrix, and chemically conjugating drug molecules to the polymer backbones. It was demonstrated that they result in distinct drug-loading yields and release kinetics. NPs were further formulated with the same polymer cores as RBCm-cloaked NPs, but coated with polyethylene glycol (PEG) rather than RBCm (PEGylated NPs). Comparison of the drug- release profiles for the two delivery systems demonstrated that the RBCm cloak provides a barrier, retarding the outward diffusion of encapsulated drug molecules, and can therefore potentially be exploited to better control drug release. Additionally, in an attempt to examine the therapeutic potential of the RBCm-cloaked NPs, an acute myeloid leukemia (AML) Kasumi-1 cell line was chosen, and it was demonstrated that DOX-loaded RBCm-cloaked NPs exhibited higher toxicity by comparison with the same amount of free DOX.

### **3.1.2 Experimental Methods**

#### **RBC Ghost Derivation**

RBC ghosts devoid of cytoplasmic contents were prepared following previously published protocols [9, 10]. Briefly, whole blood, withdrawn from male (imprinting control region)mice (6–8 weeks old, Charles River Laboratories) through cardiac puncture with a

syringe containing a drop of heparin solution (Cole-Parmer), was centrifuged ( $800 \times g$  for 5 min at  $4^{\circ}\text{C}$ ) to remove serum and buffy coat. The packed RBCs were washed in ice-cold  $1 \times$  phosphate-buffered solution (PBS), treated by hypotonic medium for hemolysis, and then suspended in  $0.25 \times$  PBS in an ice bath for 20 min. The hemoglobin was removed by centrifuging the suspension at  $800 \times g$  for 5 min. RBC ghosts in the form of a pink pellet were collected.

### **Preparation of RBCm-Derived Vesicles**

The collected RBC ghosts were sonicated in a capped glass vial for 5 min using a FS30D bath sonicator (Fisher Scientific) at a frequency of 42 kHz and power of 100 W. The resulting vesicles were subsequently extruded repeatedly through 400-nm and then 200-nm polycarbonate porous membranes using an Avanti mini extruder (Avanti Polar Lipids). After each extrusion, the size of the RBCm-derived vesicles was monitored using dynamic light scattering (Nano-ZS, model ZEN3600).

### **Ring-Opening Polymerization of L-lactide**

DOX–poly(lactide acid) (PLA) conjugates were synthesized based on a previously published protocol [11, 12]. Briefly, ring-opening polymerization of L-lactide (Sigma-Aldrich, USA) was catalyzed by an alkoxy complex  $(\text{BDI})\text{ZnN}(\text{SiMe}_3)_2$  in a glovebox filled with argon at room temperature.  $(\text{BDI})\text{ZnN}(\text{SiMe}_3)_2$  (6.4 mg, 0.01 mmol) and DOX (Jinan Wedo Co. Ltd, China; 5.4 mg, 0.01 mmol) were mixed in anhydrous tetrahydrofuran (0.5 ml), where l-lactide (101 mg, 0.7 mmol) dissolved in 2 ml of anhydrous THF was added dropwise.

After the L-lactide was completely consumed as indicated by proton nuclear magnetic resonance spectroscopy (Varian Mercury 400 MHz spectrometer), the crude product was

precipitated in cold diethyl ether and purified by multiple dissolution–precipitation cycles. The conjugation was confirmed by proton nuclear magnetic resonance spectroscopy and conjugates had a molecular weight (MW) of approximately 10,000 g/mol determined by gel permeation chromatography (Viscotek, USA).

### **Preparation of NP Core & Loading of DOX**

The DOX–PLA conjugate was first dissolved in acetonitrile to form 1 mg/ml solution. A total of 1 ml of such solution was added dropwise to 3 ml of water. The mixture was then stirred in open air for 2 h, allowing the acetonitrile to evaporate. The resulting solution of NP cores was washed using Amicon Ultra-4 Centrifugal Filters (Millipore, 10 kDa cut-off) to completely remove organic solvent residues. The particles were then re-suspended in 1 ml distilled water. To physically encapsulate DOX, 1 mg poly(lactic-*co*-glycolic acid [PLGA]; 0.67 dl/g, carboxy-terminated, LACTEL Absorbable Polymers) was first dissolved into 1 ml acetonitrile, followed by the addition of DOX predissolved in 25  $\mu$ l dimethyl sulfoxide. Similar procedures as described above were followed to generate suspensions containing NP cores.

### **Fusion of RBCm-Derived Vesicles with NP Cores**

To fuse the RBCm-derived vesicles with the aforementioned NP cores, a suspension containing 1 mg of NP cores was first mixed with RBCm-derived vesicles prepared from 1 ml of whole blood. The mixture was then extruded 11 times through a 100-nm polycarbonate porous membrane with an Avanti mini extruder. To fully coat 1 mg of NP cores, an excess of blood was used to compensate for the membrane loss during RBC ghost derivation and extrusion [9].

## **Preparation of PEGylated NPs**

The DOX–PLA conjugate and PLA-PEG-COOH (MW = 10 kDa, polydispersity index = 1.12; PEG = 3.5 kDa, PLA = 6.5 kDa) [13] at a weight ratio of 1:1 were first dissolved in acetonitrile at a concentration of 1 mg/ml, followed by the same procedures as described above to produce NP suspensions. To physically encapsulate DOX into PEGylated NPs, 1 mg PLGA (0.67 dl/g, MW = 40 kDa, carboxy-terminated, LACTEL Absorbable Polymers) was first dissolved into 1 ml acetonitrile, followed by the addition of 100 µg DOX dissolved in 25 µl dimethyl sulfoxide. The procedures described above were used to produce NP suspensions.

## **NP Stability Studies**

NP stability in PBS was assessed by monitoring particle size using dynamic light scattering. Specifically, 500 µg of the NPs were suspended in 1 ml 1 × PBS and the sizes were measured in triplicate at room temperature every 24 h over a period of 1 week. Between measurements, samples were incubated at 37°C with gentle shaking. NP serum stability was evaluated by monitoring the UV-absorbance at a wavelength of 560 nm. Specifically, NPs were first concentrated to 2 mg/ml in PBS, followed by the addition of 2 × fetal bovine serum (Hyclone) of equal volume. The absorbance was measured using an Infinite M200 multiplate reader at 37°C approximately every 1 min over a period of 2 h. The morphology and particle size were further characterized using scanning electron microscopy (SEM). Samples for SEM were prepared by dropping 5 µl of the NP solution onto a polished silicon wafer. After drying the droplet at room temperature overnight, the sample was coated with chromium and then imaged using SEM.

## Measurement of Drug-Loading Yield & Release

The concentration of DOX in a solution was determined by measuring fluorescence intensities at 580 nm with an excitation wavelength of 480 nm. To determine the DOX-loading yield of the NPs, the above fluorescence measurement was carried out after incubating 100  $\mu$ l NP solution with 100  $\mu$ l 0.1 M HCl in acetonitrile for 24 h. All fluorescent measurements were performed under the same conditions with 0.1 M HCl. To plot DOX release profiles, 200  $\mu$ l NP solution (1 mg/ml) was loaded into a Slide-A-Lyzer MINI dialysis microtube (Pierce, IL, USA; MW cutoff: 3.5 kDa) then dialyzed against 2 l of PBS (pH = 7.4) at 37°C. PBS buffer was changed every 12 h throughout the whole dialysis process. At each predetermined time point, NP solutions from three mini dialysis units were collected and DOX concentration was measured. Note that the hydrophobic DOX-PLA conjugates are unlikely to be released from the hydrophobic particles to aqueous solutions, as that is an energetically unfavorable process. It is expected that only drug molecules that have detached from the polymer chains will be released.

## Cell Viability Assay

Cytotoxicity of free DOX and DOX-loaded NPs was assessed against Kasumi-1 cell line established from the peripheral blood of an AML patient using MTT assay (Promega Corporation, WI, USA). Cells were first seeded ( $\sim 5 \times 10^3$  per well) in 96-well plates and incubated for 24 h. After the addition of free DOX or DOX-loaded NPs, the cells were incubated for an additional 72 h. Cell viability was then determined by using MTT assay following a protocol provided by the manufacturer.

### 3.1.3 Results and Discussion

The preparation process of RBCm-cloaked NPs was based on a previously published protocol and is schematically illustrated in Figure 2.2.1 [9]. Briefly, purified RBCs first underwent membrane rupture in a hypotonic environment to remove their intracellular contents. Next, the emptied RBCs ( $\sim 2\text{ }\mu\text{m}$  in diameter) were washed and extruded through 100-nm porous membranes to create RBC-membrane derived vesicles ( $\sim 200\text{ nm}$  in diameter). Meanwhile, polymeric cores ( $\sim 70\text{ nm}$  in diameter), such as those made from PLA or PLGA, were prepared by using a solvent displacement method. The resulting polymeric cores were subsequently mixed with RBC-membrane derived vesicles and the mixture was physically extruded through 100-nm

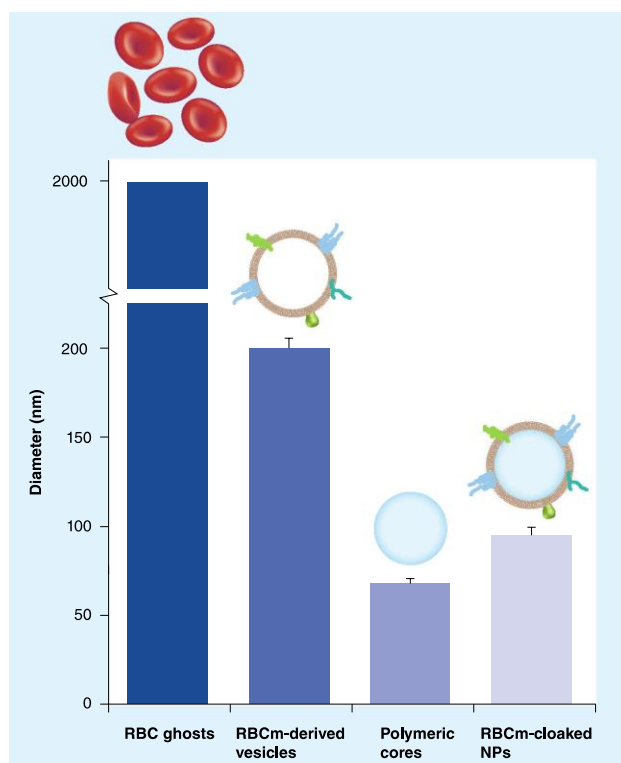


**Figure 3.1.1** Preparation process of red blood cell membrane-cloaked nanoparticles. The hydrodynamic sizes of RBC ghosts, RBCm-derived vesicles, polymeric cores and RBCm-cloaked NPs were measured using dynamic light scattering.

NP: Nanoparticle; RBC: Red blood cell; RBCm: Red blood cell membrane.

pores, where the two components fused under the mechanical force and formed RBCm-cloaked NPs (~90 nm in diameter).

In this study, two distinct methods to load DOX as a model drug into the RBCm-cloaked NPs were examined: physical encapsulation and chemical conjugation. Physical encapsulation is achieved by first mixing DOX and the polymers in acetonitrile, followed by precipitation into water. In this case, the drug-loading yield can be varied through different formulation parameters. For example, when varying initial DOX to PLGA weight ratio from 5 to 20%, the loading yield increases from 0.9 to 1.8% (Figure 2).

Alternatively, DOX molecules can be loaded into NP cores by covalently conjugating drug molecules to polymer backbones. Intuitively, DOX molecules can be directly conjugated to carboxyl-terminated PLA chains through hydroxyl groups; however, this approach causes heterogeneities for polymer–drug conjugates, owing largely to the polydispersity of the polymer chains, the lack of control over the regio- and chemo-selective conjugation of the DOX molecules containing multiple hydroxyl groups, and the lack of control over the conjugation efficiency. Therefore, an alternative approach was adopted, where the hydroxyl groups of the DOX, in the presence of using L-lactide monomer and (BDI)ZnN(SiMe<sub>3</sub>)<sub>2</sub> as a catalyst, were utilized to initiate the ring-opening polymerization and led to the formation of PLA–DOX conjugates [11, 12]. In this approach, as the polymerization reaction is initiated by the drug molecule itself, a conjugation efficiency of near 100% can be achieved. In addition, the metal amido catalyst (BDI)ZnN(SiMe<sub>3</sub>)<sub>2</sub> preferentially allows for PLA propagation at C14-OH position of DOX, instead of its more sterically hindered C4'- and C9-OH positions. After the reaction was terminated, products were purified using repeated dissolution–precipitation cycles and then characterized using <sup>1</sup>H–NMR spectroscopy. Proton resonance peaks corresponding to both DOX

molecules and PLA backbones are present, including the aromatic protons of DOX between  $\delta = 7.5$  and  $8.0$  ppm, protons of  $-\text{CH}_3$  group of PLA at  $\delta = 1.5$  ppm, and  $-\text{CH}$  group of PLA at  $\delta = 5.2$  ppm, hence confirming the formation of PLA–DOX conjugates [11]. In contrast to physical encapsulation, where the drug-loading yield primarily depends on formulation parameters, in chemical conjugation, the drug-loading yield is dictated by polymer chain length, which is in turn determined by polymerization conditions such as initiator (DOX)-to-monomer ratio. For example, the PLA–DOX conjugates synthesized in this study were found to have a molecular weight of 10 kDa and a narrow polydispersity index of 1.16, corresponding to an approximately

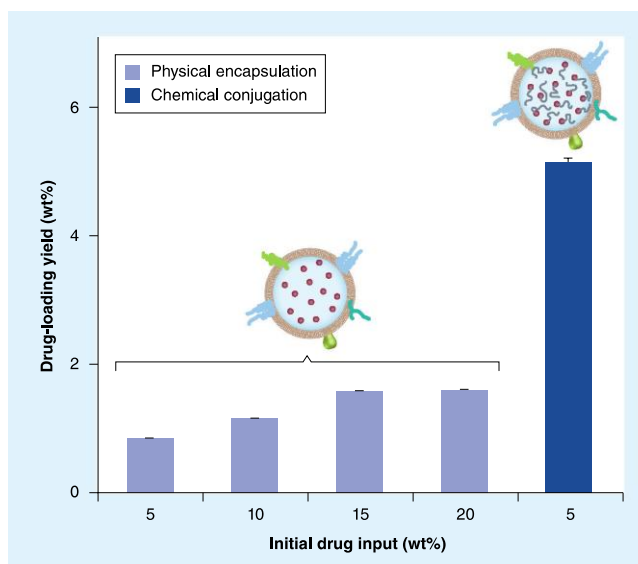


**Figure 3.1.2.** Doxorubicin loading yields in the red blood cell membrane-cloaked nanoparticles at various initial drug inputs. Drug molecules were loaded into the nanoparticles through two distinct loading mechanisms: physical encapsulation and chemical conjugation.

5% loading yield of DOX after the conjugates were formulated into the NPs (Figure 2.2.2).

Next, the stability of DOX-loaded RBCm- cloaked NPs in physiologically relevant buffer solutions was studied. In PBS, NP stability is monitored by measuring NP sizes at different time points, as unstable particles tend to aggregate and their sizes increase. In this study (Figure 2.2.3A), NPs loaded with DOX molecules by using both physical encapsulation and chemical conjugation showed similar initial diameters of approximately 90 nm; without significant size



increase over the duration of 1 week. Similarly, only a slight change in the polydispersity index of the NPs was observed over the same time period, indicating a high stability of DOX-loaded RBCm-cloaked NPs in PBS. NP stability was further examined in serum by monitoring UV absorbance at 560 nm, a characteristic wavelength reflecting the extent of particle aggregation [14, 15]. RBCm-cloaked NPs, loaded with DOX molecules by either physical encapsulation or chemical conjugation, showed a near constant absorbance at 560 nm over a time period of 2 h (Figure 2.2.3B), suggesting that the NPs are highly stable in 100% fetal bovine serum. The morphological measurements of these RBCm-cloaked NPs by SEM showed spherical structures with an average size of approximately 75 nm (Figure 2.2.3C). By contrast, absorbance of bare polymeric cores made from PLGA or PLA–DOX conjugates without RBCm cloaks immediately increased upon addition into fetal bovine serum, therefore the authors were unable to monitor their long-term stability in either PBS or serum. The results of this study showed that the RBCm cloak played a significant role in stabilizing NPs in both buffer solutions and serum. From a practical perspective, the fast aggregation of uncoated polymeric particles in buffer solutions provided a means of selective precipitation and removal of uncoated particles from RBCm-cloaked NPs after their preparation.

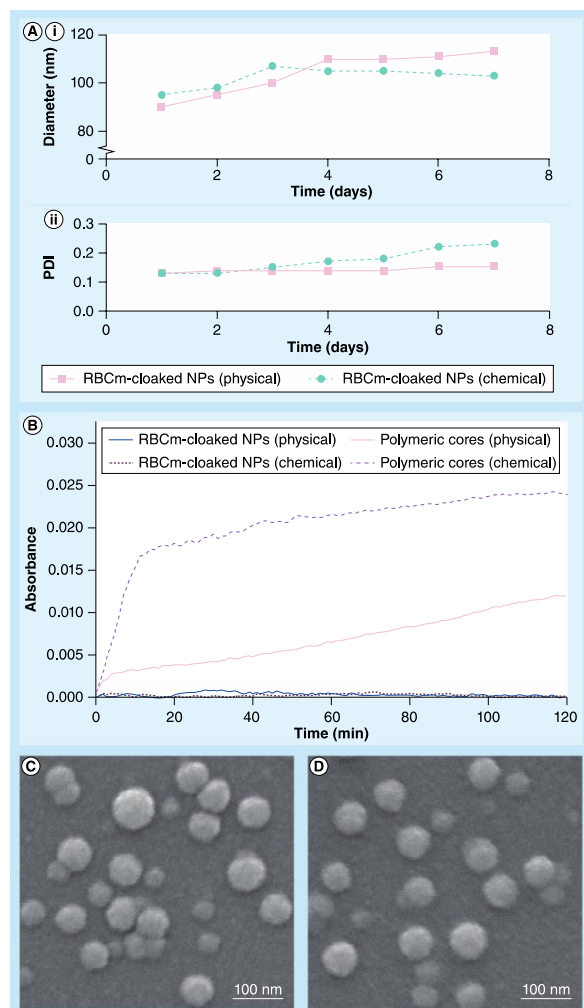


**Figure. 3.1.3** *In vitro* stability test and morphology of doxorubicin-loaded red blood cell membrane-cloaked nanoparticles. Doxorubicin (DOX) was loaded into the NPs through either chemical conjugation or physical encapsulation. (A) Long-term stability of DOX-loaded RBCm-cloaked NPs in terms of (Ai) particle size (diameter, nm) and (Aii) PDI in phosphate-buffered solution, monitored for a period of 7 days at room temperature. (B) Stability of DOX-loaded RBCm-cloaked NPs and bare NP cores (without RBCm cloak) in 100% fetal bovine serum was assessed by measuring the UV absorbance at the wavelength of 560 nm. (C & D) Representative scanning electron microscope images of DOX-loaded RBCm-cloaked NPs, of which the drugs were loaded through (C) chemical conjugation or (D) physical encapsulation. NP: Nanoparticle; PDI: Polydispersity index; RBCm: Red blood cell membrane.

Following the formulation of stable DOX- loaded RBCm-cloaked NPs, their DOX release kinetics were investigated (Figure 2.2.4). The authors first examined how different drug-loading mechanisms would affect DOX releases from RBCm- cloaked NPs. The results demonstrated that, when DOX molecules were physically encapsulated into the polymer matrix, the drug- release rate was significantly faster, as 20% of DOX molecules were released within

the first 2 h from the RBCm-cloaked NPs. By contrast, when formulations of chemical conjugation were examined, within the first 2 h only 5% of DOX molecules were released. Such difference has been attributed to the fact that covalent bonding of DOX molecules to the polymer backbone requires drug molecules to first be hydrolyzed from the polymer by bulk erosion before they can diffuse out of the polymeric matrix for release [11, 12, 16]. A more sustained-release profile resulted from drug–polymer covalent conjugation also suggests that chemical linkers responsive to environmental triggers can achieve better controlled drug releases when developing RBCm-cloaked NPs for advanced drug-delivery applications [13, 17]. It is expected that acidic pH conditions will increase the drug-release rate of the polymeric cores because the pH drop will accelerate the degradation rate of the polymer backbone and facilitate the cleavage of the ester linkage between the drugs and the polymers [11].

In order to gain a better understanding of the role played by the RBCm cloak in drug retention, an established procedure for generating NPs by blending PLA-PEG diblock copolymers was followed. PEGylated NPs, where NP cores were coated and stabilized by a PEG layer instead of RBCm cloak [18]. It was hypothesized that if two formulations have similar NP cores, the difference in drug release will be primarily caused by the different abilities of the RBCm cloak and surface PEG coating in drug retention. By comparing DOX release from

RBCm-cloaked NPs to that from PEGylated NPs, it was found that the release rate of the RBCm-cloaked NPs was lower; approximately 20% of DOX was released within the first 72 h in the RBCm-cloaked NPs, whereas 40% of DOX was released from the PEGylated NPs over the same

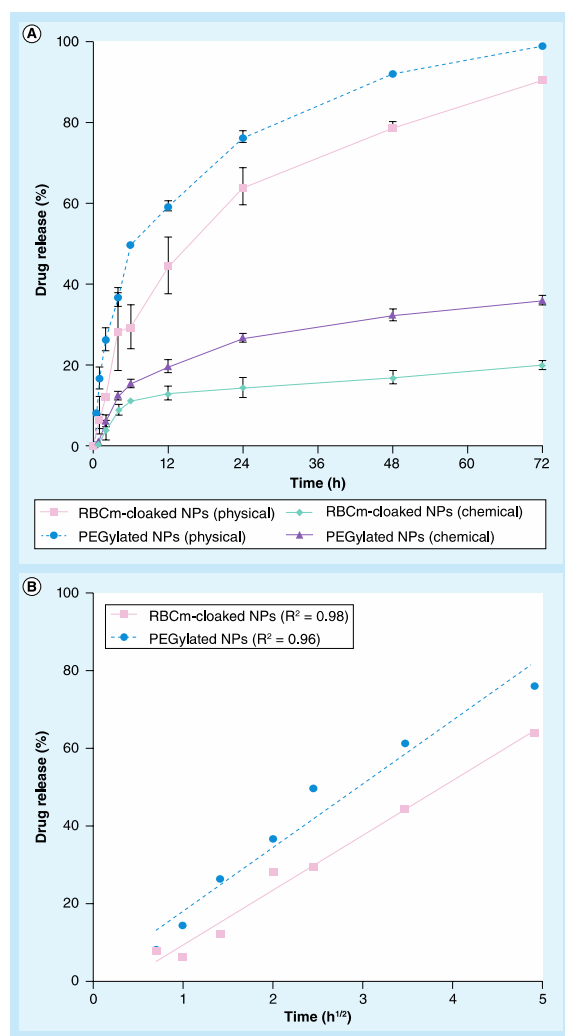


**Figure 3.1.4** Drug release profiles and kinetics of the different doxorubicin-loaded nanoparticles. (A) Doxorubicin release profiles of RBCm-cloaked nanoparticles and PEG-coated nanoparticles. For these release studies, initial doxorubicin concentration inside the nanoparticles was 5 wt% for chemical conjugation and 1.8 wt% for physical encapsulation, respectively. (B) For the physical encapsulation systems, the drug release percentage was plotted against the square root of time, which yielded linear fittings using a diffusion-dominant Higuchi model. NP: Nanoparticle; RBCm: Red blood cell membrane.

time span. In fact, by using NPs formulated by PLGA–PEG diblock copolymers, surface PEG molecules have been found to hinder drug release from NP cores [19]. Hence the observation that DOX is released at a higher rate from PEG-coated NPs compared with RBCm-cloaked NPs,

indicates that RBCm indeed acts as a diffusion barrier for DOX release. This observation is in accordance with previous studies demonstrating that phospholipid coating can act as a barrier to drug diffusion [20]. Such a role played by the RBCm cloak further suggests that strategies aimed at engineering lipid membrane coatings may allow for responsive drug releases from RBCm-cloaked NPs under certain environmental cues in addition to those achieved by chemical conjugations embedded in polymer cores [21].

To gain a quantitative understanding of the membrane-coating effect on drug retention, the drug-release profiles were analyzed using mathematical models established in previous particle drug-release studies. Since the degradation of PLGA is in the order of weeks [22, 23], markedly slower than the observed drug release for the physically loaded systems, a diffusion-dominant Higuchi model was applied to both RBCm-coated and PEGylated NPs containing physically encapsulated DOX. Plotting the drug-release percentage against the square root of time yielded linear fittings with  $R^2 = 0.98$  and  $0.96$  for the RBCm-cloaked and the PEGylated NPs, respectively (Figure 2.2.4B). The goodness of the fit implies a diffusion-controlled drug-release mechanism and further allows for the derivation of the diffusion coefficient through the following Higuchi equations 1 & 2 [24, 25]:

$$M_t = Kt^{1/2} \text{ (1)}$$

$$K = A(2C_{ini}DC_s)^{1/2} \text{ (2)}$$

Where  $M_t$  is drug release at time  $t$  in hours,  $K$  is the Higuchi constant,  $C_{ini}$  is the initial drug concentration,  $C_s$  is the drug solubility,  $A$  is the total surface area of the particles and  $D$  is the diffusion coefficient. Given the particle dimensions, the drug-loading yield, the solubility of DOX in water (1.18 g/l), and the drug-release data, the diffusion coefficients were determined to be  $6.6 \times 10^{-16} \text{ cm}^2/\text{s}$  and  $8.2 \times 10^{-16} \text{ cm}^2/\text{s}$  for the RBCm-cloaked and PEGylated NPs, respectively, which is consistent with previously reported drug diffusivities from PLGA/PLA

NPs [26]. In this study, the bilayered membrane coating reduced the drug diffusivity by 1.2-times. It is expected that this retardation effect by the RBCm cloak would likely vary with different particle sizes, polymer types and therapeutic cargo.

On the other hand, applying zero order, first order and Higuchi models to the drug-release profiles of chemically conjugated DOX yielded poor fittings (data not shown), indicating complex release kinetics when additional drug cleavage is coupled with drug diffusion out of the polymer matrix. Precise modeling of the retardation effect imposed by the RBCm cloak on the chemically conjugated DOX is beyond the scope of this study. Nevertheless, as identical particle cores are present in both RBCm-cloaked and PEGylated NPs, herein, it is hypothesized that polymer matrix relaxation and hydrolytic cleavage of the linkage are not dominant factors contributing to the difference observed in DOX release profiles. Instead, the authors attribute the slower release rate of the RBCm-cloaked NPs to two diffusion- dominated components: the diffusion of water into the polymer matrix; and the diffusion of the cleaved drugs outward across the polymer matrix [27]. As the membrane coating was shown to decrease the drug diffusivity in the physical entrapment system, it likely affected both the influx of water and the efflux of cleaved drugs in the covalent conjugate system, thereby resulting in a more sustained drug-release profile.

Finally, the therapeutic potential of the DOX-loaded RBCm-cloaked NPs against an AML Kasumi-1 cell line was examined. AML, an illness characterized by uncontrolled growth and accumulation of leukemia blasts in the bloodstream, was chosen as a disease target because of the long circulation lifetime of the RBCm-cloaked NPs in the blood stream, and their sustained drug-release profiles. The current standard of care for AML is high-dose anthracyclines, which raises serious concerns for cardiac toxicity [28]. Long-circulating NPs

releasing therapeutic compounds in a sustained manner offer the opportunity to reduce the required dosing and improve upon the treatment efficacy. RBCm-cloaked NPs, where DOX was either physically loaded or covalently conjugated, exhibited higher toxicity by comparison to free DOX over a 72-h incubation period (Figure 2.2.5). In a previous study, it was demonstrated that these RBCm-cloaked NPs can be taken up by cancer cells in a tissue culture and the NPs remain in an intact core-shell structure after cellular internalization [9]. Therefore, the observed enhancement in efficacy can be likely attributed to endocytic uptake of NPs, which enables a high payload of drugs to enter the intracellular region [29]. Several previous reports have shown enhanced cytotoxicity of DOX through NP-based delivery of DOX [30, 31]. The free DOX, by contrast, relies on passive membrane diffusion for cellular entry, which is less efficient and susceptible to membrane-bound drug efflux pumps [32–34]. AML cells, including the Kasumi-1 cell line, are known to express membrane-bound drug efflux pumps, which decrease intracellular compartmentalization of DOX [35]. In particular, the Kasumi-1 cell line has been used previously as a P-glycoprotein- positive and anthracycline-resistant cell line in AML research [36, 37]. The current study suggests that RBCm-cloaked NPs, with a prolonged circulation lifetime, sustained drug release and improved cell internalization, can become a promising platform toward the treatment of blood cancer. Further studies are warranted to investigate the therapeutic potential of these NPs *in vivo*.



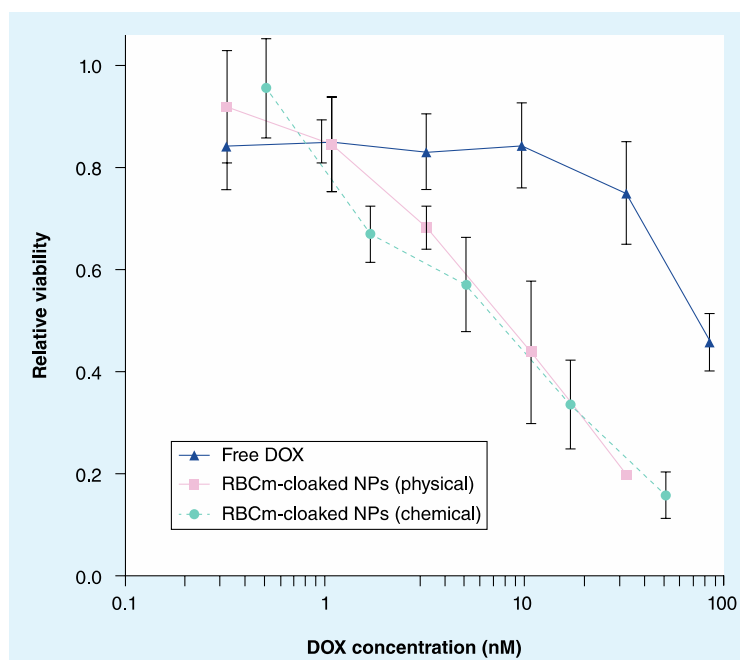


**Figure 3.1.5** Cytotoxicity study against the Kasumi-1 cell line established from the peripheral blood of an acute myeloid leukemia patient. Circles represent RBCm-cloaked NPs with chemically conjugated DOX, squares represent RBCm-cloaked NPs with physically encapsulated DOX and triangles represent free DOX. All samples were incubated with Kasumi-1 cells for 72 h prior to 3-(4,5-dimethylthiazol-2-yl)-2,5-diphenyltetrazolium bromide assay (n = 4).

DOX: Doxorubicin; NP: Nanoparticle; RBCm: Red blood cell membrane.

### 3.1.4 Conclusions

In summary, herein, we examined two strategies for loading drugs into an RBCm-cloaked NP delivery system were examined: physical encapsulation and chemical conjugation. Release studies suggest that the chemical conjugation strategy results in a more sustained drug-release profile. We further formulated PEGylated NPs that had the same NP cores but different surface coatings compared with RBCm-cloaked NPs. By comparing drug- release profiles of these two delivery systems, it was demonstrated that RBCm cloaks provide a barrier, slowing down the outward diffusion of encapsulated drug molecules. These results suggest that chemical modifications to the drug-polymer linkage in the NP core and engineering the NP surface coatings can both be explored to gain better control over drug releases of RBCm-cloaked NPs. In

a following efficacy study by using the AML Kasumi-1 cell line, RBCm-cloaked NPs exhibited higher toxicity in comparison with free DOX. The previously observed long systemic circulation lifetime in the blood stream and the sustained drug-release kinetics reported indicate that this biomimetic drug-delivery system may hold great promise for systemic delivery of payloads for the treatment of various diseases such as blood cancers. With further development, these RBCm-cloaked NPs are expected to become a robust drug-delivery system that combines the advantages of both synthetic polymers and natural cellular membranes.

RBCm-cloaked NPs represent a novel class of NP formulations bringing together both the long circulation lifetime of RBC, and the controlled drug retention and release of synthetic polymers. After gaining a deeper understanding of the roles played by the RBCm shell and the polymeric core, this NP formulation can be further tailored by engineering both parts to improve systemic delivery of therapeutic payloads. We believe that with continuing effort, this formulation will result in a robust delivery platform and make significant impact on both biomedical applications and nanotechnology research.

## **Acknowledgements**

Chapter 3.1, in full, is a reprint of the material as it appears in Nanomedicine, 2013, Aryal, S.; Hu, C-M.; Fang, R.; Dehaini, D.; Carpenter, C.; Zhang, D-E.; Zhang, L. The dissertation author was a major contributor and co-author of this paper.

## References

1. Davis, M.E., Z. Chen, and D.M. Shin, Nanoparticle therapeutics: an emerging treatment modality for cancer. *Nature Reviews Drug Discovery*, 2008. 7(9): p. 771–782.
2. Petros, R.A., and J.M. DeSimone, Strategies in the design of nanoparticles for therapeutic applications. *Nature Reviews Drug Discovery*, 2010. 9(8): p. 615–627.
3. Peer, D., J.M. Karp, S. Hong, O.C. Farokhzad, R. Margalit, and R. Langer, Nanocarriers as an emerging platform for cancer therapy. *Nature Nanotechnology*, 2007. 2(12): p. 751–760.
4. Farokhzad, O.C. and R. Langer, Impact of nanotechnology on drug delivery. *ACS Nano*, 2009. 3(1): p. 16–20.
5. Alexis, F., E. Pridgen, L.K. Molnar, and O.C. Farokhzad, Factors affecting the clearance and biodistribution of polymeric nanoparticles. *Molecular Pharmaceutics*, 2008. 5(4): p. 505–515.
6. Knop, K., R. Hoogenboom, D. Fischer, and U.S. Schubert, Poly(ethylene glycol) in drug delivery: pros and cons as well as potential alternatives. *Angewandte Chemie International Edition*, 2010. 49(36): p. 6288–6308.
7. Geng, Y., P. Dalhaimer, S. Cal, R. Tsai, M. Tewari, T. Minko, and D.E. Discher, Shape effects of filaments versus spherical particles in flow and drug delivery. *Nature Nanotechnology*, 2007. 2(4): p. 249–255.
8. Yoo, J.W., E. Chambers, and S. Mitragotri, Factors that control the circulation time of nanoparticles in blood: challenges, solutions and future prospects. *Current Pharmaceutical Design*, 2010. 16(21): p. 2298–2307.
9. Hu, C.M., L. Zhang, S. Aryal, C. Cheung, R.H. Fang, and L. Zhang, Erythrocyte membrane-camouflaged polymeric nanoparticles as a biomimetic delivery platform. *Proceedings of the National Academy of Sciences USA*, 2011. 108(27): p. 10980–10985.
10. Dodge, J.T., C. Mitchell, and D.J. Hanahan, The preparation and chemical characteristics of hemoglobin-free ghosts of human erythrocytes. *Archives of Biochemistry and Biophysics*, 1963. 100: p. 119–130.
11. Aryal, S., C.M. Hu, and L. Zhang, Polymer-cisplatin conjugate nanoparticles for acid-responsive drug delivery. *ACS Nano*, 2010. 4(1): p. 251–258.
12. Tong, R. and J. Cheng, Ring-opening polymerization-mediated controlled formulation of polylactide–drug nanoparticles. *Journal of the American Chemical Society*, 2009. 131(13): p. 4744–4754.
13. Aryal, S., C.M. Hu, and L. Zhang, Polymer–cisplatin conjugate nanoparticles for acid-responsive drug delivery. *ACS Nano*, 2010. 4(1): p. 251–258.

14. Popielarski, S.R., S.H. Pun, and M.E. Davis, A nanoparticle-based model delivery system to guide the rational design of gene delivery to the liver. 1. Synthesis and characterization. *Bioconjugate Chemistry*, 2005. 16(5): p. 1063–1070.
15. Fang, R.H., X. Aryal C.M. Hu, and L. Zhang, Quick synthesis of lipid–polymer hybrid nanoparticles with low polydispersity using a single-step sonication method. *Langmuir*, 2010. 26(22): p. 16958–16962.
16. Tong, R. and J. Cheng, Controlled synthesis of camptothecin–polylactide conjugates and nanoconjugates. *Bioconjugate Chemistry*. 2010. 21(1): p. 111–121.
17. Gao, W., J.M. Chan, and O.C Farokhzad, pH-responsive nanoparticles for drug delivery. *Molecular Pharmaceutics*, 2010. 7(6): p. 1913–1920.
18. Gu, F., L. Zhang, B.A. Teply, N. Mann, A. Wang, A.F. Radovic-Moreno, R. Langer, and O.C. Farokhzad, Precise engineering of targeted nanoparticles by using self-assembled biointegrated block copolymers. *Proceedings of the National Academy of Sciences USA*, 2008. 105(7): p. 2586–2591.
19. Takae, S., K. Miyata, M. Oba, T. Ishii, N. Nishiyama, K. Itaka, Y. Yamasaki, H. Koyama, and K. Kataoka, PEG-detachable polyplex micelles based on disulfide-linked block cationomers as bioresponsive nonviral gene vectors. *Journal of the American Chemical Society*, 2008. 130(18): p. 6001–6009.
20. Zhang, L., J.M. Chang, F.X. Gu, J.W. Rhee, A.Z. Wang, A.F. Radovic-Moreno, F. Alexis, R. Langer, and O.C. Farokhzad, Self-assembled lipid–polymer hybrid nanoparticles: a robust drug delivery platform. *ACS Nano*, 2008. 2(8): p. 1696–1702.
21. Pornpattananangkul, D., L. Zhang, S. Olson, S. Aryal, M. Obonyo, K. Vecchio, C.M. Huang, and L. Zhang, Bacterial toxin-triggered drug release from gold nanoparticle-stabilized liposomes for the treatment of bacterial infection. *Journal of the American Chemical Society*, 2011. 133(11): p. 4132–4139.
22. Avgoustakis, K., A. Beletsi, Z. Panagi, P. Klepetsanis, A.G. Karydas, and D.S. Ithakissios, PLGA–mPEG nanoparticles of cisplatin: in vitro nanoparticle degradation, in vitro drug release and in vivo drug residence in blood properties. *Journal of Controlled Release*, 2002. 79(1–3): p. 123–135.
23. Li, J., G. Jiang, and F. Ding, The effect of pH on the polymer degradation and drug release from PLGA–mPEG microparticles. *Journal of Applied Polymer Science*, 2008. 109(1): p. 475–482.
24. Higuchi, T., Rate of release of medicaments from ointment bases containing drugs in suspension. *Journal of Pharmaceutical Sciences*, 1961. 50: p. 874–875.
25. Siepmann, J. and N.A. Peppas, Higuchi equation: derivation, applications, use and misuse. *International Journal of Pharmaceutics*, 2011. 418(1): p. 6–12.

26. Budhian, A., S.J. Siegel, and K.I. Winey, Controlling the in vitro release profiles for a system of haloperidol-loaded PLGA nanoparticles. *International Journal of Pharmaceutics*, 2008. 346(1–2): p. 151–159.
27. Pitt, C.G. and A. Schindler, The kinetics of drug cleavage and release from matrices containing covalent polymer–drug conjugates. *Journal of Controlled Release*, 1995. 33(3): p. 391–395.
28. Lowenberg, B., G.J. Ossenkoppele, W. van Putten, H.C. Schouten, C. Graux, A. Ferrant, P. Sonneveld, J. Maertens, M. Jongen-Lavrencic, M. von Lilienfeld-Toal, B.J. Biemond, E. Vellenga, M. van Marwijk Kooy, L.F. Verdonck, J. Beck, H. Dohner, A. Gartwohl, T. Pabst, and G. Verhoef, High-dose daunorubicin in older patients with acute myeloid leukemia. *The New England Journal of Medicine*, 2009. 361(13): p. 1235–1248.
29. Hu, C.M. and L. Zhang, Therapeutic nanoparticles to combat cancer drug resistance. *Current Drug Metabolism*, 2009. 10(8): p. 836–841.
30. Ayen, W.Y., K. Garkhal, and N. Kumar, Doxorubicin-loaded (PEG)3–PLA nanopolymerosomes: effect of solvents and process parameters on formulation development and in vitro study. *Molecular Pharmaceutics*, 2011. 8(2): p. 466–478.
31. Yoo, H.S. and T.G. Park, Folate-receptor-targeted delivery of doxorubicin nano–aggregates stabilized by doxorubicin–PEG–folate conjugate. *Journal of Controlled Release*, 2004. 100(2): p. 247–256.
32. Huwyler, J., A. Cerletti, G. Fricker, A.N. Eberle, and J. Drewe, By-passing of P-glycoprotein using immunoliposomes. *Journal of Drug Targeting*, 2002. 10(1): p. 73–79.
33. Rapoport, N., A. Marin, Y. Luo, G.D. Prestwich, and M.D. Muniruzzaman, Intracellular uptake and trafficking of pluronic micelles in drug- sensitive and MDR cells: effect on the intracellular drug localization. *Journal of Pharmaceutical Sciences*, 2002. 91(1): p. 157–170.
34. Sahoo, S.K. and V. Labhasetwar, Enhanced anti proliferative activity of transferrin-conjugated paclitaxel-loaded nanoparticles is mediated via sustained intracellular drug retention. *Molecular Pharmaceutics*. 2(5): p. 373–383.
35. Dordal, M.S., M. Jackson-Stone, A.C. Ho, J.N. Winter and A.J. Atkinson Jr., Decreased intracellular compartmentalization of doxorubicin in cell lines expressing P-glycoprotein. *Journal of Pharmacology and Experimental Therapeutics*, 1994. 271(3): p. 1286–1290.
36. Mizutani, M., M. Yamaguchi, H. Miwa, T. Kawamura, T. Okuno, K. Nishii, H. Shiku, N. Kamada, and K. Kita, Frequent expression of MDR1 and MDR3 genes in acute myelocytic leukemia cells with t(8;21) (q22;q22). *International Journal of Oncology*, 1997. 10(3): p. 473–479.
37. Rao, J., D.R. Xu, F.M. Zheng, Z.J. Long, S.S. Huang, X. Wu, W.H. Zhou, R.V. Huang, and Q. Liu, Curcumin reduces expression of Bcl-2, leading to apoptosis in daunorubicin-

insensitive CD34+ acute myeloid leukemia cell lines and primary sorted CD34+ acute myeloid leukemia cells. *Journal of Translational Medicine*, 2011. 9: p. 71.

## **3.2 Interfacial interactions between natural RBC membranes and synthetic polymeric nanoparticles**

### **3.2.1 Introduction**

Enabling active immune evasion through biomimetic surface functionalization presents an emerging stealth strategy for developing long-circulating delivery vehicles [1, 2]. The identification of CD47, a transmembrane protein that serves as a universal molecular ‘marker-of-self’, has led to its utilization in the growing development of bio-inspired, immune-evasive devices. Capable of inhibiting phagocytosis and conferring anti-inflammatory properties through interactions with signal regulatory protein alpha (SIRP $\alpha$ ) expressed by macrophages, CD47 and its analogs have been found to contribute to the *in vivo* survival of red blood cells (RBCs) [3], cancer cells [4], and viruses [5]. Application of CD47 to modulate the immune responses against synthetic devices was first demonstrated with macrophages treated by purified recombinant, soluble CD47, which showed reduced uptake of colloidal emulsions [6]. Synthetic materials covalently conjugated with recombinant CD47 further advanced this biomimetic stealth approach, yielding polymeric microspheres [7] and implant surfaces with reduced affinity to inflammatory cells [8, 9]. On nanoscale particles, however, interfacing with native biological components through chemical conjugation of immunomodulatory proteins to particle surfaces can be difficult to manipulate. In particular, inconsistent protein surface density and randomized ligand orientations are notable issues that can greatly undermine the performance of the resulting nanocarriers.

Toward engineering nanocarriers that can actively suppress immune attack by macrophages, herein we demonstrate a robust ‘top-down’ approach to functionalizing nanoscale particles with native CD47 by cloaking sub-100 nm nanoparticles with cellular membranes derived directly from natural RBCs (Figure 2.6). The uniqueness of this membrane coating approach lies in its ability to functionalize nanoparticles with native immunomodulatory proteins including CD47 at an equivalent density to that on natural RBCs. In this study, we show direct evidence that the ‘marker-of-self’ proteins are transferred to the particle surfaces and present in the right-side-out orientation. A macrophage uptake study confirms the stealth functionality

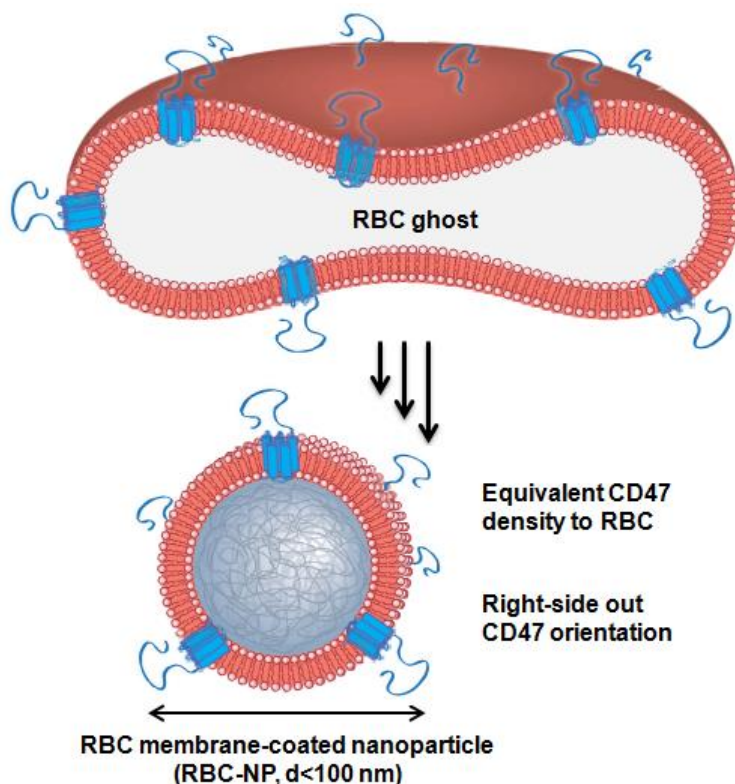


**Figure 3.2.1.** Controlled CD47 functionalization enabled by RBC membrane coating. The resulting RBC membrane-coated nanoparticle (RBC-NP) is expected to have a CD47 density equivalent to that on a natural RBC.

conferred by the immunomodulatory proteins. Since cellular membranes anchor the many molecular tags that define cellular identities, attaching these membranes to nanoparticle surfaces provides unparalleled control over the functionalization of synthetic nanocarriers toward



biomimicry.

### **3.2.2 Experimental Section**

#### **Preparation of RBC Membrane-Coated NPs**

RBCs were collected from 10 week-old male ICR mice (Charles River Laboratories) by centrifuging the whole blood at 2000 x g for 5 min, following which the supernatant and buffy coat were removed. Collected RBCs were then subject to hypotonic treatment to remove interior contents. The resulting RBC ghosts were extruded through 100 nm polycarbonate porous membranes using an extruder (Avanti Polar Lipids) to prepare RBC membrane-derived vesicles with a diameter of approximately 120 nm. Poly(lactic-co-glycolic acid) (PLGA) polymeric cores were prepared using 0.67 dL/g carboxy-terminated 50:50 PLGA polymer (LACTEL Absorbable Polymers) through a solvent displacement process, during which 1 mg of PLGA was dissolved in 200  $\mu$ L of acetone and added drop-wise to 3 mL of water. Following solvent evaporation for 2 hr, the particles were washed using 10 kDa molecular weight cutoff (MWCO) Amicon Ultra-4 Centrifugal Filters (Millipore). The RBC-NPs were then prepared by fusing the RBC membrane-derived vesicles onto the PLGA particles by extruding the particles with the RBC membrane-derived vesicles through 100 nm polycarbonate porous membranes. The size and the zeta potential of the resulting RBC-NPs were obtained from three dynamic light scattering (DLS) measurements using a Malvern ZEN 3600 Zetasizer, which showed an average hydrodynamic diameter of 70 and 85 nm before and after the extrusion process, respectively. The particle morphology was characterized using scanning electron microscopy (SEM). Samples for SEM imaging were prepared by dropping 5  $\mu$ L of the RBC-NP solution onto a polished silicon wafer. After drying the droplet at room temperature overnight, the sample was coated with chromium

and then imaged by SEM.

### **Identification of Membrane Proteins and CD47**

RBC-NPs were isolated from free RBC membrane materials by ultracentrifugation at 14000 x g for 30 min. The resulting RBC-NPs were lyophilized, prepared in lithium dodecyl sulfate (LDS) sample loading buffer (Invitrogen), and separated on a 4-12% Bis-Tris 10-well minigel in MOPS running buffer using a Novex® Xcell SureLock Electrophoresis System (Invitrogen). For membrane protein identification, the gel was stained using SimplyBlue™ SafeStain solution (Life Technologies) following the manufacturer's instructions and imaged using a gel imager. For CD47 identification, the resulting gel was transferred to a nitrocellulose membrane. The membrane was then stained with a primary rat anti-mouse CD47 antibody (BD Biosciences) and a secondary goat anti-rat IgG HRP conjugate (Millipore). The membrane was then subject to ECL western blotting substrate (Pierce) and developed with the Mini-Medical/90 Developer (ImageWorks).

### **Quantification of CD47 on RBC-NPs**

The amount of CD47 retained on the RBC-NPs was quantified by comparing the CD47 protein intensity to protein standards prepared on the same western blotting membrane. The protein standards were prepared from predetermined volumes of blood, which yielded a positive linear correlation between the CD47 band intensity and the blood volume following western blotting. The band intensities were quantified through an image analysis with Adobe Photoshop software. A CD47 standard curve was then established by converting the blood volumes to their corresponding CD47 quantity, using an estimated concentration of mouse RBCs in the blood ( $10^{10}$ /mL) [10] and an average number of CD47 per mouse RBC (16,500 copies/cell) [11].

## **Transmission Electron Microscopy**

A drop of the RBC-NP or bare PLGA nanoparticle (bare NP) solution (1 mg/mL) was deposited onto a glow-discharged carbon-coated grid. For immunostaining, the sample droplet was washed with 3 drops of 0.5 mg/mL rat anti-mouse CD47 antibody solution. For staining the intracellular sequence of CD47, an intracellular sequence specific rabbit anti-CD47 antibody (GeneTex). Following 30 sec of incubation, the sample was rinsed with 3 drops of either a goat anti-rat IgG gold conjugate (5 nm) solution (Canemco, Inc.) or a anti-rabbit IgG gold conjugate (5 nm) solution (Sigma-Aldrich) and then washed with 10 drops of distilled water. For negative staining, the particle sample droplet was washed with 10 drops of distilled water and stained with 1% uranyl acetate. These samples were then imaged using an FEI Sphera Microscope at 200kV.

## **Macrophage Uptake Study**

PLGA nanoparticles encapsulating 0.05% (w/w) 1,1'-dioctadecyl-3,3,3',3'-tetramethylindodicarbocyanine, 4-chlorobenzenesulfonate salt (DiD) dye (Life Technologies) were prepared for fluorescence quantification using flow cytometry. CD47-blocked RBC-NPs were prepared by incubating 1 mg of the DiD-loaded RBC-NPs with 400 µg of rat anti-mouse CD47 antibodies (BD Biosciences) for 1 hr. For the macrophage uptake study, J774 murine macrophage cells were cultured in DMEM media (Invitrogen) supplemented with 10% FBS (Sigma-Aldrich) and plated at a density of  $10^5$  cells/well on 12-well plates (BD Biosciences). On the day of the experiment, the cells were washed and cultured in fresh culture media. Bare PLGA nanoparticles (bare NPs), RBC-NPs, and CD47-blocked RBC-NPs were incubated at a concentration of 25 µg/mL with the macrophage cells at 37°C for 10 min. Non-internalized nanoparticles were washed away with PBS. The macrophage cells were then scraped off the

plates and analyzed using flow cytometry. All flow cytometry studies were conducted on a FACSCanto II flow cytometer (BD Biosciences) and the resulting data was analyzed using FlowJo software from Tree Star. Thirty thousand events were collected per sample and gated using control cells that were not incubated with any nanoparticles. Histograms were plotted with fluorescence intensity as the x-axis using a biexponential scale. The mean fluorescence was plotted in a bar chart with error bars representing the standard error. Statistical analysis was performed based on a two-tailed, unpaired t-test.

### **3.2.3 Results and Discussion**

With five membrane-spanning regions, CD47 is an integral membrane protein firmly embedded in RBC membranes, exhibiting an IgV-like extracellular domain that helps maintain the RBCs' survival in the circulation [12]. While it was previously shown that RBC membrane coating associated nanoparticles with the majority of the membrane materials [13], it remained to be investigated whether these RBC membrane-coated nanoparticles (RBC-NPs) properly present the CD47 for immunomodulation. Verification of the protein, its density, and its orientation on the RBC-NP surfaces demands a molecular examination of these RBC-mimicking nanocarriers. To investigate the functionalization of native CD47 on RBC-NPs, 70 nm poly(lactic-co-glycolic acid) (PLGA) particles were first extruded with RBC membrane-derived vesicles following a previously described protocol [13]. Through scanning electron microscopy (SEM) visualization, a spherical morphology was observed for the resulting RBC-NPs (Figure 2.7A), and dynamic light scattering measurements showed a mean particle diameter of  $85 \pm 2$  nm. The purified particles were then solubilized in a lithium dodecyl sulphate (LDS) sample loading buffer, following which the protein contents stripped from the nanoparticles were separated by SDS-

PAGE. The resulting protein gel was subsequently subjected to western blotting using anti-CD47

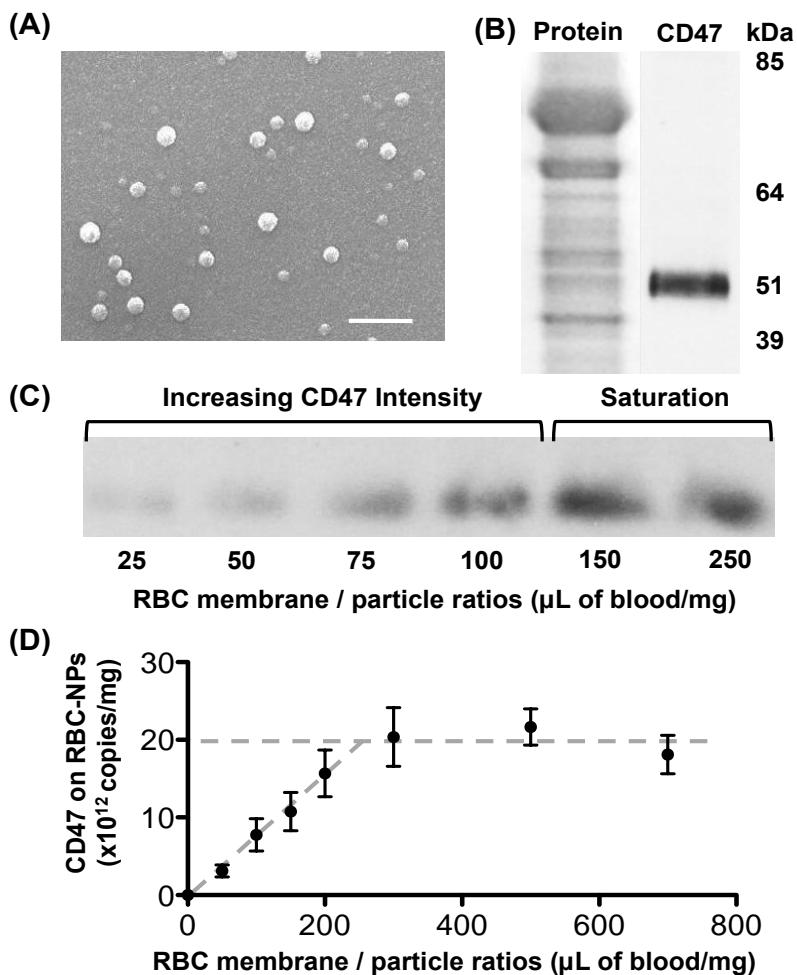


**Figure. 3.2.2** Characterization and quantification of CD47 on the RBC-NPs. (A) A representative scanning electron microscopy (SEM) image shows the spherical structure and morphology of the prepared RBC-NPs (scale bar = 250 nm). (B) Coomassie staining (left) and CD47 western blot (right) of the RBC-NPs' protein contents following SDS-PAGE separation. (C) Comparison of CD47 contents on the RBC-NPs prepared from different RBC membrane to polymer ratios. (D) Quantitative analysis of CD47 density on the RBC-NPs prepared from different RBC membrane to polymer ratios (n=5).

antibody as the primary immunostain. The presence of CD47 on the RBC-NPs was confirmed by a distinct, single band at 50 kDa (Figure 2.7B), which is the characteristic molecular weight of the CD47 protein self-marker [12].

To further examine the extent of CD47 protein on the particle surfaces, the RBC-NPs prepared with different RBC membrane to polymeric particle ratios were collected and analysed for retained CD47 contents. An ultracentrifugation process was applied to isolate the resulting

RBC-NPs from free RBC membranes, following which protein contents on the nanoparticles was processed through SDS-PAGE and examined by western blotting analysis. Figure 2.7C shows the relative CD47 retention on the different particle formulations. As the RBC membrane to polymeric particle ratio increased from 25 to 150  $\mu\text{L}$  of blood per mg of polymer, a corresponding increase in the CD47 intensity was observed. This positive correlation reflects the increasing particle functionalization by the increasing RBC membrane inputs, as more CD47 could be identified in the isolated nanoparticle samples. Saturation in CD47 band intensity was observed upon further raising the RBC membrane to polymer ratio above 150  $\mu\text{L}/\text{mg}$ , which reflected the upper limit of CD47 functionalization achievable by the RBC membrane coating. To quantitatively analyze the protein density on the RBC-NPs, CD47 standards were prepared from predetermined volumes of blood, from which CD47 content was estimated based on the average CD47 number on a mouse RBC (16,500 copies per cell) [11] and the RBC concentration in mouse blood ( $10^{10}$  cells per mL of blood) [10]. Comparing the CD47 retention from the different RBC-NP formulations to the protein standards showed that the saturation level corresponded to approximately  $2 \times 10^{13}$  copies of CD47 per mg of polymeric particles (Figure 2.7D), yielding on average  $\sim 5$  copies of CD47 per RBC-NP. To put the CD47 density into perspective, the surface area of the 85 nm RBC-NPs was calculated ( $\sim 1 \times 10^{11}$   $\mu\text{m}^2/\text{mg}$ ), from which a surface density of  $\sim 200$  molecules of CD47 per  $\mu\text{m}^2$  at saturation on the RBC-NPs can be derived. Given that natural RBCs possess 200~250 copies of CD47 per  $\mu\text{m}^2$  [11, 14], the close match in the CD47 density on the RBC-NPs suggests that the membrane coating brought nearly all of RBCs' CD47 content onto the sub-100 nm particles. The result reflects the robustness of the membrane functionalization technique, as most of the membrane proteins were retained within the cellular membranes throughout the particle preparation process.

It should also be noted that the RBC membrane to polymer ratio corresponding to the onset of CD47 saturation was in close match to the theoretical ratio for complete unilamellar particle coating. Based on surface area estimations, approximately 125  $\mu\text{L}$  of blood is required to completely cover the surfaces of 1 mg of the 70 nm PLGA particles. Experimental observations showed that above the ratio of  $\sim 130$   $\mu\text{L}$  of blood/mg PLGA polymer, additional RBC membrane materials did not further functionalize the particles with CD47. As additional membrane materials in excess of complete unilamellar particle coverage were removed during the isolation of RBC-NPs, it can be inferred that the RBC membrane coating precluded further membrane interactions and that multilamellar membrane coating on the nanoparticles was unfavorable. To further investigate the RBC-NP formation under excessive RBC membrane to polymer ratios, RBC-NPs prepared with 250  $\mu\text{L}$  of blood per mg of polymer were visualized under TEM. It was found that despite the availability of excess membrane materials in the samples, the nanoparticles were covered by a single, unilamellar coating of lipid membranes with a thickness of 6~8 nm, which is in agreement with the characteristic membrane thickness of RBCs [15]. Excess membranes remained in vesicular forms, which helped to explain the CD47 saturation on the RBC-NPs. In contrast to the unfavored multilamellar coating, unilamellar membrane coating on the RBC-NPs appeared to be highly efficient. By converting the RBC membrane input in Figure 2.7D to its corresponding CD47 content, the resulting correlation showed that, below the CD47 saturation, approximately 92% of the input membrane proteins were utilized for particle functionalization. This observation suggests that the RBC membrane coating to the PLGA particle surfaces was a favorable process that readily took place. The high efficiency in translocating CD47 onto nanoparticle surfaces confers a unique advantage to the RBC membrane coating approach.

To verify that the CD47 functionalized RBC-NPs possessed the properly oriented self-markers for molecular interactions, the particle surfaces were examined for the presence of CD47's extracellular domains. Rat anti-CD47 antibodies specific to the CD47's extracellular region were applied to the RBC-NPs on a glow-discharged carbon-coated grid. Following 1 min of incubation, the sample was washed and subsequently incubated with anti-rat IgG gold conjugate, which labelled the anti-CD47 antibodies that were retained on the grid. The immunogold-labelled sample was then rinsed with water prior to visualization by transmission electron microscopy (TEM). Figure 2.8A shows the attachment of the electron-dense gold particles to multiple gray circular patterns 60-80 nm in diameter, which confirmed that the gold conjugates were attached to the RBC-NPs. A negative control prepared in the absence of the primary stain showed that the gold labelling was specific to the anti-CD47 antibodies. Together, these TEM results confirm the presence of right-side-out CD47 on the RBC-NPs. To further examine the presence of inside-out CD47 on the RBC-NPs, an antibody that specifically targets an intracellular sequence of CD47 was used. Curiously, while the antibody bound to the CD47 on RBC-NPs in western blotting, it did not yield observable immune-gold staining on either RBC-NPs or bare nanoparticles under TEM. This result indicates the relative absence of intracellular CD47 sequences on the particle surfaces. Even though the immunostaining experiment provides a qualitative rather than a quantitative measure of the membrane sidedness on the RBC-NPs, it suggests that the right-side-out membrane orientation was dominant on the RBC-NPs. Given that the extracellular side of RBC membranes possess a strong negative charge owing to high abundance of sialated moieties [16], it is likely that electrostatic effects favored the interactions between negatively charged polymeric cores and the less negatively charged intracellular side of the RBC membranes, giving rise to a right-side-out orientation bias. This



orientation bias also helps explain the unilamellar coating on the RBC-NPs, which could result from the rich surface glycan content that precludes membrane-membrane interactions. Figure 2.8B provides a juxtaposition of magnified images of RBC-NPs and the corresponding bare PLGA nanoparticles under negative staining or immunostaining. It can be observed that, following the RBC membrane coating, the particles were bestowed with a unilamellar membrane shell containing CD47 that predominantly exposes their extracellular domains. The proper CD47 orientation is crucial for their molecular interactions.

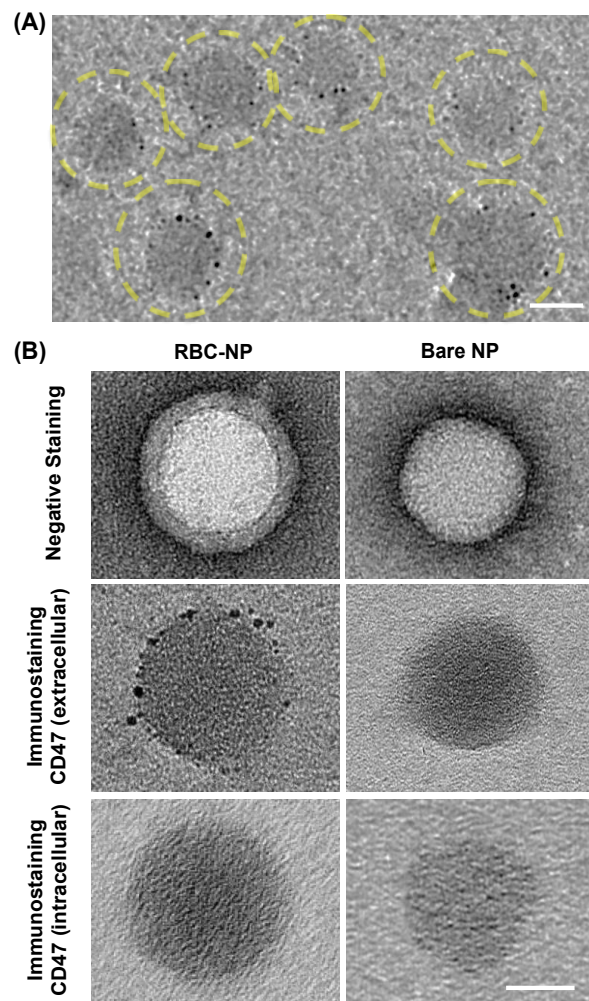


**Figure. 3.2.3** CD47 orientation on the RBC-NPs. (A) A representative transmission electron microscopy (TEM) image of the RBC-NPs under immunostaining, consisting of a primary stain by rat anti-mouse CD47 antibodies and a secondary stain by anti-rat IgG gold conjugates (scale bar = 50 nm). (B) Comparison of the RBC-NPs and the corresponding bare PLGA nanoparticles (bare NPs) and under negative staining with uranyl acetate or immunostaining with anti-CD47 antibodies that target either the extracellular or the intracellular protein domains. (scale bar = 30 nm).

Lastly, the immunomodulatory effect of the CD47 functionalized RBC-NPs was studied. Bare PLGA nanoparticles and RBC-NPs loaded with hydrophobic DiD fluorophores (excitation/emission = 644 nm/655 nm) were first incubated with J774 murine macrophage cells and examined for particle internalization. Following 10 min of incubation, the macrophage cells were washed and examined using flow cytometry, which revealed that the RBC membrane coating rendered the particles less prone to the macrophage uptake, resulting in a 64% reduction in particle internalization (Figure 2.9). The reduced susceptibility to macrophage engulfment

confirmed the translocation of immune-evasive functionality from RBCs to RBC-NPs and helped to explain the long *in vivo* circulation previously observed for the RBC-NPs [13]. To identify CD47's contribution to RBC-NPs' immune-evasive property, saturating amounts of anti-CD47 antibodies were applied to the RBC-NPs to block the right-side-out CD47 proteins. The antibody blocking was previously demonstrated to disrupt SIRP $\alpha$  signalling and increased macrophage engulfment of RBCs [17]. Similarly, depriving the particles of the molecular protection from phagocytosis resulted in an increase in particle internalization by 20%, which confirmed the immunomodulatory functionality conferred by the particle-bound CD47. Curiously, the CD47-blocked RBC-NPs remained significantly more “stealthy” than the bare PLGA nanoparticles. Given that RBCs have a variety of proteins and glycans on their surface, many of which have been identified to modulate their immunological properties [18, 19], other surface moieties in addition to CD47 on the RBC-NPs likely functioned collectively to inhibit

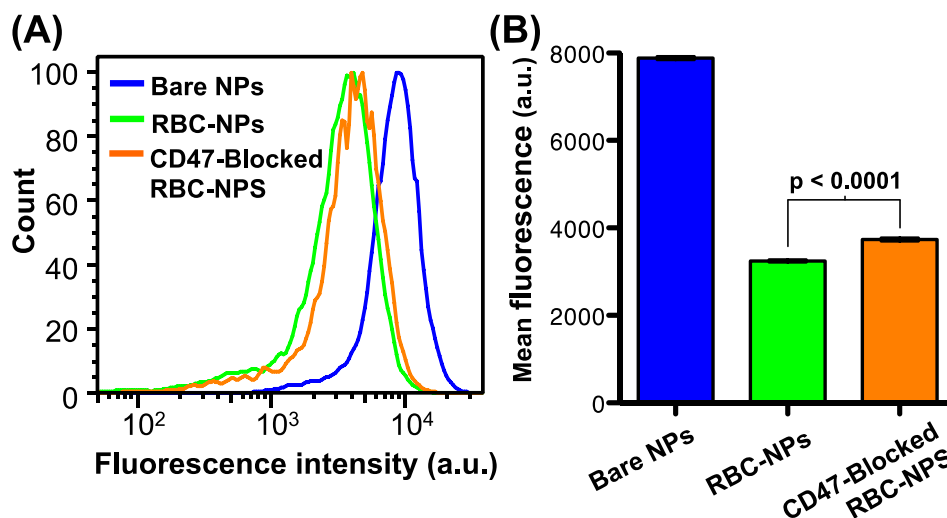


**Figure. 3.2.4.** Inhibition of macrophage uptake. (A) Flow cytometry analysis of particle internalization by murine macrophage cells. The blue, green, and orange lines represent the bare PLGA nanoparticles (bare NPs), RBC-NPs, and CD47-blocked RBC-NPs, respectively. (B) Mean fluorescence intensity reflecting the overall particle uptake by the macrophage cells.

the macrophage activity. Future studies are warranted to verify these other membrane moieties and to examine their implications in nanodevice functionalization.

### **3.2.4 Conclusions**

In summary, RBC membrane coating was demonstrated to functionalize sub-100 nm substrates with native CD47, yielding nanoparticles with equivalent CD47 surface density to natural RBCs. Right-side-out CD47 proteins were identified on the particle surfaces, readily exposing their extracellular domain for molecular interactions. The immune-evasive property of the RBC-NPs, as indicated by their reduced susceptibility to macrophage uptake, further verified the presence of functional immunomodulatory proteins on the particle surfaces. These biomimetic nanocarriers have tremendous potential in drug delivery applications, as they provide the opportunity to actively inhibit the immune clearance of their therapeutic cargo, thereby improving drug pharmacokinetics and therapeutic efficacy. The in-depth examination of the RBC-NPs also provides an up-close look at the fusion process between RBC membranes and PLGA polymeric particles, which appears to favour the formation of unilamellar membrane coated particles with the right-side-out membrane orientation. From synthesis and fabrication perspectives, the membrane coating technique contrasts with bottom-up functionalization schemes, which often employ chemical conjugation methods that can alter proteins' innate structures. The non-disruptive protein functionalization through the coating of natural cellular membranes presents a robust and versatile approach in interfacing synthetic materials with biological components, offering a compelling technique for the development of bio-inspired and biomimetic nanodevices.

## Acknowledgements

Chapter 3.2, in full, is a reprint of the material as it appears in *Nanoscale*, 2014, Brian Luk, Che-Ming Hu, Ronnie Fang, Diana Dehaini, Cody Carpenter, Weiwei Gao, and Liangfang Zhang; *Nanoscale*, 2013, Che-Ming Hu, Ronnie Fang, Brian Luk, Kevin Chen, Cody Carpenter, Weiwei Gao, Kang Zhang, and Liangfang Zhang. The dissertation author was a major contributor and co-author of this paper.

## References

1. Yoo, J.W., D.J. Irvine, D.E. Discher, and S. Mitragotri, *Bio-inspired*, bioengineered and biomimetic drug delivery carriers. *Nature Reviews Drug Discovery*, 2011. 10(7): p. 521-535.
2. Balmert, S.C. and S.R. Little, Biomimetic delivery with micro- and nanoparticles. *Advanced Materials*, 2012. 24(28): p. 3757-3778.
3. Oldenburg, P.A., A. Zheleznyak, Y.F. Fang, C.F. Iaghenaur, H.D. Greshan, and F.P. Lindberg, Role of CD47 as a marker of self on red blood cells. *Science*, 2000. 288(5473): p. 2051-2054.
4. Jaiswal, S., C.H. Jamieson, W.W. Pang, C.Y. Park, M.P. Chao, R. Majeti, D. Traver, N. van Rooijen, and I.L. Weissman, CD47 is upregulated on circulating hematopoietic stem cells and leukemia cells to avoid phagocytosis. *Cell*, 2009. 138(2): p. 271-285.
5. Cameron, C.M., J.W. Barrett, M. Mann, A. Lucas, and G. McFadden, Myxoma virus M128L is expressed as a cell surface CD47-like virulence factor that contributes to the downregulation of macrophage activation in vivo. *Virology*, 2005. 337(1): p. 55-67.
6. Hsu, Y.C., M. Acuna, S.M. Tahara, and C.A. Peng, Reduced phagocytosis of colloidal carriers using soluble CD47. *Pharmaceutical Research*, 2003. 20(10): p. 1539-1542.
7. Tsai, R.K., P.L. Rodriguez, and D.E. Discher, Self inhibition of phagocytosis: the affinity of 'marker of self' CD47 for SIRPalpha dictates potency of inhibition but only at low expression levels. *Blood Cells, Molecules, and Diseases*, 2010. 45(1): p. 67-74.
8. Finley, M.J., L. Rauova, I.S. Alferiev, J.W. Weisel, R.J. Levy, and S.J. Stachelek, Diminished adhesion and activation of platelets and neutrophils with CD47 functionalized blood contacting surfaces. *Biomaterials*, 2012. 33(24): p. 5803-5811.
9. Stachelek, S.J., M.J. Finley, I.S. Alferiev, F. Wang, R.K. Tsai, E.C. Eckells, N. Tomczyk, J.M. Connolly, D.E. Discher, D.M. Eckmann, and R.J. Levy, The effect of CD47 modified polymer surfaces on inflammatory cell attachment and activation. *Biomaterials*, 2011. 32(19): p. 4317-4326.
10. Russell, E.S., E.F. Neufeld, and C.T. Higgins, Comparison of normal blood picture of young adults from 18 inbred strains of mice. *Proceedings of the Society for Experimental Biology and Medicine*, 1951. 78(3): p. 761-766.
11. Subramanian, S., R. Tsai, S. Sen, K.N. Dahl, and D.E. Discher, Membrane mobility and clustering of Integrin Associated Protein (IAP, CD47)--major differences between mouse and man and implications for signaling. *Blood Cells, Molecules, and Diseases*, 2006. 36(3): p. 364-372.

12. Brown, E.J. and W.A. Frazier, Integrin-associated protein (CD47) and its ligands. *Trends in Cell Biology*, 2001. 11(3): p. 130-135.
13. Hu, C.M., L. Zhang, S. Aryal, C. Cheung, R.H. Fang, and L. Zhang, Erythrocyte membrane-camouflaged polymeric nanoparticles as a biomimetic delivery platform. *Proceedings of the National Academy of Sciences USA*, 2011. 108(27): p. 10980-10985.
14. Mouro-Chanteloup, I., J. Delaunay, P. Gane, V. Nicolas, M. Johansen, E.J. Brown, L.L. Peters, C.L. Van Kim, J.P. Cartron, and Y. Colin, Evidence that the red cell skeleton protein 4.2 interacts with the Rh membrane complex member CD47. *Blood*, 2003. 101(1): p. 338-344.
15. Hochmuth, R.M., C.A. Evans, H.C. Wiles, and J.T. McCown, Mechanical measurement of red cell membrane thickness. *Science*, 1983. 220(4592): p. 101-102.
16. Jan, K.M. and S. Chien, Role of surface electric charge in red blood cell interactions. *The Journal of General Physiology*, 1973. 61(5): p. 638-654.
17. Oldenborg, P.A., H.D. Gresham, and F.P. Lindberg, CD47-signal regulatory protein alpha (SIRPalpha) regulates Fcgamma and complement receptor-mediated phagocytosis. *The Journal of Experimental Medicine*, 2001. 193(7): p. 855-862.
18. Hu, C.M., R.H. Fang, and L. Zhang, Erythrocyte-Inspired Delivery Systems. *Advanced Healthcare Materials*, 2012. 1(5): p. 537-547.
19. Durocher, J.R., R.C. Payne, and M.E. Conrad, Role of sialic acid in erythrocyte survival. *Blood*, 1975. 45(1): p. 11-20.

### **3.3 Safe and immunocompatible nanocarriers cloaked in RBC membranes for drug delivery to treat solid tumors**

#### **3.3.1 Introduction**

Nanoparticle-based drug delivery platforms are often tasked with navigating complex biological environments, and their performance can ultimately be governed by their ability to avoid nonspecific interactions while exhibiting a high degree of target selectivity [1-3]. As such, the facile incorporation of complex functionalities onto nanoparticle surfaces has long been desirable [4-7]. Recently, the direct use of naturally derived biomembrane as a coating material represents an emerging strategy for nanoparticle functionalization [8-10]. The faithful, right-side-out translocation of all membrane-bound moieties from the cell surface onto the surface of a nanoparticle can naturally bestow the nanoparticle with desirable properties such as long circulation, immune evasion, and targeting affinity without the need to explicitly engineer these functionalities from the bottom-up [11-13]. This cell membrane cloaking strategy has demonstrated utility for a variety of purposes, including biodetoxification [14-16], antibacterial vaccination [17, 18], antibiotic delivery [19], photothermal therapy [20], and cancer immunotherapy [13, 21]. Using this approach, an endless number of applications can be envisioned, as it should be possible to combine the membrane from any cell type with a variety of different nanoparticle core materials [22-25].

One cell type that has been widely explored as a source for membrane coating is the red blood cell (RBC), which represents nature's own long circulating carrier. RBCs express a variety of immunomodulatory markers that enable the body to recognize them as self [26, 27], and



functionalization of nanoparticles with RBC membrane has been proven to promote immune evasion and significantly enhance circulation residence time [10, 22]. These properties make RBC membrane-coated nanocarriers a truly appealing candidate for cancer drug delivery, which is a field that has long benefited from the use of long-circulating, lowly immunogenic nanocarriers [28, 29]. As more nanoparticle-based chemotherapies are being investigated in the clinic, a great deal of emphasis has been placed on safety and immunocompatibility [30, 31]. To this end, RBC membrane-coated polymeric nanoparticles (denoted RBC-NP), consisting of a poly(lactic-*co*-glycolic acid) (PLGA) core and an RBC membrane shell, represent a promising delivery system due to their combination of high drug carrying capacity along with an inherently biocompatible membrane coating [32]. Here, we demonstrate that RBC-NP can be effectively used to deliver a model chemotherapeutic drug, doxorubicin (DOX), in a mouse model of lymphoma. We study the ability of the drug-loaded nanoparticles to control tumor growth while concurrently assessing their ability to eliminate the toxicities commonly associated with free drug administration. Further, the short- and long-term immune effects of the RBC-NP upon systemic administration are studied as well.

### **3.3.2 Experimental Methods**

#### **Preparation of RBC-NP and RBC-NP(DOX)**

Whole blood was collected from C57BL/6 mice (Harlan Sprague Dawley) and collected by centrifugation at  $500 \times g$  for 10 min. RBC membrane vesicles were then prepared using a sonication approach. PLGA polymeric cores loaded with DOX were prepared with carboxy-terminated 50:50 PLGA polymer (LACTEL Absorbable Polymers) using a double emulsion process. DOX was dissolved in 25  $\mu$ L of 500 mM Tris-HCl at pH 8 as the inner phase, and

sonicated with 500  $\mu$ L of PLGA in dichloromethane (DCM) at 10 mg/mL. The solution was then added to 5 mL of 10 mM Tris-HCl at pH 8 and sonicated again. This final solution was then added to an additional 10 mL of 10 mM Tris-HCl at pH 8 and allowed to evaporate for at least 4 h with stirring. Empty PLGA cores were prepared in the same fashion, but without DOX in the inner phase. RBC-NP were prepared by fusing RBC membrane vesicles on preformed PLGA cores using a previously established protocol [15]. The size and zeta potential of the RBC-NP were obtained from three dynamic light scattering (DLS) measurements using a Malvern ZEN 3600 Zetasizer. Transmission electron microscopy (TEM) was used to characterize the morphology of RBC-NP. Briefly, a drop of RBC-NP solution (1 mg/mL) was deposited onto a glow-discharged carbon-coated TEM grid, followed by washing with 10 drops of distilled water and staining with 1 wt% uranyl acetate. An FEI Sphera Microscope operating at 200 kV was used to image the sample. The DOX loading was evaluated by measuring its fluorescence (excitation at 480 nm; emission at 580 nm). Drug release was studied by dialyzing samples against phosphate buffered saline (PBS) buffer (1 X, pH = 7.4) using Slide-A-Lyzer MINI Dialysis Cups (Thermo Scientific) with a molecular weight cut-off of 10 kDa.

### ***In Vitro* Cytotoxicity and Uptake**

EL4 cells (American Type Culture Collection) were plated at 5,000 cells per well. Free DOX and RBC-NP(DOX) at varying drug concentrations were incubated with the cells for 72 h at 37 °C and 5% CO<sub>2</sub>, after which an XTT Cell Proliferation Kit (Roche Diagnostics) was used to assess cell viability. DOX uptake was assessed by incubating 100,000 EL4 cells with varying concentrations of free DOX or RBC-NP(DOX) for 1 h at 37 °C. After 1 h, the samples were washed and fixed with 10% formalin for analysis. Flow cytometry was used to measure the DOX signal in the cells using a Becton Dickinson FACSCanto II.

### ***In Vivo* Antitumor Efficacy**

75,000 EL4 cells were implanted subcutaneously into the right flank of 6-week-old male C57BL/6 mice. The tumors were allowed to grow for 9 days. RBC-NP(DOX), free DOX, empty RBC-NP, or sucrose was administered every other day starting from day 9 post-implantation of the tumor cells for 2 weeks ( $n = 5$  per group). Where applicable, 200  $\mu\text{L}$  of each respective formulation was administered intravenously via tail vein injection at a concentration equivalent to 3 mg/kg DOX, which was found to be the maximum tolerated dose of the drug. Tumor dimensions and mouse weights were measured every other day beginning on day 8 post-implantation and every 3 days beginning on day 35. Tumor volume was calculated using the equation  $V = \frac{\pi}{6}LW^2$ , where  $V$  is volume,  $L$  is length, and  $W$  is width. Survival was pre-defined as tumor size  $< 2000 \text{ mm}^3$  prior to the initiation of the study.

### ***In Vivo* Safety Studies**

To examine the effect of RBC-NP(DOX) on normal physiological parameters, 200  $\mu\text{L}$  of sucrose, RBC-NP(DOX), or free DOX at 3 mg/kg of drug was injected intravenously into the tail vein of C57BL/6 mice ( $n = 3$  per group). Whole blood was collected into heparinized tubes before and 24 h after injection. Hematological parameters (RBC count, platelet count, hemoglobin, hematocrit, white blood cell count, neutrophil count, lymphocyte count, and monocyte count) were evaluated using a Drew Scientific Hemavet 950 FS Multi-Species Hematology System. To evaluate serum chemistry, blood was collected and allowed to clot for 4 h at room temperature. Samples were then centrifuged at  $7000 \times g$ , and 300  $\mu\text{L}$  of serum was collected. Serum chemistry components were measured using the SEAL AutoAnalyzer 3 HR.

### ***In Vivo* Immunogenicity Studies**

To examine the safety of the RBC-NP platform, 200  $\mu$ L of RBC-NP at a particle dosing of 30 mg/kg was injected intravenously into the tail vein of C57BL/6 mice; additional mice were administered isotonic sucrose solution or a mixture of lipopolysaccharide (10  $\mu$ g/kg) and D-galactosamine (100 mg/kg) (n = 3 per group). Blood was collected 6 h post-injection and the plasma was separated. An IL-6 ELISA kit (Biolegend) was used to measure the levels of IL-6 following the manufacturer's protocol. To study the anti-RBC IgG and IgM titers, blood was collected at day 30 post-challenge from tumor-bearing mice administered with RBC-NP in the above antitumor efficacy study (n = 5). In the study, mice were injected with RBC-NP at a particle dosing of 30 mg/kg every other day for 2 weeks starting from day 9 post-challenge. Plasma was separated from whole blood. To measure anti-RBC titers, RBCs in PBS were coated onto Costar 96 well plates (Corning) at  $10^6$  RBCs per well. The collected plasma was used as the primary immunostain. Goat anti-mouse IgG-HRP (Biolegend) or goat anti-mouse IgM-HRP (Santa Cruz Biotechnology) was used as the secondary antibody for detecting the presence of autoantibodies against RBCs, and TMB substrate (Thermo Scientific) was used to develop the plate.

### **3.3.3 Results and Discussion**

Empty or DOX-loaded PLGA nanoparticles were prepared using a double emulsion method. RBC membrane derived from the blood of C57BL/6 mice was coated onto the polymeric cores using a sonication approach as previously described [15]. The general structure of the resulting nanoparticles is depicted in Figure 3.1A with the DOX loaded inside the PLGA core and the RBC membrane coating, with all its associated proteins, forming the outer layer. Drug loading into the PLGA cores could be controlled by varying the initial input concentration

of DOX (Figure 3.1B). By increasing the input of DOX, loading of the drug was also increased, and a saturation level was reached at approximately 40 wt% (DOX weight/PLGA weight) drug input, corresponding to approximately 10 wt% loading. As the drug input concentration was increased, the encapsulation efficiency decreased markedly, dropping from 50% efficiency at an input of 10 wt% down to 20% efficiency at the maximal tested input of 50 wt%. A formulation approaching the saturation loading level of 10 wt% DOX was used for subsequent *in vitro* and *in vivo* studies.

Coating of 140 nm empty or DOX-loaded PLGA cores with RBC membranes resulted in a size increase to approximately 155 nm and an increase in zeta potential of approximately 15 mV, from ~-45 mV to -30 mV (Figure 3.1C). This is consistent with previous findings, as the membrane layer adds to the hydrodynamic size, while the membrane coating, which is less negatively charged than the core, shields the highly negative carboxyl groups present on the surface of the core [13]. The core-shell structure of the drug-loaded RBC-NP, herein denoted RBC-NP(DOX), was confirmed by visualization using transmission electron microscopy (TEM) with uranyl acetate negative staining (Figure 3.1D). Morphologically, the drug-loaded RBC-NP are similar in appearance to unloaded PLGA coated with the same membrane, suggesting that drug-loaded RBC-NP of varying sizes can easily be fabricated to meet the requirements of future applications [12]. The resulting RBC-NP(DOX) demonstrated sustained release over time (Figure 3.1E); approximately 80% of the encapsulated drug was released over the course of 7 days, with the majority of the release occurring within the first 72 h. This observed prolonged release is due in part to the RBC membrane coating acting as a diffusional barrier for DOX release, a phenomenon that has been previously reported [32, 33].

To evaluate whether the drug encapsulated within the RBC-NP(DOX) could

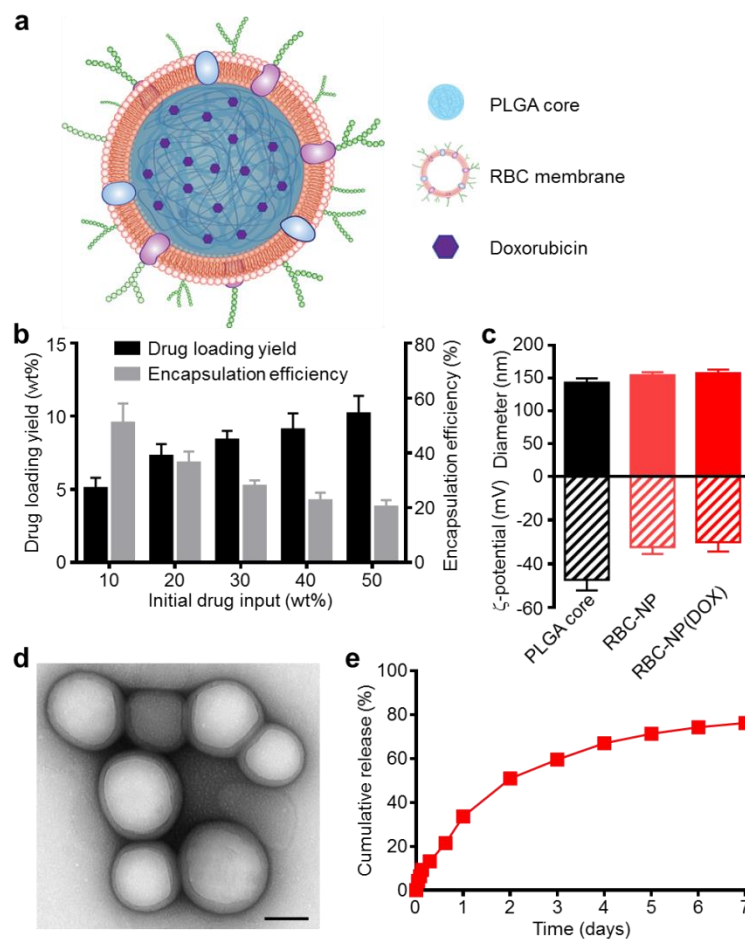


**Figure 3.3.1** Physicochemical characterization and drug loading of RBC-NPs. (A) Schematic of doxorubicin (DOX)-loaded RBC-NP, denoted “RBC-NP(DOX)”. (B) Loading yield and loading efficiency of DOX into PLGA nanoparticles at various initial drug inputs. (C) Dynamic light scattering (DLS) measurements of the size and surface zeta potential of bare PLGA core, RBC-NP, and RBC-NP(DOX) with a drug loading yield of 10 wt%. (D) Transmission electron microscopy (TEM) visualization of RBC-NP(DOX) with uranyl acetate negative staining (scale bar = 100 nm). (E) Cumulative release profile of DOX from RBC-NP(DOX) with 10 wt% DOX loading yield over a period of 7 days.

retain its tumor killing activity, an *in vitro* cytotoxicity test was conducted. It was shown that RBC-NP(DOX) exhibited cytotoxicity when incubated together with EL4 mouse lymphoma cells for 72 h *in vitro* (Figure 3.2A). Under the conditions tested, the nanoparticle formulation had an apparent drug  $IC_{50}$  of 5.6 ng/mL. Free DOX demonstrated slightly better efficacy against EL4 tumor cells *in vitro* compared with RBC-NP(DOX) with an  $IC_{50}$  of 1.4 ng/mL. This difference can be rationalized by the fact that, at the 72 h conclusion of the experiment, there was still

incomplete release of drug from RBC-NP(DOX). Additionally, free DOX can easily diffuse into the cancer cells, making it extremely potent over extended incubation periods, especially given that the EL4 cell line is not inherently DOX-resistant [34]. While RBC-NP(DOX) and free DOX showed similar activity over longer incubation periods, encapsulated DOX showed enhanced uptake by EL4 cells after a short, 1 h incubation (Figure 3.2B). The observed difference in intracellular localization is likely due to the fact that nanoparticles are taken up via active mechanisms such as endocytosis [35], enabling a higher capacity for transport across the cellular membrane compared with pure diffusion. This effect can be further enhanced with active targeting ligands, which can be introduced onto the surface of RBC-NP [36]. These observations indicate that encapsulating DOX into RBC-NP has the potential to facilitate quick uptake of the drug by tumor cells and slow release in a sustained manner over time.

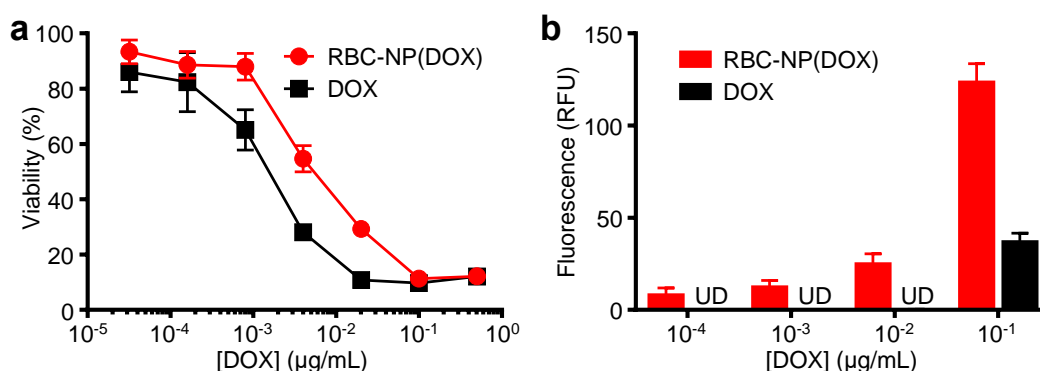


**Figure 3.3.2** *In vitro* antitumor efficacy and uptake. (A) *In vitro* cytotoxicity of RBC-NP(DOX) in comparison with free DOX against EL4 murine lymphoma cells after 72 h of incubation. (B) Uptake of DOX by EL4 cells after 1 h incubation with either RBC-NP(DOX) or free DOX.

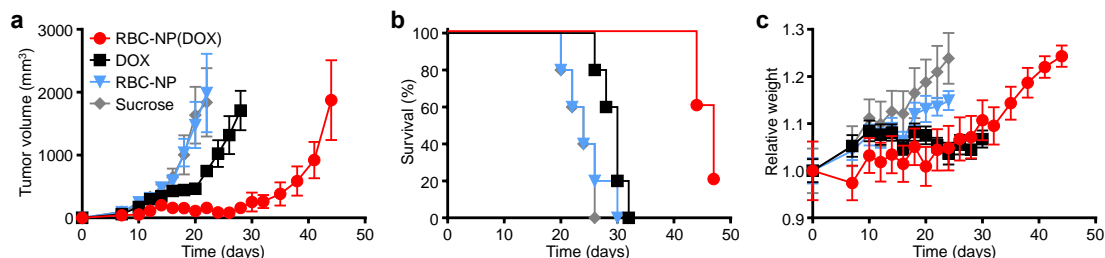


**Figure 3.3.3** *In vivo* treatment of solid tumors. (A) Tumor growth inhibition in mice treated with RBC-NP(DOX), free DOX, RBC-NP, or isotonic sucrose by tail vein injection (n=5). Treatment was initiated 9 days post-challenge, and mice were administered formulations every other day for 2 weeks. (B) Survival of mice treated with RBC-NP(DOX), free DOX, RBC-NP, or isotonic sucrose. (C) Relative weights of tumor-bearing mice treated with RBC-NP(DOX), free DOX, RBC-NP, or isotonic sucrose. Values were normalized within each group using the measurements on day 0.

To determine the ability of drug-loaded RBC-NP to function as effective therapy against tumor growth *in vivo*, we analyzed long-term tumor burden in a murine lymphoma model. EL4 cells were implanted subcutaneously into the right flank of C57BL/6 mice and were first allowed to develop for 9 days, after which tumor-bearing mice were treated every other day with RBC-NP(DOX), free DOX, empty RBC-NP, or isotonic sucrose at a drug dosage of 3 mg of DOX per kg of body weight (3 mg/kg) (Figure 3.3A). The dosing was determined to be just under the maximum tolerated dose for 6-week-old male C57BL/6 mice, designated as the dose at which the mouse body weight decreases 10% (data not shown). Isotonic sucrose and RBC-NP treatment alone did not affect tumor growth. Mice treated with free DOX exhibited marginal control of tumor growth, extending median survival by 6 days compared with no treatment. The RBC-NP(DOX) treatment group showed the most significant efficacy in terms of tumor growth inhibition, with the median survival nearly doubling from 24 days for the control group to 47 days for the treated group (Figure 3.3B). Though not an actively targeted formulation, it is believed that RBC-NP(DOX) was able to accumulate at the tumor site via the enhanced permeation and retention (EPR) effect [37, 38], thereby substantially increasing the local drug concentration at the tumor site. It should be noted that it was not until treatment ceased on day 23 post-implantation that the tumor growth kinetics started to accelerate. During this period, mice



treated by RBC-NP(DOX) showed no appreciable decrease in weight, a global parameter of formulation safety (Figure 3.3C). It should also be noted that, for the free DOX treatment group, the observed steady weight kinetics reflects an increase in tumor burden, which indicates an appreciable toxic effect. Mice treated with RBC-NP(DOX) continued to increase in weight despite minimal tumor burden during the treatment period, suggesting that, in future explorations, the nanoparticle formulation can be further increased to exert an even more potent antitumor effect.

Next, we evaluated the safety profile of RBC-NP(DOX) in order to assess the formulation's potential as a clinically translatable drug delivery platform. Isotonic sucrose, RBC-NP(DOX), or free DOX was administered at a drug dosage of 3 mg/kg, and whole blood was collected prior to injection and 24 h post-injection. Hematological parameters largely showed no difference between the sucrose, RBC-NP(DOX), and free DOX treatment groups (Figure 3.4A-D). RBC, platelet, hemoglobin, and hematocrit quantifications were all normal 24 h after injection. Free DOX, however, is known to have myelosuppressing effects, which can lead to severe complications in the clinic such as neutropenic fever, infections, hemorrhage, and even death [39]. This was reflected in the white blood cell (WBC) quantifications (Figure 3.4E-H). When free DOX was administered, the mice suffered a significant decrease in WBC count. This decrease in overall WBC count was seen across different leukocyte subsets, with the sharpest reduction occurring in the number of lymphocytes. The RBC-NP(DOX) formulation was able to stably sequester the drug, delivering it for potent tumor control with no observable myelosuppression, which is often the dose-limiting toxic side effect of DOX in a clinical setting.

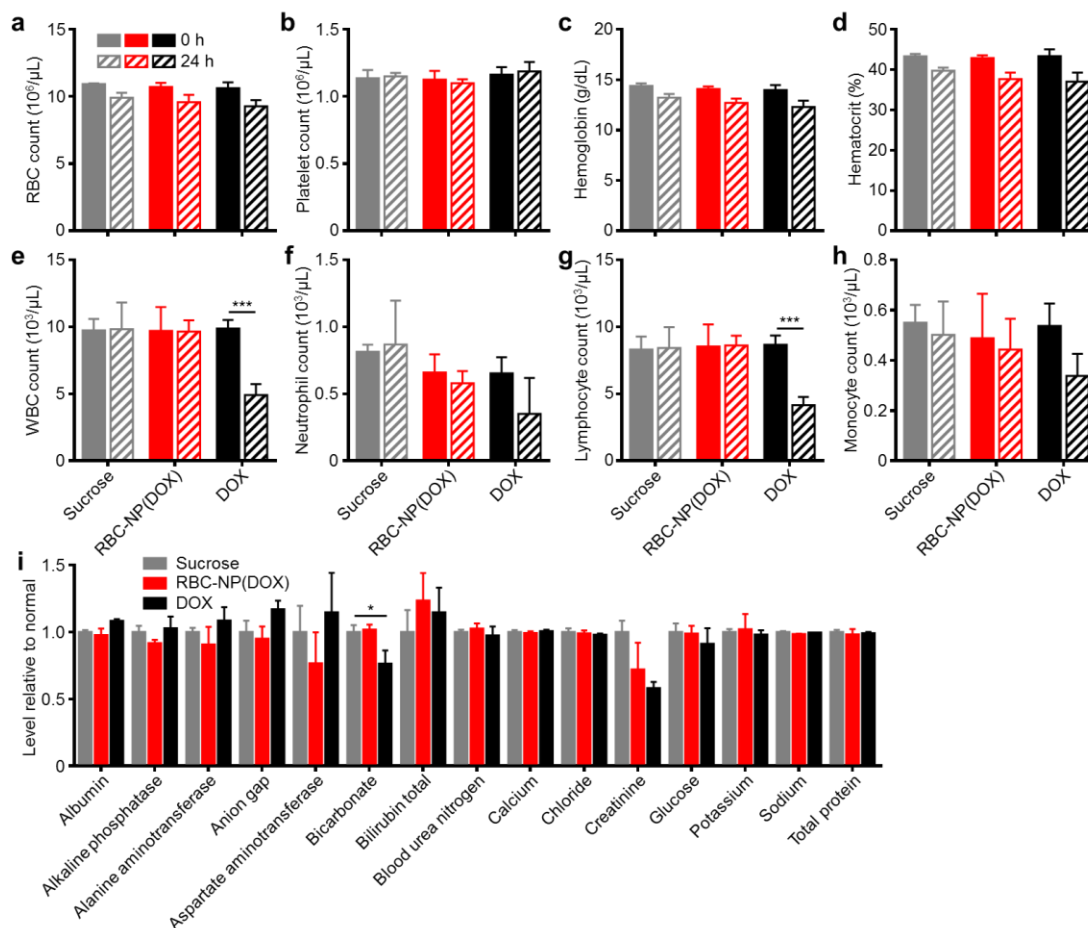


**Figure 3.3.4** *In vivo* safety studies of RBC-NP(DOX). (A) RBC count, (B) platelet count, (C) hemoglobin quantification, (D) hematocrit, (E) white blood cell count, (F) neutrophil count, (G) lymphocyte count, and (H) monocyte count in mice before and 24 h after injection of sucrose, RBC-NP(DOX) or free DOX. (I) Comprehensive serum chemistry panel conducted on mice intravenously injected with isotonic sucrose, RBC-NP(DOX), or free DOX. Serum was collected 24 h post-injection ( $n = 3$  for all experiments; \* $P \leq 0.05$ ; \*\*\* $P \leq 0.001$ ).

Additionally, RBC-NP(DOX) did not elicit any adverse physiological effects based on a comprehensive chemistry panel of mouse serum (Figure 3.4I). The creatinine levels for mice treated with free DOX were significantly decreased, possibly indicating increased activity of the kidneys to remove excess free drug. Of potential note are the decrease in bicarbonate and concurrent increase in anion gap for mice treated with free DOX only. These results, when taken together, can indicate a shift towards acidosis, which can be an early sign of kidney failure. Furthermore, RBC-NP(DOX) treatment did not result in any increase in serum alanine aminotransferase (ALT) or aspartate aminotransferase (AST) levels, suggesting that RBC-

NP(DOX) administration does not induce liver injury. As is the case with most nanoparticle formulations, RBC-NPs are cleared by the liver [22], so it is important that the DOX-loaded RBC-NPs do not induce any acute hepatic damage. Compared with free DOX, RBC-NP(DOX) demonstrated a lack of acute systemic abnormalities after administration of a therapeutic dose, thereby underscoring the biocompatibility and safety of RBC-NP as a drug carrier.

To further evaluate the translatability of RBC-NP as a cancer drug carrier, we investigated the immunological implications of RBC-NP administration. RBC-NP did not induce elevated serum levels of interleukin-6 (IL-6), which indicates lack of an acute systemic inflammatory response against the nanocarrier (Figure 3.5A). Nanoscale drug delivery vehicles must also not induce any long-term immune responses, the lack of which helps to preserve functionality of the particles upon repeated injections [40]. Multiple administrations of RBC-NP induced no detectable serum IgM or IgG titers against RBCs after 30 days (Figure 3.5B,C), indicating that RBC-NPs can be used *in vivo* repeatedly without reduction in their abilities to function as a drug delivery vehicle. Additionally, the lack of antibody titers against RBCs reveals that no autoimmunity against self-RBCs is developed as a result of repeated RBC-NP injections. Taken together, these results demonstrate that RBC-NP themselves produce no significant acute or long-term immunological responses as a delivery vehicle, highlighting the “self” nature of the RBC-NP platform. Thus, RBC-NP can serve as an effective option for drug delivery to overcome the limitations of traditional chemotherapy.

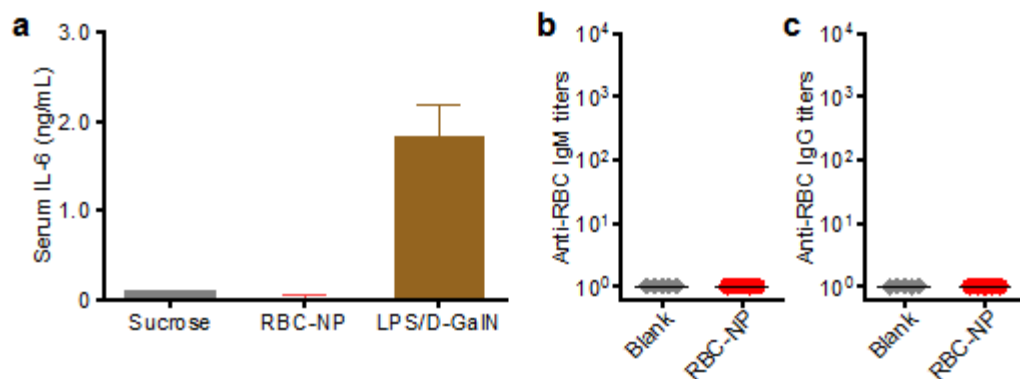


**Figure 3.3.5** *In vivo* immunogenicity of RBC-NP. (A) Serum analysis of interleukin-6 (IL-6) production in mice administered with isotonic sucrose, RBC-NP, or lipopolysaccharide with D-galactosamine (LPS/D-GalN) as a positive control (n = 3). (B) anti-RBC IgM and (C) anti-RBC IgG titers produced in mice receiving repeated dosing of RBC-NP (n = 5). Tumor-bearing mice were administered with RBC-NP every other day starting from day 9 post-implantation of the tumor cells for 2 weeks and blood was collected on day 30 post-implantation for titer analyses.

The focus of these studies as a whole was to evaluate a biocompatible nanoparticle drug delivery agent with clinical translation potential to treat solid tumors with enhanced efficacy. Therapeutic nanocarriers must be safe for use *in vivo*. Previous nanoparticle studies on bare materials such as carbon nanotubes [41, 42], iron nanoparticles [43], and titanium dioxide [44], have shown adverse responses indicative of material toxicity. RBC-NP(DOX), employing a highly generalizable membrane cloaking approach, was able to deliver a toxic chemotherapy drug payload to the tumor site and significantly prolong survival without any acute increases in myelosuppression, systemic immune response, or abnormal blood chemistry parameters. Furthermore, early mortality and toxicity from high DOX dosages were not observed during long-term and repetitive treatment with RBC-NP(DOX).

### 3.3.4 Conclusions

The studies described here indicate that the RBC-NP platform is able to unite several important drug delivery properties into a single system. Of great importance, RBC-NP with its natural membrane coating, demonstrated good biocompatibility and did not elicit immune

reactions. Furthermore, the versatility of the inner polymeric core provides opportunities to deliver a wide variety of therapeutics (i.e. hydrophilic/hydrophobic small molecules, proteins, nucleic acids, etc.) [45]. Although translating RBC-NP to human use remains to be investigated, large-scale synthesis of the particles should be feasible given the existing infrastructure for blood collection and transfusion as well as the maturing development of polymeric therapeutics [46]. Ultimately, the safety and biocompatibility of RBC-NP paired with its efficacy against solid tumors reveal that this platform possesses many of the requisite characteristics for a clinically translatable drug delivery system. The results presented here provide a promising foundation for continued development and future clinical tests of the RBC-NP platform.

## **Acknowledgements**

Chapter 3.3, in full, is a reprint of the material as it appears in *Theranostics*, 2016, Luk, B.; Fang, R.; Hu, C-M.; Copp, J.; Thamphiwatana, S.; Dehaini, D.; Gao, W.; Zhang, K.; Li, S.; Zhang, L. The dissertation author was a major contributor and co-author of this paper.

## References

1. Desai, N., Challenges in development of nanoparticle-based therapeutics. *American Association of Pharmaceutical Scientists Journal*, 2012. 14(2): p. 282-295.
2. Mitragotri, S., P.A. Burke, and R. Langer, Overcoming the challenges in administering biopharmaceuticals: formulation and delivery strategies. *Nature Reviews Drug Discovery*, 2014. 13(9): p. 655-672.
3. De Jong, W.H. and P.J. Borm, Drug delivery and nanoparticles: applications and hazards. *International Journal of Nanomedicine*, 2008. 3(2): p. 133-149.
4. Jiang, S., K.Y. Win, S. Liu, C.P. Teng, Y. Zheng, and M.Y. Han, Surface-functionalized nanoparticles for biosensing and imaging-guided therapeutics. *Nanoscale*, 2013. 5(8): p. 3127-3148.
5. Mout, R., D.F. Moyano, S. Rana, and V.M. Rotello, Surface functionalization of nanoparticles for nanomedicine. *Chemical Society Reviews*, 2012. 41(7): p. 2539-2544.
6. Sperling, R.A. and W.J. Parak, Surface modification, functionalization and bioconjugation of colloidal inorganic nanoparticles. *Philosophical Transactions of the Royal Society A Mathematical, Physical and Engineering Sciences*, 2010. 368(1915): p. 1333-1383.
7. Hu, C.M., R.H. Fang, B.T. Luk, and L. Zhang, Polymeric nanotherapeutics: clinical development and advances in stealth functionalization strategies. *Nanoscale*, 2014. 6(1): 65-75.
8. Yoo, J.W., D.J. Irvine, D.E. Discher, and S. Mitragotri, Bio-inspired, bioengineered and biomimetic drug delivery carriers. *Nature Reviews Drug Discovery*, 2011. 10(7): p. 521-535.
9. Fang, R.H., C.M. Hu, and L. Zhang, Nanoparticles disguised as red blood cells to evade the immune system. *Expert Opinion on Biological Therapy*, 2012. 12(4): p. 385-389.
10. Hu, C.M., R.H. Fang, and L. Zhang, Erythrocyte-inspired delivery systems. *Advanced Healthcare Materials*, 2012. 1(5): p. 537-547.
11. Hu, C.M., R.H. Fang, B.T. Luk, K.N. Chen, C.W. Carpenter, W. Gao, K. Zhang, and L. Zhang, 'Marker-of-self' functionalization of nanoscale particles through a top-down cellular membrane coating approach. *Nanoscale*, 2013. 5(7): p. 2664-2668.
12. Luk, B.T., C.M. Hu, R.H. Fang, D. Dehaini, C. Carpenter, W. Gao, and L. Zhang, Interfacial interactions between natural RBC membranes and synthetic polymeric nanoparticles. *Nanoscale*, 2014. 6(5): p. 2730-2737.

13. Fang, R.H., C.M. Hu, B.T. Luk, W. Gao, J.A. Copp, Y. Tai, D.E. O'Connor, and L. Zhang, Cancer cell membrane-coated nanoparticles for anticancer vaccination and drug delivery. *Nano Letters*, 2014. 14(4): p. 2181-2188.
14. Hu C.M., R.H. Fang, J.A. Copp, B.T. Luk, and L. Zhang, A biomimetic nanosponge that absorbs pore-forming toxins. *Nature Nanotechnology*, 2013. 8(5): p. 336-340.
15. Copp J.A., R.H. Fang, B.T. Luk, C.M. Hu, W. Gao, K. Zhang, and L. Zhang, Clearance of pathological antibodies using biomimetic nanoparticles. *Proceedings of the National Academy of Sciences USA*, 2014. 111(37): p. 13481-13486.
16. Pang, Z., C.M. Hu, R.H. Fang, B.T. Luk, W. Gao, F. Wang. Detoxification of organophosphate poisoning using nanoparticle bioscavengers. *ACS Nano*, 2015. 9(6): p. 6450-6458.
17. Gao, W., R.H. Fang, S. Thamphiwatana, B.T. Luk, J. Li , P. Angsantikul. Modulating antibacterial immunity via bacterial membrane-coated nanoparticles. *Nano Letters*, 2015, 15(2): p. 1403-1409.
18. Hu, C.M., R.H. Fang, B.T. Luk, and L. Zhang, Nanoparticle-detained toxins for safe and effective vaccination. *Nature Nanotechnology*, 2013. 8(12): p. 933-938.
19. Hu, C.M., R.H. Fang, K.C. Wang, B.T. Luk, S. Thamphiwatana, D. Dehaini. Nanoparticle biointerfacing by platelet membrane cloaking. *Nature*, 2015. 526(7571): p. 118-121.
20. Piao, J.G., L. Wang, F. Gao, Y.Z. You, Y. Xiong, and L. Yang, Erythrocyte membrane is an alternative coating to polyethylene glycol for prolonging the circulation lifetime of gold nanocages for photothermal therapy. *ACS Nano*, 2014. 8(10): p. 10414-10425.
21. Guo, Y., D. Wang, Q. Song, T. Wu, X. Zhuang, Y. Bao. Erythrocyte membrane-enveloped polymeric nanoparticles as nanovaccine for induction of antitumor immunity against melanoma. *ACS Nano*, 2015. 9(7): p. 6918-6933.
22. Hu, C.M., L. Zhang, S. Aryal, C. Cheung, R.H. Fang, and L. Zhang, Erythrocyte membrane-camouflaged polymeric nanoparticles as a biomimetic delivery platform. *Proceedings of the National Academy of Sciences USA*, 2011. 108(27): p. 10980-10985.
23. Gao, W., C.M. Hu, R.H. Fang, B.T. Luk, J. Su, and L. Zhang. Surface functionalization of gold nanoparticles with red blood cell membranes. *Advanced Materials*, 2013. 25(26): p. 3549-3553.
24. Zhang, J., W. Gao, R.H. Fang, A. Dong, and L. Zhang, Synthesis of nanogels via cell membrane-templated polymerization. *Small*, 2015. 11(34): p. 4309-4313.
25. Parodi, A., N. Quattrocchi, A.L. van de Ven, C. Chiappini, M. Evangelopoulos, J.O. Martinez. Synthetic nanoparticles functionalized with biomimetic leukocyte membranes possess cell-like functions. *Nature Nanotechnology*, 2013. 8(1): p. 61-68.

26. Oldenborg, P.A., A. Zheleznyak, Y.F. Fang, C.F. Iaghenaur, H.D. Greshan, and F.P. Lindberg, Role of CD47 as a marker of self on red blood cells. *Science*, 2000. 288(5473): p. 2051-2054.
27. Rodriguez, P.L, T. Harada, D.A. Christian, D.A. Pantano, R.K. Tsai, and D.E. Discher, Minimal "Self" peptides that inhibit phagocytic clearance and enhance delivery of nanoparticles, *Science*, 2013. 339(6122): p. 971-975.
28. Davis, M.E., Z.G. Chen, and D.M. Shin, Nanoparticle therapeutics: an emerging treatment modality for cancer. *Nature Reviews Drug Discovery*, 2008. 7(9): p. 771-782.
29. Peer, D., J.M. Karp, S. Hong, O.C. Farokhzad, R. Margalit, and R. Langer, Nanocarriers as an emerging platform for cancer therapy. *Nature Nanotechnology*, 2007. 2(12): p. 751-760.
30. Ishida, T., R. Maeda, M. Ichihara, K. Irimura, and H. Kiwada, Accelerated clearance of PEGylated liposomes in rats after repeated injections. *Journal of Controlled Release*, 2003. 88(1): p. 35-42.
31. Knop, K., R. Hoogenboom, D. Fischer, and U.S. Schubert, Poly(ethylene glycol) in drug delivery: pros and cons as well as potential alternatives. *Angewandte Chemie International Edition*, 2010. 49(36): p. 6288-6308.
32. Aryal, S., C.M. Hu, R.H. Fang, D. Dehaini, C.W. Carpenter, D.E. Zhang, and L. Zhang, Erythrocyte membrane-cloaked polymeric nanoparticles for controlled drug loading and release. *Nanomedicine*, 2013. 8(8): p. 1271-1280.
33. Zhang, L., J.M. Chan, F.X. Gu, J.W. Rhee, A.Z. Wang, A.F. Radovic-Moreno. Self-assembled lipid-polymer hybrid nanoparticles: a robust drug delivery platform. *ACS Nano*, 2008, 2(8): p. 1696-1702.
34. Maccubbin, D.L., K.R. Wing, K.F. Mace, R.L. Ho, M.J. Ehrke, and E. Mihich, Adriamycin-induced modulation of host defenses in tumor-bearing mice. *Cancer Research*, 1992. 52(13): p. 3572-3576.
35. Iversen, T.G., T. Skotland, and K. Sandvig, Endocytosis and intracellular transport of nanoparticles: present knowledge and need for future studies. *Nano Today*, 2011. 6(2): p. 176-185.
36. Fang, R.H., C.M. Hu, K.N. Chen, B.T. Luk, C.W. Carpenter, W. Gao. Lipid-insertion enables targeting functionalization of erythrocyte membrane-cloaked nanoparticles. *Nanoscale*, 2013. 5(19): 8884-8888.
37. Matsumura, Y. and H. Maeda, A new concept for macromolecular therapeutics in cancer chemotherapy: mechanism of tumor-tropic accumulation of proteins and antitumor agent smancs. *Cancer Research*, 1986. 46(12): p. 6387-6392.



38. Maeda, H., Macromolecular therapeutics in cancer treatment: the EPR effect and beyond. *Journal of Controlled Release*, 2012. 164(3): p. 138-144.
39. Rostad, M.E., Current strategies for managing myelosuppression in patients with cancer. *Oncology Nursing Forum*, 1991. 18(2 Suppl): p. 7-15.
40. Rao, L., L.L. Bu, J.H. Xu, B. Cai, G.T. Yu, X. Yu. Red blood cell membrane as a biomimetic nanocoating for prolonged circulation time and reduced accelerated blood clearance. *Small*, 2015. 11(46): p. 6225-6236.
41. Kam, N.W., M. O'Connell, J.A. Wisdom, and H. Dai, Carbon nanotubes as multifunctional biological transporters and near-infrared agents for selective cancer cell destruction. *Proceedings of the National Academy of Sciences USA*, 2005. 102(33): p. 11600-11605.
42. Monteiro-Riviere, N.A., R.J. Nemanich, A.O. Inman, Y.Y. Wang, and J.E. Riviere, Multi-walled carbon nanotube interactions with human epidermal keratinocytes. *Toxicology Letters*, 2005. 155(3): p. 377-384.
43. Pisanic, T.R., J.D. Blackwell, V.I. Shubayev, R.R. Finones, and S. Jin, Nanotoxicity of iron oxide nanoparticle internalization in growing neurons. *Biomaterials*, 2007. 28(16): p. 2572-2581.
44. Warheit, D.B., T.R. Webb, K.L. Reed, S. Frerichs, and C.M. Sayes, Pulmonary toxicity study in rats with three forms of ultrafine-TiO<sub>2</sub> particles: differential responses related to surface properties. *Toxicology*, 2007. 230(1): p. 90-104.
45. Luk, B.T. and L. Zhang, Current advances in polymer-based nanotheranostics for cancer treatment and diagnosis. *ACS Applied Materials and Interfaces*, 2014. 6(24): 21859-21873.
46. Hrkach, J., D. Von Hoff, A.M. Mukkaram, E. Andrianova, J. Auer, T. Campbell. Preclinical development and clinical translation of a PSMA-targeted docetaxel nanoparticle with a differentiated pharmacological profile. *Science Translational Medicine*, 2012. 4(128): p. 128ra39.

## **3.4 Remote Loading of Small Molecule Therapeutics into Cholesterol-Enriched Cell Membrane-Derived Vesicles**

### **3.4.1 Introduction**

The increasing popularity of biomimetic design principles in nanomedicine has led to therapeutic platforms with enhanced performance and biocompatibility. This includes the direct use of naturally derived cell membranes, which can bestow nanocarriers with cell-specific functionalities. Herein, we report on a strategy enabling the efficient encapsulation of drugs via remote loading into membrane vesicles derived from red blood cells. This is accomplished by supplementing the membrane with additional cholesterol, stabilizing the nanostructure and facilitating the retention of a pH gradient. We demonstrate the loading of two model drugs: the chemotherapeutic doxorubicin and the antibiotic vancomycin. The therapeutic implications of these naturally derived, remote-loaded nanoformulations are studied both *in vitro* and *in vivo* using animal disease models. Ultimately, this approach could be used to design new biomimetic nanoformulations with higher efficacy and improved safety profiles.

The field of nanomedicine has grown significantly over the past several decades.[1] Starting with the U.S. Food and Drug Administration's approval of Doxil, a liposomal formulation of doxorubicin (Dox), numerous other nanoparticulate drugs have since been translated for clinical use.[2] Delivery via a nanocarrier has many distinct advantages compared with the administration of free drug, including improved blood residence, sustained release, and enhanced tumor targeting. All of these benefits ultimately lead to improved efficacy and patient compliance, better enabling clinicians to care for those with life-threatening diseases.

More recently, researchers have begun focusing on next-generation platforms that can build upon the initial successes of the drug delivery field. Along these lines, there has been a significant shift towards bioinspired or biomimetic design principles.[3] This is motivated by the fact that biological systems have been carefully cultivated over time by the process of evolution. Despite the significant advances made in bottom-up, synthetic nanofabrication, it is still incredibly difficult to replicate the complex functionalities found in nature. One such biomimetic strategy involves the combination of cell-derived membranes with artificial nanocarriers, leading to the generation of natural–synthetic hybrids with unique functionalities.[4] Benefits can include enhanced biocompatibility, lowered immunogenicity, heightened affinity for toxins, and the ability to target diseased tissues.[5] This approach has been proven highly generalizable and has utility across a wide range of different applications.

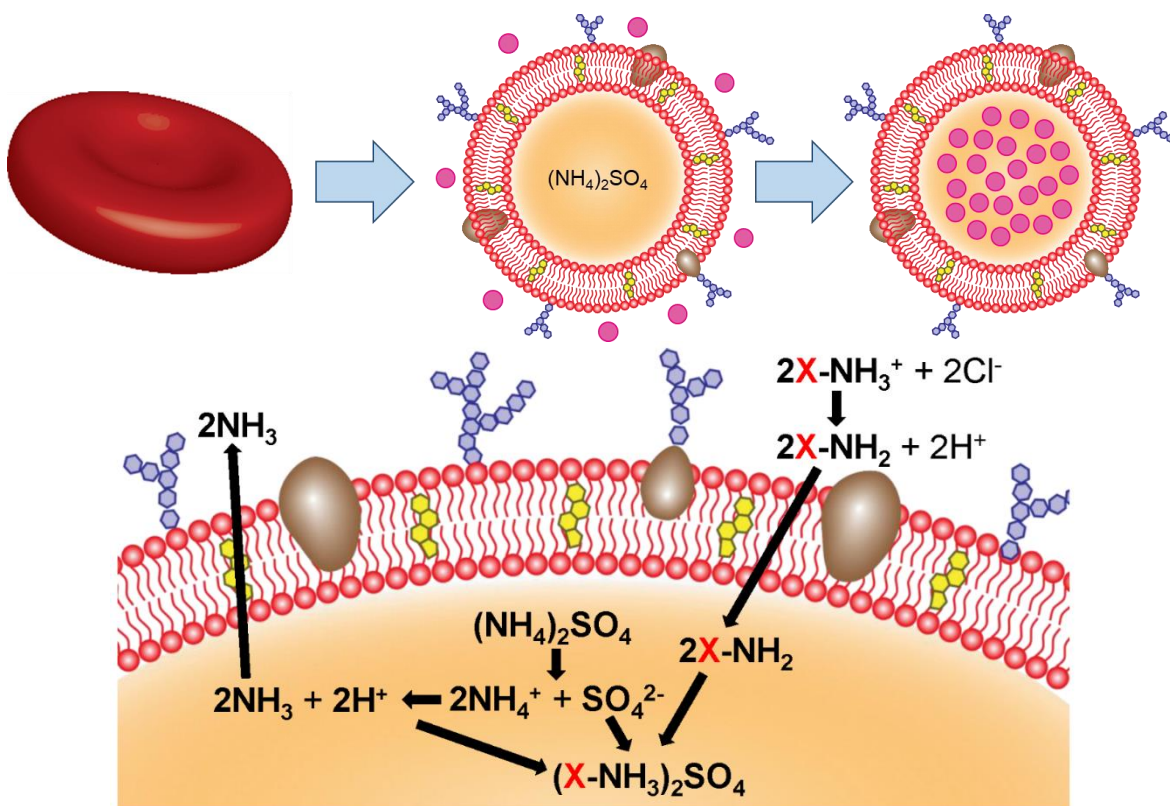


**Figure 3.4.1.** Schematic of remote loading into RBC vesicles. Natural cell membrane vesicles are fashioned from RBC ghosts supplemented with cholesterol (yellow). Ammonium sulfate (orange) is used to generate a pH gradient, which facilitates accumulation of the drug (X) inside the cholesterol-enriched RBC vesicle.

The remote loading of drugs into liposomal carriers represents one of the most highly used and effective means of nanoencapsulation.[6] In this work, we explored a strategy to adapt this approach for use with red blood cell (RBC) membrane-derived vesicles (Figure 1). It was demonstrated that membrane vesicles supplemented with exogenous cholesterol could more effectively retain a pH gradient, which was used to drive the successful loading of two model drugs: the chemotherapeutic doxorubicin (Dox) and the antibiotic vancomycin (Vanc). The Dox formulation (Dox-RBC) was used to treat a murine model of breast cancer, significantly controlling tumor growth, while the Vanc formulation (Vanc-RBC) was used to reduce bacterial load in a methicillin-resistant *Staphylococcus aureus* (MRSA) skin infection model.

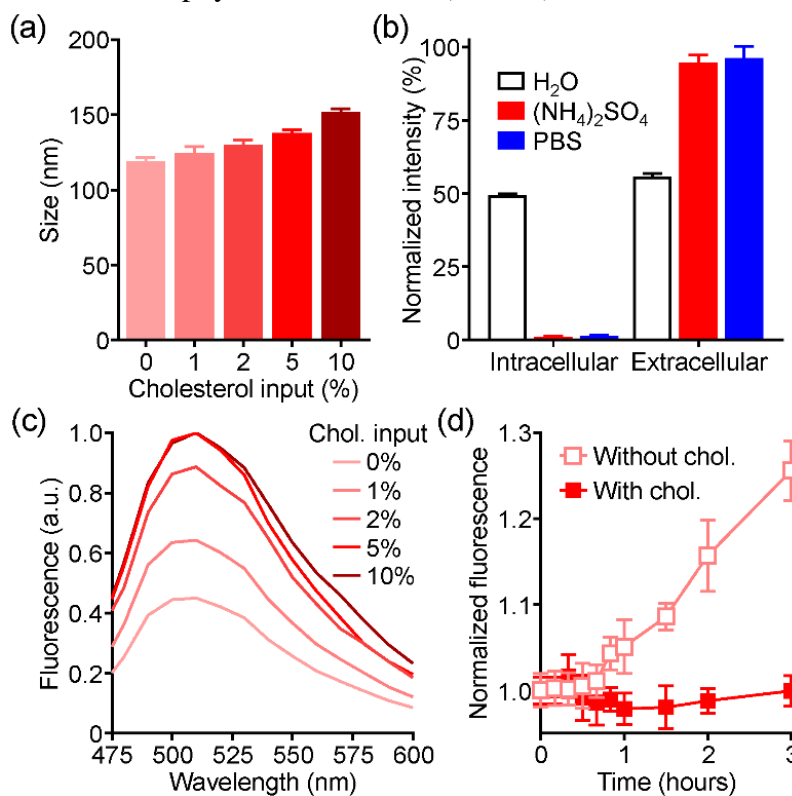


**Figure 3.4.2.** Remotely loaded RBC vesicles are fabricated by enriching the naturally derived cell membrane with additional cholesterol. Two model drugs, doxorubicin and vancomycin, are successfully loaded and show efficacy in animal models of disease. The reported approach may pave the way for biomimetic nanoformulations with high potency and safety.

### 3.4.2 Results and Discussion

To fabricate cholesterol-enriched RBC vesicles, membrane ghosts were first obtained from purified RBCs by hypotonic lysis. Free cholesterol was then incubated with the ghosts in 300 mM ammonium sulfate, followed by physical disruption to induce vesiculation. Finally, the outer phase was exchanged to phosphate buffered saline (PBS) by size exclusion chromatography, resulting in a pH gradient. At increasing cholesterol input, the final nanovesicles exhibited a corresponding increase in size up to approximately 150 nm (Figure 2a). To characterize the membrane sidedness, which is important for retention of the membrane's biological functions,[7] non-denaturing immunoblotting was employed (Figure 2b). When probed for either the intracellular or extracellular domains of the transmembrane protein CD47, ammonium sulfate-loaded vesicles had

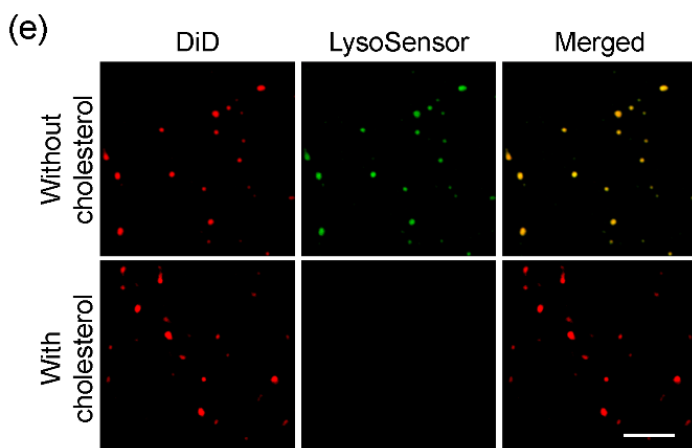


**Figure 3.4.3** Characterization of cholesterol-enriched RBC vesicles. a) Size of RBC vesicles with varying cholesterol inputs ( $n = 3$ ; mean  $\pm$  SD). b) Normalized dot blot intensities of RBC vesicles under various conditions and probed with antibodies against the intracellular or extracellular domains of CD47 ( $n = 3$ ; mean  $\pm$  SD). c) Fluorescence spectrum of ammonium sulfate-loaded RBC vesicles when co-loaded with a pH-sensitive LysoSensor Green dye. d) Leakage of calcein from RBC vesicles ( $n = 3$ ; mean  $\pm$  SD). e) Confocal fluorescence imaging of ammonium sulfate-loaded RBC vesicles co-loaded with LysoSensor Green (red: DiD, green: LysoSensor Green; scale bar = 5  $\mu$ m).

a predominantly right-side-out orientation, which was retained after transferring the vesicles to PBS. In contrast, vesicles made in water, which lacks the ions necessary to preserve orientation,[8] displayed equivalent amounts of both signals. Co-loading of the pH-sensitive dye LysoSensor Green was used to assess membrane integrity (Figure 2c). With increasing cholesterol, higher

fluorescence was observed, indicating that the ammonium sulfate was being retained within the vesicles and maintaining a low inner pH. This effect plateaued at 5% cholesterol input, and using this formulation it was demonstrated that the enriched vesicles were also impermeable to calcein dye (Figure 2d). Visualization by fluorescence microscopy showed that the signal of dye loaded into the vesicles colocalized well with dye labeling the membrane, further confirming successful encapsulation and retention (Figure 2e).

We next sought to demonstrate remote loading into the RBC vesicles. First, the chemotherapeutic doxorubicin (Dox), which represents the most classical example of a remotely loaded drug,<sup>(1)</sup> was employed. After fabricating the vesicles at a 5% cholesterol input, loading yield was quantified using various Dox input concentrations (Figure 3a). With increasing inputs, it was observed that increasing amounts of Dox could be loaded, up to approximately 10%. This process was also dependent on both temperature (Figure 3b) and time (Figure 3c), with optimal loading occurring at 37 °C and saturating at 40 minutes of reaction time. Observation of the Dox-loaded RBC vesicles (Dox-RBC) negatively stained with uranyl acetate by transmission electron microscopy revealed vesicular structures (Figure 3d). Notably, elongated crystals were visualized, consistent with reports on Dox-loaded synthetic liposomes.<sup>(2)</sup> Drug release was also evaluated over a period of 2 days at different pH values (Figure 3e). Regardless of pH, a burst release occurred in the first 12 hours, followed by more gradual, sustained release. Lowering the pH from

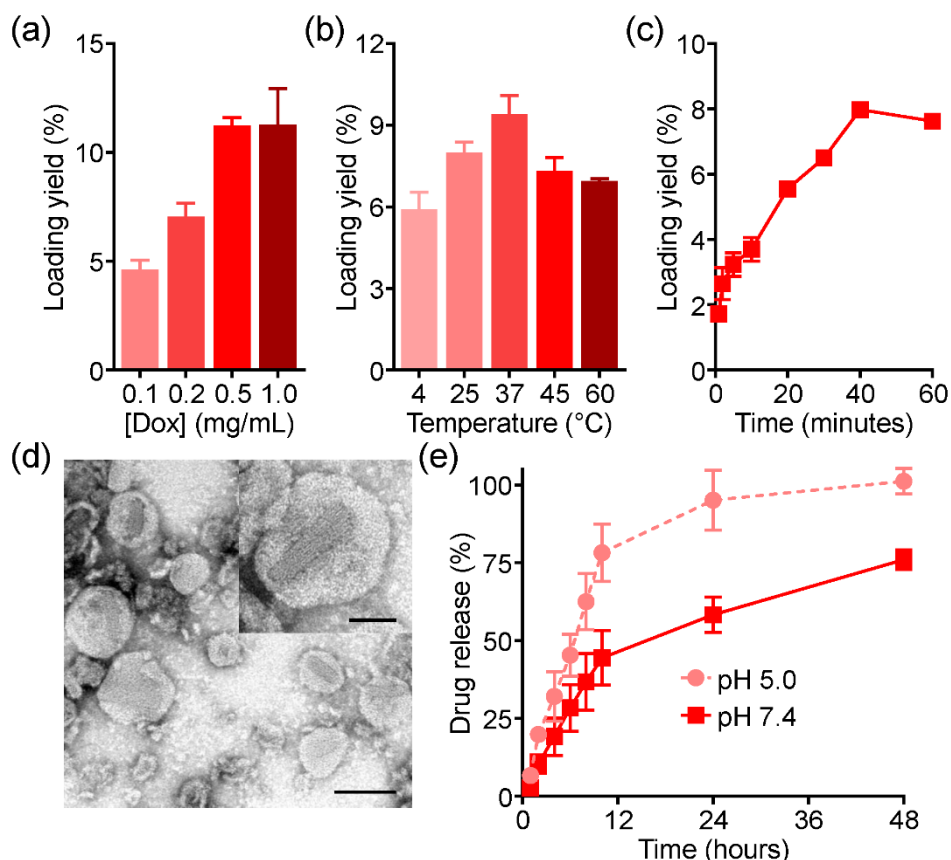


**Figure 3.4.4.** Dox loading into RBC vesicles. a) Loading yield at different drug inputs ( $n = 3$ ; mean  $\pm$  SD). b) Loading yield at different temperatures ( $n = 3$ ; mean  $\pm$  SD). c) Loading yield over time ( $n = 3$ ; mean  $\pm$  SD). d) Transmission electron microscopy images of Dox-RBC after negative staining with uranyl acetate (scale bar = 100 nm). Inset depicts a single Dox-RBC particle (scale bar = 50 nm). e) Release of Dox over time at pH 5.0 or pH 7.4 ( $n = 3$ ; mean  $\pm$  SD).

a physiological value of 7.4 down to 5.0 facilitated drug release, likely due to the instability of RBC membrane under acidic conditions.

The potency of Dox-RBC was next evaluated *in vitro*. When incubated with murine 4T1 breast cancer cells for 24 hours, the nanoformulation showed better efficacy compared to free Dox (Figure 4a). This increased potency may be explained by the fact that nanoparticulate delivery more effectively enables cellular uptake via endocytic pathways,<sup>(3)</sup> the result of which was confirmed by flow cytometric analysis (Figure 4b,c). When visualized by fluorescence microscopy, it was further revealed that Dox-RBC facilitated retention of the drug across the entirety of the cell, whereas the free drug was only found in the nucleus (Figure 4d). This ability

to facilitate uptake and enhance intracellular retention is a unique advantage of nanodelivery and could help to overcome drug-resistance by lessening drug efflux.(4)

Therapeutic efficacy was evaluated using an orthotopic 4T1 breast cancer model. Tumors were implanted in the mammary fat pads of female BALB/c mice. Once palpable, treatment was initiated using either Dox-RBC or free Dox. Over the course of the treatment, the nanoformulation had a marked effect, significantly slowing tumor growth compared to the free drug (Figure 4e). Median survival was also extended from 24 days for the untreated control group to 36 days for the

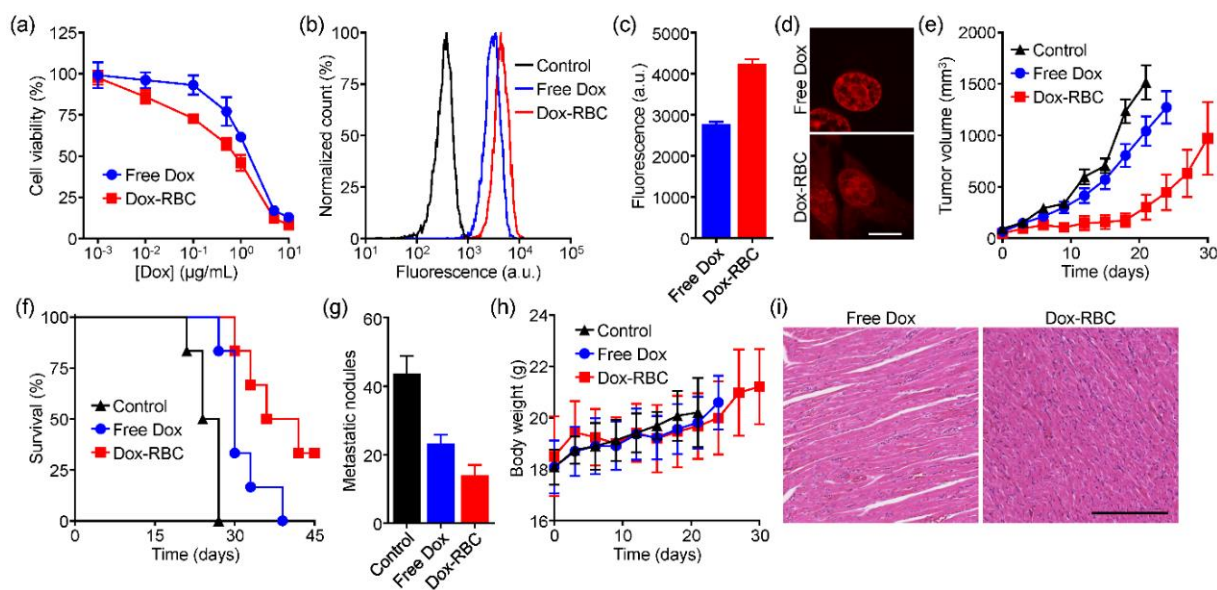


**Figure 3.4.5.** Antitumor activity of Dox-RBC. a) Viability of 4T1 breast cancer cells after incubation free Dox or Dox-RBC for 24 hours ( $n = 4$ ; mean  $\pm$  SD). b) Representative flow cytometry histograms of control 4T1 cells or 4T1 cells incubated with free DOX or Dox-RBC. c) Mean fluorescence intensities from (b) ( $n = 3$ ; mean  $\pm$  SD). d) Confocal fluorescence imaging of cells incubated with either free DOX or Dox-RBC (red: Dox; scale bar = 10  $\mu$ m). e) Growth kinetics of 4T1 tumors that were implanted orthotopically into BALB/c mice and treated with either free Dox or Dox-RBC ( $n = 6$ ; mean  $\pm$  SEM). f) Survival of the mice in (e) over time ( $n = 6$ ). g) Enumeration of metastatic nodules present on the lungs after treatment ( $n = 3$ ; mean  $\pm$  SD). h) Body weight of treated tumor-bearing mice over time ( $n = 6$ ; mean  $\pm$  SD). i) Representative H&E-stained histological sections of cardiac tissue after treatment (scale bar = 250  $\mu$ m).

Dox-RBC group (Figure 4f). Notably, 33% of the mice receiving nanoparticles had complete regressions and remained tumor-free long-term. The Dox-RBC formulation was also better at preventing the formation of lung metastases, reducing the number of nodules after 21 days of



treatment (Figure 4g). With regards to safety, mice subject to a full course of Dox-RBC treatment did not experience any weight loss (Figure 4h). While also true of the free Dox group, it should be noted that their loss of body weight was likely counteracted by rapid tumor growth. The difference in safety could more readily be seen upon histopathological examination of the cardiac tissue (Figure 4i). Chronic myocardial toxicity with free Dox is a well-known occurrence in the clinic.<sup>(5)</sup> For this group, we observed that the myocardial fibers became thin and loose, with varying degrees of rupture. On the other hand, the hearts from mice treated with Dox-RBC did not show any significant alterations in the fiber architecture. In all, it was demonstrated that Dox-RBC could more effectively control tumor growth compared with free drug while also displaying evidence of increased safety.

Following the antitumor studies, we explored if the remote loading strategy could be generalized to additional payloads. For this purpose, the antibiotic vancomycin (Vanc), another amine-containing small molecule drug, was employed. At increasing input concentrations, a loading yield of up to approximately 40% could be achieved (Figure 5a). The higher yield compared with Dox may be explained by the higher molecular weight of Vanc. Like Dox loading, the optimal temperature was 37 °C (Figure 5b), whereas saturation took longer and occurred at 1 hour (Figure 5c). Drug release kinetics followed a similar trend, with an initial burst observed in the first several hours and lower pH accelerating the process (Figure 5d). The absolute rate of release was slower when compared with Dox, and it took approximately 48 hours for all the drug to release at pH 5.0.

After confirming Vanc loading, we sought to test the nanoformulation against MRSA. A Förster resonance energy transfer (FRET) study was performed to demonstrate the ability of the membrane vesicles to interact with the bacteria (Figure 6a). As increasing amounts of bacteria

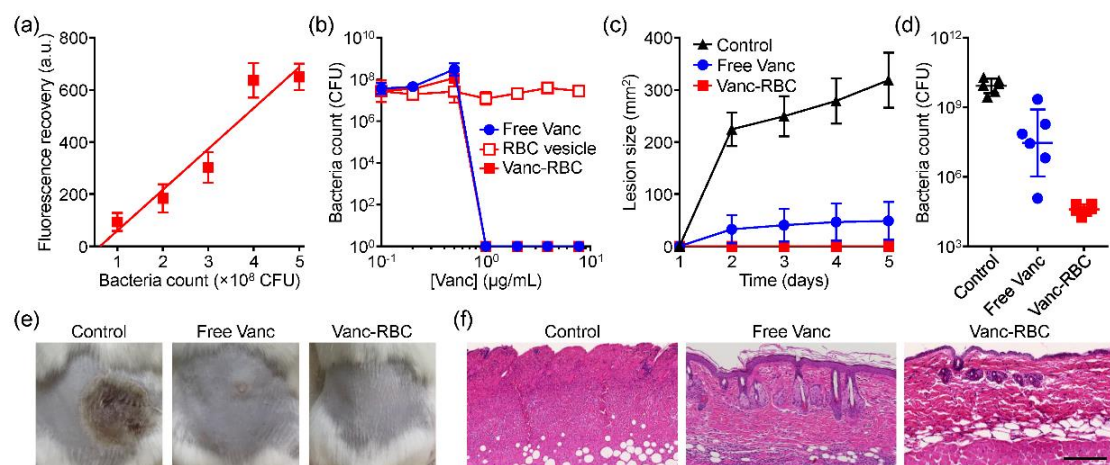


**Figure 3.4.6.** Antibacterial activity of Vanc-RBC. a) Fluorescence recovery of donor dye after incubation of FRET pair-doped RBC vesicles with MRSA ( $n = 6$ ; mean  $\pm$  SD; linear regression). b) Bacteria count after incubation with free Vanc, RBC vesicles, or Vanc-RBC ( $n = 3$ ; mean  $\pm$  SD). c) Lesion size on the skin of mice challenged with MRSA and treated with free Vanc or Vanc-RBC ( $n = 6$ ; mean  $\pm$  SEM). d) Enumeration of bacteria in the skin tissue on day 5 ( $n = 6$ ; geometric mean  $\pm$  SD). e) Representative macroscopic images of bacterial challenge site on day 5. f) Representative H&E-stained histological sections of skin from the challenge site on day 5 (scale bar = 200  $\mu\text{m}$ ).

were incubated with FRET pair-doped RBC vesicles, more of the donor signal was recovered, signaling that fusion was occurring. This effect could potentially be leveraged to facilitate delivery of loaded drugs to bacteria upon contact.(6) To confirm drug activity, Vanc-RBC or free Vanc was incubated at increasing concentrations with MRSA in culture, and viability was assessed after 24 hours (Figure 6b). The results confirmed that the remotely loaded drug still retained its activity, with a near identical profiles between the free drug and Vanc-RBC. No effect was observed from RBC vesicles alone, precluding the possibility of nanocarrier fusion influencing bacteria viability.

Therapeutic efficacy of the Vanc-RBC formulation was tested using a murine model of MRSA skin infection. Mice were challenged subcutaneously with a bolus dose of bacteria, followed by administration of either free Vanc or Vanc-RBC. Over the course of 5 days, the nanoformulation proved to be exceptionally potent, completely inhibiting the formation of skin lesions at the challenge site (Figure 6c,e). The free Vanc group experienced subtle lesion formation, which was much improved compared with the untreated controls. While the difference in physical effect between the treatment groups was slight, bacterial enumeration at the infection

sites revealed that Vanc-RBC outperformed the free drug by around 3 orders of magnitude (Figure 6d). Histological analysis showed that MRSA-induced lesions were marked by the loss of cilia and columnar morphology, characteristic of acanthosis and apoptosis (Figure 6f). These symptoms were decreased with free Vanc, although hyperkeratosis with aberrant hair shafts could still be observed. Samples from the Vanc-RBC group appeared normal. Ultimately, the enhanced performance of the nanoformulation could likely be attributed to its retention at the treatment site, preventing the Vanc from diffusing away.

### **3.4.3 Experimental Section**

#### **Preparation of cholesterol-enriched red blood cell (RBC) vesicles.**

Human RBCs were derived from whole blood (BioreclamationIVT). Erythrocyte membrane ghosts were obtained by hypotonic lysing. To produce cholesterol-enriched RBC vesicles, cholesterol (Avanti Polar Lipids) dissolved at 50 mg/mL in chloroform was added at varying inputs to RBC ghosts suspended in 300 mM ammonium sulfate (Sigma Aldrich), followed by gentle mixing at 37 °C for 10 minutes. To form vesicles, the suspensions were either sonicated for 6 minutes in a Fisher Scientific FS30D bath sonicator, or they were extruded sequentially through 1- $\mu$ m, 400-nm, and 200-nm pore size polycarbonate membranes (Whatman) using an Avanti Polar Lipids mini extruder. The ammonium sulfate gradient was obtained by transferring the resulting vesicles into phosphate buffered saline (PBS) using a column packed with Sephadex G-75, fine (GE Healthcare). Hydrodynamic size was measured by dynamic light scattering using a Malvern ZEN 3600 Zetasizer. Unless specified, further experiments were performed with RBC vesicles inputted with 5% cholesterol.

#### **Examination of membrane sidedness by dot blotting.**

To prepare standards in which both the intracellular and extracellular portions of CD47 could be accessed, RBC ghosts were serially diluted and prepared in a 4× detergent solution made with 37% glycerol (Fisher Chemical), 55% 1 M Tris-HCl pH 8 (Mediatech), and 8% Triton X-100 (EMD Millipore). RBC vesicles prepared in either water, ammonium sulfate, or prepared in ammonium sulfate and transferred to PBS were used natively without denaturation to keep the vesicle structure intact. Using 5 µL drops, standards were blotted twice and samples were blotted three times onto nitrocellulose membrane (Pierce). After air-drying the membrane in a fume hood the membrane was blocked with 5% bovine serum albumin (BSA; Sigma Aldrich) prepared in PBS with 0.05% Tween-20 (National Diagnostics) for 1 hour. Blots were then probed using anti-CD47 (extracellular domain) (ARP63284; Aviva Systems Biology) or anti-CD47 (intracellular domain) (EPR4150(2); GeneTex) followed by the corresponding HRP- conjugated secondary antibody (Biolegend). The membrane was then incubated with ECL western blotting substrate (Pierce) and developed using an ImageWorks Mini-Medical/90 Developer. ImageJ software was used to quantify the signal from each individual spot.

#### **Stabilizing effect of cholesterol on RBC vesicles.**

To evaluate the ability of RBC vesicles to compartmentalize the inner aqueous chamber, RBC vesicles, either unmodified or enriched with 5% cholesterol input, were loaded with calcein dye (Sigma Aldrich) at 5 µg/mL and purified. Dye that remained loaded self-quenched, and release of the dye was evaluated by measuring the fluorescence (excitation 495 nm, emission 515 nm) using a BioTek Synergy Mx microplate reader. To investigate the effect of cholesterol on the ability of RBC vesicles to maintain an ammonium sulfate gradient, LysoSensor Green DND-189 (Invitrogen) at 1 nM was loaded along with ammonium sulfate into RBC vesicles made using

varying concentrations of cholesterol. After purification, the emission spectrum of the dye, using an excitation wavelength of 445 nm, was measured using a microplate reader. To visualize the pH gradient, LysoSensor-loaded RBC vesicles, either without cholesterol or with 5% cholesterol input, were fabricated with 2% 1,1'-dioctadecyl-3,3,3',3'- tetramethylindodicarbocyanine (DiD; Invitrogen) to label the membrane. The samples were immobilized on glass slides with Tissue-Tek OCT compound (Sakura Finetek). Visualization was performed using an Olympus FV1000 confocal laser scanning microscope.

### **Optimization and characterization of remote-loaded RBC vesicles.**

RBC vesicles with a 5% cholesterol input and with an ammonium sulfate gradient were prepared as described above. Subsequently, doxorubicin-HCl (Dox; Biotang) or vancomycin-HCl (Vanc; Sigma Aldrich) was added to the RBC vesicle dispersion. The non-encapsulated free drug was separated by passing the solution through a Sephadex G-75 column. The drug loaded RBC vesicles were quantified by detecting the absorbance of Dox at 480 nm or the Vanc at 230 nm using a microplate reader after disruption of the RBC vesicles with acetonitrile and removal of precipitated proteins by centrifugation. The loading yield was calculated as the mass of the loaded drug divided by the protein mass of the RBC membrane vesicles. To optimize drug loading, the effect of initial drug concentration, temperature, and incubation time on drug loading yield were studied evaluated. The morphology of drug-loaded formulations was visualized by negatively staining the samples with 1% uranyl acetate (Electron Microscopy Sciences) and observing using a Zeiss Libra 120 PLUS EF-TEM transmission electron microscope. Drug release from the RBC vesicles was evaluated by loading 500  $\mu$ L of either Dox-loaded RBC vesicles (Dox-RBC) or Vanc-loaded RBC vesicles (Vanc-RBC) into 100,000 molecular weight cut-off Slide-A-Lyzer MINI

dialysis units (Thermo Scientific), followed by immersion into PBS at pH 5.0 or pH 7.4. Samples were agitated at 100 rpm in a shaking incubator at a temperature of 37 °C. At predetermined time intervals, samples were withdrawn from the outer media and an equal volume of fresh PBS was immediately replenished. The amount of drug released was determined by absorbance measurements using a microplate reader.

### **Antitumor activity and safety of Dox-RBC.**

All antitumor experiments were performed using mouse RBCs, which were purified from whole blood collected via submandibular puncture of female BALB/c mice (Envigo) using sodium heparin (Sigma Aldrich) as the anticoagulant. All animal experiments were performed in accordance with NIH guidelines and approved by the Institutional Animal Care and Use Committee (IACUC) of the University of California, San Diego. Mouse 4T1 breast cancer cells (CRL-2539; American Type Culture Collection) were maintained in RPMI 1640 media (Gibco) supplemented with 10% fetal bovine serum (Hyclone) and penicillin-streptomycin (Gibco). For the *in vitro* cytotoxicity study, 4T1 cells were seeded in a 96-well plate at a density of 5,000 cells per well and cultured overnight. Free Dox and Dox-RBC at varying drug concentrations were incubated with the cells for 24 hours at 37 °C, after which an MTS cell proliferation kit (Promega) was used to assess cell viability according to the manufacturer's instructions. To study cellular uptake, 4T1 cells were seeded on a 12-well plate at a density of  $1 \times 10^5$  cells per well and incubated with the Dox formulations at a final drug concentration of 3 µg/mL for 1 hour. After incubation, the culture media was removed and cells were detached, washed, and fixed with 10% formalin (Fisher Scientific) for data collection using a BD Biosciences FACSCanto-II flow cytometer. Analysis was performed using Flowjo software. For imaging, the same cells were cultured on a

glass coverslip followed by incubation with the different samples for 30 minutes. After washing and fixation, the samples were mounted in 50% glycerol in PBS and imaging was performed on an Olympus FV1000 confocal laser scanning microscope.

For the *in vivo* antitumor efficacy study,  $2 \times 10^5$  4T1 cells were implanted into the mammary fat pads of 6-week-old female BALB/c mice. The tumors were allowed to grow to a size of approximately 50 mm<sup>3</sup>. The mice were then randomly divided into 3 different experimental groups. Dox-RBC, free Dox, or PBS was administered intravenously via the tail every 3 days at a drug dosage of 3 mg/kg for 7 times. Tumor size (volume = (length  $\times$  width<sup>2</sup>)/2) and weight were recorded over time. Survival was defined as either natural death or tumor size > 2000 mm<sup>3</sup>. To evaluate the effect on metastasis and assess safety,  $5 \times 10^5$  4T1 cells were implanted, and the same treatment schedule as above was followed. At day 21 after start of treatment, the mice were euthanized and their lungs and hearts excised for further evaluation. The numbers of metastatic nodules in lungs were visually enumerated, while the heart tissues were sectioned for histological analysis and stained with hematoxylin and eosin (H&E; Leica Biosystems). Images were acquired using a Hamamatsu Nanozoomer 2.0-HT slide scanning system.

**Antimicrobial efficacy of Vanc-RBC** Methicillin-resistant *Staphylococcus aureus* (MRSA) strain USA300 (BAA-1717; American Type Culture Collection) was cultured on tryptic soy broth (TSB; Sigma Aldrich) agar overnight at 37 °C. Then a single colony was inoculated in TSB medium and the medium was cultured in a rotary shaker at 37 °C. Overnight culture was refreshed in TSB medium at a 1:100 dilution under shaking for another 3 hours until the OD600 of the culture medium reached approximately 1.0, corresponding to the logarithmic growth phase. The bacteria were then harvested by centrifugation at 5000  $\times$ g for 5 minutes and washed with sterile

PBS twice. To assess the fusion between cholesterol-enriched RBC vesicles and MRSA, a Förster resonance energy transfer (FRET) study was performed. Both a fluorescent donor *N*-[6-[(7-nitro-2-1,3-benzoxadiazol-4-yl) amino]hexanoyl]-phytosphingosine (C6-NBD, excitation/emission = 460/534 nm; Avanti Polar Lipids) and a fluorescent acceptor 1,2-dimyristoyl-*sn*-glycero-3-phosphoethanolamine- *N*-(lissamine rhodamine B sulfonyl) (DMPE-RhB, excitation/emission = 560/583 nm; Avanti Polar Lipids) were incorporated into the RBC membrane by mixing the dyes dissolved in chloroform with cholesterol prior to the preparation of the RBC vesicles. The final ratios of C6-NBD and DMPE-RhB to RBC membrane protein were 0.08% and 0.8%, respectively. FRET pair-labeled RBC vesicles at 1 mg/mL were then incubated with MRSA at concentrations of  $1 \times 10^8$ ,  $2 \times 10^8$ ,  $3 \times 10^8$ ,  $4 \times 10^8$ , and  $5 \times 10^8$  CFU/mL. After 30 minutes of incubation at 37 °C, unbound nanoparticles were removed by centrifugation at 5000  $\times$ g. The bacterial suspensions were excited at 470 nm and the fluorescence emission spectrum of each sample was recorded using a microplate reader. Fluorescence recovery of the donor (C6-NBD) at the lower emission peak (534 nm) was used to indicate increasing amounts of fusion.

For the *in vitro* antimicrobial efficacy study, 100  $\mu$ L MRSA USA300 suspensions at  $5 \times 10^6$  CFU/mL ( $OD_{600} = 0.05$ ) were added to 1 mL of Vanc-RBC or free Vanc at various concentrations. Empty RBC vesicles in PBS were used as a negative control. The mixtures were incubated at 37 °C for 24 hours under shaking. Following incubation, the mixtures were diluted from  $10^6$  to  $10^7$  times with sterile PBS, and 5  $\mu$ L of each solution was spotted onto TSB agar plates. After 24 hours of incubation at 37°C, the colonies were enumerated.

To evaluate *in vivo* efficacy, a murine subcutaneous infection model was employed. Prior to the study, the backs of male 6-week-old ICR mice (Envigo) were carefully shaved. Then  $3 \times 10^7$  CFU of MRSA USA300 suspended in 50  $\mu$ L of PBS was injected subcutaneously. For the



treatment groups, 200  $\mu$ L of Vanc-RBC or free Vanc in PBS, each containing 200  $\mu$ g of drug, were injected subcutaneously into the infected area. For the negative control group, 200  $\mu$ L of PBS was injected. The lesion of each mouse was carefully monitored over the course of 5 days, and lesion size was measured from photographs using ImageJ software. On day 5, the mice were euthanized and the infected skin regions were collected. The tissues were homogenized using a Biospec Mini Beadbeater in 1 mL of PBS for 3 minutes. The homogenate was then serially diluted from 10 to  $10^3$  times with sterile PBS and plated onto agar plates with a spotting volume of 50  $\mu$ L. After 24 hours of culture, bacterial colonies were enumerated to determine the bacterial load in each organ. For histological analysis, skin samples from each group were fixed in 10% formalin and stained with H&E. The sections were visualized by a Hamamatsu Nanozoomer 2.0-HT slide scanning system.

#### **3.4.4 Conclusion**

In conclusion, we have demonstrated a method of remote loading drugs into naturally derived RBC vesicles. The process is greatly facilitated by supplementing the cell membrane with additional cholesterol, which facilitates the maintenance of a pH gradient. This concept was demonstrated using two small molecule model drugs, a chemotherapeutic drug and an antibiotic drug. In both cases, the nanoformulations were able to outperform the corresponding drugs in the free form using appropriate animal disease models. By employing a naturally derived nanocarrier, it is possible to leverage the benefits of nanoparticulate delivery, such as improved localization to diseased tissue, with fewer concerns regarding safety and immunogenicity. The work presented here can help to provide guiding principles for the development of next-generation, remote-loaded drug platforms.

## **Acknowledgements**

This work is supported by the National Institutes of Health under Award Number R01CA200574. X. Z. was supported by the China Scholarship Council (No. 201604910276).

Chapter 3.4 is, in full, is a reprint of the material as it appears in *Angewandte Chemie International Edition*, 2018, Zhang, X.; Angsantikul, P.; Ying, M.; Zhuang, J.; Zhang, Q.; Wei, X.; Jiang, Y.; Zhang, Y.; Dehaini, D.; Chen, M.; Chen, Y.; Gao, W.; Fang, R.; Zhang, L. The dissertation author was a major contributor and co-author of this paper.

## References:

1. A.Z. Wang, R. Langer, O.C. Farokhzad, Nanoparticle delivery of cancer drugs, *Annu. Rev. Med.*, 63 (2012) 185-198.
2. O.C. Farokhzad, R. Langer, Impact of nanotechnology on drug delivery, *ACS Nano*, 3 (2009) 16-20.
3. L. Zhang, F.X. Gu, J.M. Chan, A.Z. Wang, R.S. Langer, O.C. Farokhzad, Nanoparticles in medicine: therapeutic applications and developments, *Clin. Pharmacol. Ther.*, 83 (2008) 761-769.
4. A.C. Anselmo, S. Mitragotri, A Review of Clinical Translation of Inorganic Nanoparticles, *AAPS J.*, 17 (2015) 1041-1054.
5. J.W. Yoo, D.J. Irvine, D.E. Discher, S. Mitragotri, Bio-inspired, bioengineered and biomimetic drug delivery carriers, *Nat. Rev. Drug Discov.*, 10 (2011) 521-535.
6. R.H. Fang, Y. Jiang, J.C. Fang, L. Zhang, Cell membrane-derived nanomaterials for biomedical applications, *Biomaterials*, 128 (2017) 69-83.
7. C.M. Hu, L. Zhang, S. Aryal, C. Cheung, R.H. Fang, L. Zhang, Erythrocyte membrane-camouflaged polymeric nanoparticles as a biomimetic delivery platform, *Proc. Natl. Acad. Sci. U.S.A.*, 108 (2011) 10980-10985.
8. C.M. Hu, R.H. Fang, K.C. Wang, B.T. Luk, S. Thamphiwatana, D. Dehaini, P. Nguyen, P. Angsantikul, C.H. Wen, A.V. Kroll, C. Carpenter, M. Ramesh, V. Qu, S.H. Patel, J. Zhu, W. Shi, F.M. Hofman, T.C. Chen, W. Gao, K. Zhang, S. Chien, L. Zhang, Nanoparticle biointerfacing by platelet membrane cloaking, *Nature*, 526 (2015) 118-121.
9. R.H. Fang, C.M. Hu, B.T. Luk, W. Gao, J.A. Copp, Y. Tai, D.E. O'Connor, L. Zhang, Cancer cell membrane-coated nanoparticles for anticancer vaccination and drug delivery, *Nano Lett.*, 14 (2014) 2181-2188.
10. B.T. Luk, R.H. Fang, C.M. Hu, J.A. Copp, S. Thamphiwatana, D. Dehaini, W. Gao, K. Zhang, S. Li, L. Zhang, Safe and Immunocompatible Nanocarriers Cloaked in RBC Membranes for Drug Delivery to Treat Solid Tumors, *Theranostics*, 6 (2016) 1004-1011.
11. C.M. Hu, R.H. Fang, B.T. Luk, L. Zhang, Nanoparticle-detained toxins for safe and effective vaccination, *Nat. Nanotechnol.*, 8 (2013) 933-938.
12. C.M. Hu, R.H. Fang, J. Copp, B.T. Luk, L. Zhang, A biomimetic nanosponge that absorbs pore-forming toxins, *Nat. Nanotechnol.*, 8 (2013) 336-340.
13. A. Fritze, F. Hens, A. Kimpfler, R. Schubert, R. Peschka-Suss, Remote loading of doxorubicin into liposomes driven by a transmembrane phosphate gradient, *Biochim. Biophys. Acta*, 1758 (2006) 1633-1640.

14. G. Haran, R. Cohen, L.K. Bar, Y. Barenholz, Transmembrane ammonium sulfate gradients in liposomes produce efficient and stable entrapment of amphipathic weak bases, *Biochim. Biophys. Acta*, 1151 (1993) 201-215.
15. C.M. Hu, R.H. Fang, B.T. Luk, K.N. Chen, C. Carpenter, W. Gao, K. Zhang, L. Zhang, 'Marker-of-self' functionalization of nanoscale particles through a top-down cellular membrane coating approach, *Nanoscale*, 5 (2013) 2664-2668.
16. J.A. Kant, T.L. Steck, Cation-impermeable inside-out and right-side-out vesicles from human erythrocyte membranes, *Nat. New Biol.*, 240 (1972) 26-28.
17. Y. Barenholz, Doxil(R)--the first FDA-approved nano-drug: lessons learned, *J. Control. Release*, 160 (2012) 117-134.
18. T.G. Iversen, T. Skotland, K. Sandvig, Endocytosis and intracellular transport of nanoparticles: Present knowledge and need for future studies, *Nano Today*, 6 (2011) 176-185.
19. X. Zeng, R. Morgenstern, A.M. Nystrom, Nanoparticle-directed sub-cellular localization of doxorubicin and the sensitization breast cancer cells by circumventing GST-mediated drug resistance, *Biomaterials*, 35 (2014) 1227-1239.
20. K. Chatterjee, J.Q. Zhang, N. Honbo, J.S. Karliner, Doxorubicin Cardiomyopathy, *Cardiology*, 115 (2010) 155-162.
21. D. Pornpattananangkul, S. Olson, S. Aryal, M. Sartor, C.M. Huang, K. Vecchio, L. Zhang, Stimuli-responsive liposome fusion mediated by gold nanoparticles, *ACS Nano*, 4 (2010) 1935-1942.

## **3.5 Nanoparticle-Based Anti-Virulence Vaccine for the Management of Methicillin-Resistant *Staphylococcus aureus* Skin Infection**

### **3.5.1 Introduction**

The continued rise of antibiotic-resistant bacteria has become a significant burden on global health and is responsible for an increased rate of life-threatening infections observed in the clinic.<sup>[1]</sup> The issue continues to rise to the forefront as the development of new antibiotics has slowed to a near halt,<sup>[2]</sup> prompting physicians and scientists to explore alternative strategies to control bacterial infections.<sup>[3]</sup> Among the different approaches, anti-virulence vaccination is a compelling strategy as it promotes host immunity by training the body to detect and disarm specific mechanisms employed by pathogens during host invasion.<sup>[4]</sup> This approach has been shown to inhibit the ability of pathogens to colonize within a host and is less susceptible to the development of resistance as it does not exert direct selective pressure on individual bacterium.<sup>[5]</sup> Anti-virulence vaccination is most commonly accomplished through the use of toxoids, or inactivated forms of live bacterial toxins, which include the commonly used tetanus toxoid<sup>[6]</sup> and diphtheria toxoid.<sup>[7]</sup> Conventionally, these toxoids are prepared by denaturation via either chemical or heat treatment in order to eliminate the dangerous effects of the original toxin.<sup>[8]</sup> However, such inactivation methods are often disruptive and can lead to altered antigen presentation as well as compromised immunogenicity.<sup>[9]</sup> To overcome the tradeoff between safety and efficacy, emerging techniques are being developed to produce vaccine candidates that faithfully present antigenic epitopes for immune processing.<sup>[10]</sup>

Methicillin-resistant *Staphylococcus aureus* (MRSA) is an antibiotic-resistant pathogen that represents a significant threat to public health, especially in hospital environments where

many patients have weakened immune systems that are incapable of naturally fending off infection.<sup>[11]</sup> It can cause severe skin lesions and can ultimately be life-threatening upon systemic invasion.<sup>[12]</sup> The pace of resistance exhibited by MRSA has severely limited treatment options, with many strains of the bacteria being unresponsive to all of the most commonly used antibiotics.<sup>[13, 14]</sup> This has led researchers to explore other forms of treatment, including the aforementioned anti-virulence therapy. Known to secrete many different types of exotoxins, MRSA represents a good target for such therapies. One of its major virulence factors is  $\alpha$ -hemolysin (Hla),<sup>[15]</sup> a toxin that forms heptameric pores on cell surfaces, which contributes greatly to the pathogenesis of MRSA during the process of infection.<sup>[16]</sup> In fact, it has been shown that the virulence of the pathogen correlates strongly with the level of Hla production.<sup>[17, 18]</sup> Further, immunization with a mutant form of Hla has been shown to confer protection against *Staphylococcus aureus* (*S. aureus*) pneumonia in mice.<sup>[19]</sup> Passive immunization with anti-Hla antibodies also protected against skin lesions caused by subsequent *S. aureus* infection, further attesting to the utility of such a strategy for combating the pathogen.

The application of novel nanomaterials towards vaccine design has the potential to bring about significant improvements via efficient and finely controlled immune manipulation.<sup>[20-23]</sup> We have previously demonstrated a nanoparticle-mediated toxin detainment strategy for the preparation of a safe and potent toxoid formulation. Biomimetic nanoparticles are fabricated with a cell membrane-derived coating that presents a natural substrate for pore-forming toxins,<sup>[24, 25]</sup> leading to their stable entrapment onto the nanoparticles and enabling safe delivery *in vivo* for immune processing.<sup>[26]</sup> Owing to the non-disruptive approach of this detainment strategy, the platform was demonstrated to be superior to a traditionally formed toxoid by generating higher anti-Hla titers with increased avidity. Further, vaccination with the detained toxin conferred a

significant survival benefit in a murine model of lethal toxin challenge. In the present work, we investigated the protective capabilities of nanoparticle-detained staphylococcal Hla, denoted nanotoxoid(Hla), against live bacterial challenge using a mouse model of MRSA skin infection (**Figure 1**). The immune potentiating effect of the nanoparticle formulation was studied more in-depth by looking at the formation of germinal centers in the draining lymph nodes of vaccinated mice, which was then correlated to anti-Hla titer production. The ability of the nanotoxoid(Hla) vaccine to protect against MRSA infection and lessen bacterial colonization was evaluated in a mouse model of skin lesion formation. Beyond local infection, the effect of the nanoparticle vaccination on bacterial invasiveness was further studied by enumerating the bacterial load in major organs.

### **3.5.2 Results and Discussion**

#### **Nanotoxoid(Hla) Synthesis and Characterization**

Nanoparticles coated with red blood cell (RBC) membrane were prepared using a previously described protocol.<sup>[27]</sup> Briefly, mouse RBCs were subjected to hypotonic treatment to obtain purified RBC membrane ghosts, which were then fused onto the surface of preformed nanoparticle cores made using poly(lactic-*co*-glycolic acid) (PLGA) through a sonication method. As the RBC membrane coating serves as a natural substrate for the pore-forming Hla, nanotoxoid(Hla) complexes were formed by incubating free Hla with unloaded nanoparticles, herein denoted nanotoxoid(-). Free Hla was subsequently removed from the nanotoxoid(Hla) complexes by size exclusion chromatography to obtain a purified formulation. Physicochemical characterization showed that the resulting nanotoxoid(Hla) was about 115 nm in diameter and had a surface zeta potential of -32 mV (**Figure 2a,b**), both of which were similar to those of the

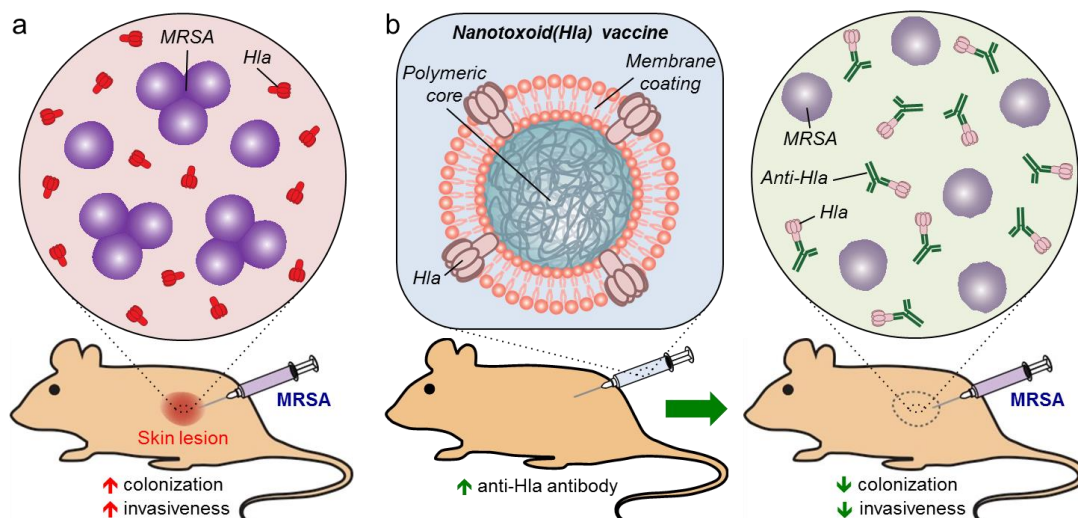


**Figure 3.5.1.** Schematic of nanotoxoid(Hla) protection against MRSA infection. (a) Under normal conditions, MRSA bacteria employ Hla to help them colonize the site of challenge, resulting in significant skin lesion formation and systemic invasiveness. (b) After vaccination with the nanotoxoid(Hla) formulation, anti-Hla titers are induced. These antibodies neutralize the toxin produced by the MRSA bacteria at the site of challenge, reducing the ability of the pathogen to colonize and enter into systemic circulation.

unloaded nanotoxoid(-), suggesting that toxin insertion did not have a major impact on overall nanoparticle properties. This was further confirmed via transmission electron microscopy (TEM) of negatively stained nanotoxoid(Hla), which revealed that the characteristic core-shell structure of the RBC membrane-coated nanoparticle was preserved even after toxin loading, consistent with what has been previously observed<sup>[24, 26]</sup> (Figure 2c).

To confirm successful detainment of Hla by the RBC membrane-coated nanoparticles, different immunoassays were performed. On TEM image, Hla-specific antibody labeling of nanotoxoid(Hla) followed by secondary labeling using an immunogold conjugate showed significant colocalization of the electron-dense gold signal with regions of intermediate density occupied by the nanoparticles, indicating a significant presence of Hla-specific epitopes on the nanotoxoid(Hla) (Figure 2d). Conversely, nanotoxoid(-) sample subjected to the exact same staining procedure was absent of any gold signal, confirming that the positive signal seen in the nanotoxoid(Hla) was not due to non-specific antibody staining. Dot blot analysis was used to further confirm the presence of Hla on nanotoxoid(Hla) samples (Figure 2e). Using anti-Hla as



the primary immunostain, nanotoxoid(HIa) gave a positive signal whereas nanotoxoid(-) did not give any discernable signal. As a positive control, free HIa at the initial input concentration used to prepare nanotoxoid(HIa) was tested in parallel, and image analysis of the blot intensities revealed that approximately 95% of the HIa was retained on the nanoparticles after purification, suggesting high affinity of the toxin for the membrane-coated nanoparticles. It has been shown previously that the strong sequestration of toxin by the nanoparticle detainment strategy resulted in little release over time, which effectively neutralized the activity of the toxin and enables safe delivery both *in vitro* and *in vivo*.<sup>[26]</sup>

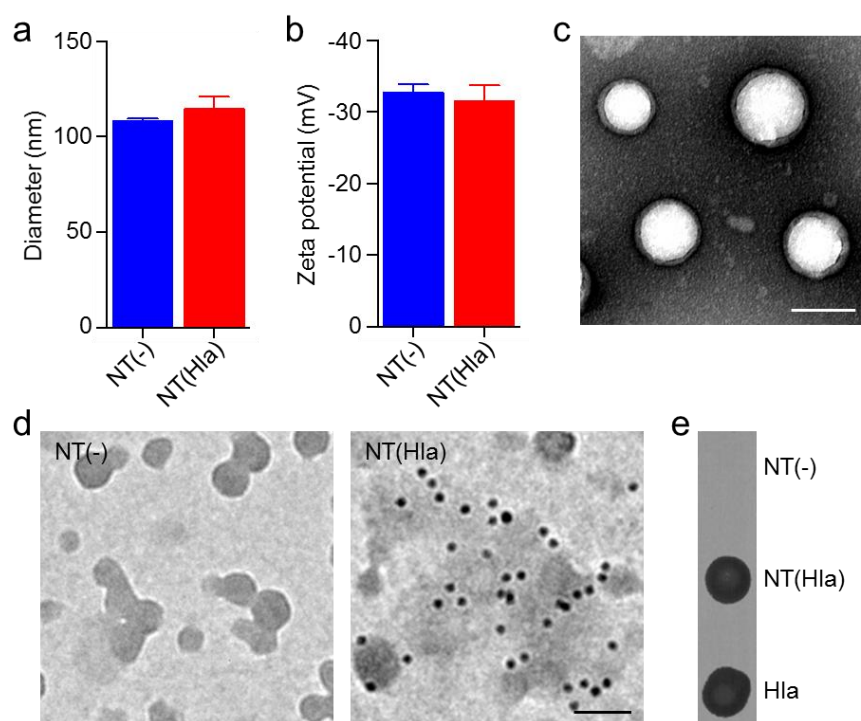


**Figure 3.5.2.** Nanotoxoid(HIa) characterization. (a) Size and (b) zeta potential of nanotoxoid(-) [denoted “NT(-)”] and nanotoxoid(HIa) [denoted “NT(HIa)”] (n=3). Error bars represent standard deviation. (c) TEM image of nanotoxoid(HIa) after negative staining with uranyl acetate. Scale bar = 100 nm. (d) TEM images of immunogold-stained NT(-) and NT(HIa) with anti-HIa as the primary immunostain and gold-labeled anti-IgG as the secondary stain. The gold (~10 nm) appears as dark punctates on the images. Scale bar = 100 nm. (e) Dot blotting results using anti-HIa as the primary immunostain. Quantification by image analysis revealed that 95.2% of the HIa input was retained on the final NT(HIa) formulation.

Next, the ability of the nanotoxoid(HIa) formulation to promote anti-HIa immune responses was studied. Of particular interest was the formation of germinal centers (GCs), which is a critical step in the potentiation of the humoral immune response against foreign antigens.<sup>[28, 29]</sup> It is in these regions that B cells mature, and it has been shown that improved retention of antigens via nanoparticle-mediated delivery can better facilitate GC formation.<sup>[30]</sup> We therefore sought to evaluate lymphatic B cell activation in mice immunized with the nanotoxoid(HIa) formulation. Immunostaining was employed to detect the presence of GCs in the draining lymph nodes (dLNs) of mice immunized subcutaneously with the nanoformulation. PBS and unloaded nanotoxoid(-) were administered as controls. Histological analysis of the dLNs from mice immunized with nanotoxoid(HIa) revealed GL-7<sup>+</sup> regions characteristic of GC nucleation (**Figure 3a**). In contrast, there was no visual evidence of GC formation in the PBS or nanotoxoid(-) immunization groups, confirming the non-immunogenicity of the naturally derived nanoparticle vector itself.<sup>[31]</sup> Flow cytometry results (Figure 3b) showed that 45.6% of B220<sup>+</sup>IgD<sup>low</sup> B cells in the dLNs of the nanotoxoid(HIa) group exhibited a GL-7<sup>+</sup> germinal center phenotype. In contrast, only 15.7% and 13.6% of cells in mice administered with PBS and nanotoxoid(-), respectively, exhibited the same phenotype.

The ability of nanotoxoid(HIa) to elicit a humoral immune response against HIa was further investigated. Mice were subcutaneously injected with nanotoxoid(HIa), nanotoxoid(-) or PBS on day 0 and were subsequently administered a booster on day 14. The serum of the mice in

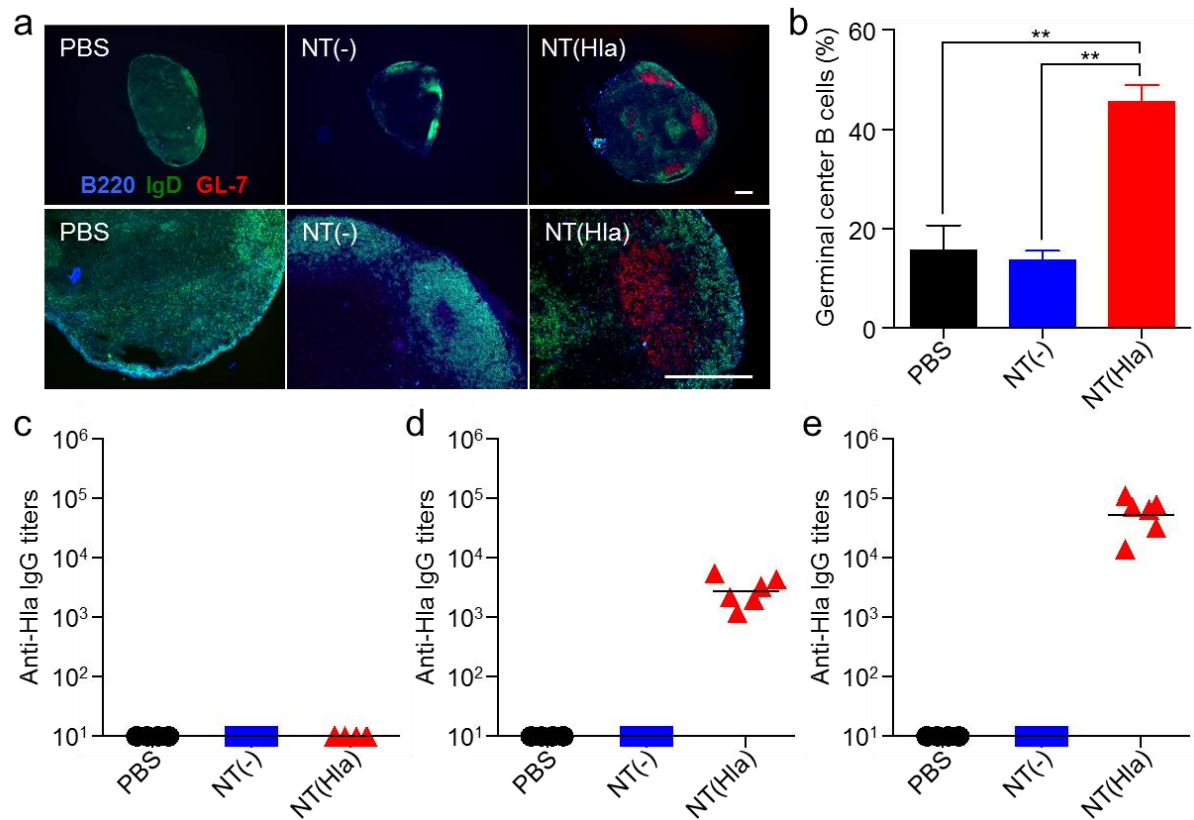


**Figure 3.5.3.** Germinal center formation and antibody production induced by nanotoxoid(HIa) vaccination. (a,b) Mice were vaccinated with PBS, nanotoxoid(-) [NT(-)], or nanotoxoid(HIa) [NT(HIa)] (n=3). The draining lymph nodes were collected 21 days later for the analysis of B220 (blue), IgD (green), and GL-7 (red) expression by either immunohistochemistry (a) or flow cytometry (b). Scale bars = 250  $\mu$ m. For flow cytometric analysis, cells were first gated on B220+IgDlow and the numbers reported are the percentage GL-7+ cells within that population. Error bars represent standard error. Statistical significance determined by one-way ANOVA (\*\*P < 0.01). (c-e) Mice were vaccinated with PBS, NT(-), or NT(HIa) on day 0 with a boost on day 14 (n=6). On days 0 (c), 14 (d), and 35 (e), serum was collected and the anti-HIa IgG titers were quantified by ELISA. Lines represent geometric means.

each group was sampled on days 0, 14 and 35 to assess Hla-specific IgG titers (Figure 3c-e). Nanotoxoid(Hla) vaccination elicited significant anti-Hla titers on day 14, and there was a further increase when assayed on day 35. In contrast, the nanotoxoid(-) and PBS vaccinations resulted in

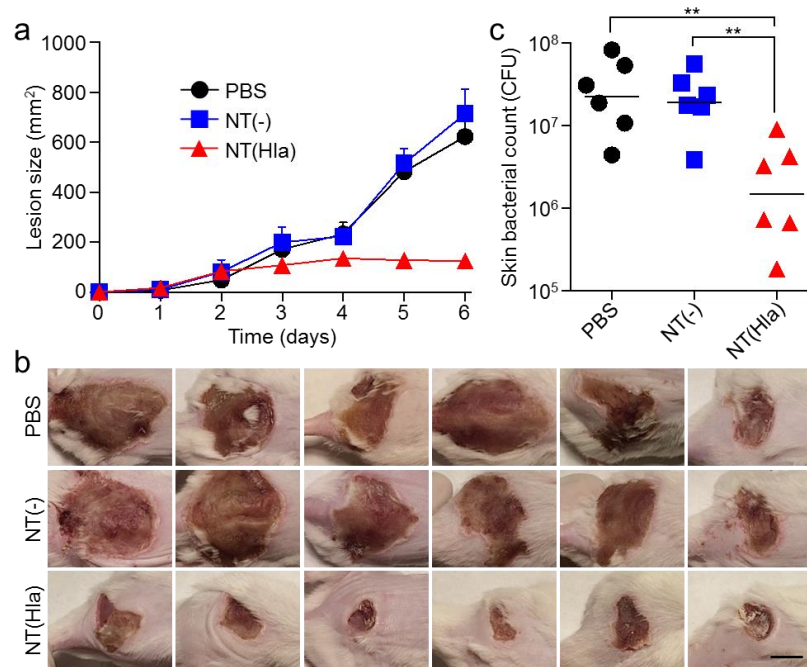


**Figure 3.5.4.** Effect of nanotoxoid (Hla) vaccination on MRSA skin colonization. Mice vaccinated with PBS, nanotoxoid(-) [NT(-)], or nanotoxoid(Hla) [NT(Hla)] on days 0 and 14 were challenged subcutaneously with  $1 \times 10^9$  CFU of MRSA bacteria on day 35. (a) The skin lesions were monitored over the course of 6 days ( $n=6$ ). Lesion size is reported as the product of the largest and smallest dimensions. Error bars represent standard error. (b) Images of skin lesions on day 6 post-infection. Scale bar = 1 cm. (c) On day 6 post-infection, the affected skin and underlying tissue were collected and the bacterial burden enumerated ( $n=6$ ). Lines represent geometric mean. Statistical significance determined by one-way ANOVA (\*\* $P < 0.01$ ).

no detectable anti-Hla titers over the course of the study. The nanotoxoid(Hla)-induced antibody responses have previously been shown to be durable, with little to no drop in titers over the course of a five-month period.<sup>[26]</sup> Taken together, the data demonstrates that the nanotoxoid(Hla) formulation can effectively elicit potent anti-Hla immune responses, despite complete deactivation of the toxin.<sup>[24]</sup> This is notable finding given that the formulation is absent of immunological adjuvants, which are commonly required for conventional toxoid formulations and help to boost germinal center antibody activity.<sup>[32]</sup>

### **Efficacy in a Mouse Model of MRSA Skin Infection**

To evaluate the protective capability of the nanotoxoid(HIa) vaccine against MRSA infection, we employed a mouse skin infection model. MRSA represents one of the most common causes of skin infections, both in the community and in hospitals.<sup>[12]</sup> Because the pathogen is hard to treat with common antibiotics, the infection can quickly progress and lead to serious complications, from physical disfigurement to permanent organ damage, and in many cases even death. For this experiment, mice were immunized with nanotoxoid(HIa) on day 0 and given a booster dose on day 14. Mice injected with nanotoxoid(-) or PBS were used as control groups. On day 35, the mice were subcutaneously challenged with live MRSA bacteria, and the efficacy in the different experimental groups was assessed over time by monitoring the dermonecrotic area resulting from bacterial burden. The progression of skin lesion development in mice immunized with nanotoxoid(HIa) was significantly attenuated compared with mice in the nanotoxoid(-) and PBS groups, which both experienced rapid lesion formation (**Figure 4a,b**). On day 6 post-infection, there was an approximately 5-fold reduction in dermonecrotic area on mice treated with the nanotoxoid(HIa) formulation compared to the control groups.

At the conclusion of the observation period, the bacterial burden was quantified in the infected skin region of each mouse (Figure 4c). For the nanotoxoid(-) and PBS groups, the bacterial burden of the infected skin tissue was  $1.7 \times 10^7$  and  $2.2 \times 10^7$  CFU, respectively. Mice immunized with nanotoxoid(HIa) showed an average burden of  $1.5 \times 10^6$  CFU, representing an 11.3- and 14.7-fold reduction compared with the nanotoxoid(-) and PBS groups, respectively. It has previously been shown that nanotoxoid(HIa) is capable of significantly inhibiting HIa-mediated skin damage in the subcutaneous space, suggesting that the titers generated by the formulation are sufficiently high to enable extravascular neutralizing activity.<sup>[26]</sup> This prevents the necrotic effect of high HIa concentrations,<sup>[33]</sup> thus preserving integrity of the local tissue. In

the present study, the nanoparticle vaccine formulation was likewise able to reduce skin lesion formation, demonstrating its ability to facilitate neutralization of Hla produced by the bacteria *in situ* upon subcutaneous challenge. Given the importance of Hla in MRSA pathogenesis, neutralization of the toxin also resulted in decreased bacterial burden, likely due to increased clearance by immune cells protected from the cytotoxic activity of Hla.<sup>[34]</sup> Despite the significant reduction in both lesion formation and bacterial load at the site of infection, the inability of the nanotoxoid(Hla) to completely mitigate disease suggests a sizable role played by other virulence factors, which can serve as targets for future nanotoxoid vaccine formulations.

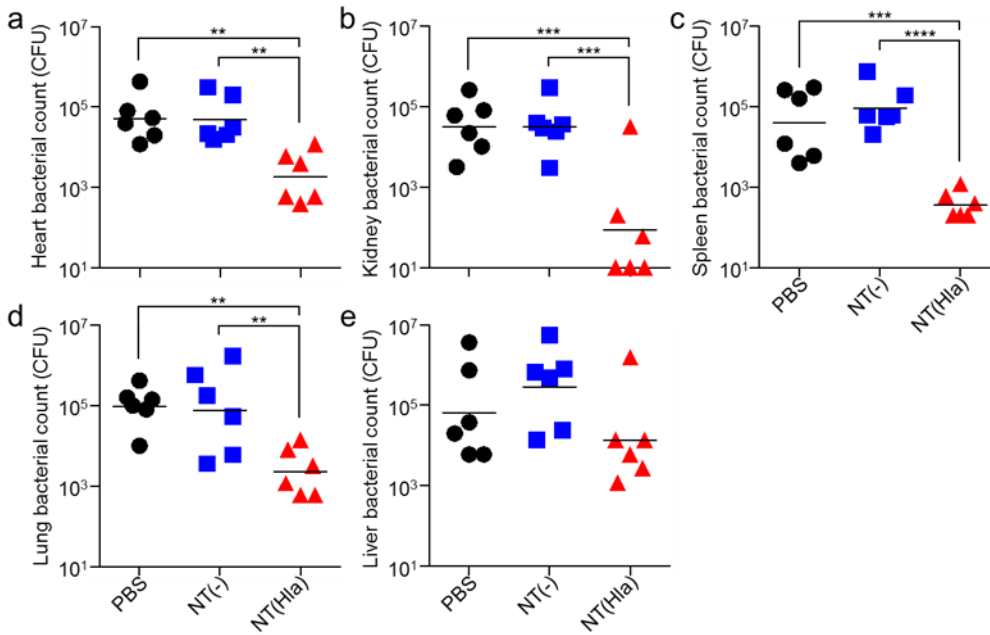


**Figure 3.5.5.** Effect of nanotoxoid(Hla) vaccination on MRSA invasiveness. Mice vaccinated with PBS, nanotoxoid(-) [NT(-)], or nanotoxoid(Hla) [NT(Hla)] on days 0 and 14 were challenged subcutaneously with  $1 \times 10^9$  CFU of MRSA bacteria on day 35. On day 6 post-infection, the major organs, including the heart (a), kidneys (b), spleen (c), lungs (d), and liver (e) were collected and the bacterial burden of each was enumerated (n=6). Lines represent geometric means. Statistical significance determined by one-way ANOVA (\*\* $P < 0.01$ , \*\*\* $P < 0.001$  and \*\*\*\* $P < 0.0001$ ).

## Prevention of Disseminative MRSA Infection

MRSA infections can quickly progress and enter systemic circulation, leading to a markedly worse prognosis in the clinic.<sup>[11]</sup> Patients with invasive MRSA can precipitously develop life-threatening infections in different organs such as the blood, heart, bones, and kidneys. As a MRSA skin infection runs the significant risk of further dissemination, the effect of nanotoxoid(Hla) vaccination on MRSA invasiveness after subcutaneous challenge was studied. Mice were vaccinated with nanotoxoid(Hla), nanotoxoid(-), or PBS on day 0 with a booster dose on day 14 and subcutaneously inoculated with MRSA on day 35. On day 6 post-infection, the bacterial counts in the heart, kidneys, spleen, lungs, and liver were analyzed (**Figure 5**). In most of the organs that were analyzed, the nanotoxoid(Hla) group showed a significant drop in bacterial burden compared to the nanotoxoid(-) and PBS control groups. Of note, the kidneys and spleen, two organs that traditionally experience heavy bacterial burden per unit weight,<sup>[35]</sup> both had reductions of approximately two orders of magnitude. The sharp decrease in organ penetration can likely be attributed primarily to better immune management at the site of infection, which results in improved integrity of the skin protective barrier and fewer bacteria entering the circulation system. Additionally, the presence of high amounts of neutralizing titers within the body can further hamper the capacity of invading MRSA bacteria to colonize individual organs, as shown by previous studies on the effect of anti-Hla vaccination in animal models of sepsis.<sup>[36]</sup> Overall, the results demonstrate that nanotoxoid(Hla) not only prevents superficial damage, but also decreases MRSA invasiveness, which can ultimately help to prevent many of the harsh complications associated with MRSA infections.

### **3.5.3 Materials and Methods**

***Preparation and characterization of nanotoxoid(Hla).*** Red blood cell (RBC) membrane-coated nanoparticles were prepared as previously described.<sup>[26]</sup> Polymeric cores were made using 0.67 dL/g carboxy-terminated 50:50 poly(lactic-*co*-glycolic acid) (PLGA; LACTEL Absorbable Polymers) with a modified nanoprecipitation method. The polymer was dissolved in acetone at a concentration of 10 mg mL<sup>-1</sup> and added rapidly to 2 mL of deionized water. The mixture was placed under vacuum for 3 h to evaporate the organic solvent. To obtain the membrane material, RBCs collected from 6-week old male CD-1 mice (Harlan Laboratories) were treated with hypotonic medium and washed multiple times by centrifugation. The final RBC membrane-coated nanoparticles, denoted nanotoxoid(-) were synthesized by sonicating a mixture of the PLGA cores and RBC membrane using a Fisher Scientific FS30D bath sonicator at a frequency of 42 kHz and a power of 100 W for 2 min. The membrane material from 1 mL of mouse blood was used to coat 5 mg of 100 nm PLGA cores. The nanotoxoid(Hla) was generated by incubating 0.2 mg of nanotoxoid(-) with 3 µg of Hla at 37 °C for 15 min. Nanoparticle concentrations for both the nanotoxoid(Hla) and nanotoxoid(-) formulations are expressed as milligrams of PLGA per 1 mL of solution (mg mL<sup>-1</sup>). The mixture was then filtered through a Sepharose CL-4B (Sigma Aldrich) column to obtain purified nanotoxoid(Hla) free of unbound toxin. The size and the zeta potential of the different nanoformulations were measured by dynamic light scattering (DLS) using a Malvern ZEN 3600 Zetasizer. The structure of the nanotoxoid(Hla) was examined using a Zeiss Libra 120 PLUS EF-TEM Transmission Electron Microscope. Samples were negatively stained with 0.1 wt% uranyl acetate prior to visualization.

***Nanotoxoid(Hla) loading analysis.*** An immunogold staining assay was carried out to confirm insertion of Hla onto the RBC membrane-coated nanoparticles. One drop of nanotoxoid(Hla) or nanotoxoid(-) solution was added onto a glow-discharged carbon coated 400-



mesh copper grid (Electron Microscopy Sciences). The grids were then washed before subjecting to blocking with 1 wt% bovine serum albumin (BSA), primary immunostaining with polyclonal rabbit anti-Hla antibody (Sigma Aldrich), and secondary staining with gold-labeled anti-rabbit IgG antibody (Sigma Aldrich). Images were obtained using a Zeiss Libra 120 PLUS EF-TEM Transmission Electron Microscope without negative staining. To analyze Hla retention by dot blot analysis, 1  $\mu\text{L}$  of nanotoxoid(Hla) solution at 2  $\text{mg mL}^{-1}$  was dropped onto a nitrocellulose membrane and allowed to fully dry under vacuum. Afterwards, the membrane was blocked with 1 wt% BSA solution and then probed with a polyclonal rabbit anti-Hla primary antibody (Sigma Aldrich) followed by a donkey anti-rabbit IgG-horseradish peroxidase (HRP) conjugate secondary antibody (Biolegend). The blot was developed with ECL western blotting substrate (Pierce) using a Mini-Medical/90 Developer (ImageWorks). Nanotoxoid(-) solution at 2  $\text{mg mL}^{-1}$  was used as negative control and Hla solution corresponding to 100% loading (30  $\mu\text{g mL}^{-1}$ ) was used as positive control. Blot intensity was measured by analyzing the mean gray values of dots via Image J software.

***Germinal center analysis.*** All animal experiments followed protocols that were reviewed, approved and performed under the regulatory supervision of the University of California, San Diego's institutional biosafety program and the Institutional Animal Care and Use Committee (IACUC). Six-week old male CD-1 mice (Harlan Laboratories) were immunized subcutaneously in the lateral tarsal region just above the ankle with 0.1 mg of nanotoxoid(Hla). Nanotoxoid(-) and PBS were used as negative controls. On day 21 post-immunization, the mice were euthanized and the draining popliteal lymph nodes were collected for analysis. For immunohistochemical analysis, the lymph nodes were cryosectioned and stained with anti-mouse/human B220-Pacific Blue, anti-mouse IgD-Alexa Fluor 488, and anti-mouse/human GL-

7-Alexa Fluor 647 antibodies (Biolegend). For flow cytometry analysis, Lymph nodes were digested in 1 mg mL<sup>-1</sup> collagenase D (Roche) solution, and stained with the above antibodies. Data was collected using a BD FACSCanto-II flow cytometer and analyzed using Flowjo software.

***Anti-Hla titer analysis.*** Mice were subcutaneously administered with 0.1 mg of nanotoxoid(Hla), 0.1 mg of nanotoxoid(-) or PBS, followed by a boost 14 days later (n=6). On days 0, 14 and 35, the serum of each mouse was collected to assay for Hla-specific antibody titers by an enzyme-linked immunosorbent assay (ELISA). A 96-well plate was coated overnight with 2 µg ml<sup>-1</sup> Hla using commercial coating buffer (Biolegend). The wells were then blocked with 5 wt% milk before adding serially diluted serum samples as the primary antibody. Goat anti-mouse IgG-HRP (Biolegend) was then employed as the secondary antibody. The plate was developed with 1-Step Slow TMB-ELISA substrate (Pierce) and measured at 450 nm with a Tecan Infinite M200 Multiplate Reader.

***MRSA infection and vaccine efficacy.*** The MRSA strain USA300 TCH1516 (American Type Culture Collection) was used in this study. The bacteria were cultured at 37 °C in tryptic soy broth, harvested by centrifugation, washed, suspended with PBS and adjusted to the appropriate concentration by optical density measurements before use. Mice immunized with 0.1 mg of nanotoxoid(Hla), 0.1 mg of nanotoxoid(-), or PBS on days 0 and 14 were challenged with 1 × 10<sup>9</sup> CFU of the bacteria on day 35. The bacteria were inoculated subcutaneously in the back region in an area that was carefully shaved using hair clippers before the challenge. The dermonecrotic area was monitored daily and reported as the width multiplied by the height of the visible lesion. On day 6 post-challenge the mice were euthanized, perfused with PBS via the heart, and the skin, heart, liver, spleen, lungs, and kidneys of each mouse were excised and

processed for enumeration. Briefly, organs were homogenized in sterile PBS using a Biospec Mini BeadBeater, diluted 10-fold serially with PBS, plated onto tryptic soy agar, and finally the colonies were counted after 24 h of incubation at 37 °C.

### **3.5.4 Conclusions**

This study investigated the use of nanoparticle-detained toxins for anti-virulence vaccination as a prophylactic strategy against live MRSA skin infection. Such strategies address an important need in the clinical management of bacterial infections as the rise of antibiotic resistance has been difficult to overcome. An increasing emphasis has been placed on novel strategies that transcend traditional treatment paradigms. The nanotoxoid(Hla) has been shown capable of safely delivering the Hla toxin in its native form without the need for subunit engineering or denaturation. Additionally, the anti-Hla titers elicited by the nanoformulation are of high avidity and long-lived. In the present study, we demonstrated that nanotoxoid(Hla) was capable of promoting strong humoral immunity in an adjuvant-free setting via efficient germinal center formation. Using a mouse skin infection model, it was demonstrated that immunity could substantially attenuate the ability of live bacteria to colonize and systemically invade their hosts, which could ultimately abrogate the negative consequences of severe MRSA infections.

Successful validation of nanotoxoid(Hla) vaccination for protection against live MRSA challenge opens the door for further development of similar platforms against many other common yet deadly bacterial pathogens. Pore-forming toxins represent a large class of virulence factors that have natural affinity for cell membrane substrates,<sup>[37]</sup> and the reported detainment strategy has been shown effective in neutralizing such toxins secreted by several different organisms.<sup>[24]</sup> It is also important to note that many pathogens secrete multiple membrane-attacking virulence factors,<sup>[38]</sup> and it can be envisioned that this platform can eventually be used

for multi-toxin vaccination, which can further increase vaccine efficacy and limit bacterial colonization. Changing the membrane coating material<sup>[39-41]</sup> could help broaden applicability to toxins that do not specifically target RBCs. Overall, the nanoparticle-based anti-virulence vaccine platform is primed to help usher in a new generation of treatments that can address some of the most critical needs in the current management of bacterial infection.

## **Acknowledgments**

This work is supported by the National Institutes of Health under Award Numbers R01EY025947 and R01DK095168 and the National Science Foundation Grant DMR-1505699. R. F. is supported by a National Institutes of Health R25CA153915 training grant from the National Cancer Institute. B. L. is supported by a National Institutes of Health 5F31CA186392 training grant from the National Cancer Institute.

Chapter 3.5, in full, is a reprint of the material as it appears in *Advanced Functional Materials*, 2016, Fei Wang, Ronnie H. Fang, Brian T. Luk, Che-Ming J. Hu, Soracha Thamphiwatana, Diana Dehaini, Pavimol Angsantikul, Ashley V. Kroll, Zhiqing Pang, Weiwei Gao, Weiyue Lu, and Liangfang Zhang. The dissertation author was a major contributor and co-author of this paper.

## References

1. D. H. Howard, R. D. Scott, 2nd, R. Packard, D. Jones, *Clin. Infect. Dis.* 2003, 36, S4.
2. K. Bush, P. Courvalin, G. Dantas, J. Davies, B. Eisenstein, P. Huovinen, G. A. Jacoby, R. Kishony, B. N. Kreiswirth, E. Kutter, S. A. Lerner, S. Levy, K. Lewis, O. Lomovskaya, J. H. Miller, S. Mobashery, L. J. Piddock, S. Projan, C. M. Thomas, A. Tomasz, P. M. Tulkens, T. R. Walsh, J. D. Watson, J. Witkowski, W. Witte, G. Wright, P. Yeh, H. I. Zgurskaya, *Nat. Rev. Microbiol.* 2011, 9, 894.
3. A. E. Clatworthy, E. Pierson, D. T. Hung, *Nat. Chem. Biol.* 2007, 3, 541.
4. G. Ramachandran, *Virulence* 2014, 5, 213.
5. D. A. Rasko, V. Sperandio, *Nat. Rev. Drug Discov.* 2010, 9, 117.
6. H. Blencowe, J. Lawn, J. Vandelaer, M. Roper, S. Cousens, *Int. J. Epidemiol.* 2010, 39, 102.
7. S. Kurosky, K. L. Davis, S. J. Karve, *Value Health* 2014, 17, A278.
8. S. J. Cryz, Jr., E. Furer, R. Germanier, *Infect. Immun.* 1982, 38, 21.
9. D. S. Kernodle, *J. Infect. Dis.* 2011, 203, 1692.
10. H. Karauzum, R. P. Adhikari, J. Sarwar, V. S. Devi, L. Abaandou, C. Haudenschild, M. Mahmoudieh, A. R. Boroun, H. Vu, T. Nguyen, K. L. Warfield, S. Shulenin, M. J. Aman, *PLoS One* 2013, 8, e65384.
11. R. M. Klevens, M. A. Morrison, J. Nadle, S. Petit, K. Gershman, S. Ray, L. H. Harrison, R. Lynfield, G. Dumyati, J. M. Townes, A. S. Craig, E. R. Zell, G. E. Fosheim, L. K. McDougal, R. B. Carey, S. K. Fridkin, M. I. Active Bacterial Core surveillance, *JAMA* 2007, 298, 1763.
12. F. D. Lowy, *N. Engl. J. Med.* 1998, 339, 520.
13. A. M. Rivera, H. W. Boucher, *Mayo Clin. Proc.* 2011, 86, 1230.
14. H. Boucher, L. G. Miller, R. R. Razonable, *Clin. Infect. Dis.* 2010, 51, S183.
15. M. Otto, *Annu. Rev. Microbiol.* 2010, 64, 143.
16. M. Li, B. A. Diep, A. E. Villaruz, K. R. Braughton, X. F. Jiang, F. R. Deleo, H. F. Chambers, Y. Lu, M. Otto, *Proc. Natl. Acad. Sci. USA* 2009, 106, 5883.
17. J. B. Wardenburg, O. Schneewind, *J. Exp. Med.* 2008, 205, 287.
18. M. O'Reilly, J. C. de Azavedo, S. Kennedy, T. J. Foster, *Microb. Pathog.* 1986, 1, 125.
19. A. D. Kennedy, J. B. Wardenburg, D. J. Gardner, D. Long, A. R. Whitney, K. R. Braughton,

- O. Schneewind, F. R. DeLeo, J. Infect. Dis. 2010, 202, 1050.
20. J. J. Moon, B. Huang, D. J. Irvine, Adv. Mater. 2012, 24, 3724.
21. R. H. Fang, A. V. Kroll, L. Zhang, Small 2015, 11, 5483.
22. Y. Tao, E. G. Ju, Z. H. Li, J. S. Ren, X. G. Qu, Adv. Funct. Mater. 2014, 24, 1004.
23. S. C. Balmert, S. R. Little, Adv. Mater. 2012, 24, 3757.
24. C. M. Hu, R. H. Fang, J. Copp, B. T. Luk, L. Zhang, Nat. Nanotechnol. 2013, 8, 336.
25. F. Wang, W. Gao, S. Thamphiwatana, B. T. Luk, P. Angsantikul, Q. Zhang, C. M. Hu, R. H. Fang, J. A. Copp, D. Pornpattananangkul, W. Lu, L. Zhang, Adv. Mater. 2015, 27, 3437.
26. C. M. Hu, R. H. Fang, B. T. Luk, L. Zhang, Nat. Nanotechnol. 2013, 8, 933.
27. J. A. Copp, R. H. Fang, B. T. Luk, C. M. J. Hu, W. W. Gao, K. Zhang, L. F. Zhang, Proc. Natl. Acad. Sci. USA 2014, 111, 13481.
28. J. J. Moon, H. Suh, M. E. Polhemus, C. F. Ockenhouse, A. Yadava, D. J. Irvine, PLoS One 2012, 7, e31472.
29. L. J. McHeyzer-Williams, M. G. McHeyzer-Williams, Annu. Rev. Immunol. 2005, 23, 487.
30. J. J. Moon, H. Suh, A. V. Li, C. F. Ockenhouse, A. Yadava, D. J. Irvine, Proc. Natl. Acad. Sci. USA 2012, 109, 1080.
31. L. Rao, L. L. Bu, J. H. Xu, B. Cai, G. T. Yu, X. Yu, Z. He, Q. Huang, A. Li, S. S. Guo, W. F. Zhang, W. Liu, Z. J. Sun, H. Wang, T. H. Wang, X. Z. Zhao, Small, DOI: 10.1002/sml.201502388.
32. A. L. DeFranco, D. C. Rookhuizen, B. Hou, Immunol. Rev. 2012, 247, 64.
33. B. J. Berube, J. Bubeck Wardenburg, Toxins (Basel) 2013, 5, 1140.
34. L. S. Miller, J. S. Cho, Nat. Rev. Immunol. 2011, 11, 505.
35. J. F. Kokai-Kun, T. Chanturiya, J. J. Mond, J. Antimicrob. Chemother. 2007, 60, 1051.
36. R. P. Adhikari, H. Karauzum, J. Sarwar, L. Abaandou, M. Mahmoudieh, A. R. Boroun, H. Vu, T. Nguyen, V. S. Devi, S. Shulenin, K. L. Warfield, M. J. Aman, PLoS One 2012, 7, e38567.
37. R. H. Fang, B. T. Luk, C. M. Hu, L. Zhang, Adv. Drug Deliv. Rev. 2015, 90, 69.
38. M. J. Aman, R. P. Adhikari, Toxins (Basel) 2014, 6, 950.
39. R. H. Fang, C. M. Hu, B. T. Luk, W. Gao, J. A. Copp, Y. Tai, D. E. O'Connor, L. Zhang,

Nano Lett. 2014, 14, 2181.

40. C. M. Hu, R. H. Fang, K. C. Wang, B. T. Luk, S. Thamphiwatana, D. Dehaini, P. Nguyen, P. Angsantikul, C. H. Wen, A. V. Kroll, C. Carpenter, M. Ramesh, V. Qu, S. H. Patel, J. Zhu, W. Shi, F. M. Hofman, T. C. Chen, W. Gao, K. Zhang, S. Chien, L. Zhang, Nature 2015, 526, 118.

41. W. Gao, R. H. Fang, S. Thamphiwatana, B. T. Luk, J. Li, P. Angsantikul, Q. Zhang, C. M. Hu, L. Zhang, Nano Lett. 2015, 15, 1403.

# Chapter 4

---

## Platelet and Neutrophil Membrane Coated Nanoparticles for Inflammation Targeting



## **4.1 Nanoparticle Functionalization with Platelet Membrane Enables Multi-Factored Biological Targeting and Detection of Atherosclerosis**

### **4.1.1 Introduction**

Cardiovascular disease is highly prevalent in many parts of the world and, depending on the population being studied, can account for nearly half of all deaths.(1, 2) Among its different forms, coronary artery disease and cerebrovascular disease are the most common. These diseases generally involve the process of atherosclerosis, which follows a well-studied progression that results in the gradual thickening of arterial walls over time.(3, 4) The condition is initiated by dysfunction of the endothelial layer, which can lead to the accumulation of oxidized low-density lipoprotein (LDL) in the intimal layer and promote local inflammation.(5, 6) This process eventually leads to the recruitment of monocytes, which traverse the endothelial layer and differentiate into macrophages.(7) As these white blood cells ingest the LDL particles, some eventually die and rupture, which potentiates a positive feedback loop that recruits even more immune cells to the area.(8, 9) Over time, a lipid core will form while a collagen-rich fibrous cap develops, covering the growing atheroma and separating it from the arterial lumen.(10, 11) As the atherosclerotic plaque continues to grow, it increasingly obstructs blood flow and can cause a variety of conditions that affect quality of life.(12) In many cases, the plaque can rupture, leading to a thrombotic event that often results in a heart attack or stroke, both of which can be fatal.(13, 14) Despite its prevalence, it is generally accepted that most deaths resulting from atherosclerosis

can be prevented with lifestyle modifications,(15) making effective detection and monitoring of plaque development of the utmost importance.(16)

A major challenge in addressing atherosclerosis as it develops is that patients are generally asymptomatic until the very late stages when significant vessel occlusion occurs, or until there is a traumatic event caused by plaque rupture.(17) Currently, there are various strategies that can be applied towards the imaging of atherosclerotic plaque in the clinic.(18-20) Non-invasive modalities such as coronary computed tomography angiography, nuclear perfusion imaging, and cardiac magnetic resonance perfusion imaging can be effective at providing physical information such as the degree of occlusion, or the presence of hard calcification. These techniques, however, are not adept at tracking the biological development of the disease, and plaque build-up generally must be fairly advanced for accurate visualization. More invasive techniques such as intravascular ultrasound, optical coherence tomography, and coronary angiography can achieve higher resolution and provide significantly more information on atherosclerotic plaques, including superficial features, vulnerability characteristics, and biological composition. A hurdle in their widespread use is that they can carry significant risks due to their invasive nature, making their application for general purpose monitoring over time impractical. As it stands, the development of a strategy for the imaging of atherosclerosis that is both facile to apply and can provide additional biological information regarding plaque development would be highly beneficial.

Platelets, which are generally responsible for maintaining hemostasis within the body, have been heavily implicated in atherogenesis at multiple stages of development.(21-24) It has become increasingly apparent that, even at the outset, there is significant crosstalk between platelets and inflamed endothelium.(25, 26) They are also capable of binding to immune cells and recruiting them to sites of inflammation. Finally, their hemostatic properties necessitate that

they bind strongly to exposed subendothelial matrices, particularly those rich in collagen, and it is their binding at sites of plaque rupture that can lead to the deadly thrombus formation commonly seen in the clinic.(27, 28) Given the multitude of interactions in which platelets participate, we sought to directly leverage these biological affinities to design a naturally targeted nanoparticle-based imaging platform capable of effectively localizing to atherosclerotic sites (**Figure 1a**). This was done by directly coating cell membrane derived from platelets onto a synthetic nanocarrier,(29) and the resulting platelet membrane-coated nanoparticles (PNPs) demonstrated a marked ability to bind different components of atherosclerotic plaques *in vitro*. The specificity afforded by the platelet membrane was further confirmed *ex vivo* using aortic arch samples obtained from mice with established atherosclerosis. This translated to effective targeting *in vivo*, effectively localizing the nanoparticles and their payload to the plaque region. Finally, it was shown that, by incorporating an MRI imaging agent into the PNP formulation, it was possible to generate sufficient contrast to distinguish the presence of plaque during live imaging. With the multifactorial detection afforded by the platelet membrane functionalization, it is possible to probe for the development of atherosclerosis and interrogate potentially diseased tissue in a biologically relevant manner.

#### **4.1.2 Materials and Methods**

##### ***Preparation and characterization of platelet membrane-coated nanoparticles (PNPs).***

PNPs were fabricated according to a previously reported method.(29) Whole blood from male ICR mice (Envigo) was collected via puncture of the submandibular vein using 10 mM ethylenediaminetetraacetic acid (EDTA; USB Corporation) as an anticoagulant. All animal experiments were performed in accordance with NIH guidelines and approved by the Institutional

Animal Care and Use Committee (IACUC) of the University of California San Diego. The platelets were isolated by differential centrifugation and the membrane was derived using a repeated freeze-thaw process.(30) Poly(lactic-*co*-glycolic acid) (PLGA; carboxyl acid-terminated, 0.67 dL/g, 50:50 monomer ratio; LACTEL Absorbable Polymers) nanoparticles were prepared by nanoprecipitation. Briefly, PLGA dissolved in acetone was precipitated into distilled water and allowed to evaporate under vacuum. Fluorescently labeled nanoparticles were fabricated by incorporating 1,1'-dioctadecyl-3,3,3',3'-tetramethylindodicarbocyanine, 4-chlorobenzenesulfonate salt (DiD; Biotium) with the PLGA at 0.1 wt% during the synthesis of the cores. The final PNPs were fabricated by coating platelet membrane onto the preformed PLGA cores at a membrane protein to polymer weight ratio of 1:1 by sonicating in a Fisher FS30D bath sonicator. Size and zeta potential were measured by dynamic light scattering using a Malvern ZEN 3600 Zetasizer. Nanoparticle stability was assessed by measuring size after adjusting nanoparticle solutions to 1× phosphate buffered saline (PBS). To visualize nanoparticle structure, transmission electronic microscopy (TEM) was performed by depositing the particles onto a 400-mesh carbon-coated copper grid (Electron Microscopy Sciences) and staining with 1 wt% uranyl acetate (Electron Microscopy Sciences), followed by observation under a Zeiss Libra 120 PLUS EF-TEM transmission electron microscope.

***In vitro foam cell binding.*** The J774 mouse macrophage cell line (TIB-67; American Type Culture Collection) was cultured and maintained in DMEM (Mediatech) supplemented with 10% FBS (Hyclone) and 1% penicillin–streptomycin (Gibco). For foam cell conversion, the J774 cells were cultured for 48 hours in the presence of 50 µg/mL oxidized low density lipoprotein (LDL) (Bio-Rad).(31) Oil Red O (Sigma Aldrich) staining was used to confirm the desired phenotype. Briefly, the cells were fixed in 10% phosphate buffered formalin (Fisher

Scientific), rinsed in 60% isopropanol, stained with filtered Oil Red O solution, destained with 60% isopropanol, and finally washed with PBS. Under bright field observation, the cells appeared red in color, confirming successful conversion. For the binding studies, the converted cells were fixed in 10% formalin and subsequently incubated with DiD-loaded PNPs, RBCNPs, or PEG-NPs at a concentration of 0.2 mg/mL for 30 minutes. The cells were then washed three times with PBS to remove unbound nanoparticles. For imaging, the cells were mounted in VECTASHIELD Antifade mounting media with DAPI (Vector Laboratories) and observed under a Keyence BZ-9000 fluorescence microscope. For flow cytometry, the cells were detached and data was collected using a FACSCanto II flow cytometer (BD Biosciences). Data analysis was performed using Flowjo software.

***Collagen binding.*** Collagen type IV (Sigma Aldrich) was dissolved in 0.25% acetic acid at a concentration of 0.5 mg/mL. Afterwards, 100  $\mu$ L of the collagen solution was added into a 96-well plate and incubated overnight at 4 °C. For the binding study, collagen-coated or non-coated plates were first blocked with 50% calf serum (Hyclone) for 1 hour and then incubated with 100  $\mu$ L of 1 mg/mL DiD-loaded nanoformulations in 25% calf serum. After 1 hour of incubation, the plates were washed with PBS containing 0.05% Tween 20 (National Diagnostics) three times. Retained nanoparticles were then dissolved with 100  $\mu$ L of dimethyl sulfoxide and quantified for fluorescence using a TeCan Infinite M200 plate reader.

***Activated endothelial cell binding.*** HUVECs; Cell Applications) were maintained in human endothelial cell growth medium (Cell Applications). Confluent cells were stimulated with 50 ng/mL of TNF- $\alpha$  (Gibco) for 24 hours. For the cell binding study, activated or non-activated HUVEC cells were fixed with 10% phosphate buffered formalin for 30 minutes and blocked with 20% calf serum for another 30 minutes, followed by incubation with 0.2 mg/mL DiD-loaded

nanoformulations in 20% calf serum. After 30 minutes of incubation on ice, the cells were washed three times and collected by scraping for data collection using a FACSCanto II flow cytometer (BD Biosciences). Data analysis was performed using Flowjo software.

***Ex vivo adherence to atherosclerotic plaque.*** ApoE KO mice (B6.129P2-Apoe<sup>tm1Unc</sup>/J; Jackson Laboratory) mice were fed with a high-fat diet (42% fat; TD88137; Envigo) for 4 months to promote the development of atherosclerotic plaque in the aortic arch. Age-matched ApoE KO mice and wild-type C57BL/6NHsd mice (Envigo) were euthanized and immediately perfused with PBS. The aortic arches were dissected and cut in half by making a longitudinal incision. For the arteries from the ApoE KO mice, samples were taken from regions with and without atherosclerotic plaque. For the wild-type mice, samples were collected from the same region where plaque usually develops in the ApoE KO mice. All samples were fixed in 10% phosphate buffered formalin for 30 minutes, blocked with 50% of calf serum for 1 hour, and then incubated with 0.2 mg/mL DiD-loaded nanoformulations for 30 minutes. The samples were then washed with PBS containing 0.05% Tween 20 three times before examination under a Keyence BZ-9000 fluorescence microscope. Afterwards, the same samples were subject to Oil Red O staining as described above to help visualize the presence of atherosclerotic plaque. For histological analysis, artery samples were embedded in Tissue-Tek OCT compound (Sakura Finetek) and cryosectioned, followed by fixation, blocking, and nanoparticle incubation using the same procedure as the whole tissue samples. The sections were mounted with DAPI-containing mounting media before imaging.

***In vivo targeting to atherosclerotic plaque.*** ApoE KO mice fed with a high-fat diet for 4 months and age-matched wild-type mice were intravenously administered with 0.5 mg of the various DiD-loaded nanoparticles via the tail vein. The nanoparticle dosage was chosen based on

previous studies using PNPs to target vascular injury.(29) After allowing the nanoparticles to distribute for 24 hours, the mice were euthanized and then perfused with PBS to remove unbound nanoparticles. The aortas were isolated for imaging using a Keyence BZ-9000 fluorescence microscope. Oil Red O staining was performed to confirm the formation of atherosclerotic plaque in the ApoE KO mice. Quantification of fluorescence intensity was carried out using ImageJ software. For histological analysis, aortas from PNP-administered ApoE KO mice were collected and embedded in OCT compound for cryosectioning. Sections were then fixed in 10% formalin for 30 minutes and blocked with 4% bovine serum albumin (Sigma Aldrich). For fluorescent imaging, sections were incubated with anti-mouse CD54 (YN1/1.7.4; Biolegend), anti-mouse CD68 (FA-11; Biolegend) or polyclonal anti-collagen IV (ab6586; Abcam) followed by an Alexa Fluor 555-conjugated secondary (Biolegend). After washing three times with PBS containing 0.05% Tween 20, the sections were mounted with DAPI-containing mounting medium. All images were taken using a Keyence BZ-9000 fluorescence microscope.

***Live magnetic resonance imaging of atherosclerotic plaque.*** To prepare nanoparticles for magnetic resonance imaging (MRI), a lipid-chelated gadolinium (Gd), DTPA-bis(stearylamide) (Gd salt) (Gd-DTPA-BSA; Avanti Polar Lipids), was used. A stock solution of the Gd-DTPA-BSA was prepared at a concentration of 10 mg/mL in 1:1 chloroform/methanol. 50  $\mu$ L of the solution was then deposited into a glass vial and allowed to evaporate. The resulting film was then hydrated with solution containing 2 mg (protein mass) of platelet membrane at 37 °C for 30 minutes. Gd-incorporated PNPs (Gd-PNPs) were fabricated by fusing the Gd-containing platelet membrane with preformed PLGA cores through a sonication process. The PNPs were purified by spinning down the unincorporated Gd-DTPA-BSA precipitate at 1,000  $\times$ g for 5 minutes. The Gd-PNPs were characterized by DLS and TEM as described above.

*In vivo* MRI was performed on a 4.7 T MR Solutions MRS 4000 preclinical MRI. The animals were anesthetized with a 3% isoflurane/O<sub>2</sub> gas mixture and maintained with a 1-1.5% isoflurane/O<sub>2</sub> gas mixture delivered through a nose cone. The mice were placed in a 30-mm birdcage coil with an animal handling system. A respiratory pillow was placed under the abdomen and ECG probes on the left forepaw and right hindpaw were used to monitor the heartrate and respiration rate. The aortic arch with all three branches (the brachiocephalic trunk, left common carotid artery, and left subclavian artery) were identified in a longitudinal position. MRI was performed using a T<sub>1</sub>-weighted cardiac sequence. A 1 mm thick slice was acquired using a flash sequence. The repetition time and echo time for the T<sub>1</sub>-weighted images were 10 ms and 3 ms, respectively. One signal average was used with a total imaging time of about 3 minutes per scan. For the experiment, ApoE KO mice fed on a high-fat diet for 4 months were first subject to a baseline scan and then administered with Gd-PNPs intravenously via the tail vein at a dose of 16  $\mu$ mol Gd/kg.(32) Postcontrast MRI was done after 1 hour using the same parameters as the baseline scan. After the live imaging, the mice were euthanized and the aortic arch was collected for Oil Red O staining to confirm the presence of plaque.

### **4.1.3 Results and Discussion**

PNPs were fabricated by coating the membrane derived from platelets onto preformed poly(lactic-*co*-glycolic acid) (PLGA) cores loaded with a far-red fluorescent dye, which was used as a model payload to demonstrate the ability of the nanoparticles to target atherosclerotic plaque. Briefly, PLGA was mixed together with 1,1'-dioctadecyl-3,3,3',3'-tetramethylindodicarbocyanine (DiD) in an organic phase, which was then precipitated into an aqueous phase to form DiD-loaded polymeric cores. Platelets were derived fresh from blood via



differential centrifugation, and platelet membrane was prepared using a repeated free-thaw process. Then the DiD-loaded cores and the membrane were mixed together and sonicated, resulting in membrane-coated nanoparticles. Using dynamic light scattering, it was determined that the final product was slightly larger than the bare PLGA cores in size (Figure 1b), and the surface zeta potential of the PNPs approached that of the platelet membrane-derived vesicles (Figure 1c), both results being indicative of successful membrane coating. The platelet membrane coating also helped to enhance the colloidal stability of the PLGA cores, which are normally unstable and aggregate when subject to physiological salt concentrations (Figure 1d). Additionally, transmission electron microscopy of PNPs negatively stained with uranyl acetate revealed the characteristic core-shell structure of membrane-coated particles,(33-35) with a lipid membrane coating forming a ring around the nanoparticulate core; the observed sizes of the nanoparticles were consistent with the dynamic light scattering measurements (Figure 1e).

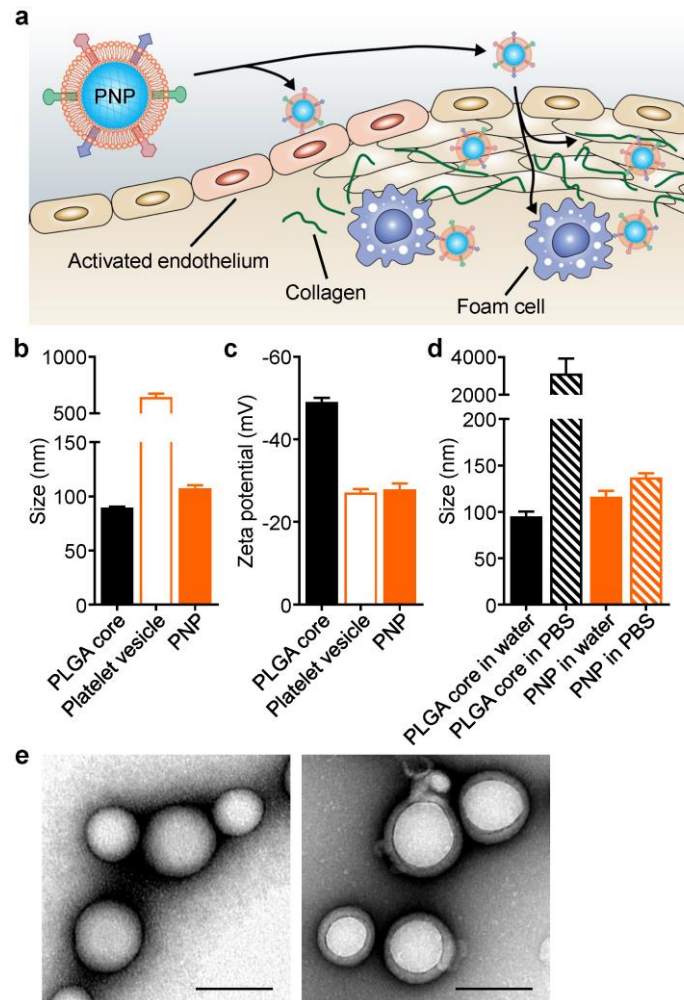


**Figure 4.1.1.** Platelet membrane-coated nanoparticle (PNP) schematic and characterization. (a) PNPs express a variety of surface markers capable of targeting different components of atherosclerotic plaques, including activated endothelium, foam cells, and collagen. (b) Z-average size of bare PLGA cores, platelet membrane-derived vesicles, and PNPs as measured by dynamic light scattering (DLS) ( $n = 3$ , mean  $\pm$  SD). (c) Surface zeta potential of bare PLGA cores, platelet membrane-derived vesicles, and PNPs as measured by DLS ( $n = 3$ , mean  $\pm$  SD). (d) Z-average size of bare PLGA cores and PNPs in water or in PBS ( $n = 3$ , mean  $\pm$  SD). (e) Transmission electron microscopy (TEM) image of bare PLGA cores (left) and PNPs (right) negatively stained with uranyl acetate (scale bars = 100 nm).

After confirming successful nanoparticle fabrication, we conducted *in vitro* evaluations to explore the binding potential of the PNPs to different elements that play a role in atherogenesis. First, the ability of the particles to bind foam cells, which are largely responsible for the deposition of lipid-rich material during plaque development,(36) was assessed. Mouse J774 macrophages were converted to foam cells by culturing them with oxidized LDL, and the cells were subsequently fixed and incubated either with PLGA nanoparticles functionalized with

polyethylene glycol (denoted 'PEG-NPs'),<sup>(37)</sup> red blood cell membrane (denoted 'RBCNPs'), or platelet membrane (PNPs). It was observed both by flow cytometric analysis, as well as by fluorescent imaging, that PNPs much more readily bound to the foam cells (**Figure 2a,b**). Next, the binding of the particles to collagen, which is a major component of the fibrous cap that sits on top of the atheroma,<sup>(10, 11)</sup> was evaluated. Assay plates were coated with type IV collagen and incubated with the different nanoparticle solutions. Again, the PNPs demonstrated significantly higher binding compared with both PEG-NPs and RBCNPs (Figure 2c). Further, this effect was specific to collagen, as uncoated wells showed similarly low levels of binding among all the nanoparticle samples. Finally, the ability of the particles to bind to activated endothelium, which plays a major role in initiating the process of atherosclerosis,<sup>(38)</sup> was tested. Human umbilical vein endothelial cells (HUVECs) were activated with tumor necrosis factor alpha (TNF- $\alpha$ ) and incubated with the various types of nanoparticles. On the activated endothelial cells, PNPs interacted much more strongly than the other samples. This difference was significantly lessened on resting HUVECs that were not subject to activation (Figure 2d). Overall, these results clearly demonstrated that PNPs possess particularly strong affinity with multiple components important to the formation of atherosclerotic plaque.

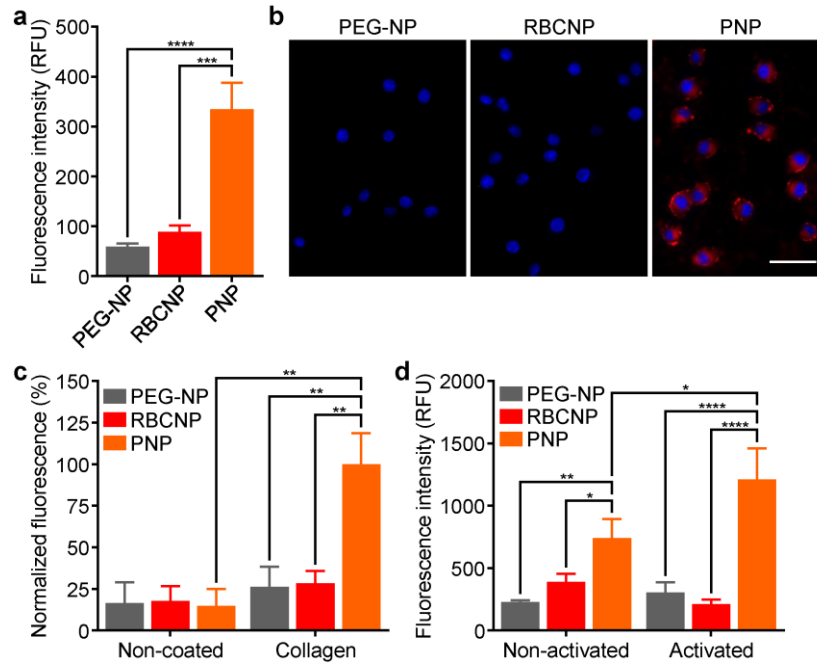


**Figure 4.1.2.** In vitro targeting of PNPs to atherosclerosis. (a,b) Binding of PEG-NPs, RBCNPs, or PNPs to foam cells as demonstrated by (a) flow cytometry ( $n = 3$ , mean  $\pm$  SD) and (b) fluorescence microscopy (blue = nuclei, red = nanoparticle; scale bar = 50  $\mu$ m). (c) Fluorescent quantification of PEG-NPs, RBCNPs, or PNPs bound to non-coated or collagen-coated surfaces ( $n = 3$ , mean  $\pm$  SEM). (d) Fluorescent quantification of PEG-NPs, RBCNPs, or PNPs bound to HUVEC cells either in their normal state or after activation with tumor necrosis factor alpha (TNF- $\alpha$ ) ( $n = 3$ , mean  $\pm$  SD). \* $p < 0.05$ , \*\* $p < 0.01$ , \*\*\* $p < 0.001$ , \*\*\*\* $p < 0.0001$ ; one-way ANOVA.

Given the encouraging *in vitro* results, we sought to further verify the ability of PNPs to bind with formed plaque by employing a murine model of atherosclerosis. ApoE knockout (KO) mice, which naturally develop plaque over time,(39) were fed on a high-fat western diet, after which their aortic arches were excised and incubated *ex vivo* with different nanoparticle types. After incubating with PEG-NPs, RBCNPs, or PNPs, the vessels were washed and observed under fluorescence microscopy. Both the PEG-NP and RBCNP controls exhibited negligible signal, whereas the high amount of signal for the PNPs demonstrated significant binding across the entirety of the plaque area (**Figure 3a**). Using Oil Red O lipid staining, the presence of plaque was then visually verified for each artery sample. This enhanced binding effect was further confirmed on histological samples, in which the different types of nanoparticles were incubated with cross-sections from a plaque-containing artery. Again, the PNPs displayed significant signal

throughout, including directly on the plaque area across the luminal face of the vessel (Figure 3b). To verify that this binding effect was specific to samples from atherosclerotic mice, the experiment was repeated using wild-type mice with healthy aortic arches. In this case, the PNPs had minimal binding to the luminal side of the vessel, with some binding along the edges where there was exposed subendothelium due to the incision that was made to flatten the tissue sample for imaging (Figure 3c,d).

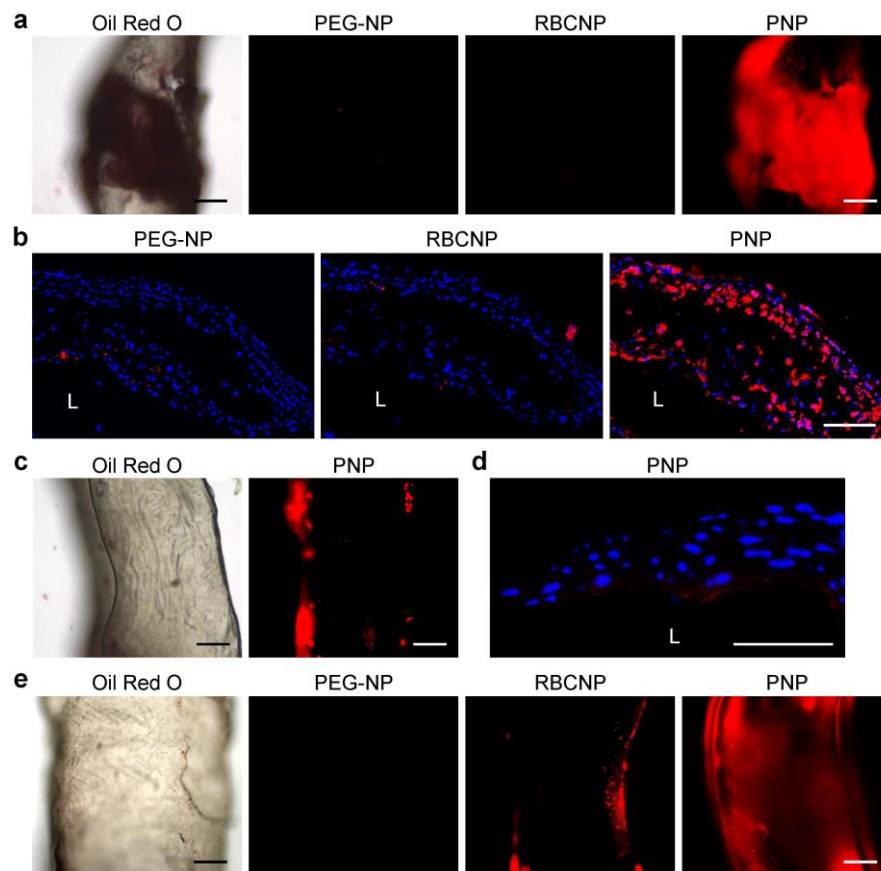


**Figure 4.1.3.** *Ex vivo* binding to atherosclerotic plaque. (a) Binding of PEG-NPs, RBCNPs, or PNPs to part of an atherosclerotic aortic arch from ApoE knockout (KO) mice fed with a high fat western diet for 4 months (fluorescent images: red = nanoparticle; scale bar = 200  $\mu$ m). Oil Red O staining was used to confirm the presence of plaque; the presented image is representative. (b) Fluorescent imaging of PEG-NPs, RBCNPs, or PNPs bound to histological cross-sections of atherosclerotic vessels of ApoE KO mice (L = luminal side; blue = nuclei, red = nanoparticle; scale bar = 100  $\mu$ m). (c) Binding of PNPs to part of the aortic arch from a wild-type mouse (fluorescent image: red = nanoparticle; scale bar = 200  $\mu$ m). Oil Red O staining was used to show the absence of plaque. (d) Fluorescent imaging of PNPs bound to a histological cross-section of a healthy vessel from a wild-type mouse (L = luminal side; blue = nuclei, red = nanoparticle; scale bar = 50  $\mu$ m). (e) Binding of PEG-NPs, RBCNPs, or PNPs to a plaque-free region of the aortic arch from ApoE KO mice fed with a high-fat western diet (fluorescent images: red = nanoparticle; scale bar = 200  $\mu$ m). Oil Red O staining was used to confirm the absence of plaque; the presented image is representative (bright field imaging scale bar = 200  $\mu$ m).

In addition to observing nanoparticle binding to areas with overt plaque formation, we also explored asymptomatic regions of arteries from the ApoE KO mice fed with the high-fat western diet. To this end, a section further down the aortic arch proximal to where plaque usually develops was chosen. With enough time, these regions will also develop visible atherosclerotic plaque, indicating that the underlying biological processes of atherogenesis are most likely present despite lack of ready evidence. For the experiment, visual observation was used to confirm the lack of plaque on these arteries, and they were then incubated with the different nanoparticle samples to assess binding. As shown in Figure 3e, while PEG-NPs and RBCNPs again showed minimal binding across the face of the arteries, the PNPs in contrast displayed an appreciable amount of signal, albeit less than was observed for the corresponding sample in Figure 3a. Afterwards, Oil Red O staining was conducted to further verify that there was no plaque present. The ability of the PNPs to bind such regions that are susceptible to plaque formation indicate that the nanoparticles may have utility for early stage detection, taking advantage of the biological mechanisms of platelet binding to probe for precursor processes before actual plaque formation.

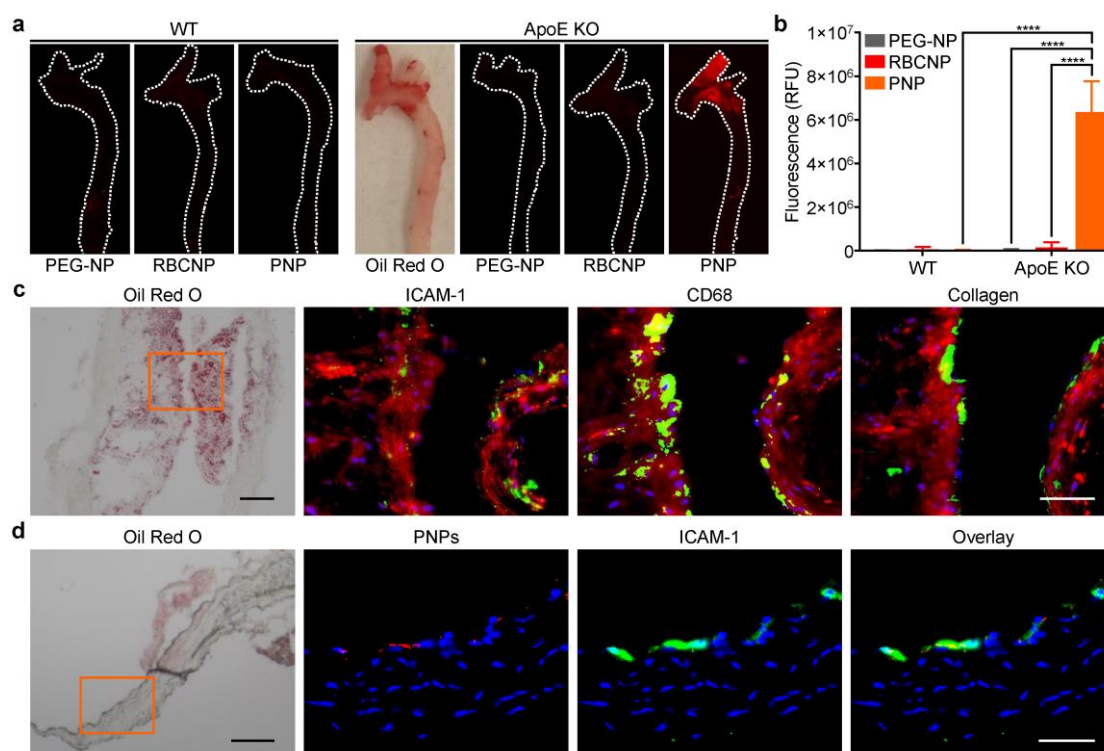


**Figure 4.1.4.** In vivo targeting of atherosclerotic plaque. (a) Macroscopic fluorescent imaging of aortic arches from wild-type (WT) or ApoE KO mice fed on a high fat western diet after intravenous administration with PEG-NPs, RBCNPs, or PNPs (white = physical outline, red = nanoparticle). Oil Red O staining was used to confirm the presence of plaque for ApoE KO mice (image is representative). (b) Fluorescent quantification of the aortic arch of wild-type or ApoE KO mice after administration with PEG-NPs, RBCNPs, or PNPs (n = 3, mean  $\pm$  SD). \*\*\*\*p < 0.0001; one-way ANOVA. (c) Histological cross-section of an aortic arch with significant atherosclerotic plaque from an ApoE KO mouse administered with PNPs. Slides were stained with antibodies against ICAM-1, CD68, or collagen (fluorescent images: blue = nuclei, red = nanoparticle, green = marker of interest, scale bar = 50  $\mu$ m). Oil Red O staining indicates presence of atherosclerotic plaque (bright field image: orange box indicates region displayed in fluorescent images, scale bar = 100  $\mu$ m). (d) Histological cross-section of an aortic arch with lesser developed atherosclerotic plaque from an ApoE KO mouse administered with PNPs. Slides were stained with an antibody against ICAM-1 (fluorescent images: blue = nuclei, red = nanoparticle, green = marker of interest, scale bar = 50  $\mu$ m). Oil Red O staining indicates presence of atherosclerotic plaque (bright field image: orange box indicates region displayed in fluorescent images, scale bar = 100  $\mu$ m).

Following the *ex vivo* binding evaluation, we next explored the ability of the PNPs to target the same atherosclerotic regions *in vivo* using a live animal model. ApoE KO mice were fed a high-fat western diet, allowing for the development of plaque over time. Subsequently, solutions of either PEG-NPs, RBCNPs, or PNPs were intravenously administered via the tail vein. After 24 hours, the mice were euthanized and their aortic arches analyzed for the presence of fluorescent signal (**Figure 4a,b**). Oil Red O staining was again used to macroscopically confirm the presence of plaque for each artery sample. Consistent with the *ex vivo* results, the

arteries of mice administered with PNPs displayed significant fluorescent signal, while the signal for the other particles was negligible. To confirm that this effect was exclusive to atherosclerotic sites, the same experiment was performed in wild-type mice, and this yielded arteries with virtually no signal for all nanoparticle types. These results suggest that the PNPs, with their natural platelet membrane coating, are well-equipped to navigate through circulation and preferentially distribute to diseased tissue over healthy tissue.

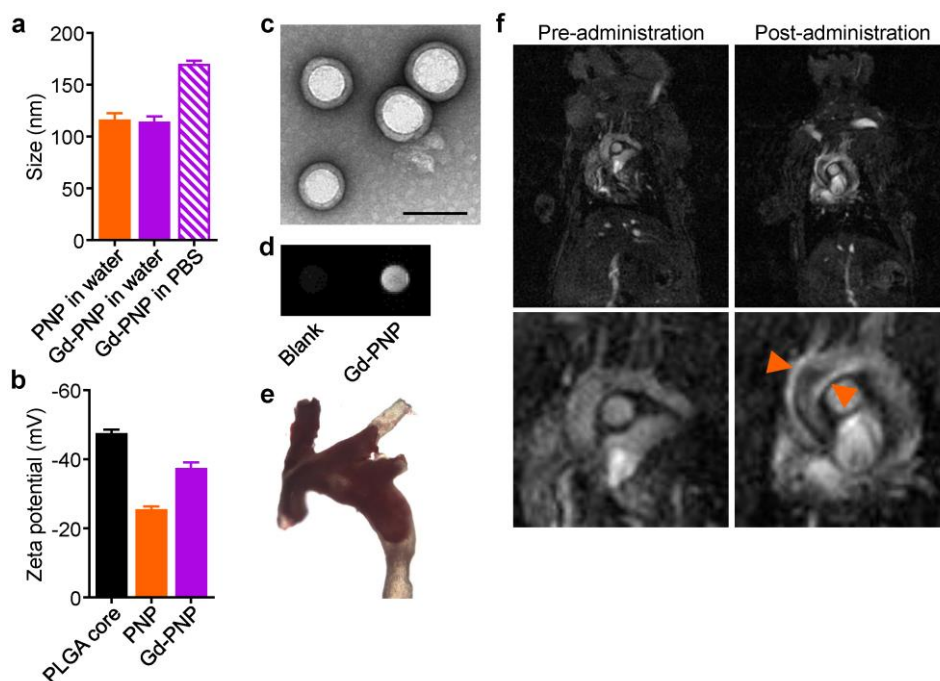


**Figure 4.1.5.** Live imaging of atherosclerotic plaque. (a) Z-average size of PNPs and PNPs incorporated with Gd-chelated lipids as a contrast agent, termed Gd-PNPs, in water or in PBS as measured by DLS ( $n = 3$ , mean  $\pm$  SD). (b) Surface zeta potential of bare PLGA cores, PNPs, and Gd-PNPs as measured by DLS ( $n = 3$ , mean  $\pm$  SD). (c) Transmission electron microscopy (TEM) image of Gd-PNPs negatively stained with uranyl acetate (scale bar = 100 nm). (d) T1-weighted signal of Gd-PNPs was confirmed by MRI. (e) Bright field image of aortic arch from ApoE KO mice stained with Oil Red O confirmed the presence of atherosclerotic plaque. (f) T1-weighted MRI images of ApoE KO mice before and 1 hour after administration with Gd-PNPs (orange arrows = regions of positive contrast along aortic arch).

Histological sections were then taken to obtain a more detailed microscopic view of the *in vivo* PNP targeting to atherosclerotic and pre-atherosclerotic regions. In the first instance, we analyzed a tissue sample with significant plaque development that resulted in a high degree of vessel occlusion (Figure 4c). By studying the distribution of the far-red dye in the PNP



formulation, it was confirmed that the nanoparticle signal could be found in significant amounts throughout the plaque region. Sections were then stained with separate antibodies to probe for various elements of atherosclerosis development. This included ICAM-1 for activated endothelial cells, CD68 for macrophages, as well as type IV collagen. Each of the three was found to be present, and they displayed high degrees of proximity or co-localization with the nanoparticle signal on the sections. In the second instance, a section was taken from a vessel with significantly less disease burden, and the region of endothelium proximal to the plaque was studied (Figure 4d). Upon staining for ICAM-1, it was confirmed that there was activated endothelial cells at this region. This signal co-localized well with PNP signal, confirming that the particles are capable of binding to regions that are plaque-free but susceptible to future development. In total, these *in vivo* targeting experiments further indicated the potential of the platelet membrane-coated formulation to bind with atherosclerotic sites at different stages of development, including pre-atherosclerotic regions with no visible sign of disease.

Finally, to confirm the utility of the PNP formulation for live imaging, PNPs were formulated with a clinically relevant magnetic resonance imaging (MRI) contrast agent. In this case, we chose to employ a lipid-chelated gadolinium (Gd), which could easily be inserted into the lipid bilayer of the platelet membrane. After using this Gd-inserted membrane to fabricate PNPs (denoted ‘Gd-PNPs’), we confirmed that the resulting nanoparticles were similar to unmodified PNPs in terms of physicochemical characteristics, stability in PBS, and morphology (**Figure 5a-c**). The zeta potential of Gd-PNPs was slightly more negative than PNPs, likely due to the acidic nature of the lipid chelator. Additionally, the ability of the particles to provide MRI contrast in T<sub>1</sub>-weighted mode was evaluated (Figure 5d). The Gd-PNPs provided a high amount of positive contrast and could easily be detected over background. The Gd-PNPs were then

administered to live ApoE KO mice that had been fed a high-fat western diet (Figure 5e,f). Prior to Gd-PNP administration, the aortic arch area did not exhibit any appreciable contrast within the vasculature when observed under MRI. However, at 1 hour post-administration of the Gd-PNPs, positive contrast can clearly be seen, strongly suggesting that the particles had specifically targeted atherosclerotic plaque at the aortic arch within this short time window. To confirm that this region was indeed atherosclerotic, the mice were euthanized after imaging, and Oil Red O staining of the aortic arch showed that there was significant fatty plaque present. This study established that PNPs could be used to successfully target and deliver a sufficient quantity of contrast agent to provide observable contrast at the site of interest. It should be noted that previous studies have demonstrated PNPs to be absent of pro-thrombotic factors, alleviating concerns of aggregation or clot formation at the target site.<sup>(29)</sup> Additionally, nanoparticulate formulations employing chelated Gd have been shown to be well tolerated at high doses in nonhuman primates.<sup>(40)</sup>

#### **4.1.4 Conclusion**

We have demonstrated that, by employing platelet membrane as a functional coating for nanocarriers, it is possible to effectively target imaging payloads to sites of atherosclerosis. This strategy leverages the natural interaction of platelet membrane markers with multiple components present during atherogenesis, including activated endothelium, foam cells, and collagen. It was shown that the PNPs can not only bind to regions with significant plaque formation, but also to areas that are pre-atherosclerotic and prone to plaque formation. Beyond simply providing contrast, this strategy also provides information about the underlying biology of the targeted regions, which may eventually be used to give a more complete picture of disease

development over time. While MRI imaging was used in the present work as a proof-of-concept modality, given the generalizability of the cell membrane-coating technology,(41-43) it can be envisioned that the strategy outlined here can be adapted towards a variety of imaging modalities. This may ultimately enable improvements in specificity that can aid in the prevention and management of cardiovascular diseases, significantly mitigating their impact on global health.

### **Acknowledgements**

This work is supported by the National Institutes of Health under Award Number R01CA200574 and the National Science Foundation Grant DMR-1505699. We thank Christopher V. Barback for his help with the MRI imaging.

Chapter 4.1, in full, is a reprint of the material as it appears in ACS Nano, 2019, Wei, X.; Ying, M.; Dehaini, D.; Su, Y.; Kroll, A.; Zhou, J.; Gao, W.; Fang, R.; Chien, S. and Zhang, L.

## References

- [1] N. Townsend, L. Wilson, P. Bhatnagar, K. Wickramasinghe, M. Rayner, M. Nichols, Cardiovascular Disease in Europe: Epidemiological Update 2016, *Eur. Heart J.*, 37 (2016) 3232-3245.
- [2] G.A. Roth, M.D. Huffman, A.E. Moran, V. Feigin, G.A. Mensah, M. Naghavi, C.J. Murray, Global and Regional Patterns in Cardiovascular Mortality from 1990 to 2013, *Circulation*, 132 (2015) 1667-1678.
- [3] R. Ross, The Pathogenesis of Atherosclerosis — An Update, *N. Engl. J. Med.*, 314 (1986) 488-500.
- [4] I. Tabas, G. Garcia-Cardena, G.K. Owens, Recent Insights into the Cellular Biology of Atherosclerosis, *J. Cell Biol.*, 209 (2015) 13-22.
- [5] S. Parthasarathy, D. Steinberg, J.L. Witztum, The Role of Oxidized Low-Density Lipoproteins in the Pathogenesis of Atherosclerosis, *Annu. Rev. Med.*, 43 (1992) 219-225.
- [6] R. Stocker, J.F. Keaney, Jr., Role of Oxidative Modifications in Atherosclerosis, *Physiol. Rev.*, 84 (2004) 1381-1478.
- [7] K.J. Moore, F.J. Sheedy, E.A. Fisher, Macrophages in Atherosclerosis: A Dynamic Balance, *Nat. Rev. Immunol.*, 13 (2013) 709-721.
- [8] I. Tabas, Macrophage Death and Defective Inflammation Resolution in Atherosclerosis, *Nat. Rev. Immunol.*, 10 (2010) 36-46.
- [9] G.K. Hansson, P. Libby, The Immune Response in Atherosclerosis: A Double-Edged Sword, *Nat. Rev. Immunol.*, 6 (2006) 508-519.
- [10] K.G. McCullagh, V.C. Duance, K.A. Bishop, The Distribution of Collagen Types I, III and V (AB) in Normal and Atherosclerotic Human Aorta, *J. Pathol.*, 130 (1980) 45-55.
- [11] B.V. Shekhonin, S.P. Domogatsky, V.R. Muzykantov, G.L. Idelson, V.S. Rukosuev, Distribution of Type I, III, IV and V Collagen in Normal and Atherosclerotic Human Arterial Wall: Immunomorphological Characteristics, *Coll. Relat. Res.*, 5 (1985) 355-368.
- [12] K. Fox, M.A. Garcia, D. Ardissino, P. Buszman, P.G. Camici, F. Crea, C. Daly, G. De Backer, P. Hjelm Dahl, J. Lopez-Sendon, J. Marco, J. Morais, J. Pepper, U. Sechtem, M. Simoons-Smit, K. Thygesen, Guidelines on the Management of Stable Angina Pectoris: Executive Summary, *Eur. Heart J.*, 27 (2006) 1341-1381.
- [13] V. Fuster, B. Stein, J.A. Ambrose, L. Badimon, J.J. Badimon, J.H. Chesebro, Atherosclerotic Plaque Rupture and Thrombosis. Evolving Concepts, *Circulation*, 82 (1990) II47-59.

- [14] E. Lutgens, R.J. van Suylen, B.C. Faber, M.J. Gijbels, P.M. Eurlings, A.P. Bijmens, K.B. Cleutjens, S. Heeneman, M.J. Daemen, Atherosclerotic Plaque Rupture: Local or Systemic Process?, *Arterioscler. Thromb. Vasc. Biol.*, 23 (2003) 2123-2130.
- [15] M.J. Stampfer, F.B. Hu, J.E. Manson, E.B. Rimm, W.C. Willett, Primary Prevention of Coronary Heart Disease in Women through Diet and Lifestyle, *N. Engl. J. Med.*, 343 (2000) 16-22.
- [16] U. Baber, R. Mehran, S. Sartori, M.M. Schoos, H. Sillesen, P. Muntendam, M.J. Garcia, J. Gregson, S. Pocock, E. Falk, V. Fuster, Prevalence, Impact, and Predictive Value of Detecting Subclinical Coronary and Carotid Atherosclerosis in Asymptomatic Adults: The BioImage Study, *J. Am. Coll. Cardiol.*, 65 (2015) 1065-1074.
- [17] P.K. Shah, Screening Asymptomatic Subjects for Subclinical Atherosclerosis: Can We, Does It Matter, and Should We?, *J. Am. Coll. Cardiol.*, 56 (2010) 98-105.
- [18] M.R. Dweck, M.K. Doris, M. Motwani, P.D. Adamson, P. Slomka, D. Dey, Z.A. Fayad, D.E. Newby, D. Berman, Imaging of Coronary Atherosclerosis — Evolution Towards New Treatment Strategies, *Nat. Rev. Cardiol.*, 13 (2016) 533-548.
- [19] F.R. Joshi, A.C. Lindsay, D.R. Obaid, E. Falk, J.H. Rudd, Non-Invasive Imaging of Atherosclerosis, *Eur. Heart J. Cardiovasc. Imaging*, 13 (2012) 205-218.
- [20] V. Sandfort, J.A. Lima, D.A. Bluemke, Noninvasive Imaging of Atherosclerotic Plaque Progression: Status of Coronary Computed Tomography Angiography, *Circ. Cardiovasc. Imaging*, 8 (2015) e003316.
- [21] M.A. Packham, J.F. Mustard, The Role of Platelets in the Development and Complications of Atherosclerosis, *Semin. Hematol.*, 23 (1986) 8-26.
- [22] Y. Huo, K.F. Ley, Role of Platelets in the Development of Atherosclerosis, *Trends Cardiovasc. Med.*, 14 (2004) 18-22.
- [23] D. Lievens, P. von Hundelshausen, Platelets in Atherosclerosis, *Thromb. Haemost.*, 106 (2011) 827-838.
- [24] C. Weber, Platelets and Chemokines in Atherosclerosis: Partners in Crime, *Circ. Res.*, 96 (2005) 612-616.
- [25] M. Gawaz, H. Langer, A.E. May, Platelets in Inflammation and Atherogenesis, *J. Clin. Invest.*, 115 (2005) 3378-3384.
- [26] S. Lindemann, B. Kramer, P. Seizer, M. Gawaz, Platelets, Inflammation and Atherosclerosis, *J. Thromb. Haemost.*, 5 Suppl 1 (2007) 203-211.
- [27] L. Badimon, G. Vilahur, Thrombosis Formation on Atherosclerotic Lesions and Plaque Rupture, *J. Intern. Med.*, 276 (2014) 618-632.

- [28] L. Badimon, T. Padro, G. Vilahur, Atherosclerosis, Platelets and Thrombosis in Acute Ischaemic Heart Disease, *Eur. Heart J. Acute Cardiovasc. Care*, 1 (2012) 60-74.
- [29] C.M. Hu, R.H. Fang, K.C. Wang, B.T. Luk, S. Thamphiwatana, D. Dehaini, P. Nguyen, P. Angsantikul, C.H. Wen, A.V. Kroll, C. Carpenter, M. Ramesh, V. Qu, S.H. Patel, J. Zhu, W. Shi, F.M. Hofman, T.C. Chen, W. Gao, K. Zhang, S. Chien, L. Zhang, Nanoparticle Biointerfacing by Platelet Membrane Cloaking, *Nature*, 526 (2015) 118-121.
- [30] R.H. Fang, C.M. Hu, B.T. Luk, W. Gao, J.A. Copp, Y. Tai, D.E. O'Connor, L. Zhang, Cancer Cell Membrane-Coated Nanoparticles for Anticancer Vaccination and Drug Delivery, *Nano Lett.*, 14 (2014) 2181-2188.
- [31] C.M. Hu, L. Zhang, S. Aryal, C. Cheung, R.H. Fang, L. Zhang, Erythrocyte Membrane-Camouflaged Polymeric Nanoparticles as a Biomimetic Delivery Platform, *Proc. Natl. Acad. Sci. U.S.A.*, 108 (2011) 10980-10985.
- [32] Z. Pang, C.M. Hu, R.H. Fang, B.T. Luk, W. Gao, F. Wang, E. Chuluun, P. Angsantikul, S. Thamphiwatana, W. Lu, X. Jiang, L. Zhang, Detoxification of Organophosphate Poisoning Using Nanoparticle Bioscavengers, *ACS Nano*, 9 (2015) 6450-6458.
- [33] J.F. Bentzon, F. Otsuka, R. Virmani, E. Falk, Mechanisms of Plaque Formation and Rupture, *Circ. Res.*, 114 (2014) 1852-1866.
- [34] L. Zhang, J.M. Chan, F.X. Gu, J.W. Rhee, A.Z. Wang, A.F. Radovic-Moreno, F. Alexis, R. Langer, O.C. Farokhzad, Self-Assembled Lipid-Polymer Hybrid Nanoparticles: A Robust Drug Delivery Platform, *ACS Nano*, 2 (2008) 1696-1702.
- [35] G. Desideri, C. Ferri, Endothelial Activation. Sliding Door to Atherosclerosis, *Curr. Pharm. Des.*, 11 (2005) 2163-2175.
- [36] S. Zadelaar, R. Kleemann, L. Verschuren, J. de Vries-Van der Weij, J. van der Hoorn, H.M. Princen, T. Kooistra, Mouse Models for Atherosclerosis and Pharmaceutical Modifiers, *Arterioscler. Thromb. Vasc. Biol.*, 27 (2007) 1706-1721.
- [37] S. Kotb, J. Piraquive, F. Lamberton, F. Lux, M. Verset, V. Di Cataldo, H. Contamin, O. Tillement, E. Canet-Soulas, L. Sancey, Safety Evaluation and Imaging Properties of Gadolinium-Based Nanoparticles in Nonhuman Primates, *Sci. Rep.*, 6 (2016) 35053.
- [38] J.G. Piao, L. Wang, F. Gao, Y.Z. You, Y. Xiong, L. Yang, Erythrocyte Membrane is an Alternative Coating to Polyethylene Glycol for Prolonging the Circulation Lifetime of Gold Nanocages for Photothermal Therapy, *ACS Nano*, 8 (2014) 10414-10425.
- [39] J.Y. Zhu, D.W. Zheng, M.K. Zhang, W.Y. Yu, W.X. Qiu, J.J. Hu, J. Feng, X.Z. Zhang, Preferential Cancer Cell Self-Recognition and Tumor Self-Targeting by Coating Nanoparticles with Homotypic Cancer Cell Membranes, *Nano Lett.*, 16 (2016) 5895-5901.
- [40] W. Gao, R.H. Fang, S. Thamphiwatana, B.T. Luk, J. Li, P. Angsantikul, Q. Zhang, C.M. Hu, L. Zhang, Modulating Antibacterial Immunity via Bacterial Membrane-Coated

Nanoparticles, *Nano Lett.*, 15 (2015) 1403-1409.

[41] X.L. Wei, J. Gao, R.H. Fang, B.T. Luk, A.V. Kroll, D. Dehaini, J.R. Zhou, H.W. Kim, W.W. Gao, W.Y. Lu, L.F. Zhang, Nanoparticles Camouflaged in Platelet Membrane Coating as an Antibody Decoy for the Treatment of Immune Thrombocytopenia, *Biomaterials*, 111 (2016) 116-123.

[42] S.W. Xu, Y. Huang, Y. Xie, T.A. Lan, K. Le, J.W. Chen, S.R. Chen, S. Gao, X.Z. Xu, X.Y. Shen, H.Q. Huang, P.Q. Liu, Evaluation of Foam Cell Formation in Cultured Macrophages: An Improved Method with Oil Red O Staining and DiI-oxLDL Uptake, *Cytotechnology*, 62 (2010) 473-481.

[43] V. Amirbekian, M.J. Lipinski, K.C. Briley-Saebo, S. Amirbekian, J.G.S. Aguinaldo, D.B. Weinreb, E. Vucic, J.C. Frias, F. Hyafil, V. Mani, E.A. Fisher, Z.A. Fayad, Detecting and Assessing Macrophages In Vivo to Evaluate Atherosclerosis Noninvasively using Molecular MRI, *Proc. Natl. Acad. Sci. U.S.A.*, 104 (2007) 961-966.

## **4.2 Neutrophil membrane-coated nanoparticles suppress synovial inflammation and ameliorate joint destruction in inflammatory arthritis**

### **4.2.1 Introduction**

Rheumatoid arthritis (RA) is a widespread and devastating autoimmune disease characterized by systemic inflammation that causes progressive joint damage and disability[1, 2]. The precise cause of RA remains elusive and current treatment are primarily targeting inflammatory response[3]. Although there has been success, especially with the use of biologics that inhibit tumor necrosis factor alpha (TNF- $\alpha$ ) and interleukin (IL)-1, existing approaches carry considerable limitations[4, 5]. In particular, pathological inflammation in RA is orchestrated by a large number of molecules [6, 7]. Inhibition of one or a few may not be adequate to halt or reverse disease progression[8, 9]. Indeed, under current treatment regimens, RA remains poorly controlled in up to 30% of patients and only a minor proportion of patients reach sustained clinical remission[10, 11]. Moreover, due largely to the multiplicity of cytokine targets, the toxicity of cytokine-inhibition remains highly unpredictable, causing substantial adverse effects and safety concerns[12]. Therefore, alternative anti-inflammatory approaches that overcome the complexity and heterogeneity of the inflammatory network are highly desirable for effective RA treatment[13].

Recently, the rapid advance of nanomedicine has led to the development of cell membrane-coated nanoparticles as an emerging therapeutic platform[14, 15]. Made by the fusion of natural cell membranes onto synthetic cores, these nanoparticles inherit the antigenic profile of the source



cells, enabling them to act as decoys that can absorb and neutralize pathological molecules regardless of their structural specificity[14]. For example, nanoparticles coated with the membrane of red blood cells (RBC-NPs) have demonstrated the ability to bind bacterial pore-forming toxins[14] and pathological autoantibodies[16], diverting them away from and preventing their attack of healthy RBCs. Furthermore, macrophage membrane-coated nanoparticles have shown the ability to bind and neutralize endotoxins that would otherwise trigger immune activation[17] .

The advancement of cell membrane-coated nanoparticles in biodetoxification, particularly their unique capability of neutralizing pathological targets that are heterogeneous and complex in nature, inspired us to develop these nanoparticles as a novel anti-inflammatory strategy to address the aforementioned challenges facing current RA treatment. Joint inflammation and damage in RA are mediated by the influx of an innate and adaptive immune cell mixture into the synovial joint space[18]. Among them, neutrophils play an important role because of their actions in resolving inflammation and repairing tissues damages[19]. Neutrophils have been found to produce microvesicles that entered cartilage and protected the joint in inflammatory arthritis[20, 21]. Moreover, neutrophils are also responsible for initiating and perpetuating RA progression[22]. In RA, various chemoattractants have been identified that promote neutrophil migration into the joints[23]. Subsequent neutrophil activation stimulates synovial cells to produce chemokines that amplify neutrophil recruitment[24]. Neutrophil activation and granular content release contribute directly to cartilage destruction and bone resorption[25]. Importantly, remission and subsequent reversion of RA have been linked with a decrease in neutrophil recruitment to the synovial fluid[26].

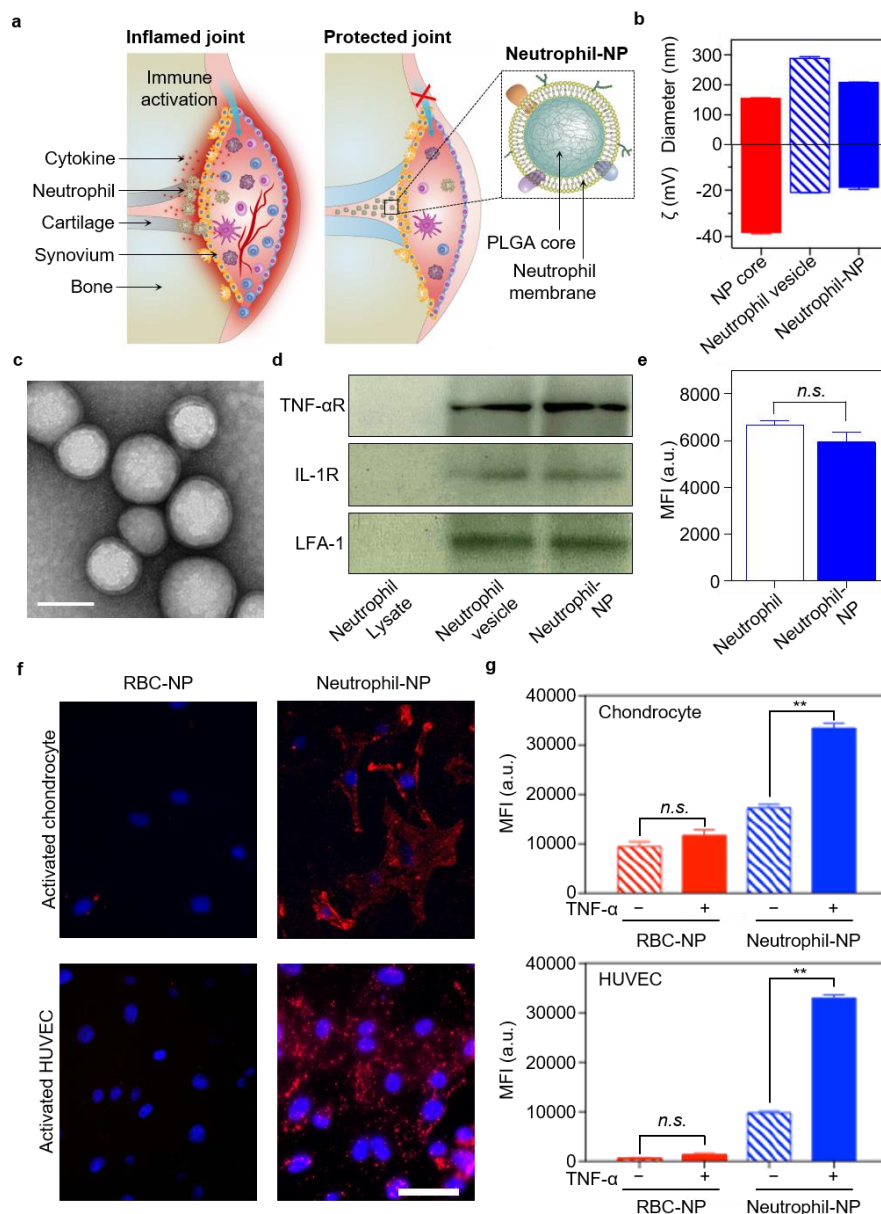


**Figure 4.2.1.** Preparation and characterization of neutrophil-NPs. a, Schematic b, Dynamic light scattering measurements of neutrophil-NP hydrodynamic size (diameter) and zeta potential ( $\zeta$ , n = 3). c, Representative images of neutrophil-NPs examined with transmission electron microscopy. Samples were stained with uranyl acetate (scale bar, 100 nm). d, Characteristic protein bands of neutrophil cell lysates, neutrophil membrane-derived vesicles, and neutrophil-NPs resolved by using western blotting. e, Comparison of the fluorescence intensity measured from neutrophils (approximately  $2.5 \times 10^6$  cells) and neutrophil-NPs (100  $\mu$ L of suspensions, 0.2 mg/mL protein content) stained with APC anti-mouse LFA antibodies. (n.s. = not significant, n=3). f, Fluorescent images of chondrocytes and human umbilical vein endothelial cells (HUVECs) after incubation with neutrophil-NPs or RBC-NPs. Red color represents nanoparticles and blue represents nuclei. Cells were activated with TNF- $\alpha$  prior to nanoparticle incubation (scale bar, 50  $\mu$ m). g, Flow cytometric analysis of nanoparticle binding to human chondrocytes or HUVECs (n = 3). Statistical analysis was performed using paired t-test. All bars represent means  $\pm$  s.d. (n = 3). n.s.: not significant, \*\*P  $\leq$  0.01.

Based on the active roles played by neutrophils in RA, herein, we developed neutrophil-like nanoparticles (denoted ‘neutrophil-NPs’) by fusing neutrophil membrane onto polymeric cores and investigated their use as a broad-spectrum anti-inflammatory agent for RA management. By displaying neutrophil plasma membrane on their surface, the neutrophil-NPs were anticipated to mimic the source cells and thus to bind with immunoregulatory molecules that would otherwise target endogenous neutrophils (Fig. 1a).

#### **4.5.2 Results and Discussion**

While To synthesize neutrophil-NPs, plasma membrane derived from purified and activated human peripheral blood neutrophils (Supplementary Fig. 1) was coated onto poly(lactic-*co*-glycolic acid) (PLGA) polymeric cores. The completeness of membrane coating was verified, which provided neutrophil-NPs with superior colloidal stability (Supplementary Fig. 2). Dynamic light scattering measurements revealed that the hydrodynamic diameter of the neutrophil-NPs increased approximately 18 nm from the uncoated PLGA cores; the surface zeta potential was less negative than the cores but comparable to neutrophil membrane-derived vesicles (Fig. 1b). The neutrophil-NPs were visualized by transmission electron microscopy after uranyl acetate staining and showed a spherical core-shell structure (Fig. 1c), consistent with a unilamellar membrane coating around the polymeric core[14, 27]. Furthermore, immunoblotting confirmed the presence and enrichment of key surface antigens, including TNF- $\alpha$  receptor (TNF- $\alpha$ R), IL-1 receptor (IL-1R), and lymphocyte function-associated antigen 1 (LFA-1) on neutrophil-NPs, further confirming the translocation of neutrophil membrane onto the polymeric cores (Fig. 1d). A right-side-out protein orientation was verified by immunostaining and quantifying LFA-1 antigen on neutrophil-NPs as compared to that on neutrophil cells with equal amount of membrane proteins (Fig. 1e).

Overall, a series of quality assurance specifications for the production of neutrophil-NPs were established to ensure physicochemical and biological reproducibility of the nanoparticles (Supplementary Table 1).

In RA, neutrophils are known to engage in receptor-mediated adhesion with cytokine-activated chondrocytes[28]. Herein, human neutrophil-NPs were fluorescently labeled and added to monolayers of chondrocytes activated with TNF- $\alpha$  and human umbilical vein endothelial cells (HUVECs). RBC-NPs were tested as a control because they had similar particulate structures as neutrophil-NPs but RBCs are less plastic in promoting and resolving inflammations compared to neutrophils[29]. After incubation and washing, significant fluorescence was observed on cells incubated with neutrophil-NPs, but not with RBC-NPs (Fig. 1f). Flow cytometry measurements confirmed that activated chondrocytes and HUVECs, when incubated with neutrophil-NPs, showed a significant increase in mean fluorescence intensity (MFI) compared to naïve cells (without TNF- $\alpha$  activation) (Fig. 1g). These results demonstrate the ability of neutrophil-NPs to target inflamed cells conferred by their neutrophil membrane coating. The binding is likely attributed to specific interactions between LFA-1 on the neutrophil membrane and the intercellular activation molecule 1 (ICAM-1) overexpressed on activated chondrocytes and HUVECs[22, 23].

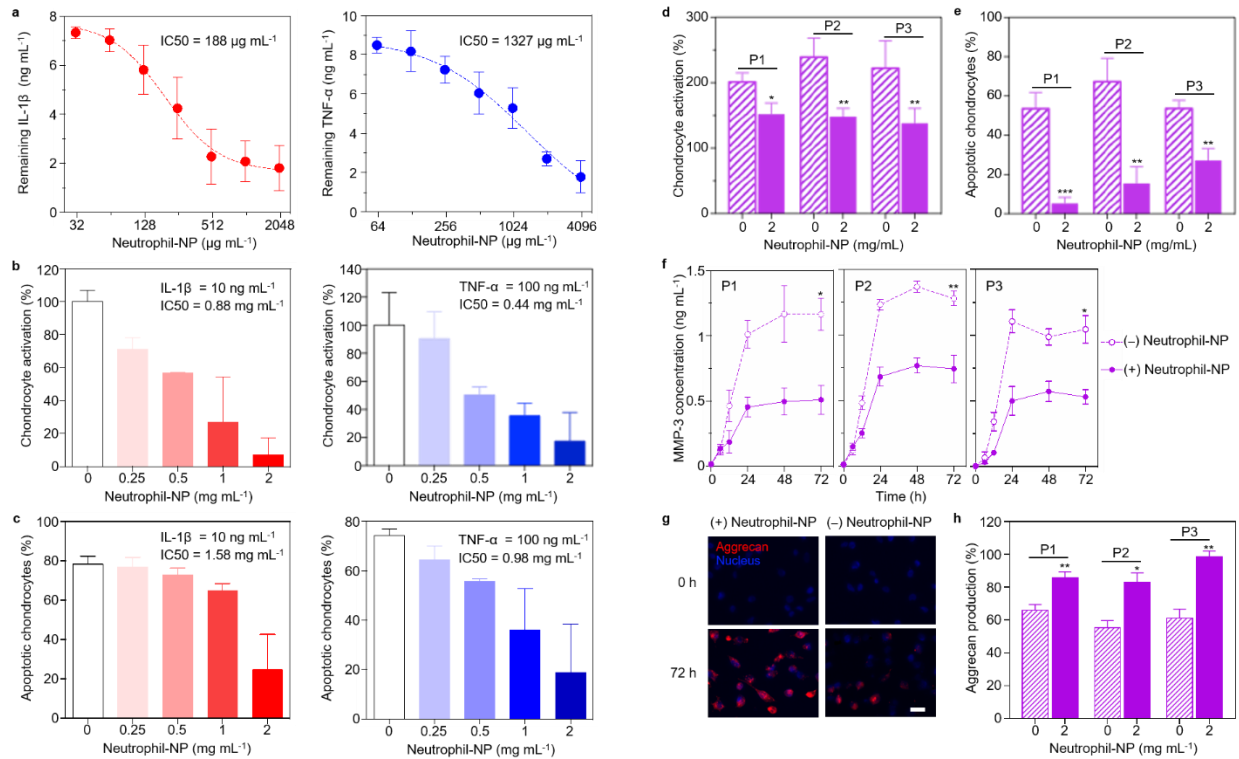


**Figure 4.2.2.** Neutrophil-NPs inhibit pro-arthritis factors in vitro. a, Binding capacity of human neutrophil-NP with IL-1 $\beta$  and TNF- $\alpha$ , respectively. b-c, Dose-response inhibition of chondrocyte activation (b) and chondrocyte apoptosis (c), induced by IL-1 $\beta$  or TNF- $\alpha$ . Concentration of IL-1 $\beta$  was maintained at 10 ng mL $^{-1}$  and that of TNF- $\alpha$  at 100 ng mL $^{-1}$ ; neutrophil-NP concentrations were varied from 0 to 2 mg mL $^{-1}$ . Values measured from chondrocytes treated with cytokines only (without neutrophil-NPs) served as 100%. d-f, Effects of neutrophil-NPs on chondrocyte activation (d), apoptosis (e), and matrix metalloproteinase-3 (MMP-3) secretion (f), elicited by human synovial fluid (hSF) samples collected from three rheumatoid arthritis patients. In the study, chondrocyte activation was quantified by measuring the level of ICAM-1 expression. Chondrocyte apoptosis was measured by examining mitochondrial activity through cell staining with 3,3'-dihexyloxycarbocyanine iodide (DiOC6)

We next investigated the ability of human neutrophil-NPs to inhibit pro-arthritis factors, with a focus on IL-1 $\beta$  and TNF- $\alpha$  due to their prominent roles in initiating RA and promoting disease progression[6, 8]. We first tested the binding capability of neutrophil-NPs to IL-1 $\beta$  and TNF- $\alpha$ . Based upon the measured binding kinetic profiles, it was determined using Hill equation that neutrophil-NPs had an IC $_{50}$  (half maximal inhibitory concentration) value of 188  $\mu$ g mL $^{-1}$  for IL-1 $\beta$  binding and 1327  $\mu$ g mL $^{-1}$  for TNF- $\alpha$  binding (Fig. 2a, Supplementary Fig. 3). We then evaluated the inhibition of chondrocyte activation induced by IL-1 $\beta$  and TNF- $\alpha$ . In the study, 10 ng mL $^{-1}$  IL-1 $\beta$  or 100 ng mL $^{-1}$  TNF- $\alpha$  was added to the culture medium. After 6 h of incubation,

significant chondrocyte activation was observed, indicated by an increased level of ICAM-1 expression (Supplementary Fig. 4a). However, expression levels decreased with the increase of neutrophil-NPs added to the medium, suggesting a dose-dependent inhibition effect (Fig. 2b, Supplementary Fig. 4b). An IC<sub>50</sub> value of 0.88 mg mL<sup>-1</sup> for inhibiting IL-1 $\beta$  and 0.44 mg mL<sup>-1</sup> for TNF- $\alpha$  were obtained by fitting the data. We also evaluated the capability of neutrophil-NPs in inhibiting chondrocyte apoptosis caused by the cytokines. In the study, 48 h incubation of IL-1 $\beta$  or TNF- $\alpha$  with chondrocytes resulted in 80% of apoptotic cells (Supplementary Fig. 5a). However, the fraction of apoptotic cells decreased with the increase of neutrophil-NPs (Fig. 2c, Supplementary Fig. 5b). An IC<sub>50</sub> value of 1.58 mg mL<sup>-1</sup> for inhibiting IL-1 $\beta$  and 0.98 mg mL<sup>-1</sup> for inhibiting TNF- $\alpha$  were observed. Neutrophil-NPs also inhibited HUVEC activation in a similar dose-dependent manner (Supplementary Fig. 6). In contrast, the control group RBC-NPs did not show any detectable cytokine neutralization effects (Supplementary Fig. 7).

The ability of human neutrophil-NPs to inhibit pro-arthritis factors was further tested with human synovial fluid (hSF) samples obtained from three RA patients. Chondrocytes showed enhanced activation after 6 h of incubation with all three hSF samples, with 2.0, 2.4, and 2.2-fold increases, respectively. In contrast, when the hSF samples were pre-treated with neutrophil-NPs at a concentration of 2 mg mL<sup>-1</sup> for 2 h, they showed significantly reduced activation of chondrocytes with 1.5, 1.5, and 1.4-fold increase, respectively (Fig. 2d, Supplementary Fig. 8a). Meanwhile, prolonged incubation with hSF samples caused 53.5, 67.3, and 53.6% chondrocyte apoptosis, while pre-treatment with neutrophil-NPs reduced these values to 5.3, 15.4, and 27.2%, respectively (Fig. 2e, Supplementary Fig. 8b). Neutrophil-NPs also inhibited HUVEC activation by all three hSF samples (Supplementary Fig. 8c). Moreover, the presence of neutrophil-NPs induced near 2-fold decrease of matrix metalloproteinase-3 (MMP-3) plateau concentration in the

culture medium for all three samples (Fig. 2f). Neutrophil-NPs also significantly increased the production of aggrecan from hSF-activated chondrocytes (Fig. 2g). Quantitatively, the three hSF-activated chondrocyte samples had aggrecan production of 65.8%, 55.4%, and 61.1%, respectively, compared to naïve chondrocytes, which were increased to 85.9%, 82.8%, and 98.6%, respectively, in the presence of neutrophil-NPs (Fig. 2h). Neutrophil-NPs reduced aggrecanolysis caused by either aggrecanase or MMP, attributable to their neutralization of pro-arthritis cytokines (Supplementary Fig. S9). It should be noted that different hSF samples caused different levels of cell activation, apoptosis, and catabolic status, likely due to the variation of pro-arthritis profiles of different individuals[30]. Nevertheless, neutrophil-NPs showed varying but significant neutralization efficacy across all samples without pre-existing knowledge of the hSF composition. Further study found that the catabolic status of chondrocytes remained unaltered when neutrophil-NPs alone were used without hSF, suggesting that the observed effects of neutrophil-NPs on chondrocytes were indeed related to their neutralization of pro-arthritis factors (Supplementary Fig. S10).

To study the ability of neutrophil-NPs to penetrate injured cartilage in a mouse model, the nanoparticles were fabricated using mouse neutrophil membrane, which showed comparable properties with human neutrophil-NPs (Supplementary Fig. S11-14, Supplementary Table 2). Mouse femoral head explants were collected and cultured in media supplemented with IL-1 $\beta$  to mimic inflammatory arthritis[21]. Fluorescently labeled mouse neutrophil-NPs or RBC-NPs were then added to the explants, followed by 18 h of incubation before sectioning. Using fluorescence microscopy, we observed the accumulation of neutrophil-NPs on the distal region of the femoral heads with clear penetration into the tissue (**Fig. 3a**). Dual fluorescence labeling demonstrated colocalization of the polymeric cores and the neutrophil membranes during cartilage penetration

(Supplementary Fig. 15). Below the surface zone, nanoparticles distributed throughout the cartilage matrix. Strong nanoparticle signal in close proximity to the stained nuclei implied an intracellular uptake by stimulated chondrocytes (Supplementary Fig. 16). RBC-NPs also showed accumulation in the distal surface region, but with much weaker fluorescence intensity (Fig. 3b). Below the distal surface, RBC-NPs accumulated primarily around the chondrocytes, and the pericellular matrix was essentially free of nanoparticles. Fluorescence intensity at different penetration depths was quantified by sampling image stacks with a width of 5  $\mu\text{m}$  and normalized to the outmost section of tissue treated with neutrophil-NPs. The signal from neutrophil-NPs decayed with increasing penetration depth, which dropped to approximately 1% at a penetration depth of 140  $\mu\text{m}$  (Fig. 3c). In contrast, the signal of RBC-NPs was about 60% at the distal surface compared to that from neutrophil-NPs, which decayed rapidly to 1% at a penetration depth of 30  $\mu\text{m}$ . The enhanced cartilage penetration of neutrophil-NPs is likely attributable to the adhesion interactions between neutrophils and chondrocytes. Besides LFA-1 and ICAM-1, neutrophils may exploit other ligands for adhesion[31, 32]. Despite the complexity of cell ligands, the top-down fabrication of neutrophil-NPs can bypass the need for ligand identification and conjugation[14, 15].

We further examined whether neutrophil-NPs, with their combined ability to neutralize cytokines and penetrate deep into cartilage, would provide chondroprotection in inflammation-induced cartilage damage. We extracted the femoral heads from mice and maintained them in culture media under various conditions, followed by safranin-O staining for cartilage histopathology analysis[21]. The control femoral head sample without additional manipulation showed cartilage with an intact surface and perichondrium with homogenous cartilage matrix (Fig.3d). When the culture medium was supplemented with 10 ng mL<sup>-1</sup> IL-1 $\beta$ , the femoral head



showed obvious cartilage loss with matrix fibrillation that extended vertically downward into the mid zone. The sample also showed significant cartilage matrix loss in both superficial zones and fissured domains (Fig. 3e). When RBC-NPs were added, the stained section showed similar pathology as the sample treated with IL-1 $\beta$  alone (Fig. 3f). However, when neutrophil-NPs were added to the tissue culture, cartilage damage induced by IL-1 $\beta$  was halted. The sample showed a mostly intact surface with a large area of continuous cartilage matrix preserved below the superficial zone with reduced areas of disorganization, increased number of chondrocytes, and absence of fissures (Fig. 3g). The cartilage content of the samples represented by areas with Safranin-O staining (dark red) was further quantified (Fig. 3h). In tissues cultured with IL-1 $\beta$  alone or with supplemented RBC-NPs, only about 40% of the cartilage remained when compared to the unmanipulated control. In contrast, the tissue cultured with IL-1 $\beta$  and neutrophil-NPs was able to maintain more than 80% of its cartilage, suggesting a strong chondroprotection effect conferred by neutrophil-NPs. Notably, without adding cytokines, neutrophil-NPs or RBC-NPs alone did not alter the cartilage content, implying that the observed chondroprotective effect was mediated by neutralization of arthritic factors (Supplementary Fig. 17).

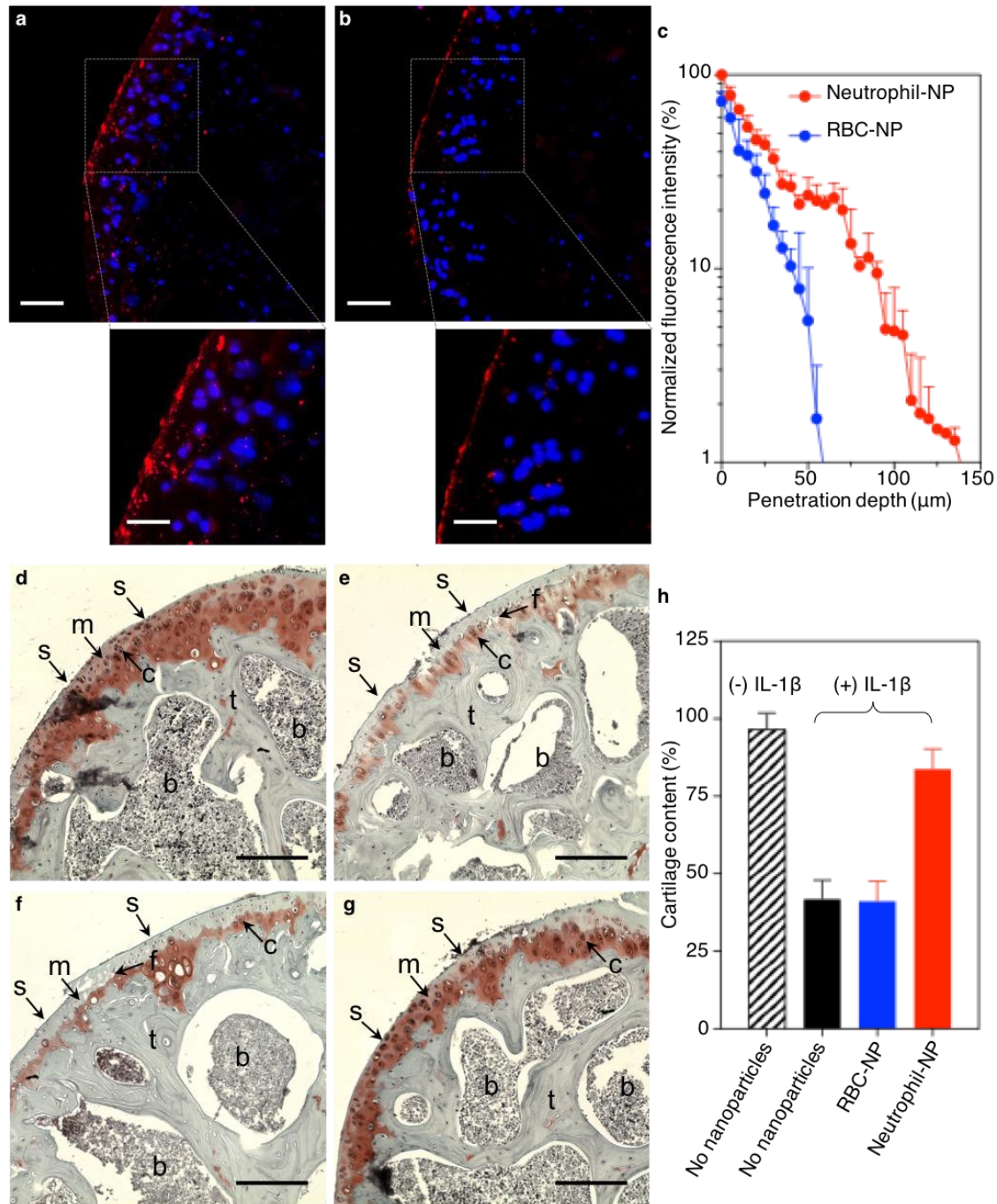


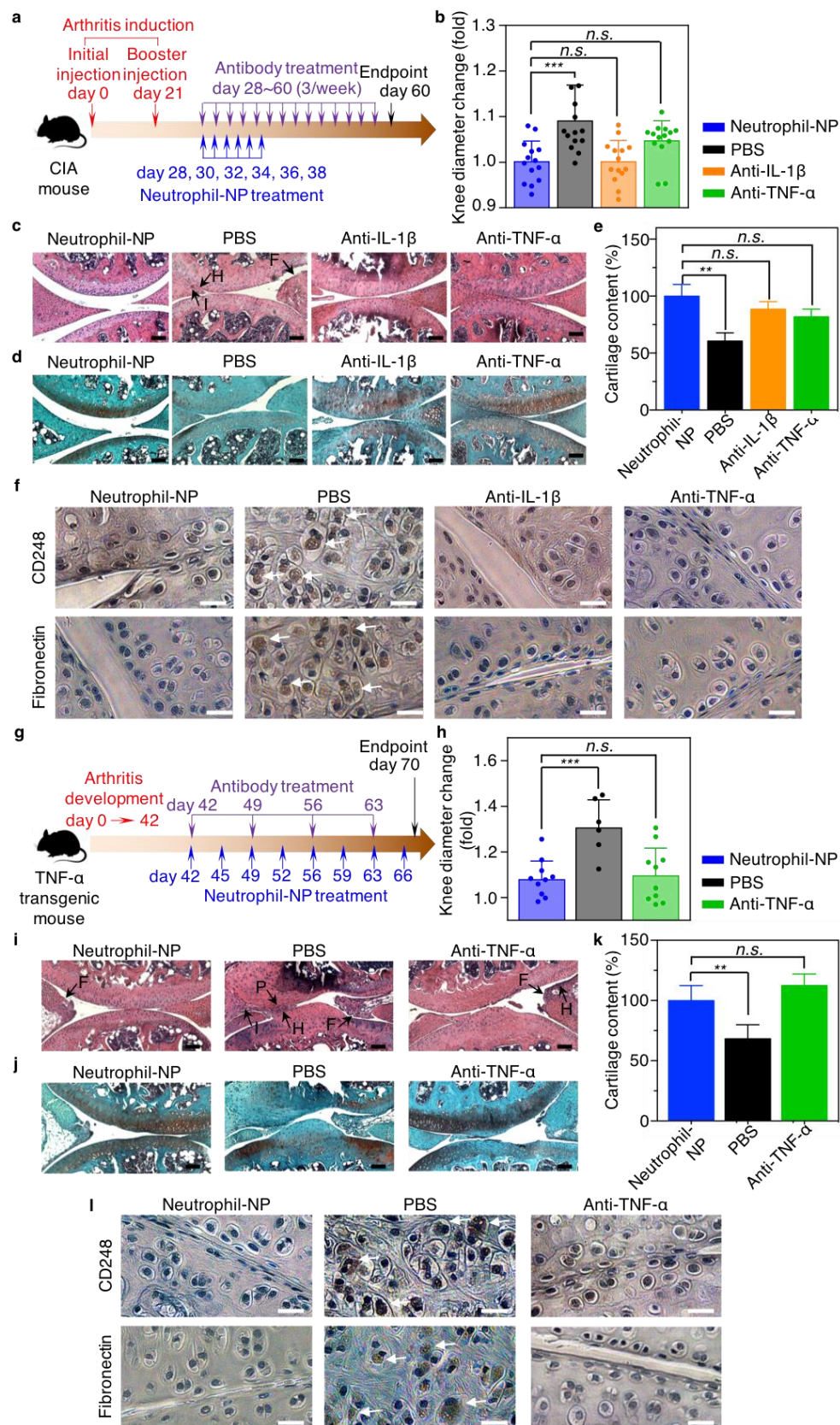
**Figure 4.2.3.** Neutrophil-NPs enhance cartilage penetration and confer chondroprotection. a-b, Representative fluorescence images of the cross-section of mouse femoral heads stimulated with recombinant mouse IL-1 $\beta$  and incubated with fluorescence-labeled mouse neutrophil-NPs (a) or RBC-NPs (b) (scale bar, 100  $\mu$ m). c, Quantitative analysis of nanoparticle penetration depth into IL-1 $\beta$ -stimulated mouse femoral heads (n = 3). d-g, Representative safranin-O stained cross-sections of mouse femoral head explants under various treatment conditions, including without either IL-1 $\beta$  stimulation or nanoparticle treatment (d), stimulated but without nanoparticle treatment (e), stimulated and treated with RBC-NPs (f), and stimulated and treated with neutrophil-NPs (g). On the images, s: superficial zone, m: mid zone, c: chondrocytes, f: fissure, b: bone marrow, t: bone trabeculae. Scale bar = 100  $\mu$ m. (h) Quantitative analysis of safranin-O positive area among the above groups (n = 3).

The efficacy of neutrophil-NPs to ameliorate joint destruction was first evaluated using a murine model of collagen-induced arthritis (CIA)[33]. Following arthritis induction, CIA mice developed mild swelling of the knee joints, where mouse neutrophil-NPs were injected (**Fig. 4a**). Mice injected with PBS, anti-IL-1 $\beta$ , or anti-TNF- $\alpha$  served as controls[34, 35]. At the study endpoint, the transverse knee diameter of mice injected with neutrophil-NPs was comparable to that of mice treated with anti-IL-1 $\beta$  or anti-TNF- $\alpha$ , but significantly smaller than the PBS control group, indicating a reduction in cellular influx and oedema formation (Fig. 4b). Knee joints of the mice were also sectioned for histological analysis. Haemotoxylin and Eosin (H&E)-stained sections from neutrophil-NP group showed an even distribution of chondrocytes within the articulate cartilage without obvious degeneration. In contrast, chondrocytes in PBS group were largely absent and an intense neutrophil infiltration was observable in the joints and synovium. Anti-cytokines treated groups showed less neutrophil infiltration but slight enlargement and depletion of chondrocytes (Fig. 4c). Sections stained with Safranin-O showed a higher level of sulfated glycosaminoglycans (sGAGs) in the cartilage of neutrophil-NP group than PBS group, but similar to anti-IL-1 $\beta$  and anti-TNF- $\alpha$  groups (Fig. 4d, e). The phenotype of fibroblast-like synoviocytes (FLS) in the synovial intimal lining was also examined. Specifically, we stained FLS for the expression of CD248 and fibronectin known to upregulate with IL-1 $\beta$  and TNF- $\alpha$ [36, 37]. Elevated expression of these markers indicates an aggressive phenotype that invades the extracellular matrix and exacerbates joint damage in RA[38]. As shown in Fig. 4f, neutrophil-NP group showed weak staining of CD248 with few positively stained cells in synovium. In contrast, a large number of CD248-positive cells were found in sections of PBS group. Similarly, fibronectin-positive cells were largely present in PBS control joints, but not within the synovium of neutrophil-NP and anti-

cytokine groups. Collectively, these results demonstrate an effective protective role of neutrophil-NPs against joint destruction in the CIA mouse model.

**Figure 4.2.4.** a, The study protocol of a therapeutic regimen with a collagen-induced arthritis (CIA) mouse model. b, Change of hind knee diameter on day 60 after CIA induction compared to that on day 0. c-d, Representative images of H&E staining (c) and safranin-O staining (d) on knee sections from mice treated with neutrophil-NPs, PBS, anti-IL-1 $\beta$  antibody, or anti-TNF- $\alpha$  antibody (scale bar, 100  $\mu$ m). On the images, F: synovial membrane fibrillation, H: synovium hyperplasia, I: immune cell infiltration. e, Cartilage content was quantified from safranin-O stained sections of mice treated with different groups. f, Representative images of immunohistochemical staining for CD248 (top row) and fibronectin (bottom row) on knee sections from mice treated with different groups (scale bar, 10  $\mu$ m). g, The study protocol of a therapeutic regimen with a human TNF- $\alpha$  transgenic mouse model of inflammatory arthritis. h, Change of hind knee diameter on day 70 compared to that on day 0. i-j, Representative images of H&E staining (i) and safranin-O staining (j) on knee sections from mice treated with neutrophil-NPs, PBS, or anti-TNF- $\alpha$  antibody (scale bar, 100  $\mu$ m). On the images, F: synovial membrane fibrillation, H: synovium hyperplasia, I: immune cell infiltration. P: pannus formation. k, Cartilage content was quantified from safranin-O stained sections of mice treated with different groups. l, Representative images immunohistochemical staining for CD248 (top row) and fibronectin (bottom row) on knee sections from mice treated with different groups (scale bar, 10  $\mu$ m). Statistical analysis was performed using one-way ANOVA with Dunnett's post hoc analysis. All bars represent means  $\pm$  s.d. In CIA mouse study, n = 7 for all groups. In transgenic mouse study, n = 5 for neutrophil-NP and anti-TNF- $\alpha$  antibody groups, n = 3 for PBS group. \*P  $\leq$  0.05, \*\*P  $\leq$  0.01, and \*\*\*P  $\leq$  0.001.

Image on next page



We further examined the cartilage protection efficacy of neutrophil-NPs using a human transgenic mouse model of inflammatory arthritis, where mice express a human TNF- $\alpha$  transgene and spontaneously develop arthritis[39]. In the study, mouse neutrophil-NPs or controls including PBS and anti-TNF- $\alpha$  were injected into the knee of transgenic mice after 6 weeks of arthritis development (Fig. 4g)[40]. Similar as observed in the CIA model, at the study endpoint, the knee diameter of neutrophil-NP group was smaller than that of the PBS group, but comparable with the anti-TNF- $\alpha$  group (Fig. 4h). H&E-stained sections from neutrophil-NP group showed the preservation of chondrocytes in the articular cartilage, contrasting with the chondrocyte depletion and matrix deformation in sections of PBS group, but consistent with features in sections of anti-TNF- $\alpha$  group (Fig. 4i). In addition, neutrophil-NP group maintained a higher level of sGAGs in the cartilage than PBS group, but comparable to anti-TNF- $\alpha$  group (Fig. 4j and k). Moreover, most FLS in neutrophil-NP and anti-TNF- $\alpha$  groups remained CD248-negative and fibronectin-negative, contrasting with the positive ones in PBS group (Fig. 4l).

Finally, to evaluate the broad applicability of the neutrophil-NPs, we tested their anti-arthritis effectiveness using CIA mice with early stage arthritis following a prophylactic regimen (**Fig. 5a**). We first observed chondral protection at the knee joints where the mouse neutrophil-NPs were injected. Specifically, at the study endpoint the knee diameter measured from mice in neutrophil-NP group is significantly smaller than that in PBS group, but comparable with values in anti-IL-1 $\beta$  and anti-TNF- $\alpha$  groups (Fig. 5b). Histological analysis also confirmed reduction of immune infiltration and preservation of cartilage in mice received neutrophil-NPs (Fig. 5c-e). In addition, most FLS in PBS group showed CD248-positive and fibronectin-positive phenotypes as opposed to negative ones in neutrophil-NP and anti-cytokines groups (Fig 5f). Notably, similar



inhibition of CD248 and fibronectin expression with neutrophil-NPs was also observed in synovium tissues further away from cartilage (Supplementary Fig. 18). While the neutrophil-NPs were injected locally and retained primarily at the knee joints (Supplementary Fig. 19), they might still be able to neutralize diffusive arthritic factors and thus elicit a systemic therapeutic response, thereby alleviating overall disease progression and severity. To examine the potential systemic response, we monitored the serum levels of TNF- $\alpha$  and IL-1 $\beta$  in CIA mice, which are known to increase with the onset of arthritis and correlate strongly with disease severity. Surprisingly, alleviated concentrations of these cytokines were observed for the neutrophil-NP and anti-cytokines treated groups as compared to PBS group, indicating effective reduction of arthritis at systemic level (Fig. 5g). In addition, neutrophil-NP group showed the smallest diameter of ankle below the knee (Fig. 5h). Meanwhile, paws of the mice receiving PBS developed erythema and severe swelling; this effect was significantly lessened for mice treated with neutrophil-NPs or anti-cytokines, quantified by measuring paw volume (Fig. 5i, Supplementary Fig. 20) and paw cartilage loss (Supplementary Fig. 21). Moreover, blinded scoring of the swelling and redness of the mouse paws was conducted to evaluate the severity of arthritis of the experimental mice[41]. The results showed that neutrophil-NP treated mice had significantly lower arthritis score as compared to the



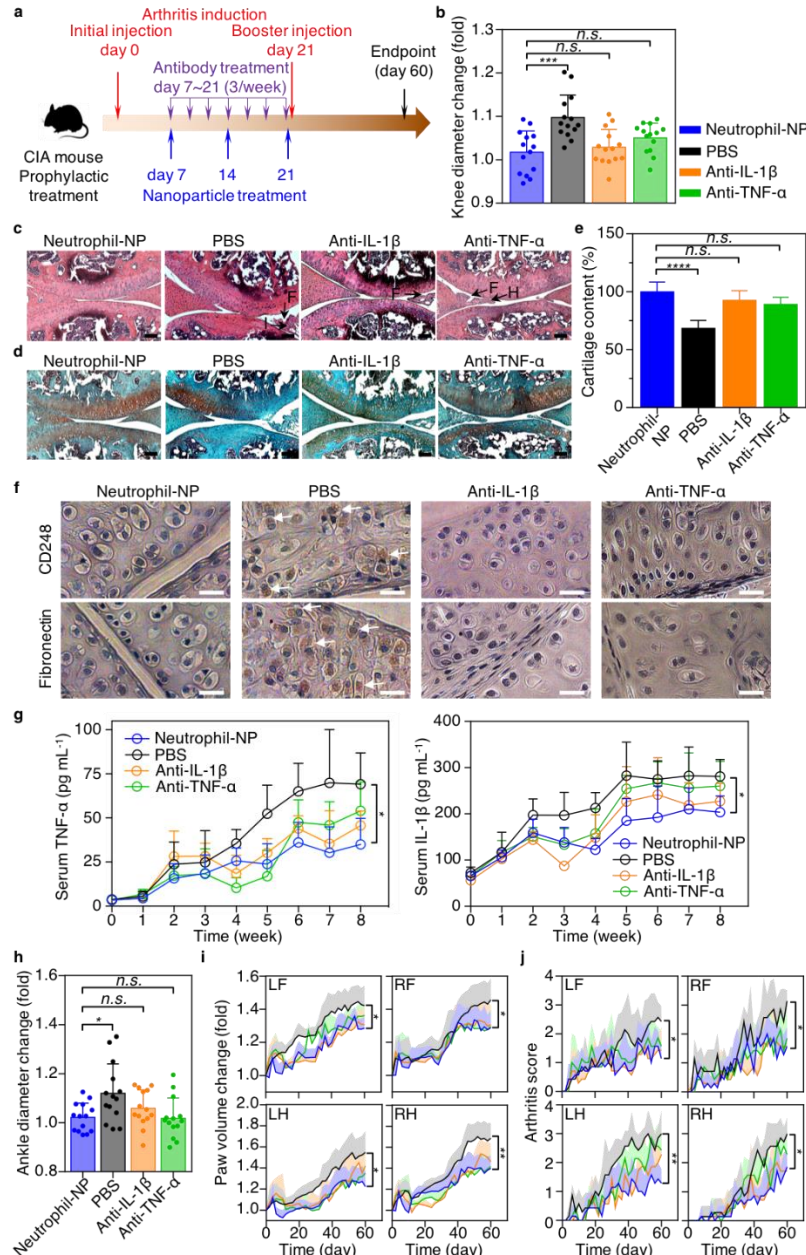


**Figure 4.2.5.** Neutrophil-NPs ameliorate joint destruction and elicit systemic therapeutic response following a prophylactic regimen. **a**, The study protocol of a prophylactic regimen with a collagen-induced arthritis (CIA) mouse model. **b**, Change of hind knee diameter on day 60 after arthritis induction compared to that on day 0. On day 60, mice were euthanized and the hind knees were sectioned for histological analysis. **c-d**, Representative images of H&E staining (**c**) and safranin-O staining (**d**) on knee sections from mice treated with neutrophil-NPs, PBS, anti-IL-1 $\beta$  antibody, or anti-TNF- $\alpha$  antibody (scale bar, 100  $\mu$ m). On the images, F: synovial membrane fibrillation, H: synovium hyperplasia, I: immune cell infiltration. **e**, cartilage content was quantified from safranin-O stained sections of mice treated with neutrophil-NPs, PBS, anti-IL-1 $\beta$  antibody, or anti-TNF- $\alpha$ . **f**, Representative images of CD248 and fibronectin immunohistochemical staining on knee sections (scale bar, 10  $\mu$ m). **g**, Concentration profiles of TNF- $\alpha$  and IL-1 $\beta$  in the serum of CIA mice treated with different groups. **h**, Change of hind ankle diameter on day 60 after arthritis induction compared to that on day 0. **i-j**, Values of paw volume (**i**) and arthritis score (**j**) were recorded every other day for a total of 60 days. Statistical analysis was performed using one-way ANOVA with Dunnett's post hoc analysis. Arthritis score was analyzed by Kruskal-Wallis non-parametric test with Dunnett's post hoc analysis. All data points represent means  $\pm$  s.d. ( $n = 7$ )

PBS group (Fig. 5j). These results clearly demonstrate promising efficacy of neutrophil-NPs in suppressing systemic inflammation and overall arthritis severity.

### **4.2.3 Materials and Methods**

#### **Animal care**

Mice were housed in an animal facility at the University of California San Diego (UCSD) under federal, state, local, and National Institutes of Health (NIH) guidelines for animal care. All animal experiments were performed in accordance with NIH guidelines and approved by the Institutional Animal Care and Use Committee (IACUC) of UCSD.

#### **Neutrophil collection**

Fresh human peripheral blood neutrophils were purchased from ZenBio Inc. and activated within 16 h after the blood collection from human donors. Neutrophils were purified by the manufacturer with OptiPrep<sup>TM</sup> density gradient centrifugation to a purity of approximately 95%[42]. Briefly, leukocyte-rich plasma was layered over a 1.077/1.090 g mL<sup>-1</sup> OptiPrep gradient and centrifuged at 800 ×g for 25 min. Neutrophil fraction was collected between 1.077 and 1.090 g mL<sup>-1</sup> interface. Cells received were washed with 1× PBS and then suspended in serum-free RPMI media (ThermoFisher Scientific) at a density of  $2 \times 10^7$  cells mL<sup>-1</sup>. Neutrophils were then stimulated with 50 ng mL<sup>-1</sup> recombinant human TNF- $\alpha$  (ThermoFisher Scientific) for 2 h at 37 °C in order to activate cells and upregulate adhesion molecules and cytokine receptor expression. Stimulated cells were then washed with 1X PBS, resuspended in 1:1 mixture of serum-free RPMI and HyCryo 2× cryopreservation medium (GE Healthcare), and stored at -80 °C for subsequent membrane derivation. Mouse neutrophils were collected from whole blood of ICR mice (six-week-old, male, Harlan Laboratories) using a modified Percoll® gradient method. Specifically, prior to

the blood collection,  $1.5 \text{ mg kg}^{-1}$  Lipopolysaccharide from *Escherichia coli* K12 (LPS,  $1 \text{ mg mL}^{-1}$  in 1X PBS, InvivoGen) was injected intraperitoneally into the mice to activate neutrophils *in vivo*. After 6 h, blood was collected by submandibular bleeding into heparin tubes. Pooled blood was centrifuged ( $3220 \times g$ , 5 min,  $4^\circ \text{C}$ ) and the buffy coat layer on the top was carefully transferred to the top of a three-layer Percoll® gradient of 78%, 69% and 52%. Samples were centrifuged ( $1500 \times g$ , 30 min,  $4^\circ \text{C}$ ) and cell contents from the interface of the 69% and 78% gradient layers and the upper part of 78% layer were collected. RBC lysis buffer was then added to the sample to lyse the erythrocytes. Neutrophils were purified by washing with 1X PBS three times, suspended, and stored at  $-80^\circ \text{C}$  for subsequent membrane derivation.

A series of experiments were conducted to optimize the neutrophil isolation process and ensure high yield of uniformly activated mouse neutrophils. Mouse neutrophils were co-stained with FITC anti-mouse Gr-1 antibody and PE anti-mouse LFA-1 antibody (Biolegend) to identify mouse neutrophils and examine LFA-1 expression on neutrophil plasma membrane. In the mouse neutrophil activation optimization experiment,  $2 \times 10^6$  mouse neutrophils were stimulated *in vitro* with  $100 \text{ ng mL}^{-1}$  LPS for 6 h. In the collection time optimization experiment, mice were injected with  $1.5 \text{ mg kg}^{-1}$  LPS and whole blood was collected at the designated time points. In the LPS dosage optimization experiment, mice were injected with the designated dosage of LPS, and whole blood was collected at 6 h post-injection. Washed mouse neutrophils were resuspended in PBS at  $1 \times 10^6 \text{ cells mL}^{-1}$  and analyzed by a Becton Dickinson FACSCanto-II flow cytometer. Results were analyzed using FlowJo software.

### **Neutrophil membrane derivation**

Plasma membrane of neutrophils was harvested by following a previously published protocol[43]. Briefly, frozen cells were thawed and washed with 1X PBS three times by

centrifugation at  $800 \times g$ . Cells were then suspended in a hypotonic lysing buffer containing 30 mM Tris-HCl (pH = 7.5), 225 mM D-mannitol (Sigma Aldrich), 75 mM sucrose, 0.2 mM EGTA, and protease and phosphatase inhibitor cocktail (Pierce). Cells were further disrupted using a dounce homogenizer with a tight-fitting pestle. The cell suspension was subjected to 20 passes, followed by centrifugation ( $800 \times g$ , 5 min,  $4^\circ\text{C}$ ). The supernatant was collected while the pellet was suspended in the hypotonic lysing buffer and homogenized again with 20 passes. The solution was combined with supernatant from the first homogenate and centrifuged at  $20,000 \times g$  for 25 min at  $4^\circ\text{C}$ . The pellet was discarded and the supernatant was centrifuged at  $100,000 \times g$  for 35 min at  $4^\circ\text{C}$ . Following the centrifugation, the supernatant was removed and the pellet was washed twice with 0.2 mM EDTA in water. Membrane content was quantified by using a BCA kit (Pierce) to measure the absorbance at 562 nm in comparison with bovine serum albumin (BSA) protein standards. Approximately 125 million human neutrophils or 200 million mouse neutrophils were able to yield 1 mg membrane material (protein weight). Membrane was suspended with 0.2 mM EDTA at a protein concentration of  $4 \text{ mg mL}^{-1}$  and stored at  $-80^\circ\text{C}$  for subsequent studies.

### **RBC membrane derivation**

RBC membrane was derived based on a previously published protocol<sup>18</sup>. Briefly, washed RBCs were resuspended in 0.25X PBS in an ice bath for 20 minutes, then centrifuged at  $800 \times g$  for 5 min. The hemoglobin was removed, and the pink pellet was resuspended in 0.25X PBS in an ice bath again for 20 min. The process was repeated until hemoglobin was completely removed. The RBC membrane was resuspended in water at a protein concentration of  $4 \text{ mg mL}^{-1}$  and stored at  $-80^\circ\text{C}$  for subsequent studies.

### **Synthesis of neutrophil membrane-coated nanoparticles (neutrophil NPs)**

Neutrophil-NPs were synthesized by using a sonication method. Briefly, to synthesize nanoparticle cores, 0.2 mL poly(dl-lactic-co-glycolic acid) (50:50 PLGA, 0.67 dL g<sup>-1</sup>, Lactel Absorbable Polymers) in acetone (20 mg mL<sup>-1</sup>) was added dropwise into 1 mL water. The solution was placed under a vacuum aspirator until organic solvent evaporated completely. For fluorescence imaging experiments, 1,1'-dioctadecyl-3,3,3',3'-tetramethylindodicarbocyanine perchlorate (DiD, excitation = 644 nm/emission = 665 nm, ThermoFisher Scientific) was encapsulated into PLGA cores (0.1 wt%). For membrane coating, neutrophil membrane was mixed with PLGA cores at a polymer-to-membrane protein weight ratio of 2:1. The mixture was then sonicated with a bath sonicator for 2 min (Fisher Scientific FS30D). Red blood cell membrane-coated nanoparticles (RBC-NPs) used in control groups were synthesized by following the same procedure. Coating completeness was confirmed by studying the nanoparticle stability in 1X PBS[44].

### **Nanoparticle characterization**

Neutrophil-NPs were measured for hydrodynamic size and surface zeta potential with dynamic light scattering (DLS) using a Malvern ZEN 3600 Zetasizer. Nanoparticle morphology was studied with transmission electron microscopy (TEM). In the study, samples were deposited on a glow-discharged, carbon-coated, 400-mesh copper grid (Electron Microscopy Sciences). The grid was then washed with distilled water and negatively stained with uranyl acetate (0.2 wt%). The grid was subsequently dried and visualized using an FEI 200 kV Sphera microscope. Neutrophil-specific surface markers on neutrophils, neutrophil membranes and neutrophil-NPs were examined by western blotting. In the study, all samples were prepared in lithium dodecyl sulfate (LDS) sample loading buffer and run at equivalent protein concentrations on NuPAGE Novex 4%-12% Bis-Tris minigels in MOPS running buffer. The gel was transferred onto a

nitrocellulose membrane and probed with antibodies specific for human or mouse CD120b, IL-1R, LFA-1, along with HRP-conjugated secondaries against mouse IgG or rat IgG (Biolegend).

### **Cell culture**

Primary human chondrocytes (Cell Applications) were cultured in human chondrocyte growth medium (Cell Applications) at 37 °C in a 5% CO<sub>2</sub> environment. Cells were used between passages 2 and 6. Human umbilical vein endothelial cells (HUVECs, ATCC) were maintained in human endothelial cell growth medium (Cell Applications) at 37 °C in a 5% CO<sub>2</sub> environment.

### **Neutrophil-NP adhesion assay**

HUVECs or human chondrocytes were seeded in 12-well tissue culture plates at 50% confluency and cultured overnight. Cell culture media was changed and recombinant human TNF- $\alpha$  or IL-1 $\beta$  (ThermoFisher Scientific) was added to the desired concentration. After 6 h of stimulation, cells were washed with 1 $\times$  PBS and fixed with 10% phosphate buffered formalin (Fisher Scientific) for 10 min. Fixed cells were washed and then incubated with 1X PBS containing 1% BSA for 1 h to block the non-specific binding. The cells were then incubated with 0.2 mg mL<sup>-1</sup> DiD-labeled neutrophil-NPs or RBC-NPs in PBS at 4 °C for 60 s. After the incubation, cells were washed five times with ice-cold PBS. Cells were mounted with Vectashield Antifade Mounting Medium with DAPI (Vector Laboratories) and imaged with an EVOS® inverted fluorescence microscope (Thermo Fisher Scientific). For flow cytometric analysis, cells were scraped and collected after PBS wash, then analyzed with a Becton Dickinson FACSCanto-II flow cytometer. Results were analyzed using FlowJo software.

### **Quantification of cytokine binding by neutrophil-NPs**

Recombinant human TNF- $\alpha$  (Thermo Fisher Scientific, final concentration 8.82  $\pm$  0.80 ng mL<sup>-1</sup>) or human IL-1 $\beta$  (Thermo Fisher Scientific, final concentration 7.92  $\pm$  1.28 ng mL<sup>-1</sup>) was

mixed with neutrophil-NPs at final concentrations ranging from 0 to 4 mg mL<sup>-1</sup>. The mixtures were incubated for 2 h at 37 °C and then centrifuged at 16,100 ×g for 10 min to remove the nanoparticles. Nanoparticle removal was confirmed by comparing fluorescence signal from DiD-labeled neutrophil-NP suspension and supernatant after nanoparticles were centrifuged at 16,100 ×g for 10 min. Remaining cytokine concentration in the supernatant was quantified by human TNF-α or human IL-1β ELISA kits (Biolegend) per manufacturer's instruction. Non-linear fitting of the curves was performed in GraphPad Prism 7.

### **Chondrocyte apoptosis assay**

Human chondrocytes were seeded in 12-well tissue culture plates at a density of 1 × 10<sup>6</sup> cells per well and cultured overnight. TNF-α or IL-1β were incubated with neutrophil-NPs or RBC-NPs in chondrocyte culture medium at the desired concentrations at 37 °C for 2 h. Synovial fluid samples from human rheumatoid arthritis patients (Bioreclamation) were filtered with sterile 0.22 μm syringe filter (Spectrum Laboratories) and incubated with neutrophil-NPs or RBC-NPs in chondrocyte culture medium at 37 °C for 2 h. The mixture was then centrifuged at 16,100 ×g for 10 min to remove the nanoparticles. The supernatant was used to stimulate chondrocytes for 48 h. The cells were detached with 0.25% trypsin-EDTA (Life Technologies) and washed with sterile PBS. To determine mitochondrial activity, cells were stained with DiOC<sub>6</sub> (100 nM final concentration from 10 mM stock in 100% ethanol, Life Technologies) for 30 min at 37°C. The cells were washed with PBS and analyzed using a Becton Dickinson FACSCanto-II flow cytometer. Results were analyzed using FlowJo software. For fluorescent imaging experiments, a chondrocyte monolayer was cultured, stimulated, and imaged with an EVOS® inverted fluorescence microscope in tissue culture plates. Apoptotic cells are FITC<sup>dim</sup> while non-apoptotic cells are FITC<sup>bright</sup>. In human synovial fluid experiments, human synovial fluids (Bioreclamation)

were incubated with neutrophil-NPs or RBC-NPs in the same condition. Supernatant was used to stimulate the cells as described above. Statistical analysis was performed using paired t-test ( $n \geq 3$ ).

### **Chondrocyte activation assay**

Cells were prepared in the same way as described above. Cytokines were incubated with nanoparticles in culture media at 37 °C for 2 h. Filtered human rheumatoid arthritis patient synovial fluid samples were incubated with neutrophil-NPs or RBC-NPs in chondrocyte culture medium at 37 °C for 2 h. The mixture was then centrifuged at 16,100  $\times g$  for 10 min to remove the nanoparticles. The supernatant was used to stimulate chondrocytes for 6 h. The cells were then washed with PBS and fixed with 10% phosphate buffered formalin. Cells were stained with anti-human CD54 antibody (Biolegend) for 30 min at room temperature, then stained with FITC-anti-mouse IgG (Biolegend) antibody. Washed cells were scraped and analyzed by a Becton Dickinson FACSCanto-II flow cytometer. Results were analyzed using FlowJo software. For fluorescent imaging experiments, chondrocyte and HUVEC monolayers were cultured and stimulated in tissue culture plates. ICAM-1 expression was probed with anti-human CD54 antibody as described above, then detected with Alexa647-anti-mouse IgG antibody (for HUVECs, Biolegend) and FITC-anti-mouse IgG antibody (for chondrocytes). Cells were then mounted with Vectashield Antifade Mounting Medium with DAPI. An EVOS® inverted fluorescence microscope was used to image the cells. In human synovial fluid experiments, human synovial fluids were incubated with neutrophil-NPs or RBC-NPs in the same condition. Supernatant was used to stimulate the cells as described above. Statistical analysis was performed using paired t-test ( $n \geq 3$ ).



### **Chondrocyte MMP-3 secretion assay**

Chondrocytes were seeded into 96-well tissue culture plates at a concentration of  $1 \times 10^5$  cells/well and cultured overnight. Filtered human rheumatoid arthritis patient synovial fluid samples were diluted  $4 \times$  with chondrocyte culture medium and added to chondrocytes. Neutrophil-NPs or RBC-NPs were added to chondrocytes to achieve a final concentration of  $2 \text{ mg mL}^{-1}$ . At designated timepoint, MMP-3 concentration from undiluted culture medium was quantified with human MMP-3 PicoKine™ ELISA kit per manufacturer's instruction (Boster Biological Technology). Statistical analysis was performed using repeated-measure one-way ANOVA ( $n \geq 3$ ).

### **Chondrocyte aggrecan production assay**

Cells were prepared in the same way described above. Filtered human rheumatoid arthritis patient synovial fluid samples were diluted  $4 \times$  with chondrocyte culture medium and added to chondrocytes. Neutrophil-NPs or RBC-NPs were added to chondrocytes to achieve a final concentration of  $2 \text{ mg mL}^{-1}$ . Cells were cultured at  $37^\circ\text{C}$  for 24 h. After 24 h, culture medium was replaced with fresh culture medium, and fresh synovial fluid samples and nanoparticles were added to the cells. After 3 identical treatments, chondrocytes were washed and stained with anti-human aggrecan antibody (Biolegend) at room temperature for 2 h, and further probed with FITC-anti-mouse IgG antibody at room temperature for 30 min. Washed cells were analyzed by a Becton Dickinson FACSCanto-II flow cytometer. Results were analyzed using FlowJo software. For fluorescence imaging experiment, cells were mounted with Vectashield Antifade Mounting Medium with DAPI and imaged with an EVOS® inverted fluorescence microscope. Statistical analysis was performed using paired t-test ( $n \geq 3$ ).

### **Neutrophil-NP penetration study**

Mouse femoral heads were collected from 12-week-old ICR mice. The femoral heads were cultured for 48 h in high glucose serum-free DMEM medium (4.5 g L<sup>-1</sup> glucose, Hyclone). Following the culture, 10 ng mL<sup>-1</sup> of recombinant mouse IL-1 $\beta$  (ThermoFisher Scientific) was added to the culture on days 0, 1, and 2. Culture medium was changed each time before IL-1 $\beta$  was added. On day 3, 0.2 mg mL<sup>-1</sup> of DiD-labeled mouse neutrophil-NPs were incubated with the femoral heads at 37 °C for 24 h. After incubation, femoral heads were washed with PBS and embedded in Tissue-Tek® O.C.T. Compound (Sakura® Finetek) for frozen sectioning. Frozen sections were mounted with Vectashield Antifade Mounting Medium with DAPI and imaged with an EVOS® inverted fluorescence microscope. Images were analyzed by ImageJ to quantify nanoparticle penetration depth into the inflamed cartilage. Specifically, images were divided into 5  $\mu$ m thick sections, starting from the distal femoral head surface. Fluorescence within each image section was measured by ImageJ and normalized to the fluorescence of the outermost tissue of the neutrophil-NP-treated femoral head. Mouse RBC-NPs were used in the control group.

### **Mouse femoral head degradation assay**

Mouse femoral heads were collected using the same procedure as described above and maintained in high glucose serum-free DMEM medium. To study degradation, 10 ng mL<sup>-1</sup> of IL-1 $\beta$  was mixed with 2 mg mL<sup>-1</sup> neutrophil-NPs in medium and added to femoral head cultures to stimulate cartilage degradation for 48 h. The medium was then changed, and the same amount of cytokine-nanoparticle mixture was added to the femoral heads. A total of 3 treatments, 48 h each, was administered to the samples. The samples were then fixed and processed for safranin-O staining

to detect cartilage loss. The safranin-O positive area was quantified by ImageJ. PBS and mouse RBC-NP-treated samples were used as control groups.

### **Mouse models of inflammatory arthritis**

A collagen-induced arthritis mouse model was established by following a previously published protocol[33]. Specifically, initial immunization was prepared by dropping 1 mg mL<sup>-1</sup> of chicken type-II collagen slowly into 1 mg mL<sup>-1</sup> of Complete Freund's Adjuvant (Sigma Aldrich) while sonicating with a probe sonicator (2 min, 70% power with pulsing of 2 s on and 1 s off, Fisher Scientific 150E Sonic Dismembrator). Then 100 µL of the obtained emulsion was injected intradermally into the tail of DBA/1J mice (8-week-old male, Jackson Laboratory), approximately 1.5 cm distal from the base of the tail. On day 21, a booster immunization was prepared by dropping 1 mg mL<sup>-1</sup> of chicken type-II collagen slowly into 1 mg mL<sup>-1</sup> of Incomplete Freund's Adjuvant (Sigma Aldrich) while sonicating with a probe sonicator. Then 100 µL of the obtained emulsion was administered using the same procedure. Human TNF-α transgenic mice (5-week-old male) were obtained from Taconic Biosciences and allowed to accustom to standard housing conditions for one week. Mice were randomized before the experiment.

### **Study protocols for evaluating neutrophil-NPs in vivo**

To study joint protection with CIA mice, 20 µL of mouse neutrophil-NPs (2 mg mL<sup>-1</sup>) was injected into each knee joint of the hind legs on days 28 (first day of obvious clinical signs of arthritis), 30, 32, 34, 36, and 38. Sterile PBS was injected intra-articularly on the same days as negative control. Positive control mice were injected intraperitoneally with an anti-mouse IL-1β antibody (3 mg kg<sup>-1</sup>) or an anti-mouse TNF-α antibody (3 mg kg<sup>-1</sup>) three times a week from day 28 to 60. To study joint protection with human TNF-α transgenic mice, 20 µL of mouse neutrophil-

NPs ( $2 \text{ mg mL}^{-1}$ ) was injected into each knee joint of the hind legs on days 42, 45, 49, 52, 56, 59, 63, and 66. Sterile PBS was injected intra-articularly on the same days as negative control. An anti-human TNF- $\alpha$  antibody ( $10 \text{ mg kg}^{-1}$ , Biolegend) was administered intraperitoneally on days 42, 49, 56, and 63 as positive control. To study the reduction of overall arthritis with CIA mice,  $20 \text{ }\mu\text{L}$  of mouse neutrophil-NPs ( $2 \text{ mg mL}^{-1}$ ) was injected into each knee joint of the hind legs on days 7, 14, and 21. Sterile PBS was injected intra-articularly on the same days as negative control. Positive control mice were injected intraperitoneally with an anti-mouse IL-1 $\beta$  antibody ( $3 \text{ mg kg}^{-1}$ ) or an anti-mouse TNF- $\alpha$  antibody ( $3 \text{ mg kg}^{-1}$ ) three times a week from day 7 to 21.

### **Histological analysis of mouse knee joints**

Mice were euthanized on day 60 of CIA studies and on day 70 of human TNF- $\alpha$  transgenic mouse study and hind knee joints were collected and processed for histological analysis. To study immune cell infiltration, morphological change in the joint space, and cartilage erosion, mouse hind knee joints were sectioned and stained with hematoxylin and eosin (H&E) staining and safranin-O staining. To analyze fibroblast-like synoviocyte activation, knee joint sections were stained with a rabbit anti-CD248 antibody (Bioss Antibodies) or a rabbit anti-fibronectin antibody (Novus Biologicals). CD248 and fibronectin were detected using biotinylated anti-rabbit IgG secondary antibody for chromagen development. Sections were counter-stained with hematoxylin to visualize cell nuclei. Images were taken with a Micromaster<sup>TM</sup> II Microscope (Fisher Scientific). The safranin-O positive area was quantified by using ImageJ.

### **Quantification of serum cytokines**

To study the attenuation of systemic inflammatory response, CIA mouse serum samples were collected on days 8, 15, 22, 29, 36, 43, 50, 57 and concentrations of IL-1 $\beta$  and TNF- $\alpha$  were quantified with ELISA. Specifically, CIA mouse whole blood was collected by submandibular

bleeding into Eppendorf tube and was allowed to clot at room temperature for 30 min. Samples were then centrifuged at  $2,000 \times g$  for 6 min to collect serum from supernatant. Serum samples were immediately frozen at  $-20^{\circ}\text{C}$  until analysis by using mouse IL- $1\beta$  and mouse TNF- $\alpha$  ELISA kits (Biolegend) within 3 days after collection.

### **Joint swelling assessment and arthritis scoring**

Mouse hind knee joint diameters were measured with a digital caliber at study endpoint of CIA studies and human TNF- $\alpha$  transgenic mouse study. To study the reduction of overall arthritis with CIA mice, images of mouse paws were taken every 2 days from day 0 to day 60 and paw volumes were calculated by analyzing images with ImageJ. Specifically, paw volume was measured by taking top and side view images of each paw on a ruler. The length, width, and thickness of mouse paws were measured against the ruler. Paw volume was approximated as the product of these three parameters in order to assign equivalent importance to each parameter in reflecting the extent of inflammation in the paw. In addition, paw scorings (score = 0~4) were given from day 0 to day 60 by a blinded researcher based on the following criteria: 0—normal; 1—mild redness of ankle or tarsal joints; 2—mild redness and swelling extending from ankle to the tarsals; 3—moderate redness and swelling from ankle to metatarsal joints; 4—severe redness and swelling encompassing the ankle, foot and digits. Hind ankle joint diameters were measured with a digital caliber at day 60.

Statistical analysis was performed using one-way ANOVA. Paw scoring data was analyzed by using Kruskal-Wallis test. Replicates represent different mice subjected to the same treatment. In CIA studies,  $n = 7$  for all groups. In human TNF- $\alpha$  transgenic mouse study,  $n = 5$  for neutrophil-NP group and anti-TNF- $\alpha$  antibody group,  $n = 3$  for PBS group

#### 4.2.4 Conclusion

In summary, we have developed neutrophil-NPs and demonstrated their potential as an anti-inflammatory strategy for RA management. Neutrophil-NPs inherit the antigenic exterior of their sources cells and act as decoys capable of engaging in the interfacing roles of neutrophils without potentiating inflammatory processes that can promote RA. Unlike existing anti-cytokine agents that inhibit specific and limited targets, neutrophil-NPs provide a function-driven, broad-spectrum, and disease-relevant blockade that dampens the inflammation cascade in the disease process. In addition, the direct use of membrane from the effector cells of the disease allows neutrophil-NPs to neutralize highly relevant inflammatory factors without the need to identify them. Even if the target is known, the top down fabrication of neutrophil-NPs can avoid the necessity to engineer binding motifs that are often difficult to identify, synthesize, and conjugate.

In this work we chose to mimic neutrophils for nanoparticle fabrication and anti-inflammatory efficacy. Notably, the rheumatoid synovium contains a mixture of cells with origins of monocytes, macrophages, dendritic cells, and T cells, which together orchestrate RA process[6, 45]. Membrane of these cells can be also derived for coating and combined with other nanotherapeutic agents for targeted and synergistic therapy for RA[46][47]. Similarly to RA, various infections, traumatic injuries, and chronic diseases are marked by inflammatory responses that can damage host tissue and cause organ dysfunction[48]. The neutrophil-NPs developed here can likely be adopted to address some of these diseases, promising to eventually improve the clinical outcomes of the patients. Regarding future clinical translation of neutrophil-NPs, it is critical to consider scale-up and manufacturing issues because of the use of naturel cell membranes. In terms of the source materials, bioprocesses for *ex vivo* production of neutrophils at a clinical scale can supply large quantity of neutrophil membranes[49]. Meanwhile, significant

progress has been made in producing human cells with universal immune compatibility, which would also enable cell supply for clinical studies[50]. These technological advances together offer a promising prospect to the translation of neutrophil-NPs and cell membrane-coating technology in general.

### **Acknowledgements**

This work is supported by the Defense Threat Reduction Agency Joint Science and Technology Office for Chemical and Biological Defense under Grant Number HDTRA1-14-1-0064 and the National Science Foundation Grant DMR-1505699.

Chapter 4.2 is, in full, is a reprint of the material as it appears in Nature Nanotechnology, 2018, Qiangzhe Zhang, Diana Dehaini, Yue Zhang, Julia Zhou, Xiangyu Chen, Lifen Zhang, Ronnie H. Fang, Weiwei Gao, Liangfang Zhang. The dissertation author was a major contributor and co-author of this paper.

## References:

- [1] J.S. Smolen, D. Aletaha, Rheumatoid arthritis therapy reappraisal: strategies, opportunities and challenges, *Nat. Rev. Rheumatol.*, 11 (2015) 276-289.
- [2] G.S. Firestein, Evolving concepts of rheumatoid arthritis, *Nature*, 423 (2003) 356-361.
- [3] G.S. Firestein, I.B. McInnes, Immunopathogenesis of Rheumatoid Arthritis, *Immunity*, 46 (2017) 183-196.
- [4] G.R. Burmester, E. Feist, T. Doerner, Emerging cell and cytokine targets in rheumatoid arthritis, *Nat. Rev. Rheumatol.*, 10 (2014) 77-88.
- [5] G.N. Goulielmos, M.I. Zervou, E. Myrthianou, A. Burska, T.B. Niewold, F. Ponchel, Genetic data: The new challenge of personalized medicine, insights for rheumatoid arthritis patients, *Gene*, 583 (2016) 90-101.
- [6] I.B. McInnes, G. Schett, Cytokines in the pathogenesis of rheumatoid arthritis, *Nat. Rev. Immunol.*, 7 (2007) 429-442.
- [7] M. Noack, P. Miossec, Selected cytokine pathways in rheumatoid arthritis, *Semin. Immunopathol.*, 39 (2017) 365-383.
- [8] E.H.S. Choy, G.S. Panayi, Mechanisms of disease: Cytokine pathways and joint inflammation in rheumatoid arthritis, *New Engl. J. Med.*, 344 (2001) 907-916.
- [9] J.S. Smolen, D. Aletaha, M. Koeller, M.H. Weisman, P. Emery, New therapies for treatment of rheumatoid arthritis, *Lancet*, 370 (2007) 1861-1874.
- [10] V. Bykerk, Unmet Needs in Rheumatoid Arthritis, *J. Rheumatol.*, 36 (2009) 42-46.
- [11] P.C. Taylor, A. Moore, R. Vasilescu, J. Alvir, M. Tarallo, A structured literature review of the burden of illness and unmet needs in patients with rheumatoid arthritis: a current perspective, *Rheumatol. Int.*, 36 (2016) 685-695.
- [12] S. Iwata, Y. Tanaka, Progress in understanding the safety and efficacy of Janus kinase inhibitors for treatment of rheumatoid arthritis, *Expert Rev. Clin. Immunol.*, 12 (2016) 1047-1057.
- [13] J.S. Smolen, F.C. Breedveld, G.R. Burmester, V. Bykerk, M. Dougados, P. Emery, T.K. Kvien, M.V. Navarro-Compan, S. Oliver, M. Schoels, M. Scholte-Voshaar, T. Stamm, M. Stoffer, T. Takeuchi, D. Aletaha, J.L. Andreu, M. Aringer, M. Bergman, N. Betteridge, H. Bijlsma, H. Burkhardt, M. Cardiel, B. Combe, P. Durez, J.E. Fonseca, A. Gibofsky, J.J. Gomez-Reino, W. Graninger, P. Hannonen, B. Haraoui, M. Kouloumas, R. Landewe, E. Martin-Mola, P. Nash, M. Ostergaard, A. Ostor, P. Richards, T. Sokka-Isler, C. Thorne, A.G. Tzioufas, R. van Vollenhoven, M. de Wit, D. van der Heijde, Treating rheumatoid arthritis to target: 2014 update of the recommendations of an international task force, *Ann. Rheum. Dis.*, 75 (2016) 3-15.



- [14] C.M.J. Hu, R.H. Fang, J. Copp, B.T. Luk, L. Zhang, A biomimetic nanosponge that absorbs pore-forming toxins, *Nat. Nanotechnol.*, 8 (2013) 336-340.
- [15] C.M.J. Hu, R.H. Fang, K.C. Wang, B.T. Luk, S. Thamphiwatana, D. Dehaini, P. Nguyen, P. Angsantikul, C.H. Wen, A.V. Kroll, C. Carpenter, M. Ramesh, V. Qu, S.H. Patel, J. Zhu, W. Shi, F.M. Hofman, T.C. Chen, W. Gao, K. Zhang, S. Chien, L. Zhang, Nanoparticle biointerfacing by platelet membrane cloaking, *Nature*, 526 (2015) 118-121.
- [16] J.A. Copp, R.H. Fang, B.T. Luk, C.M.J. Hu, W. Gao, K. Zhang, L. Zhang, Clearance of pathological antibodies using biomimetic nanoparticles, *Proc. Natl. Acad. Sci. U. S. A.*, 111 (2014) 13481-13486.
- [17] S. Thamphiwatana, P. Angsantikul, T. Escajadillo, Q. Zhang, J. Olson, B.T. Luk, S. Zhang, R.H. Fang, W. Gao, V. Nizet, L. Zhang, Macrophage-like nanoparticles concurrently absorbing endotoxins and proinflammatory cytokines for sepsis management, *Proc. Natl. Acad. Sci. U. S. A.*, 114 (2017) 11488-11493.
- [18] P.P. Tak, T.J.M. Smeets, M.R. Daha, P.M. Kluin, K.A.E. Meijers, R. Brand, A.E. Meinders, F.C. Breedveld, Analysis of the synovial cell infiltrate in early rheumatoid synovial tissue in relation to local disease activity, *Arthritis Rheum.*, 40 (1997) 217-225.
- [19] M. Horckmans, L. Ring, J. Duchene, D. Santovito, M.J. Schloss, M. Drechsler, C. Weber, O. Soehnlein, S. Steffens, Neutrophils orchestrate post-myocardial infarction healing by polarizing macrophages towards a reparative phenotype, *Eur. Heart J.*, 38 (2017) 187-197.
- [20] J. Dalli, T. Montero-Melendez, L.V. Norling, X.K. Yin, C. Hinds, D. Haskard, M. Mayr, M. Perretti, Heterogeneity in Neutrophil Microparticles Reveals Distinct Proteome and Functional Properties, *Mol. Cell. Proteomics*, 12 (2013) 2205-2219.
- [21] S.E. Headland, H.R. Jones, L.V. Norling, A. Kim, P.R. Souza, E. Corsiero, C.D. Gil, A. Nerviani, F. Dell'Accio, C. Pitzalis, S.M. Oliani, L.Y. Jan, M. Perretti, Neutrophil-derived microvesicles enter cartilage and protect the joint in inflammatory arthritis, *Sci. Transl. Med.*, 7 (2015) article number 315ra190.
- [22] H.L. Wright, R.J. Moots, S.W. Edwards, The multifactorial role of neutrophils in rheumatoid arthritis, *Nat. Rev. Rheumatol.*, 10 (2014) 593-601.
- [23] B.T. Wipke, P.M. Allen, Essential role of neutrophils in the initiation and progression of a murine model of rheumatoid arthritis, *J. Immunol.*, 167 (2001) 1601-1608.
- [24] J. Cedergren, T. Forslund, T. Sundqvist, T. Skogh, Intracellular oxidative activation in synovial fluid neutrophils from patients with rheumatoid arthritis but not from other arthritis patients, *J. Rheumatol.*, 34 (2007) 2162-2170.
- [25] A. Chakravarti, M.A. Raquil, P. Tessier, P.E. Poubelle, Surface RANKL of Toll-like receptor 4-stimulated human neutrophils activates osteoclastic bone resorption, *Blood*, 114 (2009) 1633-1644.

- [26] H.L. Wright, T. Cox, R.J. Moots, S.W. Edwards, Neutrophil biomarkers predict response to therapy with tumor necrosis factor inhibitors in rheumatoid arthritis, *J. Leukocyte Biol.*, 101 (2017) 785-795.
- [27] C.-M.J. Hu, L. Zhang, S. Aryal, C. Cheung, R.H. Fang, L. Zhang, Erythrocyte membrane-camouflaged polymeric nanoparticles as a biomimetic delivery platform, *Proc. Natl. Acad. Sci. U. S. A.*, 108 (2011) 10980-10985.
- [28] L.S. Declerck, C.M. Degendt, C.H. Bridts, N. Vanosselaer, W.J. Stevens, EXPRESSION OF NEUTROPHIL ACTIVATION MARKERS AND NEUTROPHIL ADHESION TO CHONDROCYTES IN RHEUMATOID-ARTHRITIS PATIENTS - RELATIONSHIP WITH DISEASE-ACTIVITY, *Res. Immunol.*, 146 (1995) 81-87.
- [29] E. Karsten, E. Breen, B.R. Herbert, Red blood cells are dynamic reservoirs of cytokines, *Sci. Rep.*, 8 (2018) article number 3101.
- [30] E. Brzustewicz, I. Bzoma, A. Daca, M. Szarecka, M.S. Bykowska, J.M. Witkowski, E. Bryl, Heterogeneity of the cytokinome in undifferentiated arthritis progressing to rheumatoid arthritis and its change in the course of therapy. Move toward personalized medicine, *Cytokine*, 97 (2017) 1-13.
- [31] K. Ley, C. Laudanna, M.I. Cybulsky, S. Nourshargh, Getting to the site of inflammation: the leukocyte adhesion cascade updated, *Nat. Rev. Immunol.*, 7 (2007) 678-689.
- [32] E.P. Schmidt, Y.M. Yang, W.J. Janssen, A. Gandjeva, M.J. Perez, L. Barthel, R.L. Zemans, J.C. Bowman, D.E. Koyanagi, Z.X. Yunt, L.P. Smith, S.S. Cheng, K.H. Overdier, K.R. Thompson, M.W. Geraci, I.S. Douglas, D.B. Pearce, R.M. Tuder, The pulmonary endothelial glycocalyx regulates neutrophil adhesion and lung injury during experimental sepsis, *Nat. Med.*, 18 (2012) 1217-1223.
- [33] D.D. Brand, K.A. Latham, E.F. Rosloniec, Collagen-induced arthritis, *Nat. Protoc.*, 2 (2007) 1269-1275.
- [34] R.O. Williams, L. Marinova-Mutafchieva, M. Feldmann, R.N. Maini, Evaluation of TNF-alpha and IL-1 blockade in collagen-induced arthritis and comparison with combined anti-TNF-alpha/anti-CD4 therapy, *J. Immunol.*, 165 (2000) 7240-7245.
- [35] L.A.B. Joosten, M.M.A. Helsen, T. Saxne, F.A.J. van de Loo, D. Heinegard, W.B. van den Berg, IL-1 alpha beta blockade prevents cartilage and bone destruction in murine type II collagen-induced arthritis, whereas TNF-alpha blockade only ameliorates joint inflammation, *J. Immunol.*, 163 (1999) 5049-5055.
- [36] M. Maia, A. de Vriese, T. Janssens, M. Moons, K. Van Landuyt, J. Tavernier, R.J. Lories, E.M. Conway, CD248 and Its Cytoplasmic Domain A Therapeutic Target for Arthritis, *Arthritis Rheum.*, 62 (2010) 3595-3606.

- [37] V. Pascual, F. Allantaz, E. Arce, M. Punaro, J. Banchereau, Role of interleukin-1 (IL-1) in the pathogenesis of systemic onset juvenile idiopathic arthritis and clinical response to IL-1 blockade, *J. Exp. Med.*, 201 (2005) 1479-1486.
- [38] B. Bartok, G.S. Firestein, Fibroblast-like synoviocytes: key effector cells in rheumatoid arthritis, *Immunol. Rev.*, 233 (2010) 233-255.
- [39] P. Li, E.M. Schwarz, The TNF-alpha transgenic mouse model of inflammatory arthritis, *Springer Semin. Immunopathol.*, 25 (2003) 19-33.
- [40] D.J. Shealy, P.H. Wooley, E. Emmell, A. Volk, A. Rosenberg, G. Treacy, C.L. Wagner, L. Mayton, D.E. Griswold, X.Y.R. Song, Anti-TNF-alpha antibody allows healing of joint damage in polyarthritic transgenic mice, *Arthritis Res.*, 4 (2002) article number R7.
- [41] S. Seeuws, P. Jacques, J. Van Praet, M. Drennan, J. Coudenys, T. Decruy, E. Deschepper, L. Lepescheux, P. Pujuguet, L. Oste, N. Vandeghinste, R. Brys, G. Verbruggen, D. Elewaut, A multiparameter approach to monitor disease activity in collagen-induced arthritis, *Arthrit. Res. Ther.*, 12 (2010) article number R160.
- [42] J.M. Graham, Isolation of human polymorphonuclear leukocytes (granulocytes) from a leukocyte-rich fraction, *Scientific World Journal*, 2 (2002) 1393-1396.
- [43] R. Fang, C.-M. Hu, B. Luk, W. Gao, J. Copp, Y. Tai, D. O'Connor, L. Zhang, Cancer cell membrane-coated nanoparticles for anticancer vaccination and drug delivery, *Nano Lett.*, 14 (2014) 2181-2188.
- [44] B.T. Luk, C.M.J. Hu, R.N.H. Fang, D. Dehaini, C. Carpenter, W. Gao, L. Zhang, Interfacial interactions between natural RBC membranes and synthetic polymeric nanoparticles, *Nanoscale*, 6 (2014) 2730-2737.
- [45] J.M. Kremer, R. Westhovens, M. Leon, E. Di Giorgio, R. Alten, S. Steinfeld, A. Russell, M. Dougados, P. Emery, I.F. Nuamah, G.R. Williams, J.C. Becker, D.T. Hagerty, L.W. Moreland, Treatment of rheumatoid arthritis by selective inhibition of T-cell activation with fusion protein CTLA4Ig, *New Engl. J. Med.*, 349 (2003) 1907-1915.
- [46] T. Kang, Q.Q. Zhu, D. Wei, J.X. Feng, J.H. Yao, T.Z. Jiang, Q.X. Song, X.B. Wei, H.Z. Chen, X.L. Gao, J. Chen, Nanoparticles Coated with Neutrophil Membranes Can Effectively Treat Cancer Metastasis, *ACS Nano*, 11 (2017) 1397-1411.
- [47] S. Dolati, S. Sadreddini, D. Rostamzadeh, M. Ahmadi, F. Jadidi-Niaragh, M. Yousefi, Utilization of nanoparticle technology in rheumatoid arthritis treatment, *Biomed. Pharmacother.*, 80 (2016) 30-41.
- [48] I. Tabas, C.K. Glass, Anti-Inflammatory Therapy in Chronic Disease: Challenges and Opportunities, *Science*, 339 (2013) 166-172.

[49] Z. Jie, Y. Zhang, C. Wang, B. Shen, X. Guan, Z. Ren, X. Ding, W. Dai, Y. Jiang, Large-scale ex vivo generation of human neutrophils from cord blood CD34(+) cells, PLoS One, 12 (2017) article number e0180832.

[50] Q. Feng, N. Shabrani, J.N. Thon, H. Huo, A. Thiel, K.R. Machlus, K. Kim, J. Brooks, F. Li, C. Luo, E.A. Kimbrel, J. Wang, K.-S. Kim, J. Italiano, J. Cho, S.-J. Lu, R. Lanza, Scalable Generation of Universal Platelets from Human Induced Pluripotent Stem Cells, Stem Cell Reports, 3 (2014) 817-831.

# Chapter 5

---

## Cell Membrane Fusion Platforms for Multifunctional Nanoparticles

## **5.1 Erythrocyte-Platelet Hybrid Membrane Coating for Enhanced Nanoparticle Functionalization**

### **5.1.1 Introduction**

Nanotechnology has increasingly been employed for the design of drug delivery and imaging modalities in order to further improve efficacy in the clinic. There are many classes of nanoscale delivery vehicles, including liposomes, polymeric nanoparticles, and inorganic systems among many others.<sup>[1–4]</sup> For applications such as cancer treatment, the use of such nanoparticle platforms has the potential to enable greatly enhanced potency while minimizing the systemic toxicity associated with traditional therapeutics.<sup>[5–9]</sup> Recently, a new class of drug nanocarrier has been reported that is fabricated by combining synthetic nanoparticulate cores with a biologically derived membrane coating.<sup>[10–13]</sup> These biomimetic, cell membrane-coated nanoparticles directly leverage the versatility and complexity of cellular membrane, which has been crafted by nature through the process of evolution to perform specific functions, especially with regards to biointerfacing.<sup>[14–17]</sup> By translocating the entire membrane from a cell onto the surface of a nanoparticle, all biologically relevant surface moieties are transferred, including those that can potentially be used for immune evasion and targeting, two highly desirable properties. Additionally, it may be possible to take advantage of cell-specific functionalities that are known to exist, but have not been well characterized on a fundamental biological level.<sup>[18–20]</sup> The first platform of this type employed red blood cells (RBCs), also known as erythrocytes, as the source material in order to achieve lengthened blood residency, and the resulting RBC membrane-coated nanoparticles (RBCNPs) displayed significantly enhanced circulation half-lives compared with a nanoparticle stabilized by a layer of polyethylene glycol (PEG).<sup>[21]</sup> It was later demonstrated that

these cell membrane-coated nanoparticles exhibited right-side-out membrane orientation and included immunomodulatory markers such as CD47 at the same density as the original RBCs.<sup>[22]</sup> RBCNPs have also been used for novel detoxification applications, including for toxic nerve agents and bacterial toxins.<sup>[23–26]</sup> More recently, many different cell types other than RBCs have been used to source the membrane material, each with its own set of unique characteristics.<sup>[14,18,27–29]</sup> Of note, expansion of the cell membrane-coated platform to other cells has enabled the fabrication of naturally targeted drug carriers.<sup>[30]</sup> This includes the use of cancer cells for homotypic delivery to the tumor of origin, or platelets, which are implicated in a wide array of different diseases that range from atherosclerosis to bacterial infection.

### 5.1.2 Results and Discussion

While cell membrane coating is a powerful method of enhancing nanoparticle utility, it is often desirable to introduce additional functionality depending on the specific application. For example, while RBCNPs can circulate for extended periods of time, the addition of a targeting ligand can help to improve localization to the desired target, such as a tumor.<sup>[31]</sup> Herein, we report on an approach for combining the functionality from two different cells into a single nanocarrier. This approach, which involves the fusion of two types of natural cell membranes, represents a facile and effective means of fashioning nanoparticles that can perform increasingly complex tasks within biologically relevant contexts. Specifically, we aimed to combine the functionality of human-derived RBCs and platelets (**Figure 1A**). The resulting RBC-platelet hybrid membrane-coated nanoparticles ([RBC-P]NPs) were thoroughly characterized, and it was demonstrated that they retained functionality that is characteristic of each individual cell type. Finally, we show that

these dual membrane-coated nanoparticles displayed *in vivo* properties consistent with expectations, warranting further study.

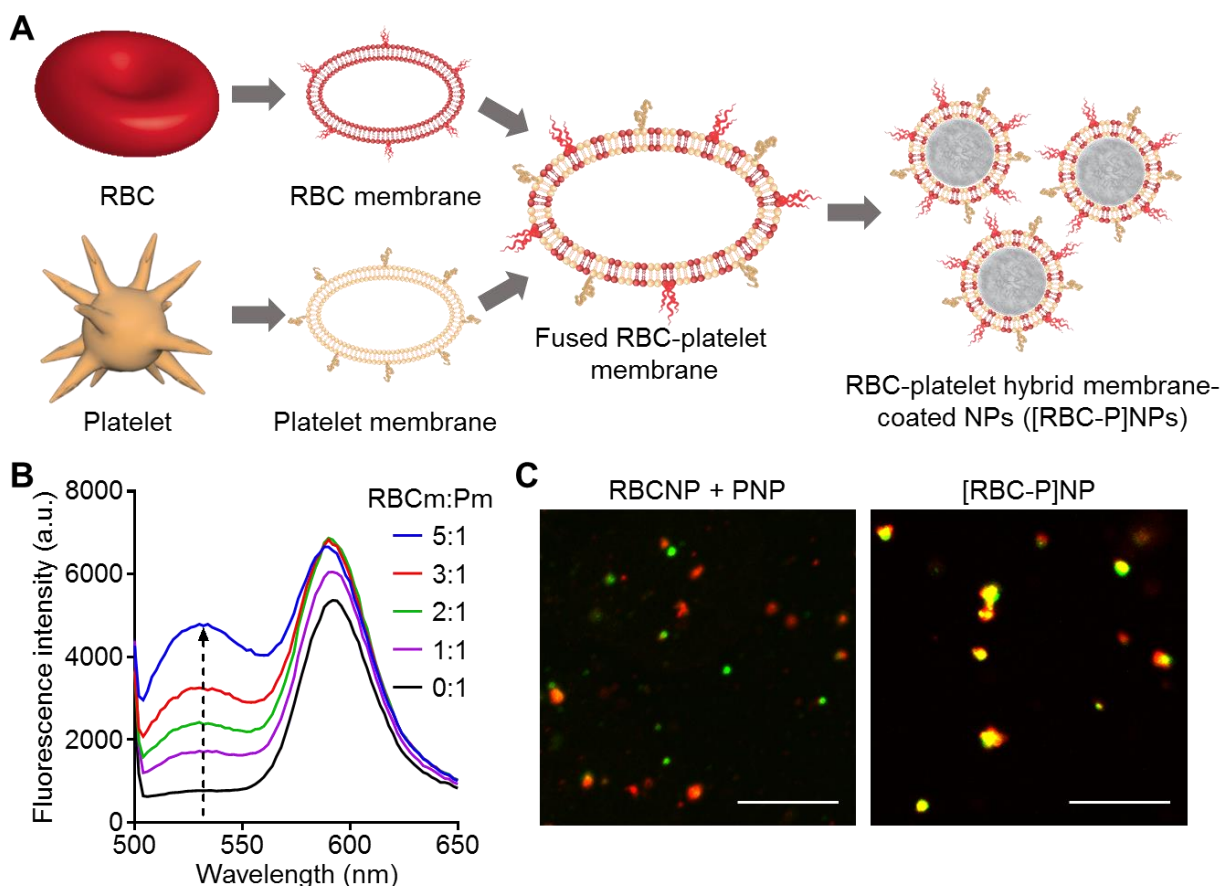


**Figure 5.1.1.** Fabrication of RBC-platelet hybrid membrane-coated nanoparticles (denoted [RBC-P]NPs). A) Schematic of membrane fusion and coating. Membrane material is derived from both RBCs and platelets and then fused together. The resulting fused membrane is used to coat poly(lactic-co-glycolic acid) (PLGA) polymeric cores to produce [RBC-P]NPs. B) Platelet membrane was doped with a FRET pair of fluorescent probes and mixed with increasing amounts of RBC membrane. The recovery of the fluorescence emission from the donor at the lower emission peak (534 nm) was monitored (RBCm:Pm = RBC membrane to platelet membrane protein ratio). C) Confocal fluorescent microscopy images of either a mixture of RBCNPs and PNPs or of the [RBC-P]NPs (red = RBC membrane, green = platelet membrane; scale bar = 10  $\mu$ m).

In order to fabricate the [RBC-P]NPs, the first step was to verify that it was possible to fuse RBC membrane and platelet membrane together, the product of which would then be used as the base material for downstream nanoparticle preparation. To test for fusion, platelet membrane was doped with two different dyes that constituted a Förster resonance energy transfer (FRET) pair and



added to increasing amounts of RBC membrane under elevated temperature and stirring (Figure 1B). It was observed that, as the amount of RBC material increased, there was a recovery of fluorescence at the lower emission wavelength around 534 nm, indicating the interspersing of the two membrane materials weakening the FRET interactions in the original platelet membrane. Using a 1:1 protein weight ratio of RBC membrane to platelet membrane, we fabricated a batch of the hybrid [RBC-P]NPs. RBC membrane labeled with a red fluorescent dye was fused with platelet

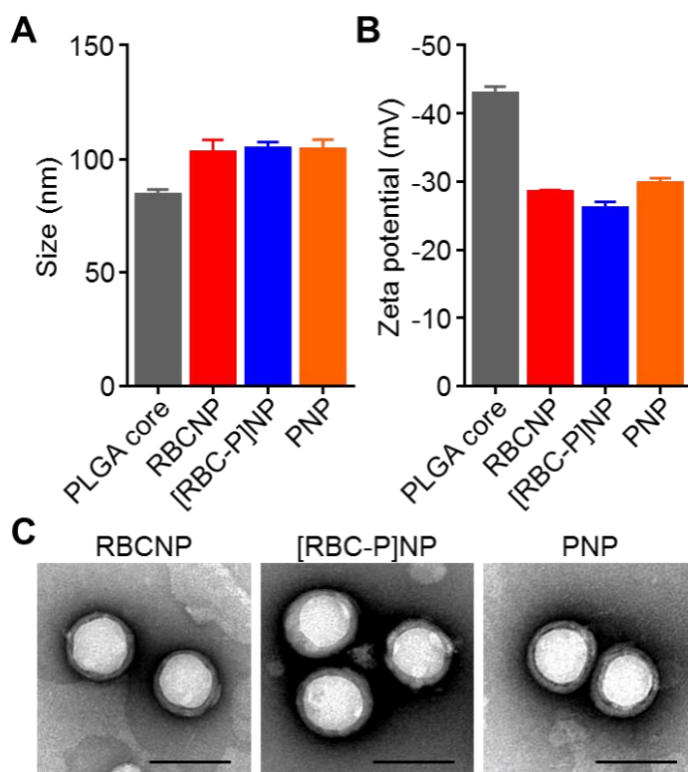


**Figure 5.1.2.** Physicochemical characterization. A) Z-average size of bare PLGA cores, RBCNPs, [RBC-P]NPs, and PNPs as measured by DLS ( $n = 3$ ; mean  $\pm$  SD). B) Surface zeta potential of bare PLGA cores, RBCNPs, [RBC-P]NPs, and PNPs as measured by DLS ( $n = 3$ ; mean  $\pm$  SD). C) Representative TEM images of RBCNPs, [RBC-P]NPs, and PNPs negatively stained with vanadium (scale bar = 100 nm).

membrane that was labeled with a green fluorescent dye, and the resultant material was coated onto preformed poly(lactic-*co*-glycolic acid) (PLGA) cores. When a dilute solution of the [RBC-P]NPs was immobilized in glycerol and viewed under confocal microscopy, significant colocalization of fluorescent signals was observed (Figure 1C). In stark contrast, a mixture of RBCNPs and platelet membrane-coated nanoparticles (PNPs) fabricated with the individual

fluorescently labeled membranes exhibited distinct red and green punctates. The results indicate that it was indeed possible to fuse the two types of natural cell membrane and incorporate the material of both onto the same nanoparticle.

Dynamic light scattering (DLS) was used to compare the [RBC-P]NPs with each single membrane formulation of RBCNPs or PNPs (**Figure 2A,B**). It was observed that bare PLGA cores, which were originally 80 nm in size, exhibited a very uniform increase in size of approximately 20 nm after coating with each membrane. Additionally, the surface zeta potential increased by over 10 mV for each of the three nanoparticle types compared with PLGA cores, a phenomenon commonly seen after membrane coating that indicates shielding of the highly negative cores with the less negative outer membrane surface.<sup>[14,21]</sup> When visualized under transmission electron microscopy (TEM), the RBCNPs, PNPs, and hybrid [RBC-P]NPs all displayed a characteristic core-shell structure that was consistent with the sizing results (Figure 2C). A set of assays were then carried out to assess nanoparticle stability in various media. To determine stability of the hybrid formulation in solution over time, samples were stored in either water or 1× phosphate buffered saline (PBS, pH 7.4) and the size was measured over time (**Figure 3A,B**). The [RBC-P]NPs, in addition to RBCNPs and PNPs, exhibited stable size over the 3 week duration of the study in both solutions. In contrast, bare PLGA cores, which are only stabilized by charge repulsion, immediately aggregated in PBS to the micron range. Additionally, [RBC-P]NPs displayed little change in absorbance before and after incubation with 100% serum, while bare PLGA cores again exhibited a large increase (Figure 3C). Taken together, the characterization data give strong physical evidence for successful coating by the fused membrane material, with results in line with what would be expected given the properties of the single membrane-coated RBCNPs and PNPs.

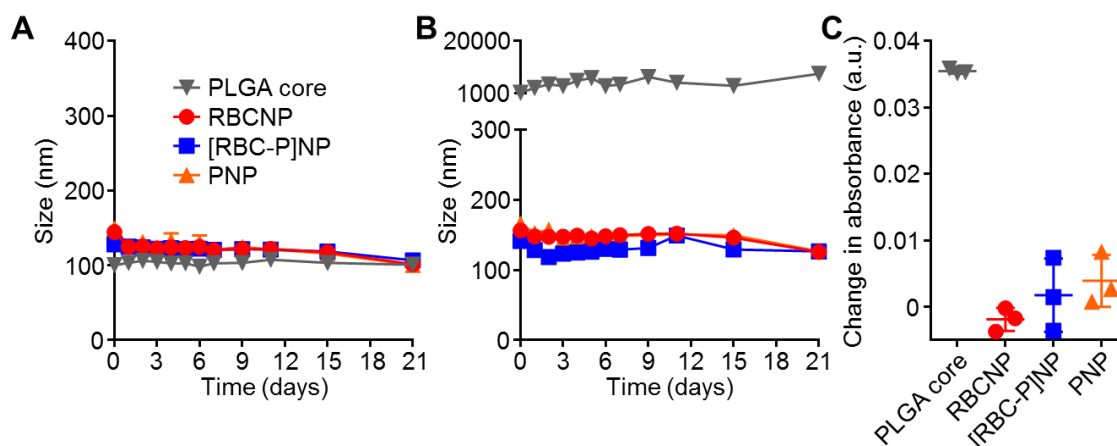


**Figure 5.1.3.** Nanoparticle stability. A) Z-average size of bare PLGA cores, RBCNPs, [RBC-P]NPs, and PNPs over 3 weeks in water ( $n = 3$ ; mean  $\pm$  SD). B) Z-average size of bare PLGA cores, RBCNPs, [RBC-P]NPs, and PNPs over 3 weeks in PBS ( $n = 3$ ; mean  $\pm$  SD). C) Change in absorbance at 560 nm of PLGA cores, RBCNPs, [RBC-P]NPs, and PNPs after transferring into 100% serum from water. An increase in absorbance was used to indicate particle aggregation.

To analyze the overall protein content of the [RBC-P]NPs, SDS-PAGE was used to run RBC membrane, platelet membrane, hybrid membrane, and all corresponding nanoparticle formulations followed by Coomassie staining for visualization (**Figure 4A**). Compared with RBCNPs and PNPs, the [RBC-P]NPs had a profile that represented the union of the two single membrane formulations. As expected, all nanoparticles had protein profiles that largely mirrored that of the corresponding membrane. Further, to analyze specific protein markers, western blotting analysis was carried out (Figure 4B). CD235a, also known as glycophorin A,<sup>[32]</sup> is one of the major sialoglycoproteins on the surface of RBCs, and it was present on RBCNPs and also to a lesser degree on [RBC-P]NPs. CD41, also known as integrin  $\alpha$ IIb,<sup>[33]</sup> is important for platelet adhesion as well as activation, and it was present on PNPs and also to a lesser degree on [RBC-P]NPs. Meanwhile, CD47,<sup>[34,35]</sup> an immunomodulatory protein responsible for inhibiting macrophage uptake that is expressed by both cell types, was found at a near equivalent degree on RBCNPs, PNPs, and [RBC-P]NPs. The protein analysis indicated that functionalization with the hybrid

membrane was able to bestow both RBC and platelet surface proteins onto the hybrid [RBC-P]NPs.

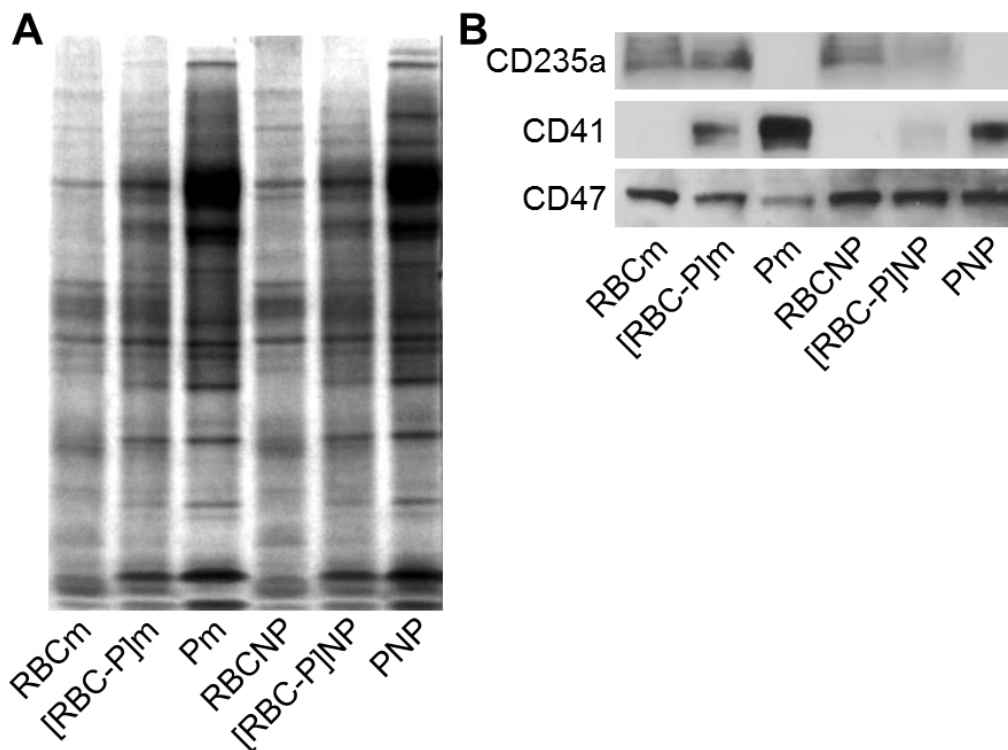


**Figure 5.1.4.** Protein characterization. A) Protein content visualization of RBC membrane (RBCm), fused RBC-platelet membrane ([RBC-P]m), platelet membrane (Pm), RBCNPs, [RBC-P]NPs, and PNPs run on SDS-PAGE at equivalent protein concentrations followed by Coomassie staining. B) Western blot analysis of RBCm, [RBC-P]m, Pm, RBCNPs, [RBC-P]NPs, and PNPs for a characteristic RBC marker CD235a (glycophorin A), a characteristic platelet marker CD41 (integrin  $\alpha$ IIb), and a shared marker CD47. All samples were run at equivalent protein concentrations.

Upon confirming successful transference of markers unique to both source cells, we next sought to characterize the hybrid membrane coating on a functional level. Both RBCNPs and PNPs, given the presence of immunomodulatory markers on their surface, have been shown to be adept at minimizing macrophage uptake.<sup>[14,22,36]</sup> An uptake study using human THP-1 monocytes differentiated into macrophage-like cells was thus carried out to evaluate this property in [RBC-P]NPs (**Figure 5A**). Using flow cytometric analysis after incubation with the macrophage-like cells, [RBC-P]NPs had low uptake consistent with both RBCNPs and PNPs, whereas PLGA cores,

without immunomodulatory membrane coatings, exhibited a high degree of uptake. As an RBC-specific functional marker, we next assessed the level of acetylcholinesterase activity (Figure 5B).

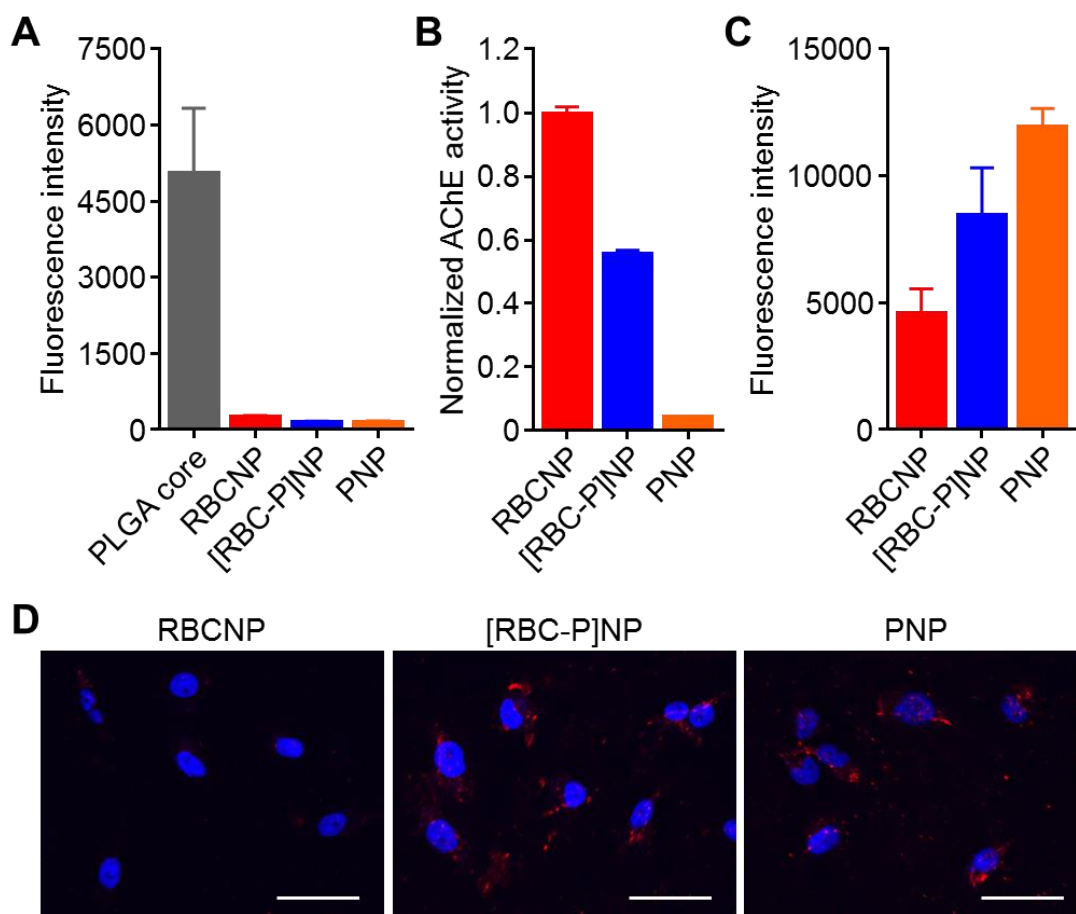


**Figure 5.1.5.** Membrane biological function assays. A) Uptake of fluorescently labeled bare PLGA cores, RBCNPs, [RBC-P]NPs, and PNPs when incubated with human macrophage-like cells as analyzed by flow cytometry ( $n = 3$ ; mean  $\pm$  SD). B) Acetylcholinesterase activity of RBCNPs, [RBC-P]NPs, and PNPs measured by an Amplex acetylcholinesterase assay kit ( $n = 3$ ; mean  $\pm$  SD). C) Binding of fluorescently labeled RBCNPs, [RBC-P]NPs, and PNPs to human MDA-MB-231 breast cancer cells as analyzed by flow cytometry ( $n = 3$ ; mean  $\pm$  SD). D) Confocal fluorescence imaging of dye-labeled RBCNPs, [RBC-P]NPs, and PNPs after incubation with MDA-MB-231 cells (red = nanoparticles, blue = nuclei; scale bar = 50  $\mu$ m)

The enzyme is important for regulating neurotransmitter concentrations, and RBCNPs have been shown to be potent decoys capable of neutralizing lethal doses of poisonous compounds that can deactivate the protein.<sup>[25]</sup> It was confirmed that [RBC-P]NPs had an intermediate level of activity compared with RBCNPs and PNPs, the latter of which had a negligible amount of activity. Regarding platelet-specific functionality, the cancer targeting properties of the hybrid [RBC-

P]NPs was evaluated (Figure 5C,D). PNPs, given the large number of disease-relevant binding markers present on their surface, have been shown to be effective at targeting certain metastatic cancers.<sup>[37]</sup> Using both flow cytometry as well as fluorescent imaging, it was demonstrated that [RBC-P]NPs bound to highly metastatic MDA-MB-231 human breast cancer cells within the spectrum between RBCNPs and PNPs, which exhibited low and high amounts of binding, respectively. Overall, the ability of [RBC-P]NPs to incorporate the functional properties of both RBCs and platelets is encouraging and provides a strong indication that other cell-specific functions should likewise be present on the dual membrane-coated nanoparticles.

Finally, to evaluate the [RBC-P]NP formulation for potential *in vivo* application, the circulation and biodistribution of the nanoparticles were evaluated using a mouse model. Murine-derived RBCs and platelets, along with fluorescently labeled PLGA cores, were used as the starting materials to fabricate RBCNPs, PNPs, and [RBC-P]NPs. To test the circulation half-life, nanoparticles were administered intravenously via the tail vein, and blood was sampled at increasing timepoints to evaluate remaining nanoparticle concentration (**Figure 6A**). After fitting to a two-phase decay model, it was apparent that all three formulations exhibited very similar circulation profiles. Indeed, both RBCNPs and PNPs have previously been reported to circulate for extended periods of time upon administration.<sup>[21,37]</sup> Numerical analysis indicated that RBCNPs, PNPs, and [RBC-P]NPs had one-phase half-lives of 5.7, 5.7, and 6.4 hours and two-phase elimination half-lives of 42.4, 38.3, and 51.8 hours, respectively. All values were within error of each other (see Experimental Section). To analyze biodistribution, nanoparticles were again administered intravenously, and the mice were euthanized 24 hours afterwards in order to collect the heart, lungs, kidneys, liver, and spleen for fluorescence analysis (Figure 6B). All three nanoformulations, including the [RBC-P]NPs, displayed similar organ-level localization, with the

majority of the nanoparticles found in the liver and spleen. This pattern is consistent with what has been previously reported for similar nanoformulations.<sup>[14,21]</sup> The similarity in circulation and distribution profiles between all experimental groups can be explained by the fact that, under normal conditions in healthy individuals, both RBCs and platelets are designed to circulate for extended periods of time and be nonreactive within the body.

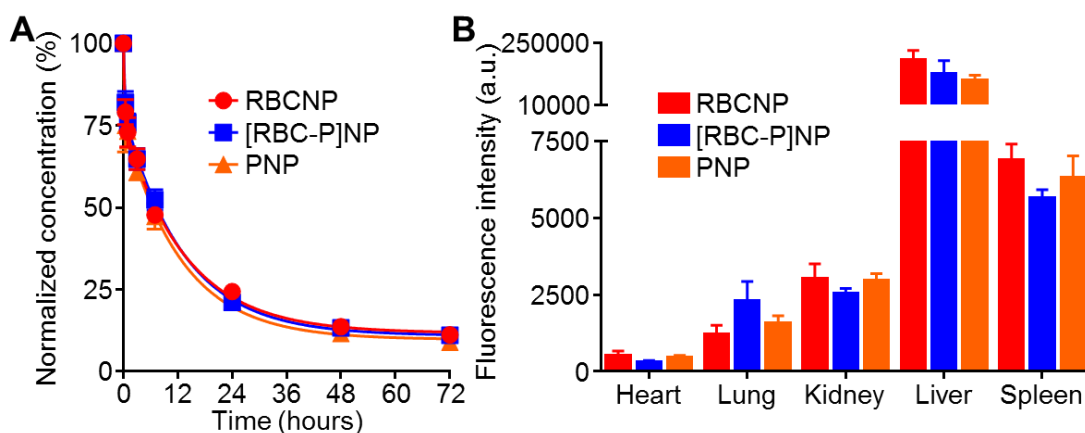


**Figure 5.1.6.** In vivo characterization. A) Circulation time of fluorescently labeled RBCNPs, [RBC-P]NPs, and PNPs after intravenous administration to mice via the tail vein ( $n = 4$ ; mean  $\pm$  SEM; lines represent two-phase decay model). B) Biodistribution of fluorescently labeled RBCNPs, [RBC-P]NPs, and PNPs 24 hours after intravenous administration to mice via the tail vein ( $n = 4$ ; mean  $\pm$  SEM).

## 5.1.3 Materials and Methods

### Membrane Fusion Study

Human RBC membrane was derived from whole blood (BioreclamationIVT) and human platelet membrane was derived from platelet-rich plasma (San Diego Blood Bank) using previously described protocols.<sup>[14,38]</sup> To conduct the Förster resonance energy transfer (FRET) study, two lipophilic dyes were employed: 1,2-dioleoyl-*sn*-glycero-3-phosphoethanolamine-N-(lissamine rhodamine B sulfonyl) (DOPE-RhB, excitation/emission = 560/583 nm; Avanti Polar Lipids) and N-[6-[(7-nitro-2-1,3-benzoxadiazol-4-yl)amino]hexanoyl]-phytosphingosine (C6-

NBD, excitation/emission = 460/534 nm; Avanti Polar Lipids). Both dyes were dissolved in chloroform and subsequently evaporated in a glass vial to form a thin film such that, with respect to platelet membrane protein, the final ratios would be 0.17 and 1.74 wt% for C6-NBD and DOPE-RhB. Solution containing platelet membrane was then added to the vial and stirred at 37 °C for 50 minutes. Afterwards, the free dye was washed away by centrifuging the membrane at 21,000 ×g for 15 minutes four times. RBC membrane was added to the DOPE-RhB/C-6NBD doped platelet membrane at RBC membrane to platelet membrane protein weight ratios of 5:1, 3:1, 2:1, 1:1, and 0:1, respectively, followed by stirring at 37 °C for 10 minutes to facilitate membrane fusion. The fluorescence spectrum of each sample was then read between 500 and 650 nm using an excitation wavelength of 470 nm on a Tecan Infinite M200 plate reader. Fluorescence recovery of the donor (C6-NBD) at the lower emission peak (534 nm) was used to indicate increasing amounts of fusion.

### **Nanoparticle Synthesis**

Membrane-coated nanoparticles were fabricated by a previously reported sonication method.<sup>[14]</sup> Briefly, poly(lactic-*co*-glycolic acid) (PLGA) cores were fabricated using carboxylic acid-terminated PLGA polymer (0.67 dL/g, 50:50 ratio; Lactel Absorbable Polymers). The polymer was dissolved at 10 mg/mL in acetone and precipitated into water. Afterwards, the solution was placed under a vacuum aspirator until the organic solvent was removed. Either RBC membrane, platelet membrane, or fused RBC-platelet membrane at a 1:1 protein weight ratio was employed as the coating material. A mixture of PLGA cores and membrane material at a polymer to membrane protein weight ratio of 2:1 was then sonicated using a Fisher Scientific FS30D bath sonicator for 2 minutes to form the final coated nanoparticles.

### **Confocal Microscopy**



To conduct the membrane colocalization study, RBC membrane was labeled with 1,1'-dioctadecyl-3,3,3',3'-tetramethylindodicarbocyanine, 4-chlorobenzenesulfonate salt (DiD; excitation/emission = 644/663 nm; Biotium) and platelet membrane with 5-(and 6)-carboxyfluorescein diacetate succinimidyl ester (CFSE, excitation/emission = 494/521 nm; eBiosciences). RBCNPs, PNPs, or [RBC-P]NPs made using these labeled membranes were then visualized under confocal fluorescence microscopy using an Olympus FV1000 microscope at a magnification of 100 $\times$ . In order to obtain stable images, the particles were dispersed in glycerol to significantly decrease their mobility.

### **Physicochemical Characterization**

Nanoparticle size and surface zeta potential were measured by dynamic light scattering (DLS) using a Malvern ZEN 3600 Zetasizer. Transmission electron microscopy (TEM) was employed to visualize the nanoparticle structure. Samples were deposited on a glow-discharged, carbon-coated 400-mesh copper grid (Electron Microscopy Sciences). The grid was then washed using distilled water and negatively stained with vanadium (Abcam). Imaging was carried out on a Zeiss Libra 120 PLUS EF-TEM transmission electron microscope.

### **Stability Study**

To evaluate the stability of the different nanoformulations in solution over time, bare PLGA cores, RBCNPs, PNPs, and [RBC-P]NPs were suspended in either water or 1 $\times$  PBS (pH 7.4) at a final concentration of 1 mg/mL. At set timepoints over the course of 3 weeks, the sizes of the samples were measured by DLS to test for aggregation. To evaluate the stability in serum, a previously reported absorbance-based method was employed.<sup>[39]</sup> Nanoparticle samples were added to an equivalent volume of 2 $\times$  fetal bovine serum (Hyclone) concentrated using 10 kDa MWCO

Amicon centrifugal filters (EMD Millipore). The absorbance at 560 nm was measured, and the background signal from equivalent blank solutions was subtracted to give the reported values.

### **Protein Characterization**

To examine the protein profile of RBCNPs, PNP, [RBC-P]NPs, and their corresponding membranes, SDS-PAGE was employed followed by incubation in InstantBlue Protein Stain (Expedeon). All samples were prepared in lithium dodecyl sulfate (LDS) sample loading buffer (Invitrogen) and run at equivalent protein concentrations on NuPAGE Novex 4–12% Bis-Tris minigels (Invitrogen) in MOPS running buffer (Invitrogen). Western blotting was conducted to assess the presence of specific protein markers. Gels were transferred onto a nitrocellulose membranes (Thermo Scientific) and probed with antibodies specific for human CD41 (Biolegend), CD47 (eBiosciences), and CD235a (Biolegend) along with the appropriate HRP-conjugated secondaries (Biolegend).

### **Macrophage Uptake Study**

Human THP-1 cells (TIB-202; American Type Culture Collection) were maintained in RPMI 1640 (Life Technologies) supplemented with 10% FBS (Sigma Aldrich) and penicillin-streptomycin (Gibco). The cells were differentiated into a macrophage-like phenotype by incubating in 100 ng/mL phorbol myristate acetate (Sigma Aldrich) for 48 hours. Fluorescently labeled nanoparticles were fabricated by incorporating 0.1 wt% DiD into the PLGA cores during synthesis. The different nanoformulations were incubated with the cells at a final concentration of 0.25 mg/mL for 10 minutes at 37 °C. The media were then replaced with fresh media and the cells were incubated for another 30 minutes. Afterwards, the cells were washed 3 times with PBS and

detached by scraping. Fluorescent signal was measured on a Becton Dickinson FACSCanto-II flow cytometer and analyzed using FlowJo software.

### **Cell-Specific Functional Study**

As an RBC-specific property, the level of acetylcholinesterase in the different nanoformulations was assessed. Samples were analyzed using an Amplex Acetylcholine/Acetylcholinesterase Assay kit (Life Technologies) according to the manufacturer's instructions. As a platelet-specific property, the ability of the nanoformulations to bind metastatic cancer cells was assessed. Human MDA-MB-231 breast cancer cells (HTB-26; American Type Culture Collection) were grown in DMEM (Corning) supplemented with FBS and penicillin-streptomycin. Nanoformulations with DiD-labeled PLGA cores were added to each well at a final concentration of 0.25 mg/mL and incubated for 5 minutes on ice to minimize cellular uptake. The cells were then washed 3 times with cold PBS and detached by scraping for flow cytometric analysis. Fluorescent signal was measured on a Becton Dickinson FACSCanto-II flow cytometer and analyzed using FlowJo software. For the fluorescent imaging, the cells were plated on 8-well Lab-Tek II chamber slides (Nunc) and incubated with the nanoformulations as described above. The cells were then fixed with 10% buffered formalin phosphate (Fisher Scientific), mounted with VECTASHIELD Antifade mounting media with DAPI (Vector Laboratories), and imaged on an Olympus FV1000 confocal microscope. Images were representative of the experiment done in triplicate and all were subjected to the same brightness and contrast adjustments.

### **In Vivo Characterization**

All animal experiments were performed in accordance with NIH guidelines and approved by the Institutional Animal Care and Use Committee (IACUC) of the University of California, San

Diego. Mouse RBCs and platelets were collected from 6-week-old male CD-1 mice (Harlan Laboratories) in order to fabricate mouse RBCNPs, PNPs, and [RBC-P]NPs. Fluorescently labeled nanoparticles were prepared using DiD-loaded PLGA cores. To perform the circulation study, 200  $\mu\text{L}$  of fluorescently labeled particles at 3 mg/mL were administered intravenously. Blood was sampled by submandibular puncture at 3 minutes, 30 minutes, 1 hour, 3 hours, 7 hours, 24 hours, 48 hours, and 72 hours. Nanoparticle retention in circulation at these timepoints was determined by measuring the fluorescence on a Tecan Infinite M200 plate reader. The data from each mouse was normalized to the very first data point and analyzed using Graphpad Prism. Using a one-phase decay model, the half-lives were calculated from the fitted  $K$  parameter in the software as  $t_{1/2} = \ln(2)/K$ . The values of  $K$  with standard error for the RBCNPs, PNPs, and [RBC-P]NPs were  $0.1213 \pm 0.0182$ ,  $0.1219 \pm 0.0240$ , and  $0.1092 \pm 0.0144 \text{ hr}^{-1}$ , respectively. To calculate the two-phase elimination half-life, the normalized signal was transformed using natural log, and the slow phase from the resulting data was fitted using a linear regression curve. Elimination half-life was calculated as  $t_{1/2} = \ln(2)/\beta$ , where  $\beta$  is the negative slope obtained from the fit. The values of  $\beta$  with standard error for the RBCNPs, PNPs, and [RBC-P]NPs were  $0.0164 \pm 0.0045$ ,  $0.0181 \pm 0.0042$ , and  $0.0134 \pm 0.0034 \text{ hr}^{-1}$ , respectively. To study the biodistribution of the different nanoparticles, 200  $\mu\text{L}$  of fluorescently labeled formulations at 3 mg/mL were administered intravenously. At 24 hours, mice were euthanized and perfused with  $1\times$  PBS. Afterwards, the heart, lungs, kidneys, liver, and spleen were collected and homogenized in 500  $\mu\text{L}$  of water using a Biospec Mini-Beadbeater-16. Fluorescence was read using a Tecan Infinite M200 plate reader.

### 5.1.4 Conclusion

In conclusion, we have successfully fabricated a new class of cell membrane-coated nanocarrier that combines the function of two different cell types. It was confirmed that it is possible to fuse RBC membrane and platelet membrane together, using it as a coating material to fabricate hybrid [RBC-P]NPs. Physically, the resultant particles were similar to pure, single membrane formulations of either RBCNPs or PNPs. On a protein and functional level, the [RBC-P]NPs represented a cross between the two parent nanoparticle types, retaining properties once only exclusive to either. The reported method of bestowing nanoparticles with enhanced functionality provides a facile and natural alternative to synthetic post-functionalization strategies. Importantly, the dual membrane-coated nanoparticles are expected to maintain excellent biocompatibility as long as the source cell types are appropriately chosen. It can easily be envisioned that, using this strategy, a countless number of different combinations can be explored, and this may ultimately give rise to new multi-membrane nanoparticle platforms that have the potential to outperform their single membrane counterparts.

### Acknowledgements

This work is supported by the National Institutes of Health under Award Numbers R01CA200574 and R01EY025947.

Chapter 5.1 is, in full, is a reprint of the material as it appears in *Advanced Materials*, 2017, Dehaini, D.; Wei, X.; Fang, R.; Masson, S.; Angsantikul, P.; Luk, B.; Zhang, Y.; Ying, M.; Jiang, Y.; Kroll, A.; Gao, W.; Zhang, L. The dissertation author is the primary author of this work.

## References

- [1] F. Alexis, E. Pridgen, L.K. Molnar, O.C. Farokhzad, Factors affecting the clearance and biodistribution of polymeric nanoparticles, *Mol Pharm*, 5 (2008) 505-515.
- [2] T.M. Allen, P.R. Cullis, Liposomal drug delivery systems: from concept to clinical applications, *Adv Drug Deliv Rev*, 65 (2013) 36-48.
- [3] D. Dehaini, R.H. Fang, B.T. Luk, Z. Pang, C.M. Hu, A.V. Kroll, C.L. Yu, W. Gao, L. Zhang, Ultra-small lipid-polymer hybrid nanoparticles for tumor-penetrating drug delivery, *Nanoscale*, 8 (2016) 14411-14419.
- [4] D. Dehaini, R.H. Fang, L. Zhang, Biomimetic strategies for targeted nanoparticle delivery, *Bioengineering & Translational Medicine*, 1 (2016) 30-46.
- [5] R.H. Fang, C.M. Hu, K.N. Chen, B.T. Luk, C.W. Carpenter, W. Gao, S. Li, D.E. Zhang, W. Lu, L. Zhang, Lipid-insertion enables targeting functionalization of erythrocyte membrane-cloaked nanoparticles, *Nanoscale*, 5 (2013) 8884-8888.
- [6] R.H. Fang, C.M. Hu, B.T. Luk, W. Gao, J.A. Copp, Y. Tai, D.E. O'Connor, L. Zhang, Cancer cell membrane-coated nanoparticles for anticancer vaccination and drug delivery, *Nano Lett*, 14 (2014) 2181-2188.
- [7] O.C. Farokhzad, Nanotechnology: Platelet mimicry, *Nature*, 526 (2015) 47-48.
- [8] W. Gao, L. Zhang, Coating nanoparticles with cell membranes for targeted drug delivery, *J Drug Target*, 23 (2015) 619-626.
- [9] W.W. Gao, L.F. Zhang, Engineering Red-Blood-Cell-Membrane-Coated Nanoparticles for Broad Biomedical Applications, *Aiche Journal*, 61 (2015) 738-746.
- [10] V.V. Glinsky, G.V. Glinsky, O.V. Glinskii, V.H. Huxley, J.R. Turk, V.V. Mossine, S.L. Deutscher, K.J. Pienta, T.P. Quinn, Intravascular metastatic cancer cell homotypic aggregation at the sites of primary attachment to the endothelium, *Cancer Res*, 63 (2003) 3805-3811.
- [11] T. Govender, S. Stolnik, M.C. Garnett, L. Illum, S.S. Davis, PLGA nanoparticles prepared by nanoprecipitation: drug loading and release studies of a water soluble drug, *J Control Release*, 57 (1999) 171-185.
- [12] C.M. Hu, R.H. Fang, J. Copp, B.T. Luk, L. Zhang, A biomimetic nanosponge that absorbs pore-forming toxins, *Nat Nanotechnol*, 8 (2013) 336-340.
- [13] C.M. Hu, R.H. Fang, B.T. Luk, L. Zhang, Nanoparticle-detained toxins for safe and effective vaccination, *Nat Nanotechnol*, 8 (2013) 933-938.
- [14] C.M. Hu, R.H. Fang, K.C. Wang, B.T. Luk, S. Thamphiwatana, D. Dehaini, P. Nguyen, P. Angsantikul, C.H. Wen, A.V. Kroll, C. Carpenter, M. Ramesh, V. Qu, S.H. Patel, J. Zhu, W. Shi,

F.M. Hofman, T.C. Chen, W. Gao, K. Zhang, S. Chien, L. Zhang, Nanoparticle biointerfacing by platelet membrane cloaking, *Nature*, 526 (2015) 118-121.

[15] C.M. Hu, L. Zhang, S. Aryal, C. Cheung, R.H. Fang, L. Zhang, Erythrocyte membrane-camouflaged polymeric nanoparticles as a biomimetic delivery platform, *Proc Natl Acad Sci U S A*, 108 (2011) 10980-10985.

[16] R. Jahn, T. Lang, T.C. Sudhof, Membrane fusion, *Cell*, 112 (2003) 519-533.

[17] N. Kolishetti, S. Dhar, P.M. Valencia, L.Q. Lin, R. Karnik, S.J. Lippard, R. Langer, O.C. Farokhzad, Engineering of self-assembled nanoparticle platform for precisely controlled combination drug therapy, *Proc Natl Acad Sci U S A*, 107 (2010) 17939-17944.

[18] B.T. Luk, R.H. Fang, C.M. Hu, J.A. Copp, S. Thamphiwatana, D. Dehaini, W. Gao, K. Zhang, S. Li, L. Zhang, Safe and Immunocompatible Nanocarriers Cloaked in RBC Membranes for Drug Delivery to Treat Solid Tumors, *Theranostics*, 6 (2016) 1004-1011.

[19] B.T. Luk, L. Zhang, Cell membrane-camouflaged nanoparticles for drug delivery, *J Control Release*, 220 (2015) 600-607.

[20] B. Mishra, B.B. Patel, S. Tiwari, Colloidal nanocarriers: a review on formulation technology, types and applications toward targeted drug delivery, *Nanomedicine*, 6 (2010) 9-24.

[21] Z. Pang, C.M. Hu, R.H. Fang, B.T. Luk, W. Gao, F. Wang, E. Chuluun, P. Angsantikul, S. Thamphiwatana, W. Lu, X. Jiang, L. Zhang, Detoxification of Organophosphate Poisoning Using Nanoparticle Bioscavengers, *ACS Nano*, 9 (2015) 6450-6458.

[22] D. Peer, J.M. Karp, S. Hong, O.C. Farokhzad, R. Margalit, R. Langer, Nanocarriers as an emerging platform for cancer therapy, *Nat Nanotechnol*, 2 (2007) 751-760.

[23] J.M. Saul, A.V. Annapragada, R.V. Bellamkonda, A dual-ligand approach for enhancing targeting selectivity of therapeutic nanocarriers, *J Control Release*, 114 (2006) 277-287.

[24] C.E. Soma, C. Dubernet, D. Bentolila, S. Benita, P. Couvreur, Reversion of multidrug resistance by co-encapsulation of doxorubicin and cyclosporin A in polyalkylcyanoacrylate nanoparticles, *Biomaterials*, 21 (2000) 1-7.

[25] S.D. Steichen, M. Caldorera-Moore, N.A. Peppas, A review of current nanoparticle and targeting moieties for the delivery of cancer therapeutics, *Eur J Pharm Sci*, 48 (2013) 416-427.

[26] H. Sun, J. Su, Q. Meng, Q. Yin, L. Chen, W. Gu, P. Zhang, Z. Zhang, H. Yu, S. Wang, Y. Li, Cancer-Cell-Biomimetic Nanoparticles for Targeted Therapy of Homotypic Tumors, *Adv Mater*, (2016).

[27] F. Wang, R.H. Fang, B.T. Luk, C.J. Hu, S. Thamphiwatana, D. Dehaini, P. Angsantikul, A.V. Kroll, Z. Pang, W. Gao, W. Lu, L. Zhang, Nanoparticle-Based Antivirulence Vaccine for the Management of Methicillin-Resistant *Staphylococcus aureus* Skin Infection, *Adv Funct Mater*, 26 (2016) 1628-1635.

- [28] Y. Wang, S. Gao, W.H. Ye, H.S. Yoon, Y.Y. Yang, Co-delivery of drugs and DNA from cationic core-shell nanoparticles self-assembled from a biodegradable copolymer, *Nat Mater*, 5 (2006) 791-796.
- [29] J. Xie, S. Lee, X. Chen, Nanoparticle-based theranostic agents, *Adv Drug Deliv Rev*, 62 (2010) 1064-1079.
- [30] Y. Zhang, J. Zhang, M. Chen, H. Gong, S. Thamphiwatana, L. Eckmann, W. Gao, L. Zhang, A Bioadhesive Nanoparticle-Hydrogel Hybrid System for Localized Antimicrobial Drug Delivery, *ACS Appl Mater Interfaces*, 8 (2016) 18367-18374.
- [31] J.Y. Zhu, D.W. Zheng, M.K. Zhang, W.Y. Yu, W.X. Qiu, J.J. Hu, J. Feng, X.Z. Zhang, Preferential Cancer Cell Self-Recognition and Tumor Self-Targeting by Coating Nanoparticles with Homotypic Cancer Cell Membranes, *Nano Lett*, 16 (2016) 5895-5901.



## **5.2 Hybrid Biomembrane–Functionalized Nanorobots for Concurrent Removal of Pathogenic Bacteria and Toxins**

### **5.2.1 Introduction**

Tiny robots at the micro- and nanoscale have recently attracted great attention because of their unprecedented features and functions as well as enormous potential applications, especially in the areas of health care and biomedicine (1, 2). These small-scale mobile devices can effectively overcome low Reynolds number viscous drag and Brownian motion by converting locally supplied chemical fuels or external energy (e.g., magnetic, acoustic, or light) into propelling force and movement (1, 3–5). More recently, the efficient propulsion of these man-made small robots has been combined with previously unknown functionalities, including advanced motion control, cargo towing and release, chemotactic and collective behavior, and facile surface modification. These features together provide the robots with capabilities for performing diverse tasks in different disciplines, including cell separation, active drug delivery, noninvasive surgery (2), environmental remediation (6–10), and nanoscale fabrication and imaging (11). With the rapid advancement of micro- and nanorobots in biomedical research, it becomes important to develop robots with biocompatible and bio-mimetic surfaces for favorable interfaces and interactions with natural biological subjects. For example, synthetic nanorobots have been integrated recently with motile cells, such as sperm and bacteria (12, 13).

Herein, we report the integration of diverse biological functions from the plasma membranes of two cell types, red blood cells (RBCs) and platelets (PLs), into a single nanorobot surface to create a robust biomimetic nanorobot for multipurpose biodetoxification and con-

current removal of pathogenic bacteria and toxins in particular. In Gram-positive bacterial infections, pathogens normally generate and release a variety of hemolytic toxins, namely, pore-forming toxins (PFTs), into the bloodstream. These toxins actuate pore formation in cell membranes, altering membrane permeability and leading to cellular lysis. This process is one of the major routes of bacterial pathogenesis and results in life-threatening infections in humans (14–16). From a therapeutic perspective, it would be ideal to remove both the hemolytic toxins and the toxin-produced bacteria to achieve desirable treatment efficacy. However, the major challenge is that the toxins and the bacteria are vastly different physicochemical structures and normally have different biological targets. For instance, PFTs typically target RBCs and destroy them, whereas bacteria may have no specific interactions with RBCs; instead, they bind with other cell types, such as PLs. To solve this problem, we hypothesized that, by coating synthetic nanorobots with a mixture of cell membranes derived from RBCs and PLs, these hybrid biomembrane-functionalized robots will bear lipid membranes and associated functions similar to both RBC and PL membranes. The dual RBC-PL membrane coating will give nanorobots a variety of functional proteins and thus multifaceted biological functions. Therefore, these biomimetic nanorobots are expected to concurrently absorb and remove RBC-targeted PFTs and PL-bound bacteria that produce the PFTs. To test this hypothesis, we adopted a recently developed cell membrane-coating technology to functionalize an acoustic gold nanowire (AuNW)-based nanorobot used as a model of fuel-free robot with potential biomedical applications.

Cell membrane coating has recently emerged as a platform technology that presents a simple top-down approach for functionalizing synthetic subjects with the highly complex functionalities associated with natural cell membranes (17–19). Specifically, cell membrane-coated nanodevices inherently mimic the surface properties of the source cells and thus bear unique

functions, such as disease-relevant targeting ability. For example, RBC membranes can target and absorb toxins, and PL membranes can adhere to pathogens (14, 17–22). Initial attempts have integrated nanorobots with singular cell membranes (23–25). The resulting biomimetic nanorobots combined the advantages of both the dynamic movement of mobile robotics and the functional versatility of the cellular membrane coatings. This coupling greatly accelerated detoxification processes compared with counterparts based solely on Brownian motion (12, 13, 23–25). For example, RBC membrane-coated robots have demonstrated effective and rapid removal of bacterial toxins and other contaminants (e.g., nerve agents) from biological samples (23, 24). So far, only singular cell membranes have been coupled with nanorobots, providing them with the specific biological function of the corresponding cells while lacking multifaceted functionality. The integration of diverse membrane functionalities from multiple cell types into single mobile nanorobots could result in broader and more robust uses, where the nanorobots could perform multiple complex therapeutic tasks in a single treatment. In this work, we prepared RBC-PL hybrid membrane-functionalized fuel-free nanorobots (denoted as “RBC-PL-robots”), by enclosing acoustic AuNW robots with the hybrid membranes derived from human RBCs and PLs, for simultaneous targeting and removal of pathogenic bacteria along with toxins secreted by the bacteria (Fig. 1A). The biomimetic robots were fabricated by using a template-assisted AuNW electrochemical deposition protocol (26), followed by a dual-cell membrane-cloaking technique (27). The dual-membrane coating contained a wide variety of functional proteins associated with human RBCs and PLs, which gave the nanorobot diverse biological functions. Coupling the biological functions of the hybrid membranes with the fuel-free navigation of ultrasound (US)-propelled mobile nanorobots thus resulted in a dynamic biomimetic multifunctional detoxification platform that locally enhanced mass transport and increased directional collisions

with biological targets and may represent a unique tool in situations where external mechanical stirring is not possible or desired. The RBC-PL-robots displayed rapid and efficient propulsion in whole blood, with no apparent biofouling, and mimicked the movement of natural motile cells. These mobile nanorobots show pulsion capabilities of the dual-membrane-functionalized nanorobots may be used for rapid bacteria isolation and efficient neutralization of PFTs in a variety of biomedical and biodefense scenarios. This dual-cell membrane coating represents a unique and robust technique to functionalize nanorobots for potential use in different fields, including targeted drug delivery, immune modulation, and de-toxification. Although acoustic propulsion was selected as a model of fuel-free propulsion, the reported dual-cell membrane coating concept can be readily expanded to other types of nanorobots involving different propulsion mechanisms.

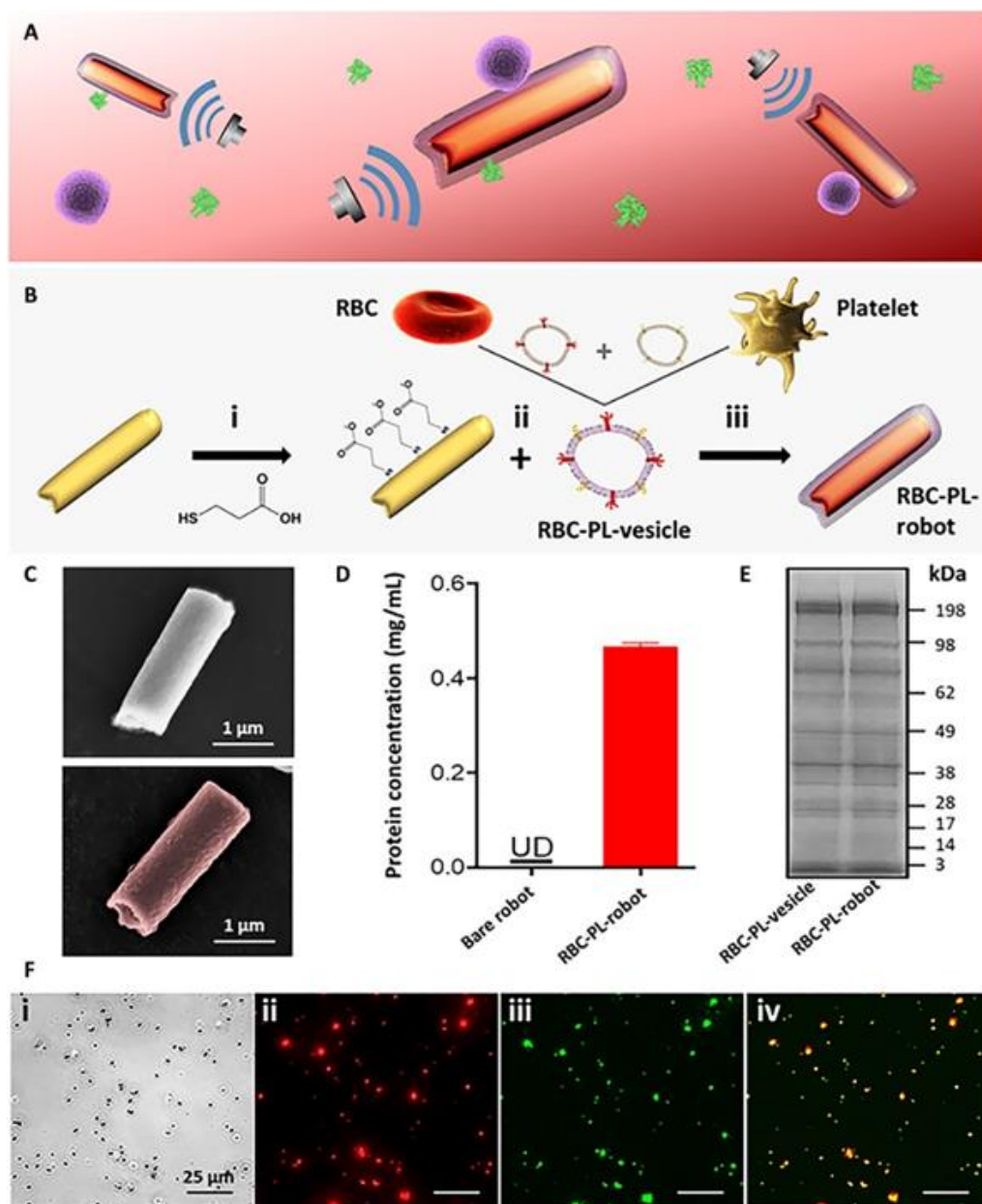


**Figure 5.2.1.** Preparation and characterization of RBC-PL-robots. (A) Schematic of biomimetic robots for binding and removal of threatening biological agents. (B) Preparation of RBC-PL-robots: (i) The gold surface of the nanowire (AuNW) robots was modified with MPA; (ii) hybrid membranes were prepared by fusion of RBC membranes and PL membranes (using 1:1 protein weight ratio), and the resulting hybrid membranes were used to coat the MPA-modified nanorobots; (iii) after 5-min sonication, the RBC-PL-robots were obtained. (C) SEM images of a bare AuNW robot without hybrid membrane coating (top) and an RBC-PL-robot (bottom). (D) The measured weight of protein content on bare robots and RBC-PL-robots (both 20 mg ml<sup>-1</sup>) stored in 1× PBS at 4°C for 24 hours. UD, undetectable. Error bars represent the SD from three different measurements. (E) SDS–polyacrylamide gel electrophoresis analysis of proteins present on the RBC-PL-vesicles and the RBC-PL-robots. The samples were run at equal protein content and stained with Coomassie blue. The RBC-PL-robots used in (D) and (E) were exposed to the acoustic field for 5 min before performing the protein analysis. (F) Optical (i) and fluorescent (ii to iv) images of a group of RBC-PL-robots, in which the RBC membranes were labeled with DiD dye (red) and the PL membranes were labeled with FITC (green). Overlay of the DiD and FITC channels is shown in (iv) (yellow).

## 5.2.2 Results and Discussion

### Preparation of RBC-PL-robots

The preparation of RBC-PL-robots involved the combination of template-assisted electrodeposition and cell membrane-cloaking techniques. As shown in Fig. 1B, the AuNW robots were prepared by a common membrane-template electrodeposition protocol (see Materials and Methods) (26) consisting of gold deposition within the nanopores (400 nm diameter) of a polycarbonate (PC) membrane, followed by the membrane dissolution and release of the resulting AuNWs. The surface of the AuNWs was then modified with 3-mercaptopropionic acid (MPA) (Fig. 1B, i) before membrane coating. In parallel, RBC-PL hybrid membrane-derived vesicles (denoted as “RBC-PL-vesicles”; diameter, 100 to 150 nm) were prepared by fusion of the RBC and PL membranes (1:1 protein weight ratio) during a 5-min ultrasonication (27). The resulting RBC-PL-vesicles, having diverse biological capabilities, were mixed with the MPA-modified AuNWs under ultrasonication for 5 min (Fig. 1B, ii). The nanoscale RBC-PL-vesicles, with high surface energy, were prone to bind and fuse onto the AuNW nanorobots to minimize the system’s free energy (Fig. 1B, iii). The ultrasonic mixing further enhanced the adsorption of the RBC-PL hybrid membranes onto the AuNWs. The fusion process allowed for the retention of the bilayer structure of the hybrid membranes and the preservation of their protein functions. In addition, because of the large asymmetric negative charge between the ectoplasmic and cytoplasmic surfaces of the hybrid membranes, the outer surface of the membranes was much more negatively charged than the inner surface. Hence, electrostatic repulsion allowed the hybrid membranes to fuse onto the negatively charged robots at the right-side-out orientation (18). This orientation of RBC-PL hybrid membranes enabled the selective adsorption and neutralization of PFTs and

pathogens and protected the nanorobots from biofouling during movement in complex biological media.

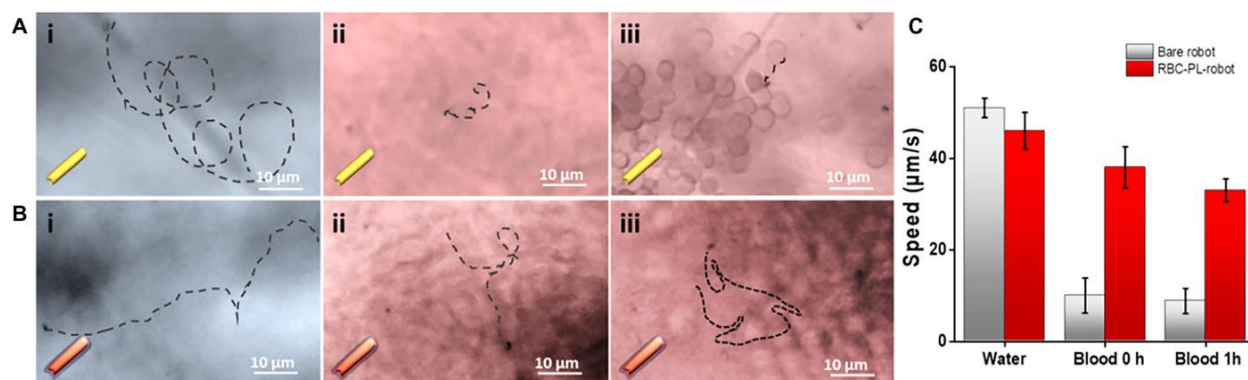


**Figure 5.2.2.** Propulsion performance and anti-biofouling property of RBC-PL-robots. Tracking trajectories showing the propulsion of bare robots (A) and RBC-PL-robots (B) in water (i) and after 0- and 1-hour incubation in blood (ii and iii, respectively). (C) Comparison of the speed of bare robots with RBC-PL-robots in water and after 0- and 1-hour incubation in blood. The acoustic nanorobots were propelled using a frequency of 2.66 MHz and a voltage of 2.0 V. Error bars estimated as a triple of SD (n = 3).

The fabricated RBC-PL-robots were characterized by different techniques. Figure 1C shows the scanning electron microscope (SEM) images of a bare AuNW robot and an RBC-PL-robot (top and bottom, respectively), both with a diameter of 400 nm and a length of 1.5 to 2.0 μm. An SEM image of the bare AuNW is shown in fig. S1. Both SEM images show the asymmetric shape of the robots containing a concave end obtained by the template electrodeposition (28). This structural asymmetry allowed each individual nanowire to convert the acoustic steady streaming produced over the surface of the nanowire into axial motion with an independent trajectory, rather than being dragged as an aggregate by the acoustic radiation or flow forces (26, 28, 29). Other key factors affecting the conversion of the acoustic energy into motion include material density and dimension, because only structures fabricated with relatively dense materials (e.g., Au, Pt, and Ru) and sizes larger than 500 nm have been reported to present autonomous propulsion (30, 31). Although there are multiple fuel-free microrobots (8, 32) and alternative acoustic propulsion mechanisms based on traveling waves (33), streaming (34), or bubble cavitation (35), the present

use of acoustically propelled nanowires produced a synergistic effect of enhancing mass transport while preconcentrating the sample in an acoustic levitation plane, thereby enhancing directional collisions between the nanorobot and the biological target. A thin coating can be observed around the RBC-PL-robot corresponding to the membrane coating. We also investigated the RBC-PL-robots in terms of their protein content from the dual-cell membrane coating. For this purpose, the RBC-PL-robots were repeatedly washed with phosphate-buffered saline (PBS) to remove uncoated membranes and exposed to the acoustic field for 5 min, and then a bicinchoninic acid (BCA) protein assay was used to quantify the level of membrane proteins on the nanorobot surface. A protein content of 0.5 mg ml<sup>-1</sup> was obtained for the RBC-PL-robots, in comparison with the undetectable protein content for the bare nanorobots, using the same robot concentration (20 mg ml<sup>-1</sup>) (Fig. 1D). Furthermore, gel electrophoresis followed by protein staining showed the protein profile of the purified RBC-PL-vesicles and RBC-PL-robots (Fig. 1E). The protein profile of the coated robots closely matched that of the hybrid membranes, indicating that the RBC-PL membranes can be translocated onto the nanorobot surface without altering their protein profile.

To further confirm the presence and cloaking of hybrid membranes onto the surface of AuNW robots, we labeled the RBC and the PL membranes before coating with the dyes 1,1'-dioctadecyl-3,3,3',3'-tetramethylindodicarbocyanine,4-chlorobenzenesulfonate salt (DiD; excitation/emission = 644/665 nm) and fluorescein isothiocyanate (FITC; excitation/emission = 495/525 nm), respectively. Figure 1F shows optical (i) and fluorescent (ii to iv) images of a group of RBC-PL-robots coated with the DiD-labeled RBC membranes (red) and FITC-labeled PL membranes (green). Full coverage of the nanorobots is illustrated in the fluorescence microscopy images, indicating the successful incorporation of the dye-labeled dual cell membranes onto the robots. The corresponding overlay of the DiD and FITC channels (shown in Fig. 1F, iv) confirmed



the effective co-localization of both cell membranes on the same robot, further verifying the successful coating of the AuNW robots with the dual membranes.

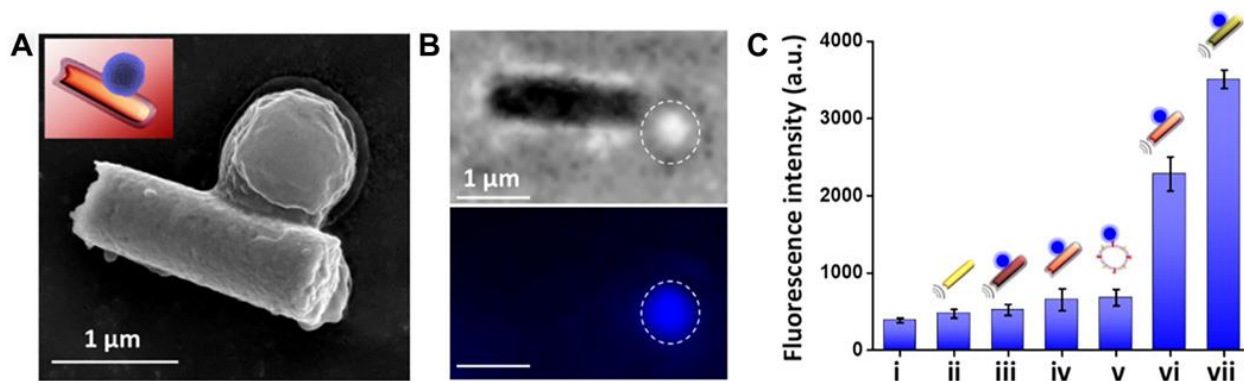


**Figure 5.2.3.** Binding and isolation of PL-adhering pathogens by RBC-PL-robots. (A) SEM image of an MRSA USA300 bacterium attached to an RBC-PL-robot. (B) Microscopic images showing the binding of an MRSA USA300 bacterium to an RBC-PL-robot: bright-field image (top) and fluorescence image showing the DAPI-stained bacterium (bottom). (C) Normalized fluorescence intensity of DAPI-stained MRSA USA300 bacteria retained on (i) PBS (no robots), (ii) bare robots, (iii) RBC-robots (without PL membranes), (iv) RBC-PL-robots under a static condition (without US), (v) RBC-PL-vesicles, (vi) US-propelled RBC-PL-robots, and (vii) PL-robots (without RBC membranes). PBS, bare robots, RBC-robots, and RBC-PL-vesicles were used as negative controls; PL-robots were used as a positive control. Error bars were estimated as a triple of SD ( $n = 3$ ). Reaction time, 5 min. Biomimetic robots, 10 mg ml<sup>-1</sup>. MRSA USA300 bacteria,  $5 \times 10^8$  CFU ml<sup>-1</sup>.

### Propulsion performance and anti-biofouling property of RBC-PL-robots

The propulsion performance and anti-biofouling ability of the RBC-PL- robots were evaluated by comparing the propulsion speed of the un- coated AuNW robots and the RBC-PL- robots in water and in whole blood, as illustrated from the stack of overlapping microscopy images in Fig. 2 (A and B) (corresponding to movies S1 and S2). The pro- pulsion of bare robots and RBC-PL-robots was examined first in water, as indicated by the 4-s tracking trajectories shown in Fig. 2 (A, i, and B, i, respectively). Both robots displayed efficient propulsion with a high speed in the aqueous medium (51 and 46  $\mu\text{m s}^{-1}$ ; Fig. 2C, gray and red bars, respectively). In contrast, when tested in whole blood, the bare robots displayed notable hindered propulsion, with a greatly diminished speed of  $\sim 10 \mu\text{m s}^{-1}$ , nearly independent of the incubation time (right after mixing

and after 1-hour incubation in blood) (Fig. 2A, ii and iii). This hindered movement reflects severe protein fouling of the robots. However, the RBC-PL-robots exhibited only a slight speed decrease when incubated in blood, as shown by the 4-s tracking trajectories of Fig. 2B (ii and iii) and demonstrated by the calculated speeds (Fig. 2C; red bars: 38 and 35  $\mu\text{m s}^{-1}$ , respectively). Although the propulsion of the RBC-PL-robots was slightly affected by the blood viscosity, the robot movement in this complex biological environment remained active over the entire 1-hour operation. Overall, these data indicate that the natural surface proteins and functions of the RBC-PL hybrid membranes enabled an effective anti-biofouling property of the biomimetic nanorobots, which allows the robots to work in complex physiological fluids continuously.

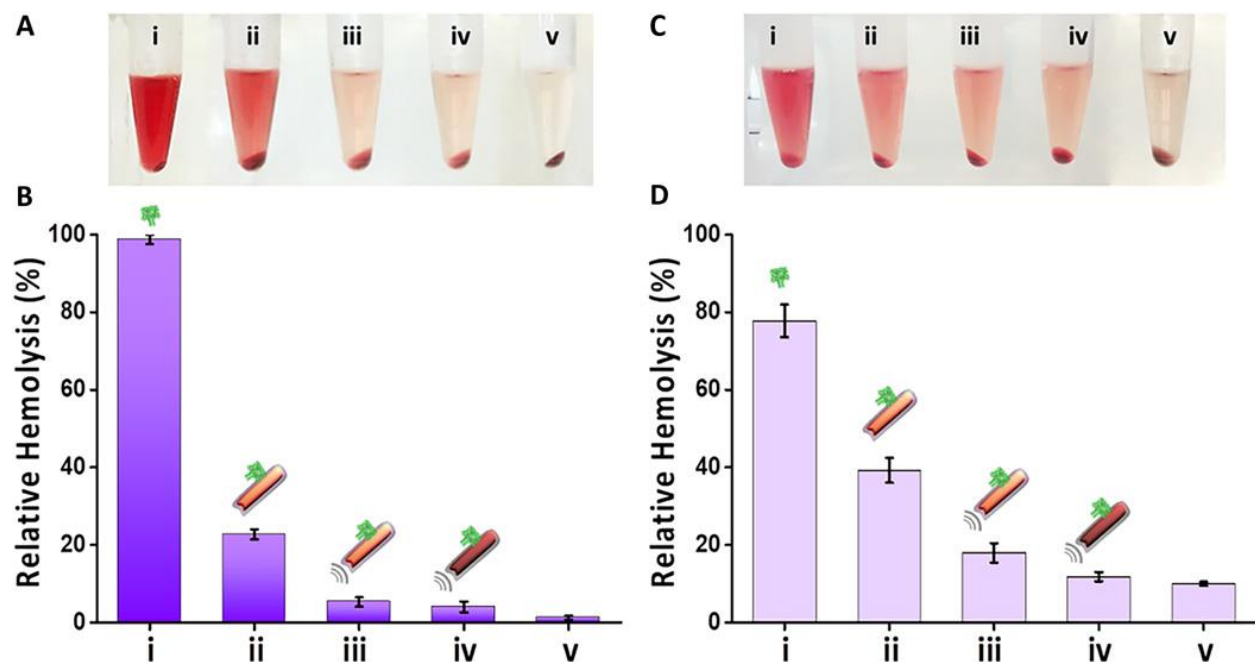


**Figure 5.2.4.** Binding and neutralization of  $\alpha$ -toxin and other PFTs by RBC-PL-robots. (A) Images of centrifuged 5% RBC solution after incubation with  $\alpha$ -toxin in (i) PBS, (ii) static RBC-PL-robots, (iii) US-propelled RBC-PL-robots, and (iv) US-propelled RBC-robots. PBS without  $\alpha$ -toxin (v) was used as a control. (B) Hemolysis quantification of the samples shown in (A). (C) Images of centrifuged 5% RBC solution after incubation with PFTs (50  $\mu\text{l}$ ) produced by MRSA bacteria (after 8-hour incubation) in (i) PBS, (ii) static RBC-PL-robots, (iii) US-propelled RBC-PL-robots, and (iv) US-propelled RBC-robots. PBS without PFTs (v) was used as a control. (D) Hemolysis quantification of the samples shown in (C). Error bars estimated as a triple of SD ( $n = 3$ ). Treatment time with samples, 5 min; hemolysis incubation time (5% RBC solution plus PFTs), 30 min at 37°C.

## **Binding and isolation of PL-adhering pathogens by RBC-PL-robots**

Characterizations of the robot structure and its US propulsion were followed by critical evaluation of the detoxification potential of the biomimetic nanorobots. Initially, the RBC-PL-robots were assessed for selective binding and rapid isolation of PL-adhering pathogens. Such bacteria binding to a PL is a postulated central event in the pathogenesis of infective endocarditis (36), and PL-bacterium interactions are also associated with bacterial immune evasion and bacteremia (37). In this study, a strain of MRSA expressing a serine-rich adhesin for PL, MRSA USA300 (36), was used as a model PL-adhering pathogen. Figure 3A (see also fig. S2) shows an SEM image indicating an MRSA USA300 bacterium binding to an RBC-PL-robot after a 5-min incubation under a US field (2.66 MHz and 2.0 V). To further characterize the robot/MRSA binding and compare it with other different controls, we incubated the RBC-PL-robots (10 mg ml<sup>-1</sup>) in the MRSA USA300 suspension [ $5 \times 10^8$  colony-forming units (CFU) ml<sup>-1</sup>] under US for 5 min, followed by collection of the robots through precipitation, fixation of adhered bacteria with formalin, and staining with 4',6- diamidino-2-phenylindole (DAPI). Subsequently, the amount of bacteria adhered to the RBC-PL- robots was calculated by measuring the DAPI fluorescence intensity. Figure 3B shows microscopic bright-field and fluorescence images (top and bottom, respectively), which further illustrate the specific binding between an MRSA USA300 bacterium and the RBC-PL-robot. The normalized fluorescence intensity of DAPI-stained MRSA USA300 was calculated and compared with other control experiments (Fig. 3C). PBS, bare nanorobots (without cell membrane coating), and RBC-robots (coated with RBC membranes) were used as negative controls and displayed a negligible fluorescent intensity due to the absence of bacterial adhesion (Fig. 3C, i to iii). Low fluorescence intensity values were also observed for MRSA USA300 incubated with RBC-PL-robots under static conditions or with RBC-PL-vesicles

(Fig. 3C, iv and v). In contrast, a remarkable fluorescence intensity increment was observed when incubating DAPI-stained MRSA bacteria with US-propelled RBC-PL-robots (vi) or PL-robots (vii, coated only with PL membranes, used as a positive control), reflecting the active bacterial recognition and binding of the PL membranes. DAPI-stained MRSA treated with US-propelled RBC-PL-robots reached a 3.5-fold increase in DAPI fluorescence intensity compared with their static counterparts {Fig. 3C, vi [2283 arbitrary units (a.u.)] versus iv (650 a.u.)}, indicating the importance of US propulsion for rapid bacteria isolation associated with the enhanced directional collisions between the RBC-PL-robots and bacteria under the acoustic field. Overall, these results demonstrate the unique characteristics of the US-propelled biomimetic robots for achieving rapid and selective isolation of PL-adhering pathogens such as MRSA.

### **Binding and neutralization of PFTs by RBC-PL-robots**

After having studied the pathogen binding capacity of the RBC-PL- robots, we evaluated their application as a powered toxin decoy to absorb and neutralize PFTs, a family of toxins that target RBCs by forming pores in cellular membranes, altering their permeability. We first used  $\alpha$ -toxin as a model PFT to test the detoxification potential of the RBC-PL-robots. *S. aureus* secretes this toxin as a water-soluble protein, which can spontaneously incorporate into lipid membranes, forming a heptameric structure with a central pore that facilitates uncontrolled permeation of different molecules, finally leading to cell lysis (38–40). Developing effective strategies for neutralizing  $\alpha$ -toxin is of great importance because it has been demonstrated that the inhibition of  $\alpha$ -toxin can reduce the severity of *S. aureus* infections (14, 41). To test such detoxification potential, we mixed a fixed amount of commercially purchased purified  $\alpha$  -toxin (1.7  $\mu$ g ml<sup>-1</sup>) with the RBC-PL-robots and incubated them for 5 min under a US field. Then, the mixed solution was added to a 5% purified RBC solution and incubated for 30 min at 37°C. After this incubation,

the 5% RBC solution was centrifuged, and the absorbance of the supernatant was measured at 540 nm to determine the degree of hemolysis. The absorbance value obtained from a 5% RBC solution sonicated for 5 min was considered as 100% hemolysis, which allowed calculating the relative hemolysis percentage of all the samples (Fig. 4). The supernatant of RBCs incubated with free  $\alpha$ -toxin at the same concentration was used as a positive control (Fig. 4A, i), which gave a relative hemolysis close to 100% (Fig. 4B, i). However, substantial lower hemolysis (5.5%) was observed when using US-propelled RBC-PL-robots in the toxin solution (Fig. 4, A and B, iii). These results confirmed the effective binding of the membrane-coated robots to the toxin and indicated that the efficient US propulsion in the  $\alpha$ -toxin solution facilitated the number of robot-toxin contacts, improving the toxin absorption and its neutralization. This hemolysis percentage was slightly larger than the one obtained from samples treated with US-propelled RBC-robots (Fig. 4, A and B, iv). PBS without toxin was included as a negative control (Fig. 4, A and B, v). A 4.5 times lower hemolysis was found when using US-propelled RBC-PL-robots compared with the use of the RBC-PL-robots under static conditions (Fig. 4, A and B, ii versus iii), highlighting the important effect of the robot propulsion upon the efficiency of the de-toxification process.

To further examine the binding of PFTs to RBC-PL-robots and the following neutralization, we performed similar experiments using toxins naturally secreted from MRSA USA300 (Fig. 4, C and D), including  $\alpha$ -toxin, Pantone-Valentine leukocidin, and  $\phi$ -toxin (42). In this experiment, MRSA USA300 bacteria were grown for 8 hours, and at this time, an aliquot of the bacterial suspension was treated for 5 min with the US-propelled RBC-PL-robots or the other controls (i to v). After each treatment, the bacterial suspension was centrifuged, and 50  $\mu$ l of the supernatant containing PFTs was mixed with 5% purified RBC solution to quantify its hemolytic activity. Similar to the previous results, the US-propelled RBC-PL-robots produced lower

hemolysis when compared with static RBC-PL-robots (17% versus 40%; Fig. 4, C and D, iii versus iv), demonstrating the effective action of the propulsion. Under the acoustic field, the collective propulsion of the RBC-PL-robots can dramatically accelerate their binding with PFT mixture, thus enhancing the neutralization process. A tendency in the hemolysis percentage similar to the one obtained with commercial toxin was found for the rest of the controls (Fig. 4, C and D, i, iii, and iv). The absorbance spectra of oxyhemoglobin after incubation with purified commercial  $\alpha$ -toxin or a cocktail of bacteria-secreted PFTs in the different control experiments are shown in figs. S3 and S4, respectively. Overall, the results of Fig. 4 demonstrate that cloaking RBC-PL membranes onto the AuNW robots and moving these biomimetic robots under a US field result in dynamic detoxification vehicles that can efficiently remove PFTs from their environment.

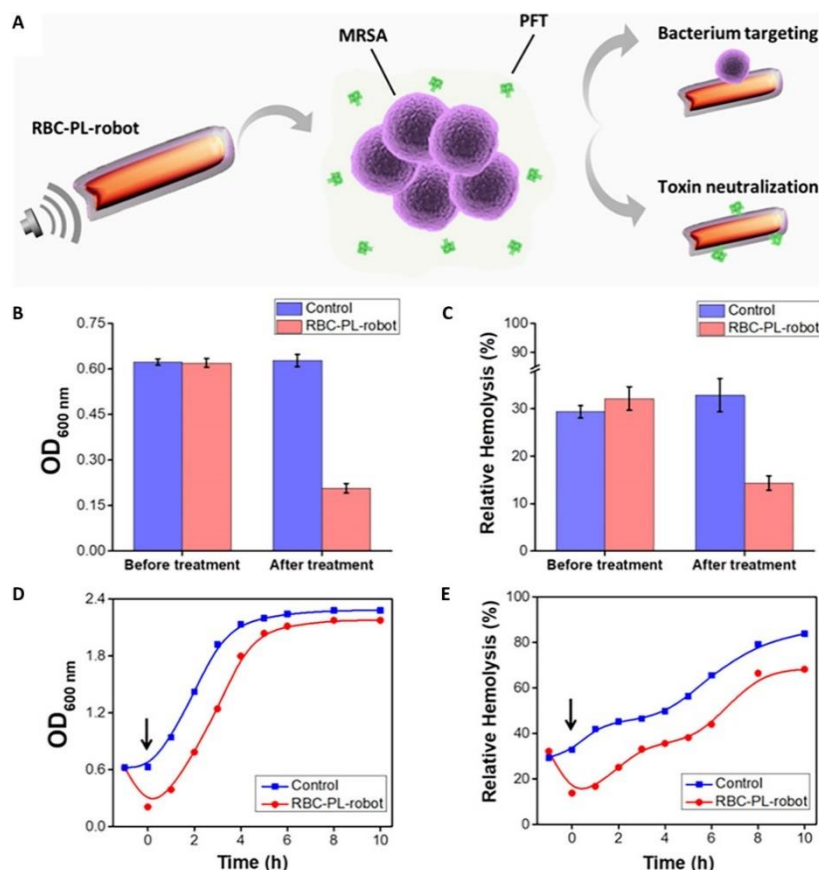


**Figure 5.2.5.** In situ concurrent removal of MRSA bacteria and MRSA-secreting PFTs by RBC-PL-robots. (A) Schematic of RBC-PL-robots for bacteria targeting and PFT neutralization. (B) Optical density values (OD<sub>600</sub>) of MRSA bacteria obtained before and after treatment (blue, without robots; red, RBC-PL-robots). (C) Relative hemolysis percentages of PFTs obtained before and after treatment (blue, without robots; red, RBC-PL-robots). Error bars estimated as a triple of SD ( $n = 3$ ). (D) MRSA bacterial growth curves (indicated by OD<sub>600</sub>) versus incubation time for nontreated bacteria and bacteria treated with RBC-PL-robots. (E) Corresponding relative hemolysis curves versus incubation time for nontreated bacteria and bacteria treated with RBC-PL-robots. Arrows indicate first measurement right after treatment.

### Concurrent removal of bacteria and bacteria-secreting PFTs by RBC-PL-robots

To further examine the dual detoxification ability of these biomimetic nanorobots for binding and isolation of PL-adhering pathogens and neutralization of bacterial toxins, we performed a combined application for MRSA targeting and PFT neutralization (Fig. 5A). In this specific study, the RBC-PL-robots were incorporated with a nickel segment to enable the magnetic separation of the robots after the treatment (fig. S5). To test the combined detoxification action, we compared an MRSA bacterial sample treated with US-propelled RBC-PL-robots with a nontreated bacterial control (Fig. 5, red versus blue). A detailed schematic showing the

experimental protocol followed to perform the combined application is shown in fig. S6 (see also Materials and Methods). Briefly, we took two aliquots of MRSA USA300 bacteria from the same culture: One was treated by US-propelled RBC-PL-robots, and one served as an untreated control.

Before performing the robot treatment, the optical density at a wave-length of 600 nm (OD<sub>600</sub>) and hemolysis percentage were calculated for aliquots taken from both MRSA samples. As shown in Fig. 5 (B and C), both OD<sub>600</sub> and hemolysis values were very similar for both bacteria samples before the treatment. Afterward, RBC-PL-robots were added to the bacterial suspension under a US field for 5 min. After the robot treatment, the robots were magnetically separated from the bacterial suspension. Then, the treated bacterial sample and the nontreated control sample were grown for 10 hours under the same conditions. The OD<sub>600</sub> of both samples was monitored every hour during the first 6 hours and then every 2 hours until the end of the experiment to construct the respective curves (Fig. 5D). In parallel, aliquots of both bacterial samples were collected and centrifuged, saving the supernatants to perform the hemolysis assay (Fig. 5, C and E). As shown in Fig. 5 (B and C, red columns), both the OD and hemolysis values notably decreased in the RBC-PL-robot sample at the 0-hour time point (right after the 5-min robot treatment or nontreatment control, indicated by black arrows). Specifically, in the robot-treated sample, the OD and the hemolysis decreased 3.1 and 2.2 times, respectively, when compared with the control sample (Fig. 5, B and C, red versus blue columns). These results demonstrate the rapid and effective detoxification ability of the RBC-PL-robots, which can simultaneously bind to MRSA bacteria and neutralize the secreted PFTs from the same sample in a single treatment step.



### 5.2.3 Experimental

#### Nanorobot fabrication

The AuNW robots were prepared by a common membrane-template electrodeposition protocol. A thin gold film was first sputtered on one side of the porous PC membrane template containing 400-nm-diameter nanopores (catalog no. 110407, Whatman Nuclepore) to serve as a working electrode. The membrane was assembled in a Teflon plating cell with aluminum foil serving as an electrical contact for the subsequent electrodeposition. A sacrificial silver layer was electrodeposited into the branched area of the PC membrane using a charge of 0.1 C and a potential of  $-0.90$  V (versus a Ag/AgCl reference electrode, along with a Pt wire as a counter electrode). Subsequently, Au was plated by using a commercial gold plating solution (Orotemp 24 RTU Rack; Technic Inc., Anaheim, CA) at  $-1.0$  V (versus Ag/AgCl), with a charge of 1.5 C. The sputtered gold was removed by mechanical polishing using 3- to 4- $\mu$ m alumina powder. The silver sacrificial layer was removed by chemical etching using a cotton tip applicator soaked with 8 M HNO<sub>3</sub> solution. The removal of this sacrificial layer helped to create the concave shape in one end of the gold wire nanorobot. The resulting AuNWs had a length between 1.5 and 2  $\mu$ m. The PC membrane was then dissolved in a pure methylene chloride solution for 30 min; this process was performed two times to completely release the AuNWs. The resulting nanorobots were separated from the solution by centrifugation at 8000 rpm for 5 min and washed two times with isopropanol, two times with ethanol, and three times with ultrapure water (18.2 megohm cm). Between washing steps, the nanorobot solution was centrifuged at 8000 rpm for 3 min. All AuNWs were stored in 1 ml of ultrapure water at room temperature until use. Magnetic robots were prepared following a similar protocol. A sacrificial silver layer was electrodeposited using a charge

of 0.1 C and a potential of  $-0.90$  V (versus a Ag/AgCl reference electrode, along with a Pt wire as a counter electrode). Subsequently, Au was plated at  $-1.0$  V (versus Ag/AgCl) using a charge of 0.6 C, followed by Ni electrodeposition at  $-1.3$  V (versus Ag/AgCl) using a charge of 0.4 C. Then, Au was electro-deposited again ( $-1.0$  V and 0.6 C), and the rest of the protocol was performed as described above.

### **RBC-PL-robot preparation**

RBC-PL-robots were prepared by enclosing AuNW robots with the dual plasma membranes derived from RBCs and PLs. Human RBC membranes were derived from whole blood (BioreclamationIVT) as previously described (43). Briefly, whole blood was centrifuged at 800g for 5 min at  $4^{\circ}\text{C}$ , and the serum and buffy coat were discarded. The remaining RBC pellet was then treated with hypotonic medium to remove hemoglobin. After three hypotonic treatment and wash cycles, the pink pellet of RBC membranes was obtained and stored at  $-80^{\circ}\text{C}$  until use. Human PL membranes were prepared from PL-rich plasma (San Diego Blood Bank) following previously described methods (22). After obtaining purified PLs, PL membranes were derived using a repeated freeze-thaw process and washed by centrifugation in PBS solution mixed with protease inhibitor tablets. Aliquots of suspensions were first frozen at  $-80^{\circ}\text{C}$ , thawed at room temperature, and pelleted by centrifugation at 4000g for 3 min. After three repeated washes, the pelleted PL membranes were suspended in water and stored at  $-80^{\circ}\text{C}$  until use. After having isolated both RBC and PL membranes, the hybrid membranes were prepared via fusion of both membranes (1:1 protein weight ratio) under 5-min ultrasonication (42 kHz, 100 W).

In parallel, the surface of the AuNWs was modified with 0.25 mM MPA (Sigma-Aldrich) through overnight incubation to introduce negative charges onto the gold surface. After the

incubation, the AuNWs were washed with deionized water three times, repeating centrifugation processes (8000 rpm, 3 min) between each washing step. Then, the MPA-AuNWs were coated with the resulting hybrid membranes after 5-min ultrasonication (42 kHz, 100 W).

### **RBC-PL-robot characterization**

SEM images of bare and RBC-PL-robots were obtained with a Philips XL30 environmental scanning electron microscope instrument using an acceleration voltage of 10 kV. To further confirm the presence and cloaking of RBC-PL hybrid membranes onto the surface of the AuNW robots, we labeled RBC membranes with DiD (excitation/ emission=644/665 nm; Sigma-Aldrich), and PL membranes were labeled with FITC (excitation/emission = 495/525 nm; Sigma-Aldrich) before being coated on the AuNWs. Fluorescence microscopy images were captured by using an EVOS FL microscope coupled with 20 $\times$  and 40 $\times$  microscope objectives. To determine the protein content of the RBC-PL-robots, we centrifuged both bare robots and RBC-PL-robots (20 mg ml<sup>-1</sup>) and resuspended them with 1 $\times$  PBS three times. After that, the RBC-PL-robots were exposed to the acoustic field for 5 min, and then a BCA colorimetric assay (Sigma-Aldrich) was used to quantitatively measure the level of membrane proteins on the nanorobot surface. Briefly, the purple-colored reaction product of this assay is formed by the chelation of two molecules of BCA with one cuprous ion, and this water-soluble complex exhibits a strong absorbance at 562 nm that is nearly linear with increasing protein concentrations. Gel electrophoresis followed by protein staining with Coomassie blue was also performed. The RBC-PL hybrid membrane and RBC-PL-robot samples containing equivalent total proteins were prepared in lithium dodecyl sulfate sample loading buffer (Invitrogen). The samples were then separated on a 4 to 12% bis-tris 17-well MiniGel in Mops running buffer using a Novex XCell SureLock Electrophoresis System (Life Technologies). Last, the protein columns were stained according to the manufacturer's protocol.

## **Ultrasound equipment and propulsion studies**

The acoustic cell setup consisted of a piezoelectric transducer (Ferroperm PZ26 disk; 10 mm diameter, 0.5 mm thickness) responsible for the generation of US waves, attached by conductive epoxy glue to the bottom center of a steel plate (50 mm by 50 mm by 0.94 mm); the steel plate was covered with a 240- $\mu$ m Kapton tape protective layer that contains a circular reservoir at the center (5 mm). A glass slide was used to cover the reservoir for US reflection and to protect the sample. The continuous US sine wave was applied via a piezoelectric transducer, through an Agilent 15-MHz arbitrary waveform generator, in connection to a homemade power amplifier. All experiments were performed by mixing the RBC-PL-robots with corresponding media (water, PBS, or whole blood) or samples (MRSA USA300 or toxins) and by applying a continuous sine wave form that had a frequency of 2.66 MHz and a voltage amplitude of 2.0 V. Videos were captured using a CoolSNAP HQ2 camera, with 20 $\times$  and 40 $\times$  objectives (unless mentioned otherwise), and acquired at 10 frames per second using the MetaMorph 7.1 software (Molecular Devices, Sunnyvale, CA). The particle displacement image stacking was performed using ImageJ software and Flow Trace Plugin (44).

## **Binding and isolation of PL-adhering pathogens**

RBC-PL-robots were assessed for selective binding and rapid isolation of PL-adhering pathogens using MRSA USA300 (BAA-1717; American Type Culture Collection) as a model pathogen. The bacteria were cultured on tryptic soy broth (TSB) agar (Becton, Dickinson and Company) overnight at 37°C. A single colony was inoculated in TSB medium at 37°C in a rotary shaker. Overnight culture was refreshed in TSB medium at a 1:100 dilution at 37°C under shaking for another 3 hours. RBC-

PL-robots ( $10 \text{ mg ml}^{-1}$ ) were mixed with the bacterial suspension ( $5 \times 10^8 \text{ CFU ml}^{-1}$ ), and they

were incubated for 5 min under a US field (2.66 MHz and 2.0 V). After the US incubation, the robots were re-collected through precipitation, and the adhered bacteria were fixed with formalin and stained with DAPI (Sigma-Aldrich).

### **Binding and neutralization of PFTs**

RBC-PL-robots were tested as a toxin decoy to absorb and neutralize PFTs using  $\alpha$ -toxin as a model toxin. A fixed amount of commercial  $\alpha$ -toxin ( $1.7 \mu\text{g ml}^{-1}$ ; IBT Bioservices) was mixed with the RBC-PL-robots ( $10 \text{ mg ml}^{-1}$ ) and incubated under a US field for 5 min (2.66 MHz and 2.0 V). After the US treatment, the mixed solution was added to a 5% purified RBC solution and incubated for 30 min at  $37^\circ\text{C}$ . After such incubation, the 5% RBC solution was centrifuged, and the absorbance of the supernatant was measured at 540 nm to determine the degree of hemolysis (corresponding to the absorbance spectra of oxyhemoglobin).

To perform the experiments using toxins naturally secreted from MRSA USA300 bacteria, we refreshed overnight bacterial culture in TSB medium at a 1:100 dilution at  $37^\circ\text{C}$  under shaking for another 8 hours. The bacterial suspension was centrifuged at 5000g for 5 min to collect the culture supernatant. We treated 50  $\mu\text{l}$  of bacterial culture medium containing secreted PFTs with the US-propelled RBC-PL-robots ( $10 \text{ mg ml}^{-1}$ ; 2.66 MHz and 2.0 V) and the rest of the controls for 5 min. After treatment and centrifugation, the supernatant from each group was collected and measured for the degree of hemolysis.

### **Concurrent removal of bacteria and bacteria-secreting PFTs**

To test the combined detoxification action of the RBC-PL-robots, we took two aliquots of MRSA USA300 bacteria from the same liquid culture to perform the RBC-PL-robot treatment and to serve as a nontreated control, respectively. Before performing the robot treatment,  $\text{OD}_{600}$  and

hemolysis percentage were measured for aliquots taken from both MRSA samples. Afterward, magnetic RBC-PL-robots ( $10 \text{ mg ml}^{-1}$ ) were added to the bacterial suspension ( $5 \times 10^8 \text{ CFU ml}^{-1}$ ) under a US field for 5 min (2.66 MHz and 2.0 V). After the robot treatment, the RBC-PL-robots were magnetically separated from the bacterial suspension. Then, the treated bacterial sample and the nontreated control sample were grown for 10 hours under the same conditions. The OD600 of both bacterial samples was monitored every hour during the first 6 hours and then every 2 hours until the end of the experiment. In parallel, 50- $\mu$ l aliquots of both bacterial samples were collected and centrifuged (13,200 rpm, 5 min), saving the supernatants to perform the hemolysis assay (5% RBC solution plus  $\alpha$ -toxin, 30 min at 37°C). The relative hemolysis percentages were calculated considering 100% hemolysis, the absorbance value obtained from 5% RBC solution sonicated for 5 min. All the hemolysis studies were performed in the presence of 200 nM 1,4-dithiothreitol (Sigma-Aldrich).

#### 5.1.4 Conclusion

In summary, we have demonstrated that the use of dual cell membranes to modify synthetic nanorobots represents a versatile approach for interfacing natural and synthetic biomaterials to form biomimetic robots. The synergy of combining hybrid biological membranes with mobile robots leads to a powerful platform for diverse biomedical applications. In particular, the biomimetic RBC-PL-robots reported in this proof-of-concept work consisted of an acoustic AuNW robot (selected as a model of fuel-free robots) cloaked with RBC-PL hybrid membranes. The resulting biomimetic fuel-free robots offer a one-step detoxification treatment for simultaneous bacterium targeting and toxin neutralization. Such hybrid cell membrane-coated nanorobots can thus act as a robust mobile therapeutic device capable of accelerating multiple processes, including

bacterial detoxification and toxin neutralization. In this work, such capability to accelerate multiple processes was demonstrated for the binding and removal of PL-adhering pathogens (e.g., *S. aureus* bacteria) and technology could be readily adapted to a wide range of nanorobots with different propulsion mechanisms. Coating nanorobots with multi-functional biomembranes imparts important capabilities to robotic technology that are difficult to achieve with uncoated robots.

Although this proof-of-concept work is still at an early stage and requires further improvement and evaluations of the cell membrane–coated robots before their potential uses, it opens the door to the use of fuel-free biomimetic nanorobots as an active broad-spectrum bio-detoxification platform. Overall, the ability to concurrently remove pathogenic bacteria and toxins of these biomimetic nanorobots offers considerable interest for diverse therapeutic and detoxification applications. Such biomimetic nanorobots that integrate natural cellular functions with synthetic nanomachines are expected to provide opportunities and inspire ideas for rapidly emerging robotic research and development.

## **Acknowledgements**

This work was supported by the Defense Threat Reduction Agency Joint Science and Technology Office for Chemical and Biological Defense (grant nos. HDTRA1-13-1-0002 and HDTRA1-14-1-0064). F.S. acknowledges fellowship from The University of California Institute for Mexico and the United States (UC MEXUS) and El Consejo Nacional de Ciencia y Tecnología (CONACYT). Author contributions: All authors contributed to the writing of the manuscript. All authors have given approval to the final version of the manuscript.

Chapter 5.2, in full, is a reprint of the material as it appears in Science Robotics, 2018, Berta Esteban-Fernández de Ávila, Pavimol Angsantikul, Doris E. Ramírez-Herrera, Fernando Soto, Hazhir Teymourian, Diana Dehaini, Yijie Chen, Liangfang Zhang and Joseph Wang. The dissertation author was a contributor and co-author of this paper.



## References

1. J. Wang, *Nanomachines: Fundamentals and Applications* (Wiley-VCH, 2013).
2. J. Li, B. Esteban-Fernández de Ávila, W. Gao, L. Zhang, J. Wang, Micro/nanorobots for biomedicine: Delivery, surgery, sensing, and detoxification. *Sci. Robot.* 2, eaam6431 (2017).
3. W. F. Paxton, K. C. Kistler, C. C. Olmeda, A. Sen, S. K. St. Angelo, Y. Cao, T. E. Mallouk, P. E. Lammert, V. H. Crespi, Catalytic nanomotors: Autonomous movement of striped nanorods. *J. Am. Chem. Soc.* 126, 13424–13431 (2004).
4. X. Yan, Q. Zhou, M. Vincent, Y. Deng, J. Yu, J. Xu, T. Xu, T. Tang, L. Bian, Y.-X. J. Wang, K. Kostarelos, L. Zhang, Multifunctional biohybrid magnetite microrobots for imaging-guided therapy. *Sci. Robot.* 2, eaaq1155 (2017).
5. W. Wang, L. A. Castro, M. Hoyos, T. E. Mallouk, Autonomous motion of metallic microrods propelled by ultrasound. *ACS Nano* 6, 6122–6132 (2012).
6. W. Gao, J. Wang, The environmental impact of micro/nanomachines: A review. *ACS Nano* 8, 3170–3180 (2014).
7. D. Vilela, M. M. Stanton, J. Parmar, S. Sánchez, Microbots decorated with silver nanoparticles kill bacteria in aqueous media. *ACS Appl. Mater. Interfaces* 9, 22093–22100 (2017).
8. M. Hoop, Y. Shen, X-Z. Chen, F. Mushtaq, L. M. Iuliano, M. S. Sakar, A. Petruska, M. J. Loessner, B. J. Nelson, S. Pané, Magnetically driven silver-coated nanocoils for efficient bacterial contact killing. *Adv. Funct. Mater.* 26, 1063–1069 (2016).
9. J. Simmchen, A. Baeza, A. Miguel-Lopez, M. M. Stanton, M. Vallet-Regi, D. Ruiz-Molina, S. Sánchez, Dynamics of novel photoactive AgCl microstars and their environmental applications. *ChemNanoMat* 3, 65–71 (2017).
10. J. Parmar, K. Villa, D. Vilela, S. Sánchez, Platinum-free cobalt ferrite based micromotors for antibiotic removal. *Appl. Mater. Today* 9, 605–611 (2017).
11. J. Li, W. Liu, T. Li, I. Rozen, J. Zhao, B. Bahari, B. Kante, J. Wang, Swimming microrobot optical nanoscopy. *Nano Lett.* 16, 6604–6609 (2016).
12. C. Chen, X. Chang, P. Angsantikul, J. Li, B. Esteban-Fernández de Ávila, E. Karshalev, W. Liu, F. Mou, S. He, R. Castillo, Y. Liang, J. Guan, L. Zhang, J. Wang, Chemotactic guidance of synthetic organic/inorganic payloads functionalized sperm micromotors. *Adv. Biosyst.* 2, 1700160 (2018).
13. O. Felfoul, M. Mohammadi, S. Taherkhani, D. de Lanauze, Y. Z. Xu, D. Loghin, S. Essa, S. Jancik, D. Houle, M. Lafleur, L. Gaboury, M. Tabrizian, N. Kaou, M. Atkin, T. Vuong,

G. Batist, N. Beauchemin, D. Radzioch, S. Martel, Magneto-aerotactic bacteria deliver drug-containing nanoliposomes to tumour hypoxic regions. *Nat. Nanotechnol.* 11, 941–947 (2016).

14. C.-M. J. Hu, R. H. Fang, J. Copp, B. T. Luk, L. Zhang, A biomimetic nanosponge that absorbs pore-forming toxins. *Nat. Nanotechnol.* 8, 336–340 (2013).

15. C. J. Rosado, S. Kondos, T. E. Bull, M. J. Kuiper, R. H. P. Law, A. M. Buckle, I. Voskoboinik, P. I. Bird, J. A. Trapani, J. C. Whisstock, M. A. Dunstone, The MACPF/CDC family of pore-forming toxins. *Cell. Microbiol.* 10, 1765–1774 (2008).

16. B. F. C. Kafsack, J. D. O. Pena, I. Coppens, S. Ravindran, J. C. Boothroyd, V. B. Carruthers, Rapid membrane disruption by a perforin-like protein facilitates parasite exit from host cells. *Science* 323, 530–533 (2009).

17. J.-G. Piao, L. Wang, F. Gao, Y.-Z. You, Y. Xiong, L. Yang, Erythrocyte membrane is an alternative coating to polyethylene glycol for prolonging the circulation lifetime of gold nanocages for photothermal therapy. *ACS Nano* 8, 10414–10425 (2014).

18. W. Gao, C.-M. J. Hu, R. H. Fang, B. T. Luk, J. Su, L. Zhang, Surface functionalization of gold nanoparticles with red blood cell membranes. *Adv. Mater.* 25, 3549–3553 (2013).

19. S. Aryal, C.-M. J. Hu, R. H. Fang, D. Dehaini, C. Carpenter, D.-E. Zhang, L. Zhang, Erythrocyte membrane-cloaked polymeric nanoparticles for controlled drug loading and release. *Nanomedicine* 8, 1271–1280 (2013).

20. Z. Pang, C.-M. J. Hu, R. H. Fang, B. T. Luk, W. Gao, F. Wang, E. Chuluun, P. Angsantikul, S. Thamphiwatana, W. Lu, X. Jiang, L. Zhang, Detoxification of organophosphate poisoning using nanoparticle bioscavengers. *ACS Nano* 9, 6450–6458 (2015).

21. F. Wang, W. Gao, S. Thamphiwatana, B. T. Luk, P. Angsantikul, Q. Zhang, C.-M. J. Hu, R. H. Fang, J. A. Copp, D. Pornpattananangkul, W. Lu, L. Zhang, Hydrogel retaining toxin-absorbing nanosponges for local treatment of methicillin-resistant *Staphylococcus aureus* infection. *Adv. Mater.* 27, 3437–3443 (2015).

22. C.-M. J. Hu, R. H. Fang, K.-C. Wang, B. T. Luk, S. Thamphiwatana, D. Dehaini, P. Nguyen, P. Angsantikul, C. H. Wen, A. V. Kroll, C. Carpenter, M. Ramesh, V. Qu, S. H. Patel, J. Zhu, W. Shi, F. M. Hofman, T. C. Chen, W. Gao, K. Zhang, S. Chien, L. Zhang, Nanoparticle biointerfacing by platelet membrane cloaking. *Nature* 526, 118–121 (2015).

23. Z. Wu, T. Li, W. Gao, T. Xu, B. Jurado-Sánchez, J. Li, W. Gao, Q. He, L. Zhang, J. Wang, Cell-membrane-coated synthetic nanomotors for effective biodetoxification. *Adv. Funct. Mater.* 25, 3881–3887 (2015).

24. Z. Wu, J. Li, B. Esteban-Fernández de Ávila, T. Li, W. Gao, Q. He, L. Zhang, J. Wang, Water-powered cell-mimicking Janus micromotor. *Adv. Funct. Mater.* 25, 7497–7501 (2015).
25. J. Li, P. Angsantikul, W. Liu, B. Esteban-Fernández de Ávila, X. Chang, E. Sandraz, Y. Liang, S. Zhu, Y. Zhang, C. Chen, W. Gao, L. Zhang, J. Wang, Biomimetic platelet-camouflaged nanorobots for binding and isolation of biological threats. *Adv. Mater.* 30, 1704800 (2018).
26. V. Garcia-Gradilla, J. Orozco, S. Sattayasamitsathit, F. Soto, F. Kuralay, A. Pourazary, A. Katzenberg, W. Gao, Y. Shen, J. Wang, Functionalized ultrasound-propelled magnetically guided nanomotors: Toward practical biomedical applications. *ACS Nano* 7, 9232–9240 (2013).
27. D. Dehaini, X. Wei, R. H. Fang, S. Masson, P. Angsantikul, B. T. Luk, Y. Zhang, M. Ying, Y. Jiang, A. V. Kroll, W. Gao, L. Zhang, Erythrocyte–platelet hybrid membrane coating for enhanced nanoparticle functionalization. *Adv. Mater.* 29, 1606209 (2017).
28. K. J. Rao, F. Li, L. Meng, H. Zheng, F. Cai, W. Wang, A force to be reckoned with: A review of synthetic microswimmers powered by ultrasound. *Small* 11, 2836–2846 (2015).
29. F. Nadal, E. Lauga, Asymmetric steady streaming as a mechanism for acoustic propulsion of rigid bodies. *Phys. Fluids* 26, 082001–082028 (2014).
30. F. Soto, G. L. Wagner, V. Garcia-Gradilla, K. T. Gillespie, D. R. Lakshmipathy, E. Karshalev, C. Angell, Y. Chen, J. Wang, Acoustically propelled nanoshells. *Nanoscale* 8, 17788–17793 (2016).
31. S. Ahmed, W. Wang, L. Bai, D. T. Gentekos, M. Hoyos, T. E. Mallouk, Density and shape effects in the acoustic propulsion of bimetallic nanorod motors. *ACS Nano* 10, 4763–4769 (2016).
32. L. Ricotti, B. Trimmer, A. W. Feinberg, R. Raman, K. K. Parker, R. Bashir, M. Sitti, S. Martel, P. Dario, A. Menciassi, Biohybrid actuators for robotics: A review of devices actuated by living cells. *Sci. Robot.* 2, eaq0495 (2017).
33. D. Ahmed, T. Baasch, B. Jang, S. Pane, J. Dual, B. J. Nelson, Artificial swimmers propelled by acoustically activated flagella. *Nano Lett.* 16, 4968–4974 (2016).
34. T. Qiu, S. Palagi, A. G. Mark, K. Melde, F. Adams, P. Fischer, Wireless actuation with functional acoustic surfaces. *Appl. Phys. Lett.* 109, 191602 (2016).
35. J. J. Kwan, R. Myers, C. M. Coviello, S. M. Graham, A. R. Shah, E. Stride, R. C. Carlisle, C. C. Coussios, Ultrasound-propelled nanocups for drug delivery. *Small* 11, 5305–5314 (2015).
36. I. R. Siboo, H. F. Chambers, P. M. Sullam, Role of SraP, a Serine-rich surface protein of *Staphylococcus aureus*, in binding to human platelets. *Infect. Immun.* 73, 2273–2280 (2005).
37. J. R. Fitzgerald, T. J. Foster, D. Cox, The interaction of bacterial pathogens with platelets. *Nat. Rev. Microbiol.* 4, 445–457 (2006).

38. C. Meesters, A. Brack, N. Hellmann, H. Decker, Structural characterization of the  $\alpha$ -hemolysin monomer from *Staphylococcus aureus*. *Proteins* 75, 118–126 (2009).
39. L. Song, M. R. Hobaugh, C. Shustak, S. Cheley, H. Bayley, J. E. Gouaux, Structure of staphylococcal  $\alpha$ -hemolysin, a heptameric transmembrane pore. *Science* 274, 1859–1866 (1996).
40. D. Pornpattananankul, L. Zhang, S. Olson, S. Aryal, M. Obonyo, K. Vecchio, C.-M. Huang, L. Zhang, Bacterial toxin-triggered drug release from gold nanoparticle-stabilized liposomes for the treatment of bacterial infection. *J. Am. Chem. Soc.* 133, 4132–4139 (2011).
41. P. O'Hanley, G. Lalonde, G. Ji, Alpha-hemolysin contributes to the pathogenicity of piliated digalactoside-binding *Escherichia coli* in the kidney: Efficacy of an alpha-hemolysin vaccine in preventing renal injury in the BALB/c mouse model of pyelonephritis. *Infect. Immun.* 59, 1153–1161 (1991).
42. X. Wei, J. Gao, F. Wang, M. Ying, P. Angsantikul, A. V. Kroll, J. Zhou, W. Gao, W. Lu, R. H. Fang, L. Zhang, In situ capture of bacterial toxins for antivirulence vaccination. *Adv. Mater.* 29, 1701644 (2017).
43. C.-M. J. Hu, L. Zhang, S. Aryal, C. Cheung, R. H. Fang, L. Zhang, Erythrocyte membrane-camouflaged polymeric nanoparticles as a biomimetic delivery platform. *Proc. Natl. Acad. Sci. U.S.A.* 108, 10980–10985 (2011).
44. W. Gilpin, V. N. Prakash, M. Prakash, Flowtrace: Simple visualization of coherent structures in biological fluid flows. *J. Exp. Biol.* 220, 3411–3418 (2017).

# Chapter 6

---

## Conclusions

## Nanoparticles for Targeted Delivery and Detoxification

Nanoparticles specifically targeted to the location of a disease or pathogen show significant benefits over untargeted delivery of free drug. Targeting can prevent toxicity, reduce unintended off-target effects of the drug, and allow for higher efficacy using less drug. Many biomimetic strategies for designing targeted nanoparticle platforms have been developed and discussed. Here we summarize the novel contributions to the nanomedicine field and new tools developed for designing drug delivery vehicles.

Ultra-small lipid-polymer hybrid nanoparticles functionalized with a folate receptor targeting molecule were built and tested for chemotherapeutic delivery. At 25nm, they are the smallest lipid polymer hybrid particle yet developed. Due to their small size they can provide significantly improved tumor penetration. These particles are coated with a PEG shell, and functionalized with folate receptor targeting moieties to promote tumor targeting. They are able to be loaded with the tumor drug docetaxel, and show improved targeting and penetration ability *in vitro* and *in vivo*, slowing the tumor progression in a xenograft mouse model and resulting in better therapeutic efficacy. This evolution of the classical lipid polymer hybrid particle can expand its application and efficacy as a drug delivery system.

Cell membrane coatings, developed in 2011, heralded in the next generation of targeting strategies. Cloaking drug loaded polymeric nanoparticles in cell membranes allows them to gain the targeting mechanisms and functionalities unique to that cell type. Red blood cell membrane coated nanoparticles are highly biocompatible and long circulating, with the stealth marker CD47 shielding them from being destroyed by the immune system. They have shown efficacy as a drug delivery carrier; loading red blood cell membrane coated nanoparticles with doxorubicin

allowed for improved efficacy against solid tumors as compared to free doxorubicin. Red blood cell membrane also has the added ability of toxin neutralization. Bacteria can secrete pore forming toxins which target and destroy red blood cells. Red blood cell nanoparticles can act as decoys, allowing these toxins to be sequestered and neutralized. This dual functionality of toxin removal and long circulation of the red blood cell membrane makes these particles a robust choice for a drug delivery vehicle.

Platelet membrane also has many surface functionalities and targeting moieties that make it an idea membrane for drug delivery, particularly for applications in bacterial infection, cardiovascular disease, and cancer treatment. Platelets possess proteins and receptors that can scavenge for and bind to sites of inflammation, and platelet membrane coated nanoparticles also have this ability. Platelet membrane coated nanoparticles were shown to bind to sites of atherosclerosis, for both treatment and imaging purposes. They were also able to successfully target bacteria, *in vitro* and *in vivo*. Platelet membrane coated particles loaded with antibiotics were also used to effectively manage a bacterial infection, with a much lower dose of antibiotics than needed to treat mice without the platelet membrane coated nanoparticle encapsulation. Platelets also naturally bind to cancer cells, particularly circulating tumor cells. Platelet membrane coated particles have been shown to bind to these cell types, making them a candidate for chemotherapeutic delivery as well.

Fusions of multiple cell types have the potential to revolutionize these cell membrane coating technologies, and allow for modular construction of particles based on the needs of the application. Membrane fusion cloaks can combine membranes from multiple cell types, and these resulting nanoparticles have expanded abilities. Two cell membranes, platelet and red blood cell, were fused together and coated onto polymeric nanoparticles, creating particles with

hybrid properties. This new particle retained functionalities from both cell types, allowing tailoring to a specific need. The fusion particles were used to neutralize toxins as well as bind to bacteria. These particles could also bind to cancer, and to hallmarks of cardiovascular disease such as exposed collagen. Recent technology, such as immunostaining and improved electron microscopy, allowed for careful evaluation of the nanoparticle surface to show both cell membrane types are present on a single nanoparticle surface.

The ability to combine cell types onto a single particle may be used in the future to create synergism between properties of different cell types, minimization of unwanted effects of a specific cell type, or dilution of a membrane type that is difficult to obtain. Fusion membranes can be designed and mixed at varying ratios with potentially unlimited cell types, which allows for facile tailoring the surface properties. Through fusion technology, nanoparticles can be easily designed to have the exact surface properties needed for a particular application, without the need for complex functionalization chemistry or synthetic materials.